

DESIGN AND DEVELOPMENT OF THE ELECTRICAL SYSTEMS IN AN ELECTRIC FORMULA SAE RACE CAR

MATT BARHAM

A THESIS SUBMITTED IN PARTIAL FULFILMENT
OF THE REQUIREMENTS FOR THE DEGREE OF
MASTER OF ENGINEERING
IN
ELECTRICAL AND ELECTRONIC ENGINEERING
AT THE
UNIVERSITY OF CANTERBURY,
CHRISTCHURCH, NEW ZEALAND.

2017

ABSTRACT

Formula SAE is a global competition which challenges students to design and build a formula-style race car, which they then compete with in a series of dynamic and static events. In 2016, the University of Canterbury Motorsport team endeavoured to produce a four-wheel drive electric race car; the first of its kind for a New Zealand team.

The race car, named UCM16, featured four individually controllable AMK DD5-14-10-POW permanent-magnet synchronous servo motors controlled by an AMKASYN KW26-S5-FSE-4Q quad-package three-phase full-bridge inverter. Two revisions of a vehicle control unit were developed in-house, which relayed driver commands to the inverter via a dual-CAN communication bus. Torque vectoring, traction control and tractive power limiting algorithms were developed on the later revision of the control unit, dramatically increasing UCM16's dynamic performance.

A 588 Vdc, 8.8 kWh tractive battery pack was initially designed; consisting of 980 Samsung 18650-25R5 LiNiCoAlO₂ cells in eight interchangeable battery modules. However, post-manufacturing tolerances meant the tractive pack had to be reduced to a 7.9 kWh, 529.2 Vdc variant. The cells in each battery module were connected by resistance welding bespoke nickel busbars to each terminal. Modules were then connected in series to complete the tractive pack.

The race car was initially tested in a rear-wheel drive configuration. During the testing sessions, the vulnerability of the purchased battery management system to the electromagnetic interference emitted by the inverter caused the tractive system to disable mid-drive. To resolve this, the core functionality of the unit was transferred to a custom controller PCB, which also incorporated the remaining monitoring systems for the tractive battery. Testing also highlighted key areas which needed to be refined for reliability and system cohesiveness.

UCM16 placed 12th overall in the 2016 Formula SAE Australasian competition, held at Calder Park Raceway, Melbourne, Australia. A first-place finish in the skid-pad event made the University of Canterbury Motorsport team the first electric team to win a dynamic event at the Australasian competition. Unfortunately, reliability issues with the electric powertrain meant UCM16 was unable to finish either of the endurance events. Whilst numerous causes were speculated, data recorded throughout the event (and pre-event testing) could not validate any theories.

ACKNOWLEDGEMENTS

First, I would like to thank my supervisor Dr Paul Gaynor for your continued support and guidance throughout both my Master's and undergraduate studies. You have been a great mentor to me.

To the technical staff of the Electrical Department (David, Edsel, Jac, Ken, Mike, Paul and Philipp), thank you for all your expertise over these last two years. Without your help, UCM16 would never have become what it is today.

Thank you to my close friends and family for your never-ending encouragement, and for keeping me going when I felt like giving up. Mum and Dad, thank you for always being there, especially when times were tough.

I would like to thank each and every member of the University of Canterbury Motorsport team. We achieved what many thought was impossible. It wasn't easy, but we produced an amazing car, and I'm proud to have worked with you all. Special thanks go to Hamish for your persistent micro-managing and timeline updates (I apologise for always missing your deadlines). Jeremy and Nick, thanks for your dedication, even when everything was going wrong and we were pushed to the limit. Without a doubt, UCM16 would not have driven without your help.

Finally, thanks to Toby White for the use of his photos in this thesis.



2016 University of Canterbury Motorsport Team, Melbourne

TABLE OF CONTENTS

ABSTRACT	iv
ACKNOWLEDGEMENTS	v
TABLE OF CONTENTS	vii
LIST OF FIGURES	xii
LIST OF TABLES	xvii
GLOSSARY OF TERMS	xviii
CHAPTER 1 INTRODUCTION	1
1.1. Formula SAE Competition Structure	4
1.2. Related Work	5
1.2.1. Electric Vehicles in the Automotive Industry	5
1.2.2. Electric Vehicle Technology in Motorsport	6
1.2.3. Electric Race Cars in Formula SAE	8
1.3. Thesis Overview	9
1.4. Author's Contribution to UCM16	9
CHAPTER 2 BACKGROUND	10
2.1. Motor Theory	10
2.2. Inverter Theory	14
2.3. Benefits of 4WD Electric Powertrains in FSAE	18
2.4. Controller Area Network	21
2.5. Electrochemical Cell Theory	23
2.6. Accumulator Management System Theory	26
2.7. Fuse Theory	27
2.8. Accumulator Isolation Relay Theory	28
2.9. Precharge & Discharge Theory	28
2.10. Chapter Summary	30

CHAPTER 3 ELECTRIC POWERTRAIN	31
3.1. AMK Formula Student Electric Racing Kit	31
3.1.1. Motor Description	32
3.1.2. Inverter Description	36
3.1.3. Motor Control	40
3.2. Initial System Development	41
3.2.1. CAN Controller	41
3.2.2. Dynamometer Testing Rig	42
3.2.3. Initial Vehicle Control Unit Design	45
3.3. Chapter Summary	46
CHAPTER 4 ACCUMULATOR & ENERGY MANAGEMENT	47
4.1. Battery Concept Designs	47
4.1.1. Capacity and Power Requirements	47
4.1.2. Design Constraints	49
4.1.3. Initial Battery Identification	50
4.1.4. AMS Selection	51
4.1.5. Concept 1: A123 Pouch Cells	52
4.1.6. Concept 2: Melasta Pouch Cells	54
4.1.7. Concept 3: 18650 Cells	59
4.2. Accumulator Isolation Relay Selection	64
4.3. Tractive Fuse Selection	64
4.4. Precharge PCB Design	66
4.4.1. Precharge Resistor Selection	66
4.4.2. Precharge Relay Selection	67
4.4.3. Precharge Fuse Selection	67
4.4.4. Control Scheme	68
4.4.5. Relay Driver & Coil Suppression	70
4.4.6. Voltage Indication Circuit	70
4.4.7. PCB Design	73
4.5. Discharge PCB Design	74
4.5.1. High Voltage Component Selection	74
4.5.2. Control Circuit Design	76
4.5.3. PCB Design	77
4.6. Precharge & Discharge Bench Testing	78
4.7. Accumulator Isolation PCB	81

4.7.1. Isolated Power Supply	81
4.7.2. Temperature Monitoring System Interface	82
4.7.3. Fault Signal Isolation	83
4.7.4. CAN Bus Isolation and STM32F105 Microcontroller	84
4.7.5. PCB Design	85
4.7.6. PCB Testing	86
4.8. Charger Selection	87
4.9. Accumulator Assembly	88
4.9.1. Battery modules	88
4.9.2. Accumulator Assembly	90
4.9.3. Final Assembly and Bench Testing	91
4.10. Chapter Summary	93
CHAPTER 5 SAFETY SYSTEM DESIGN	94
5.1. Shutdown Circuit	94
5.1.1. Interlocks	95
5.1.2. High Voltage Disconnect	98
5.2. Shutdown PCB	99
5.2.1. Insulation Monitoring Device	100
5.2.2. Brake System Plausibility Device	102
5.2.3. Supervising Microcontroller	104
5.2.4. PCB Design	104
5.3. Tractive System Activation Light	105
5.4. Chapter Summary	106
CHAPTER 6 NEW ZEALAND'S FIRST ELECTRIC FSAE CAR	107
6.1. Preliminary Vehicle Testing	107
6.1.1. RWD Inverter Wiring	107
6.1.2. RWD Inverter Commissioning with VCU	108
6.2. RWD Testing	110
6.2.1. EMI Interference with AMS	110
6.2.2. EMI Interference with Current Sensor	113
6.2.3. Accumulator Condition	117
6.2.4. Pulse Injection from dc/dc Converter	118
6.3. Transition to 4WD	119
6.3.1. Vehicle Control Unit Redesign	119
6.3.2. Motor Wiring	121

6.3.3. Inverter Reconfiguration	123
6.3.4. DC/DC Converter Redesign	125
6.3.5. Discharge PCB and IMD Repackaging	126
6.3.6. Accumulator Revision	127
6.3.7. Wiring Harness	131
6.3.8. Precharge PCB Redesign	134
6.4. Chapter Summary	137
CHAPTER 7 FORMULA SAE-A COMPETITION	138
7.1. Vehicle Dynamics Software Development	139
7.1.1. Sensor Measurements Using Direct Memory Access	139
7.1.2. Torque Vectoring	140
7.1.3. Traction Control	146
7.1.4. Power Limitation	149
7.2. Formula SAE-A Competition Results	151
7.2.1. Autocross	153
7.2.2. Endurance Event	158
7.3. Chapter Summary	165
CHAPTER 8 CONCLUSION	167
8.1. Recommendations	168
8.2. Final Mentions	169
APPENDIX A RESEARCHED ELECTRIC FSAE TEAMS	170
APPENDIX B LITTELFUSE L70S & KLKD FUSE TIME-CURRENT CURVES	171
APPENDIX C DD5-14-10-POW MOTOR DATASHEET	173
APPENDIX D AMK CAN MESSAGES	175
APPENDIX E CAN CONTROLLER PCB SCHEMATIC	177
APPENDIX F OPTIMUM LAP VEHICLE SIMULATION MODEL	178
APPENDIX G A123 AMP20M1HD-A CELL SELECTION TOOLS	180
APPENDIX H MELASTA CELL SELECTION MACRO & RESULTS	184
APPENDIX I PRECHARGE PCB SCHEMATIC	186
APPENDIX J DISCHARGE PCB SCHEMATICS	189
APPENDIX K ACCUMULATOR ISOLATION PCB SCHEMATICS	191

APPENDIX L SHUTDOWN PCB SCHEMATICS	201
APPENDIX M IMAGES OF INVERTER WIRING	208
APPENDIX N DC/DC CONVERTER SCHEMATIC	210
APPENDIX O REDESIGNED PRECHARGE PCB SCHEMATICS	211
APPENDIX P VOLTAGE INDICATION PCB SCHEMATICS	215
REFERENCES	217

LIST OF FIGURES

Figure 1.1. University of Canterbury Motorsport race cars competing at the Formula SAE Australasian competition in their respective years	3
Figure 1.2. Increase in global battery electric vehicle (BEV) and plug-in hybrid electric vehicle (PHEV) stock from 2010 to 2015	6
Figure 1.3. Image of Panasonic Jaguar Racing's Formula E race car	7
Figure 2.1. Cross-section of a permanent-magnet synchronous motor	11
Figure 2.2. Example torque-speed curves for induction and PMSM motors	13
Figure 2.3. Diagram of 3-phase full bridge inverter topology	15
Figure 2.4. Current excitation waveforms for PMAC (a) and BLDC (b) motors	15
Figure 2.5. Stator current space vector and components in three-phase time variant system	16
Figure 2.6. Stator current space vector and components in the (α, β) reference frame	16
Figure 2.7. Stator current space vector and components in (d, q) rotating reference frame	17
Figure 2.8. Example torque-speed curve of electric motor and IC engine	18
Figure 2.9. Weight transfer and corresponding friction forces generated by tyres during acceleration	20
Figure 2.10. Simplified diagram showing implementation of torque vectoring	21
Figure 2.11. Example of standard CAN message	22
Figure 2.12. Diagram of CAN bus physical layer	23
Figure 2.13. Examples of pouch (a), cylindrical (b) and prismatic (b) cell enclosures	25
Figure 2.14. Diagram of centralised (a) and distributed (b) AMS topologies	26
Figure 2.15. Diagram of centralised-slave AMS topology variation	27
Figure 2.16. Simplified diagram of UCM16 tractive system	28
Figure 2.17. Diagram of tractive system with precharge circuit	29
Figure 2.18. Diagram of tractive system with precharge and discharge circuits	30
Figure 3.1. AMK DD5-14-10-POW motor	33
Figure 3.2. DD5-14-10-POW motor performance curves	33
Figure 3.3. Adjusted peak and continuous power curves for DD5-14-10-POW motor	34
Figure 3.4. Adjusted peak and continuous torque curves for DD5-14-10-POW motor	35
Figure 3.5. Peak output torque comparison of AMK & Emrax motors adjusted for 80 kW peak power	35
Figure 3.6. CAD model of KW26-S5-FSE-4Q inverter	37
Figure 3.7. CAN network interface diagram for KW26-S5-FSE-4Q inverter	39

Figure 3.8. Graphical representation of inverter derating feature	39
Figure 3.9. Assembled CAN Controller PCB	41
Figure 3.10. Images of dynamometer test rig	42
Figure 3.11. Screenshot of datalogger application created for dynamometer test rig	43
Figure 3.12. Example data output of Profile B test	44
Figure 4.1. Performance metrics of UCM16 calculated by Optimum Lap	48
Figure 4.2. Simulated speed and power against elapsed time for 2011 FSAE-A endurance track	49
Figure 4.3. Diagram of A123 face-to-face alignment	53
Figure 4.4. Diagram of Module Layouts Considered	55
Figure 4.5. CAD model of 2p9s Melasta module concept	56
Figure 4.6. Exploded CAD model showing components of 2p9s module concept	57
Figure 4.7. Final assembly of Melasta accumulator concept	58
Figure 4.8. CAD model showing internal view of 2p9s module concept	58
Figure 4.9. CAD model of 7p18s 18650 module concept	61
Figure 4.10. Rear-view of 7p18s 18650 module concept	62
Figure 4.11. Simplified diagram of tractive system under short circuit conditions	65
Figure 4.12. Logic diagram of precharge control scheme	68
Figure 4.13. Tractive voltage measurement circuit	69
Figure 4.14. Precharge timer circuit	69
Figure 4.15. AIR coil driver and suppression Circuit	70
Figure 4.16. Depletion MOSFET constant current source	71
Figure 4.17. Voltage indication circuit schematic	72
Figure 4.18. Screenshot of Precharge PCB design	73
Figure 4.19. High voltage section of discharge circuit	75
Figure 4.20. Control section of discharge circuit	76
Figure 4.21. Screenshot of Discharge PCB design	77
Figure 4.22. Image of assembled Discharge PCB	78
Figure 4.23. Images of precharge and discharge bench testing	79
Figure 4.24. Oscilloscope plots of precharge and discharge bench tests. Channel 1 shows tractive voltage (V) and Channel 2 shows intermediate capacitor voltage (V).	80
Figure 4.25. Simplified diagram of Accumulator Isolation PCB as AMS master	81
Figure 4.26. Schematic extract of Elithion power source selector circuit	82
Figure 4.27. Schematic extract of Temperature Monitoring PCB interface circuit	82
Figure 4.28. Schematic extract of fault signal isolation circuit	83
Figure 4.29. Schematic extract of CAN repeater circuit	84
Figure 4.30. Screenshot of Accumulator Isolation PCB design	85
Figure 4.31. Assembled Accumulator Isolation PCB	86

Figure 4.32. Image of Accumulator Isolation PCB testing	86
Figure 4.33. Oscilloscope plot of repeated CAN message	87
Figure 4.34. Low voltage connection diagram for Brusa NLG514 charger	88
Figure 4.35. Image of assembled INR18650-25R5 module (excluding RadLok connectors and Formex cover)	89
Figure 4.36. Image showing good (top) and poor (bottom) resistance welds	89
Figure 4.37. Image of AMS cell boards assembled on 3D printed holder	90
Figure 4.38. Image of assembled accumulator	90
Figure 4.39. Image showing assembled front-end of Accumulator	91
Figure 4.40. Oscilloscope plot of oscillating precharge circuit	92
Figure 4.41. Image of first accumulator charge using Brusa NLG514 charger	92
Figure 5.1. Example shutdown circuit diagram	95
Figure 5.2. Diagram of shutdown circuit routing path and element location	96
Figure 5.3. Image of rear-left wheel assembly interlock	97
Figure 5.4. Diagram of tractive system with HVD	98
Figure 5.5. Images of High Voltage Disconnect	99
Figure 5.6. Shutdown circuit memory latch & power stage logic diagram	100
Figure 5.7. Image of Bender Isometer IR155-3204 Insulation Monitoring Device	101
Figure 5.8. Diagram showing location of IMD in tractive system	101
Figure 5.9. Logic diagram of IMD input stage	102
Figure 5.10. BSPD brake detection logic diagram	103
Figure 5.11. BSPD current measurement logic diagram	103
Figure 5.12. Image of assembled Shutdown PCB	104
Figure 5.13. Simplified diagram of TSAL driver	105
Figure 5.14. Screenshot of TSAL PCB design	106
Figure 5.15. Image of illuminated TSAL (rear-view) on UCM16	106
Figure 6.1. Image of inverter being wired for RWD	108
Figure 6.2. Image of stationary powertrain testing	109
Figure 6.3. Image of concentrically twisted wiring harness for inverter	109
Figure 6.4. Image of the author driving UCM16 on its first drive day	110
Figure 6.5. Screenshot of Elithion AMS graphical user interface showing a communication fault on cell bank 7 (red box with zero cells detected)	111
Figure 6.6. Concept diagram of serial-to-CAN interference solution	112
Figure 6.7. Oscilloscope plot of CAN bus at the output of the accumulator with inverter drives enabled	113
Figure 6.8. Oscilloscope plot of LEM HASS 100-S current sensor placed 1 m away from inverter	114

Figure 6.9. Oscilloscope plot of LEM HASS 100-S current sensor placed on accumulator container	115
Figure 6.10. Oscilloscope plot showing input (yellow trace) and output (green trace) of 2.3 Hz cut-off LPF	116
Figure 6.11. Plot of measured, extrapolated and expected tractive current	117
Figure 6.12. Oscilloscope plot showing Measured Disruptions of 5 V (yellow trace) and GND (green trace) planes on VCU PCB	118
Figure 6.13. Image of assembled VCU PCB (Revision 2)	121
Figure 6.14. Image of individual components for motor wiring	122
Figure 6.15. Image of assembled shield for motor connector	122
Figure 6.16. Image of assembled motor connector	123
Figure 6.17. Image of wiring on right side of inverter	124
Figure 6.18. CAD model showing inverter and accumulator location in UCM16	124
Figure 6.19. Simplified circuit diagram showing dc/dc converter with delayed ground switches	125
Figure 6.20. Screenshot of redesigned dc/dc converter PCB	126
Figure 6.21. Images of Discharge PCB and IMD enclosure	127
Figure 6.22. Image of revised battery module	128
Figure 6.23. Screenshot of Elithion AMS graphical user interface showing histogram of present cell voltages measured by each cell board (right window)	129
Figure 6.24. Image of revised accumulator assembly	130
Figure 6.25. Image of junction box mounted in UCM16	131
Figure 6.26. Diagram of low voltage routing paths	132
Figure 6.27. Diagram of tractive system routing paths	133
Figure 6.28. Schematic extract of voltage indication circuit redesign	134
Figure 6.29. Image of redesigned Precharge PCB	135
Figure 6.30. Image of replacement voltage indication PCBs	136
Figure 7.1. Pre-competition testing in Melbourne, Australia	138
Figure 7.2. Pictorial representation of direct memory access buffer measurement locations	140
Figure 7.3. Diagram of torque vectoring parameterisation	140
Figure 7.4. Torque vectoring algorithm process diagram	141
Figure 7.5. Plot of tested X _{GLOBAL} torque bias profiles against steering angle	143
Figure 7.6. Plot of positive motor torque and steering angle measurement data during FSAE-A skid-pad event	144
Figure 7.7. Plot of motor torque, steering angle and throttle measurement data during FSAE-A skid-pad event	145
Figure 7.8. Plot of motor velocity and current data showing motor becoming disabled	146
Figure 7.9. Traction control ("Anti-slip") algorithm process diagram	147

Figure 7.10. Plot of motor velocity and current data with anti-slip algorithm enabled	148
Figure 7.11. Plot of tractive power and throttle position data during FSAE-A acceleration event	149
Figure 7.12. Tractive power limiting algorithm process diagram	150
Figure 7.13. UCM16 competing in the FSAE-A skid-pad event	152
Figure 7.14. UCM16 returning from an acceleration run at FSAE-A	153
Figure 7.15. Plot of tractive power data during FSAE-A autocross event	154
Figure 7.16. Plot of motor velocity, current and error data for rear-left motor during autocross event	154
Figure 7.17. Plot of requested motor torque and throttle position for first two runs of autocross event	155
Figure 7.18. Plot of rear-left error information and motor current during the third autocross run	156
Figure 7.19. Plot of energy consumption for each run of FSAE-A autocross event	157
Figure 7.20. Plot of motor current data and powertrain shutdown points (red lines) during first endurance run	159
Figure 7.21. Plot of motor current data and powertrain shutdown points (red lines) during second endurance run	160
Figure 7.22. Plot of motor current data at first shutdown point (dashed red line) for endurance run 1	160
Figure 7.23. Plot of motor current data at first shutdown point (dashed red line) for endurance run 2	161
Figure 7.24. Plot of error information and tractive power during second endurance run, showing error code 2318 (data label) at first powertrain shutdown	162
Figure 7.25. Plot of inverter temperature data during second endurance run	163
Figure 7.26. Plot of motor temperature data during second endurance run	164
Figure 7.27. Plot of UCM16's energy consumption during FSAE-A endurance event	165

LIST OF TABLES

Table 1.1. Points allocation for Formula SAE events	4
Table 1.2. Top five electric FS teams and the University of Canterbury Motorsport (as of	8
Table 2.1. Summary of PMSM and Induction motor comparison	14
Table 2.2. Battery technology used by selected hybrid and electric vehicle manufacturers	24
Table 2.3. Summary of lithium-ion cell chemistries	25
Table 3.1. DD5-14-10-POW motor specifications	32
Table 3.2. KW26-S5-FSE-4Q inverter specifications (per sub-inverter)	37
Table 3.3. Key parameters of KW-R06 controller card	38
Table 3.4. Driving mode control requirements	40
Table 4.1. Contacted lithium-ion pouch cell manufacturers	50
Table 4.2. Summary of considered Accumulator Management Systems	51
Table 4.3. Specifications of A123 AMP20M1HD-A LFP cell	52
Table 4.4. Summary of valid A123 module configurations	53
Table 4.5. Comparison of accumulator parameters between Melasta and A123 cells	54
Table 4.6. Specifications of SLPB7864155 / SLPB7664155 cells	55
Table 4.7. Summary of 18650 cells considered	59
Table 4.8. Results of two-stage selection process for 18650 cells	60
Table 4.9. Specifications of Samsung INR18650-25R5 cells	60
Table 4.10. Summary of considered Accumulator Isolation Relays	64
Table 4.11. Overview of continuous current ratings in tractive system	65
Table 4.12. Summary of considered 100 A rated tractive fuses	66
Table 7.1. Table of 2016 FSAE-A event results for UCM	151

GLOSSARY OF TERMS

ac	Alternating current
Accumulator	Formula SAE term for the batteries (or capacitors) used to store the energy for the tractive system
AIR	Accumulator Isolation Relay, normally-open contactor used to open each pole of the accumulator
AMS	Accumulator Management System, term given to a BMS by Formula SAE
back EMF	Counter electromotive force generated in the windings of a rotating motor
BLDC	Brushless DC (motor)
BMS	Battery Management System, monitors and protects a rechargeable cell (or group of cells) to ensure it remains within its safe operating limits
BSPD	Brake System Plausibility Device, safety circuit that checks if more than 5 kW is supplied to the electric motors, and the car is braking hard for longer than 0.5 seconds
CAN	Controller Area Network, a multi-master, differential communication protocol developed for use in automotive applications
CAD	Computer-aided design
Cell (battery)	Two electrodes separated by an ion-conductive electrolyte that is used to store electrical potential energy. Multiple cells are combined to form a battery.
dc	Direct current
EMI	Electromagnetic Interference
EVX.X.X	Refers to a clause within the Formula SAE rules, where <i>X</i> denotes a number
Formula Student (FS)	The name by which Formula SAE is referred to in Europe
FSAE	Formula SAE
FSAE-A	Formula SAE Australasia
Galvanic isolation	The physical separation of two circuits to prevent cross-circuit current flow
HVD	High Voltage Disconnect (switch)
IC	Internal Combustion

IMD	Insulation Monitoring Device
Inverter	Converts dc electrical energy to ac electrical energy
Module (battery)	A group of electrochemical cells, which are then combined to form an accumulator
PMAC	Permanent-magnet AC (motor)
PMSM	Permanent-magnet Synchronous Machine (motor)
RWD	Rear-wheel drive
SAE	Society of Automotive Engineers
Sub-inverter	Term given to each quarter of the AMKASYN KW26-S5-FSE-4Q Inverter
Tractive	Denotes that a system is used for vehicle motion
Tractive battery	Stores the electrical energy for vehicle motion (referred to as an <i>accumulator</i> in FSAE)
TSAL	Tractive System Activation Light
UCM	University of Canterbury Motorsport
VCU	Vehicle Control Unit
4WD	Four-wheel drive

CHAPTER 1

INTRODUCTION

Formula SAE (FSAE) is a global competition organised by the Society of Automotive Engineers (SAE) International. FSAE tasks students with designing, building, developing and then racing a single-seat, open-wheel race car. The inaugural Formula SAE competition was held in 1981 at the University of Texas, which saw four teams compete in four dynamic events: acceleration, manoeuvrability, endurance and fuel economy [1]. Formula SAE has since expanded into eleven competitions worldwide, and consists of over 800 registered teams [2] [3]. The success of Formula SAE and its affiliated competitions means it is viewed by the automotive industry as the most established educational competition in motorsport [4]; to the point where involvement is often considered a pre-requisite to a career in automotive engineering.

The University of Canterbury Motorsport (UCM) team was founded in 2013 to compete in the Formula SAE Australasia (FSAE-A) competition. Their first car, UCM13 (Figure 1.1(a)), featured a space-frame chassis with a four-cylinder internal combustion engine. The simplicity and build-quality of UCM13 resulted in the team finishing 12th overall at the 2013 FSAE-A competition; and were the highest scoring first year team worldwide. UCM14 (2014, Figure 1.1(b)) and UCM15 (2015, Figure 1.1(c)) were further developments on the team's internal combustion concept; with the introduction of a turbo-charged single-cylinder powertrain, full aerodynamics package, and a carbon-fibre monocoque (in the case of UCM15). Following a podium finish at the 2015 FSAE-A competition with UCM15, the 2016 UCM management team¹ decided to move away from an internal combustion engine and instead explore the concept of a four-wheel drive electric Formula SAE race car, UCM16 (Figure 1.1(d)).

This thesis presents the design, manufacture and testing of the electrical systems within UCM16, where specific contribution from the author is specified. The topics discussed include the selection of the electric powertrain package; design of the lithium-ion tractive battery, and associated energy management systems; and the development of custom vehicle dynamic software, to implement features such as traction control and torque vectoring.

¹ The management team consisted of the Team Leader, Technical Director and the lead engineers of each sub-team: aerodynamics, chassis, electrical, ergonomics, powertrain and suspension. In 2016, the author was the Lead Electrical Engineer.



(a) UCM13 (2013)



(b) UCM14 (2014)



(c) UCM15 (2015)



(d) UCM16 (2016)

Figure 1.1. University of Canterbury Motorsport race cars competing at the Formula SAE Australasian competition in their respective years

1.1. FORMULA SAE COMPETITION STRUCTURE

Formula SAE fabricates the idea that teams work for a design firm that is developing a prototype vehicle for the non-professional, weekend motorsport market. Such a market has become ever-increasingly popular amongst the amateur motorsport community, with manufacturers such as Ariel (Atom), Caterham (Seven series) and KTM (X-Bow) producing cars that are specifically aimed at track days.

The present-day competition consists of five dynamic events and three static events, each with their own individual point allocation (Table 1.1). Teams are judged based upon their relative performance to other teams in the competition, in which the winner of each event is given the maximum points allocated to the event, and the lower placed teams are allocated a percentage of the available points. The dynamic events aim to test the performance of the race cars (with a focus on acceleration, braking and handling), whilst the static events evaluate the team's engineering decisions.

Table 1.1. Points allocation for Formula SAE events

Dynamic Events:	
Acceleration	75
Skid-Pad	50
Autocross	150
Endurance	300
Efficiency	100
Static Events:	
Business Presentation	75
Engineering Design	150
Cost Analysis	100
Total Points	1000

The following is a description of each event in the Formula SAE competition:

- Acceleration: Tests a race car's straight-line acceleration over 75 m from a standing start.
- Skid-pad: A course of two pairs of concentric circles in a figure-of-eight pattern. Drivers complete two rotations of each circle (turning left and right), whereby the second rotation in each direction is timed and averaged. This event tests the race car's steady-state cornering ability.
- Autocross: Tests the race car's manoeuvrability and handling performance over a 0.805 km course, which consists of numerous corners, hairpins and chicanes. In theory, the car with the greatest combination of acceleration, braking and cornering ability is most successful in this event.

- Endurance and Efficiency: The endurance and efficiency events are combined in most FSAE competitions. The endurance event aims to test a car's overall durability and reliability over a 22 km course². The energy efficiency of the car is measured simultaneously to determine how well a team has tuned their car.
- Business Presentation: The business event reinforces the idea that the team is developing a prototype car intended for market. Teams are required to present their concept in front of a panel of potential investors, with a focus on market identification, predicted sales and profitability.
- Engineering Design: The design event consists of a series of small group discussions in which a team members must present the engineering behind their car to a group of industry experts. The judged categories vary between competitions but can generally be split into the core sub-teams: aerodynamics, chassis, electrical³, ergonomics, management, powertrain and suspension.
- Cost Analysis: Prior to the competition, each team submits a document containing the cost-breakdown for every component in their car. The cost-breakdown not only includes the cost of the final part itself, but costs associated with its manufacture and assembly. At the competition, each team justifies their engineering decisions from a financial viewpoint.

As with any discipline of motorsport, Formula SAE teams must adhere to an explicit set of rules and regulations. The FSAE rules are updated bi-annually by SAE International, which are globally accepted by all competitions. In addition, each competition releases an addendum to the FSAE rules that must be adhered to. The electric race car discussed in this thesis was designed to comply with the *2015 Formula SAE Rules* [5] (2015 – 2016) and the *Local Addendum to Formula SAE 2016 Rules* [6] released by Formula SAE Australasia. Throughout this thesis there will be multiple references to a specific clause within the FSAE rules; for example, *EV3.1* refers to Clause 1 of Article 3 for electric vehicles.

1.2. RELATED WORK

1.2.1. ELECTRIC VEHICLES IN THE AUTOMOTIVE INDUSTRY

Contrary to popular belief, electric vehicles are not a new technology. The first large-scale electric vehicle (an electric locomotive) was developed by Robert Davidson in 1837 [7]. At the start of the 20th Century, electric car stock in the United States of America were almost double that of gasoline-powered cars (38% compared to 22% respectively) [8]. However, the introduction of cheap mass production

² For most competitions, the endurance event consists of multiple laps of the autocross course (in either the forward or reverse direction).

³ Split further into low voltage and high voltage systems for teams competing with an electric vehicle.

techniques (in particular those employed by Henry Ford with the Ford Model T in 1913), coupled with the desire for greater range and a lack of electric charging infrastructure, resulted in electric vehicle sales decreasing in favour of internal combustion equivalents. It was not until the early 1990s that electric vehicles began to make a significant reappearance in the automotive industry⁴. Cars such as the EV1 (General Motors, 1994), RAV4 EV (Toyota, 1997) and Prius (Toyota, 1999), the latter of which is still currently in production, redefined the battery electric vehicle⁵ (BEV) and plug-in hybrid vehicle⁶ (PHEV) market.

The worldwide adoption of electric vehicles has increased significantly over the last decade (as shown by Figure 1.2 – reproduced from [9]) to the point where electric vehicle stock in 2015 exceeded the one-million unit threshold established by the Electric Vehicles Initiative (EVI). The EVI was established in 2009 as a multi-government policy to accelerate the global uptake of electric vehicles (consequently reducing the transportation sector's energy usage and carbon dioxide emissions [10]), with the aim of deploying 20 million electric vehicles by 2020 [9]. In response to the EVI, and other such government-enforced initiatives, almost all automotive manufacturers are now either producing a commercially available electric or hybrid vehicle, or are developing their first concept.

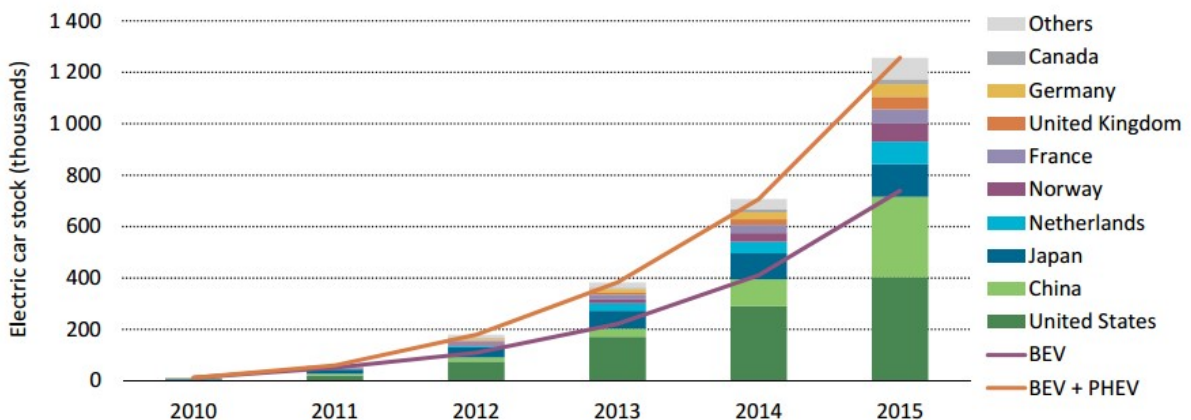


Figure 1.2. Increase in global battery electric vehicle (BEV) and plug-in hybrid electric vehicle (PHEV) stock from 2010 to 2015 [9]

1.2.2. ELECTRIC VEHICLE TECHNOLOGY IN MOTORSPORT

Although technically part of the automotive industry, motorsport should be considered a feeder industry; in which the research and developments made by engineers in the highly-competitive environment get integrated into production vehicles. Such is the case that almost all aspects of a production car have stemmed from some form of racing. Examples range from the somewhat simplistic,

⁴ Albeit, there were manufacturers who had developed electric vehicles prior to this, but these were never adopted to any meaningful extent.

⁵ Electric vehicles that rely solely on a battery for energy storage, which is by an external electricity supply.

⁶ Electric vehicles with an on-board internal combustion engine for charging the battery or as an alternative drivetrain option. PHEVs differ from hybrid electric vehicles (HEVs) as their battery can be charged via an external electricity supply.

affixing a rear-view mirror to remove the need (and weight) of a “rearward traffic watcher” (Ray Harroun at the Indianapolis 500, 1911 [11]); to the more advanced consideration of aerodynamic efficiency and the effects of downforce on handling and performance (Formula One, late 1960s [12]).

Electric vehicle technology has been making an appearance in mainstream motorsport since the late 2000s, and has already seen improvements as a result of its exposure. One of the most notable cases is the development of battery technology in response to the introduction of the kinetic energy recovery system (KERS) to Formula One in 2009 [13]. KERS was proposed by the Federation Internationale de l’Automobile (FIA) to recover and store the kinetic energy that is otherwise dissipated as heat under braking, such that it could be redeployed by the driver to increase the rate of acceleration, or to maintain pace whilst using less fuel. After considering the energy storage solutions available at the time, Mercedes-Benz High-Performance Engines (HPE) commissioned A123 Systems to refine its lithium-ion Nanophosphate chemistry to increase both power and energy density. The result was a 48% reduction in cell mass, and a 14% increase in cycling capability [14].

In response to the aforementioned increase in electric vehicles, all-electric motorsport disciplines, for example the FIA Formula E championship, have been formed to further propel the development of electric vehicles. The inaugural season of the Formula E championship (2014 - 2015) saw ten teams compete in eleven races worldwide with identical Spark-Renault SRT_01E formula-style race cars [15]. The SRT_01E was a collaboration between Spark Racing Technologies (in partnership with Renault), Dallara (chassis), McLaren Electronics Systems (electronics and powertrain), Williams Advanced Technology (battery) and Michelin (high-efficiency tires) [16]. Now in its third season, the regulations have been eased, allowing teams to produce their own electric motor, inverter and gearbox solutions.



Figure 1.3. Image of Panasonic Jaguar Racing's Formula E race car [17]

The success of Formula E, from an engineering viewpoint, is expressed in the fact that eight of the ten current teams are either automotive manufacturers, or have technical partnerships. For example, Panasonic Jaguar Racing (Figure 1.3), who joined the championship at the start of the third season, use the racing series as a development platform for Jaguar Land Rover's future range of electric cars [18]. The technical partnership with Panasonic, whom supply lithium-ion batteries to several electric vehicle manufacturers (including Tesla Motors), allows for further advances in battery technology.

1.2.3. ELECTRIC RACE CARS IN FORMULA SAE

The first electric Formula SAE race car was developed by RMIT Electric Racing in 2008 [19]. The car was a retrofit of RMIT's 2004 entry, and was built to show that an electric alternative to combustion FSAE cars was plausible. In the same year, the first official rules dictating the design of electric FSAE cars was released as an amendment to the upcoming 2009 rule set [20]. It was not until 2010 that the first all-electric FSAE competition (Formula Student Electric⁷ (FSE)) was held (Germany), in which fifteen teams competed [21]. Electric categories were also introduced at Formula Student UK and Formula Student Italy in the same year.

As of 2017, there are 110 electric teams registered in Formula SAE [3]. Table 1.2 lists the five highest ranked electric teams according to their *world ranking points*, which is calculated based upon competition results from the three previous years. Of these five teams, RMIT Electric Racing is the only team that does not compete with a four-wheel drive powertrain. Following the 2016 FSAE-A competition, the results of which will be discussed later in this thesis, the University of Canterbury Motorsport team is ranked 25th (the highest ranked first-year electric team for 2016). A summary of the electrical specifications for each of the teams' previous electric cars is documented in Appendix A, the research of which was used as a basis for the specification of UCM16.

Table 1.2. Top five electric FS teams and the University of Canterbury Motorsport (as of April 2017) [3]

Rank	Team (University)	World Ranking Points
1	KA-RaceIng (Karlsruhe Institute of Technology)	831.24
2	Formula Student Team Delft (TU Delft)	807.02
3	AMZ Racing Team (ETH Zurich)	785.85
4	TU Fast Racing Team (TU Munich)	700.47
5	RMIT Electric Racing (RMIT)	675.89
25	UCM (University of Canterbury)	445.87

⁷ The FSAE competition is called Formula Student in Europe.

1.3. THESIS OVERVIEW

This thesis presents the design, manufacture and testing of the electrical systems for New Zealand's first four-wheel drive electric race car, UCM16, where the specific contributions from the author are identified. Chapter 2 introduces important theory related to electric vehicles and their application in motorsport. The topics presented range from electric motors, inverters and dynamic control theory; to electrochemical cell theory and energy management design. Chapter 3 details the electric powertrain selected for UCM16, and includes the development and testing of the preliminary powertrain control system. Chapter 4 presents the three tractive battery concepts that were considered throughout the design process, concluding with the assembly of UCM16's first tractive pack. The detailed design and testing of the precharge and discharge energy management circuits are also discussed. Chapter 5 is dedicated to the design and testing of the various safety circuits and mechanisms implemented within UCM16. These include both tractive and low voltage emergency shutdown procedures. Chapter 6 focusses on the results acquired from the first driveable assembly (rear-wheel drive) of UCM16. The amendments required to resolve identified design issues, and to convert the race car to a four-wheel drivetrain, are discussed. Chapter 7 presents the development of the vehicle dynamic software and UCM16's competition results at the 2016 Formula SAE Australasian competition. Finally, Chapter 8 concludes this thesis, and includes future recommendations and final mentions from the author.

1.4. AUTHOR'S CONTRIBUTION TO UCM16

Since Formula SAE is a team-based endeavour, it is not uncommon for elements of a race car to be designed by multiple engineers. Throughout this thesis, there will be mentions of such collaborations between the author and other UCM team members. As Lead Electrical Engineer, the author supervised a team of four final-year electrical engineering students, of whose projects are mentioned in the following chapters. It should be noted that in almost all cases, the author was also an active designer in these projects.

Unless otherwise acknowledged, all designs and concepts detailed in this thesis were completed solely by the author. Although mentioned later, a special acknowledgement must be made to the design of UCM16's tractive pack (discussed in Chapter 4) and the development of the vehicle dynamic software (discussed in Chapter 7). Whilst the electrical design of the tractive pack was completed by the author, its assembly and subsequent amendments must be accredited to a team of dedicated electrical and mechanical engineers. As for the vehicle dynamic software, the development must be accredited as a joint development between the author and a final year electrical engineering student. Due to the complexity and number of software revisions made, it is not possible to completely distinguish each engineer's additions.

CHAPTER 2

BACKGROUND

In this chapter, the background theory relevant to the design and development of an electric race car will be discussed. A natural flow from the output actuator (electric powertrain), to the power flow systems (tractive battery and energy management systems), to the auxiliary systems can be identified; whereupon the specifications of each design stage are directly influenced by the decisions of the previous stage.

2.1. MOTOR THEORY

Motor selection is highly dependent on the intended application. A comparison can be made between electric motors and internal combustion engines; where the decision for a manufacturer to use a flathead over a rotary over a V-shaped engine, to name just a few configurations, comes down to a combination of cost, performance and packaging. Whilst there are many different motor types available, induction and permanent-magnet synchronous motors have emerged as the preferred option of electric vehicle manufacturers [22].

Three-phase induction motors have a simpler construction than synchronous motors. The stator is constructed using thin steel laminations with slots in which the windings are distributed. The rotor of an induction motor is referred to as a squirrel-cage; where conducting bars, typically aluminium or copper, are housed in laminations with radial slots and short-circuited by end rings [23]. The operation principle of an induction motor is based upon the generation of magnetic fields. Balanced poly-phase current through the stator windings generates a rotating magnetic field in the stator. The moving stator field induces current in the bars of the rotor, which in turn generates a magnetic field in the rotor that is attracted to the stator field. Since the magnetic field of the stator rotates with respect to the rotor this causes the rotor to follow (rotate).

Induction motors are asynchronous, meaning the rotor lags the stator field, and the rotor must rotate slower than the synchronous speed. The synchronous speed is the theoretical maximum speed of an

induction motor. As shown by Equation (2.1), the synchronous speed (n_s) is proportional to the supply frequency (f), as the number of poles (P) is fixed by the motor construction.

$$n_s = \frac{120f}{P} \quad (2.1)$$

The difference between the synchronous and rotor speeds, normalised by the synchronous speed, is called the “slip”.

$$s = \frac{n_s - n_r}{n_s} \quad (2.2)$$

The torque produced by an induction motor is given by the following relationship [24],

$$\tau_{em} = k\varphi_{ag}^2 f_{sl} \quad (2.3)$$

where, τ_{em} is the electromagnetic torque, k is a motor constant, φ_{ag} is the air gap flux (due to the magnetic field strength), and f_{sl} is the slip frequency (which is proportional to the motor slip). Over a very small speed range, and with a constant supply frequency and magnetic field strength, the torque produced is proportional to motor slip. Realistically, the torque-speed curve of an induction motor is non-linear and must therefore be controlled by dynamically adjusting supply frequency and voltage.

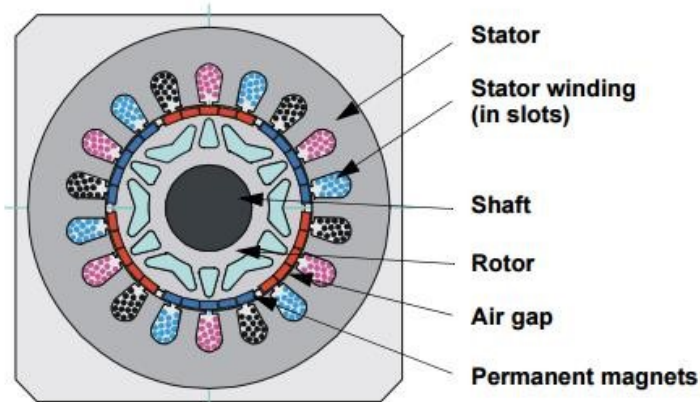


Figure 2.1. Cross-section of a permanent-magnet synchronous motor [25]

Permanent-magnet synchronous motors (PMSM) refer to the group of motors that rotate at the same speed as the supply frequency and have permanent magnets embedded in their rotor. Two of the most common synchronous motors are brushless dc (BLDC) and permanent-magnet AC (PMAC) [26]. The difference between the two can be simplified to the control waveform required (trapezoidal or sinusoidal respectively), which is a result of the winding configuration (Figure 2.1).

The torque produced by a synchronous motor is equal to the cross product of stator and rotor magnetic field vectors, as defined by Equation (2.4) [27]. This means the torque produced is maximised when the stator and rotor fluxes become orthogonal.

$$\tau_{em} = \vec{B}_{stator} \times \vec{B}_{rotor} \quad (2.4)$$

For a permanent-magnet synchronous motor, the magnets on the rotor produce a constant magnetic flux (φ) in the air gap between the rotor and stator. This allows Equation (2.4) to be rearranged in terms of the linkage flux between a reference stator winding and the rotor, and the winding current [24].

$$\tau_{em} = k_t \varphi_{fa} I_a \sin \delta \quad (2.5)$$

where, k_t is a constant, φ_{fa} is the linkage flux between the rotor and winding “a” of the stator, I_a is the current in winding “a”, and δ is the angle between φ_{fa} and I_a (referred to as the torque angle). Controlling the rotor and stator flux such that they become orthogonal makes the torque proportional to the stator current (Equation (2.6)). This is referred to Field-Oriented Control and will be discussed further in Section 2.2.

$$\tau_{em} \propto I \quad (2.6)$$

The performance output of a PMSM motor is limited by the counter (or back) electromotive force (back EMF) that is generated in the stator windings when the motor rotates. The back EMF has a polarity that opposes the voltage supplied to the motor windings. Its magnitude is proportional to the number of winding turns in the stator, the magnetic field strength of the permanent magnets, and the angular velocity of the rotor, as given by (2.7) [28].

$$\text{Back EMF} \propto N l r B \omega \quad (2.7)$$

where, N is the number of turns in the stator winding, l is the rotor length, r is the radius of the rotor, B is the magnetic field strength, and ω is the angular velocity of the rotor. Since the number of stator windings and the magnetic field strength remain constant for a constructed motor (assuming the magnets do not loss magnetisation due to heat), the back EMF generated is proportional to rotor speed. As the motor speed increases, the back EMF will increase towards the supply voltage and consequently reduce the amount of current that can be supplied to the motor. As previously stated, torque is proportional to current; therefore, the theoretical maximum speed of the motor is limited to the point where the back EMF equals the supply voltage, and both the current and torque are zero. This point is also referred to as the no-load speed of the motor.

Permanent-magnet synchronous motors are the most popular choice for electric vehicle manufacturers because of their greater power density [29] and flatter torque profile [28]. This is a direct result of recent developments in magnet technology which allow for greater magnetic field strength and therefore greater torque and power ratings. Figure 2.2 gives an example of the torque-speed curves for a typical induction and PMSM motors. Whilst it should be noted that these curves are purely illustrative, they show that the torque output of an induction motor is non-linear, whilst a PMSM motor has a relatively flat torque output up until the knee-point, where the back EMF is large enough to limit motor current.

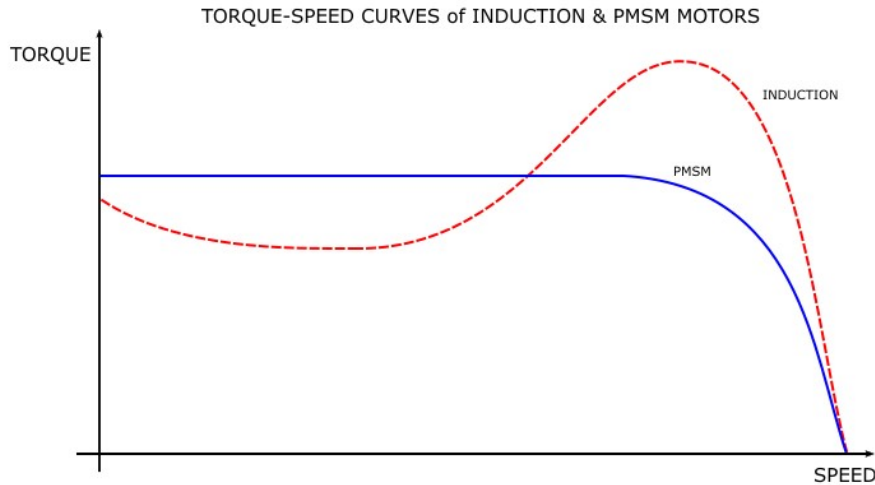


Figure 2.2. Example torque-speed curves for induction and PMSM motors

It should be noted that the flatter torque-speed relationship of the PMSM motor is due to the current limitations of the motor's inverter. In theory, the output torque increases almost linearly as rotor speed decreases. However, the current must be limited to the stator windings (thus limiting torque) to ensure the motor does not exceed its operating temperature.

In general, a PMSM motor outputs a greater torque at low speeds as the permanent magnets produce a constant magnetic field, whereas an induction motor must induce its own rotor field [28]. This difference allows for greater acceleration in a vehicle with a PMSM motor assuming two vehicles with identical mass and traction. This is particularly beneficial in a Formula SAE environment, where track layouts are tight and favour race cars with a more consistent acceleration ability.

In general, the peak efficiency of PMSM motors is also greater than that of an induction motor as there are no magnetic losses in the rotor. Despite this, Tesla Motors (considered to be at the forefront of electric vehicle development) have chosen to use induction motors coupled with their “smart inverter”. The magnetic field strength produced in the rotor is proportional to the supply voltage over frequency (V/f). By reducing the voltage, Tesla Motor’s smart inverter can reduce the field strength under light loads and reduce the magnetic losses of the induction motor, improving average efficiency [30].

Referring to the analogy at the beginning of this section, there is no one motor for all applications. Table 2.1 gives a summary of the differences between induction and PMSM motors⁸. In the case of motorsport, performance and power density is the key to success; therefore suggesting the use of a permanent-magnet synchronous motor is more appropriate.

⁸ It should be noted that the points made in Table 2.1 are generalisations of each motor technology, and that exceptions exist.

Table 2.1. Summary of PMSM and Induction motor comparison

	PMSM	Induction
Torque Density	Permanent magnets increase magnetic field strength and application torque. Flatter torque-speed profile means torque can be applied consistently over motor's speed range.	Magnetic field must be induced in rotor and is hence weaker, reducing the applicable torque. Non-linear torque-speed profile means torque is reduced at lower motor speeds (see Figure 2.2).
Power Density / Power-to-weight Ratio	Permanent magnets have lesser mass and can be packaged more compactly within the motor enclosure [31]. As such, PMSM motors can be implemented in more confined spaces, for example wheel hubs [22].	A greater amount of steel laminations is required to match the power capabilities of a PMSM motor. This, in addition to endplates and stator back iron, increases motor mass and size, thus decreasing power density and power-to-weight ratio [31].
Efficiency	Lack of rotor losses means PMSM motors are more efficient across a comparable speed range [32]. Consequently, cooling requirements are reduced – saving overall vehicle weight.	High rotor losses due to induced magnetic field reduces overall efficiency.
Durability	Permanent magnets are vulnerable to high temperatures, which cause them to demagnetise, thus reducing motor output torque and power [26]. High acceleration vibrations can also demagnetise permanent magnets over time.	Simplistic construction and lack of magnets means induction motors are more robust than PMSM motors [33].
Cost	Rare-earth permanent magnets are at the influence of the global market. Their complex construction means PMSM motors are comparatively more expensive than induction motors.	Simplistic construction and use of standard ferromagnetic materials reduces manufacture costs significantly [32].

2.2. INVERTER THEORY

An inverter converts dc (direct current) electrical energy to ac (alternating current). For an electric vehicle, the inverter often forms the connection between the battery (dc) and the motor (ac). Whilst there are multiple inverter topologies, the inverter topology mentioned in this section is the most common; consisting of six controllable switches in a 3-phase full bridge configuration to regulate the current through the windings of the motor (Figure 2.3). An induction motor or PMSM motor can both be controlled by this same topology, in which the only significant difference is the switching control. However, only the control of a PMSM motor will be discussed in this section, as it was identified as the preferred option for motorsport in the previous section.

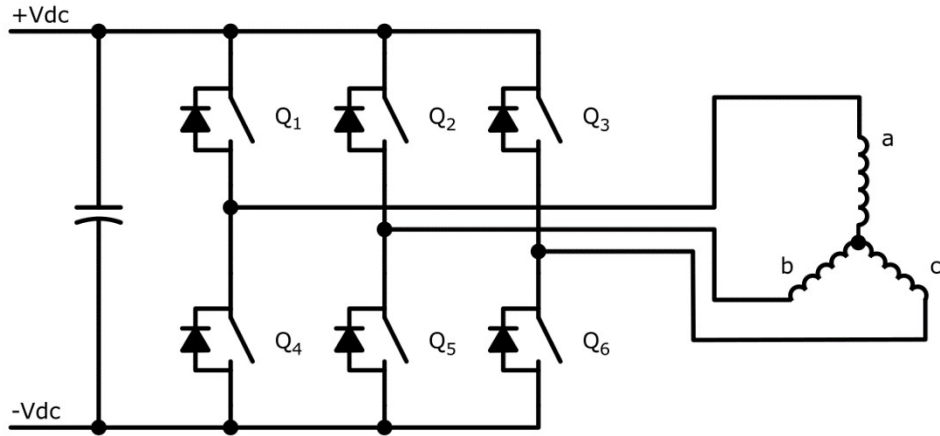


Figure 2.3. Diagram of 3-phase full bridge inverter topology

The state of the switches in Figure 2.3 determine the direction in which current flows through the windings of the motor. For example, if switches Q₁ and Q₆ were closed, the supply voltage will be connected to phases *a* and *c* of the motor, and the direction of current will be from *a* to *c*. Figure 2.4 shows the sinusoidal and trapezoidal current excitation waveforms required for a PMAC and BLDC motor respectively. It should be noted that it is possible to control a motor with the opposite control waveform without a significant loss in efficiency, although the amount of acoustic and electromagnetic noise generated will increase. The waveforms are generated by using pulse-width modulation (PWM) to chop the supply voltage at a fixed frequency. The wave shape is then determined by the duty cycle of the PWM pulses [34].

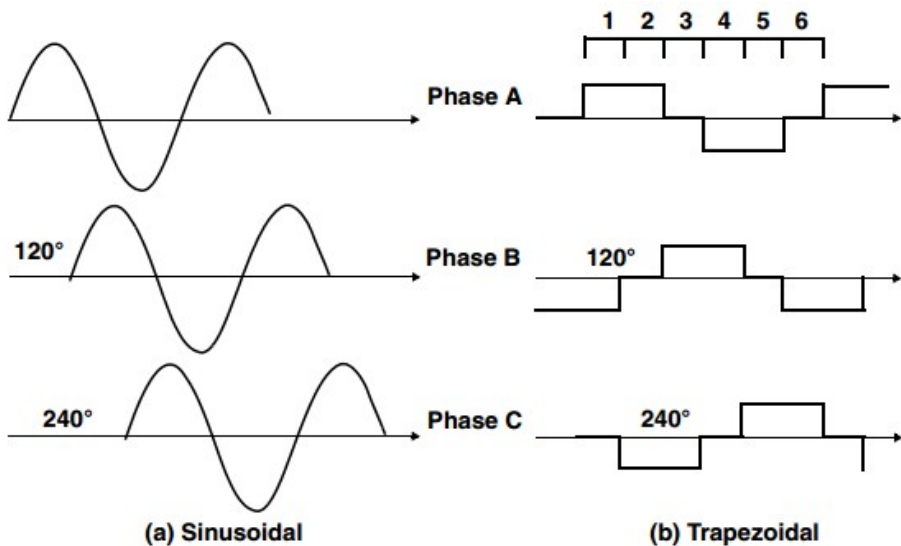


Figure 2.4. Current excitation waveforms for PMAC (a) and BLDC (b) motors [34]

Field-Oriented Control (FOC) is a control method that aims to decouple the torque and magnetising flux components of the current to provide independent control of the motor's torque [35]. This is achieved by applying Clarke's and Park's transformations, which project the three-phase time variant system into a time invariant system consisting of only two components.

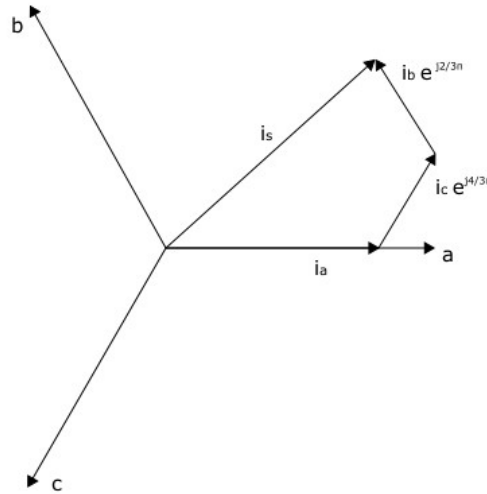


Figure 2.5. Stator current space vector and components in three-phase time variant system

Figure 2.5 shows the three-phase space vector representation of a synchronous motor. From this, it can be stated that the instantaneous stator current space vector (\vec{i}_s) is equal to the vector sum of the currents in each of the motor phases [27],

$$\vec{i}_s = \vec{i}_a + \vec{i}_b e^{j\frac{2}{3}\pi} + \vec{i}_c e^{j\frac{4}{3}\pi} \quad (2.8)$$

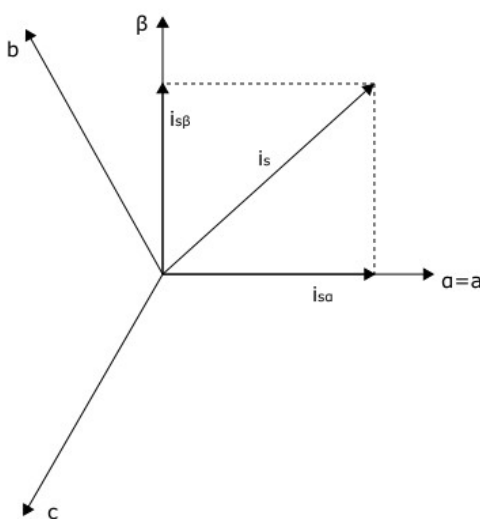


Figure 2.6. Stator current space vector and components in the (α, β) reference frame

Using Clarke's transformation, the stator current space vector is projected onto the (α, β) frame (Figure 2.6). This allows the stator current vector to be represented using only two components ($\vec{i}_{s\alpha}$ and $\vec{i}_{s\beta}$), which are defined by Equations (2.9) and (2.10) [27]. When applying Clarke's transformation, it is assumed that the α -axis of the new projection is aligned with the a-axis of the three-phase vector system.

$$\vec{i}_{s\alpha} = \vec{i}_a \quad (2.9)$$

$$\vec{i}_{s\beta} = \frac{1}{\sqrt{3}}\vec{i}_a + \frac{2}{\sqrt{3}}\vec{i}_b \quad (2.10)$$

The (α, β) frame, however, is still dependent on time and motor speed. To produce a time invariant system, Park's transformation is applied, which projects the (α, β) frame onto the Direct and Quadrature (d, q) rotating reference frame. This transformation assumes the d-axis is aligned with the vector that defines the rotor flux (φ_r), as shown in Figure 2.7.

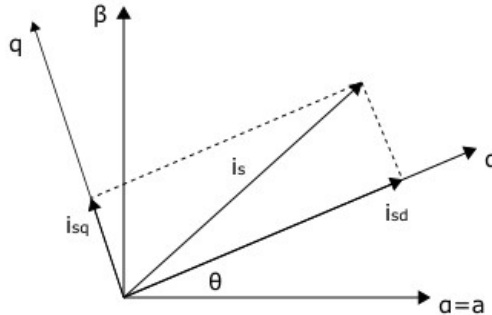


Figure 2.7. Stator current space vector and components in (d, q) rotating reference frame

The resulting components of the stator current space vector are therefore determined by Equation (2.11) and (2.12),

$$\vec{i}_{sd} = \vec{i}_{s\alpha} \cos \theta + \vec{i}_{s\beta} \sin \theta \quad (2.11)$$

$$\vec{i}_{sq} = \vec{i}_{s\alpha} \sin \theta + \vec{i}_{s\beta} \cos \theta \quad (2.12)$$

where, θ denotes the rotor flux position. Since the rotor flux speed is equal to the rotor speed for a synchronous motor, the rotor flux position can be directly measured by a position sensor on the output shaft of the motor.

Referring to Equation (2.4), if the stator and rotor flux are orthogonal they become decoupled. This means the output torque is proportional to the rotor flux and the quadrature (torque) component of the stator current. Since PMSM motors have a constant rotor flux, the motor torque can be controlled linearly by controlling the torque-component of the stator current vector [27].

$$\tau_{em} \propto \varphi_r \vec{i}_{sq} \quad (2.13)$$

2.3. BENEFITS OF 4WD ELECTRIC POWERTRAINS IN FSAE

Powertrains in Formula SAE can be summarised into one of the following groups:

- Rear-wheel drive (RWD) internal combustion (IC)
- RWD electric (either a single motor with a differential, or two motors)
- Four-wheel drive (4WD) electric

To explain the benefits of a 4WD electric powertrain, a comparison between electric motors and IC engines must be made, followed by a comparison of 4WD and RWD configurations.

The primary advantage of an electric motor is its ability to provide maximum torque⁹ over almost the entire rotational speed range, including from standstill (zero RPM). The response time between the request and generation of the torque is at least 10 – 100 times faster than an IC engine, therefore increasing the dynamic response of an electric car [36].

Figure 2.8 is a generic comparison between the torque-speed curves of an electric motor and an IC engine. The curve of the IC engine shows that the maximum torque is produced at a single speed (or practically, a small speed range), which gives rise to the need of ideally a high number of different gear ratios to shift the maximum point as the speed of the vehicle increases. In comparison, depending on the range of torque-speed requirements for an application, an electric motor may only require a single gear ratio, which allows the electric motor to output peak torque instantaneously and sustain the output without interruption.

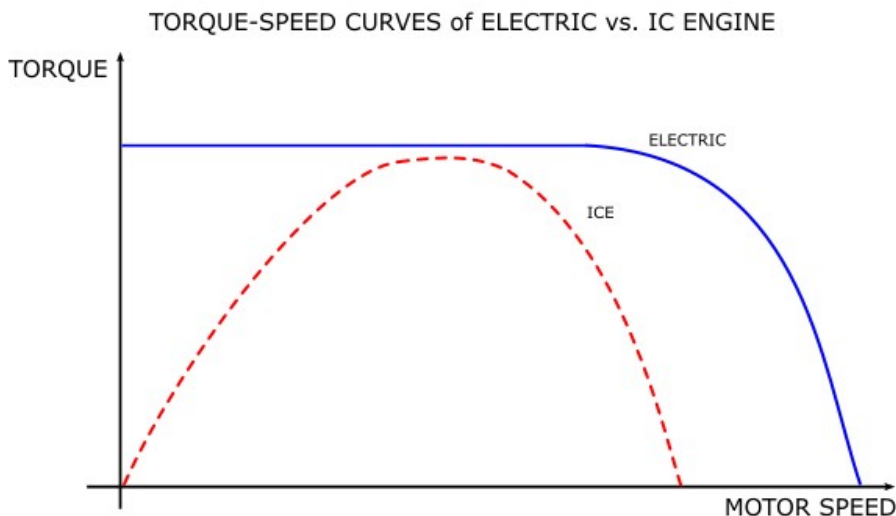


Figure 2.8. Example torque-speed curve of electric motor and IC engine

⁹ Maximum torque can be defined as either the motor's maximum continuous torque or peak torque (which can be applied for a limited amount of time, based upon heat generation within the motor windings).

Electric motors are significantly more efficient than IC engines. Conventional IC engines have a typical efficiency in the region of 15 to 25%, whilst electric motors are upwards of 80% efficient [37]. As a result, electric motors have a greater power to weight ratio and considerably smaller physical dimensions. In some applications (including FSAE cars) this allows electric motors to be mounted within the confines of a wheel hub, in conjunction with a planetary gearbox, thus producing a 4WD powertrain with independent wheel control.

To compare the benefits of 4WD over RWD, the following points will be discussed,

- Performance of 4WD using the tyre model
- Implementation of torque vectoring
- Implementation of traction control

Tyres are the only form of contact between a race car and the track, and complete the load path for accelerating, braking and cornering. It can therefore be stated that a 4WD powertrain can apply more power than a RWD equivalent because it maximises the use of the available traction; driving four tyres as opposed to two.

The reaction forces created by tyres are complex as they are not solely proportional to the vertical load, as suggested by the Coulomb frictional model. Factors related to the contact area of the tyre, for example pressure and width, have a large effect on the forces generated. However, for simplicity the Coulomb model will be used, in which the longitudinal and lateral frictional forces of a tyre are calculated by (2.14) and (2.15) respectively [38],

$$F_x = \mu_x F_z \quad (2.14)$$

$$F_y = \mu_y F_z \quad (2.15)$$

where F_x and F_y are the longitudinal and lateral frictional forces, μ_x and μ_y are the longitudinal and lateral coefficients of friction, and F_z is the vertical load force on the tyre. Assuming the coefficients of friction remain constant¹⁰, and tyre load sensitivity is ignored, the friction forces in either direction can be considered proportional to the vertical load force.

Consider the case of two near-identical race cars, where the only discerning feature is that one is 4WD and the other RWD. The race cars are “grip-limited” over their entire speed range, meaning that if the torque produced by the motor exceeds the frictional force of the tyres, the wheels will spin. During acceleration, the weight distribution of the cars is shifted rearwards, increasing the vertical load force, and therefore grip, on the rear tyres and reducing the force of the front tyres (Figure 2.9). The amount

¹⁰ In reality, the coefficient of friction varies with track surface. Assuming a constant coefficient simplifies the explanation of weight transfer.

of power that can be applied through the rear tyres of both cars will be identical; however, the 4WD car will have increased performance because it can apply additional motor power through the front tyres.

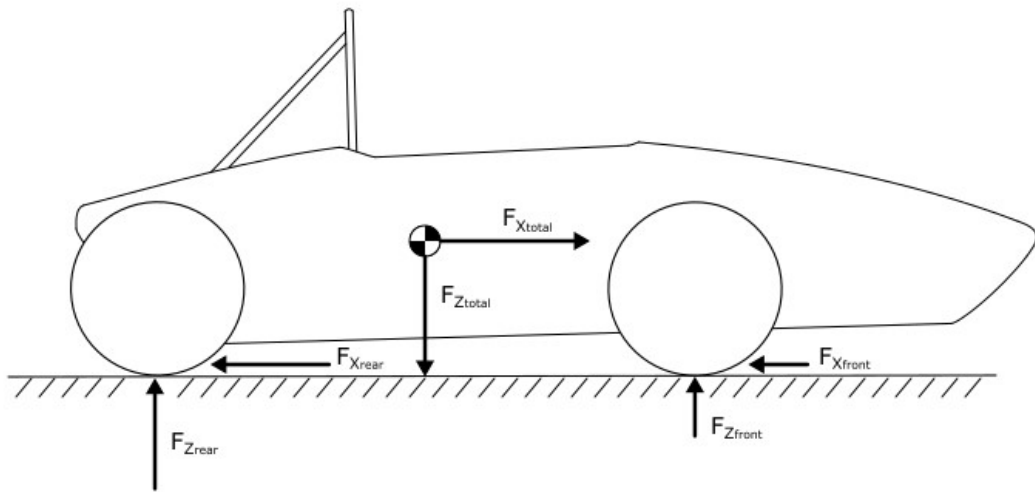


Figure 2.9. Weight transfer and corresponding friction forces generated by tyres during acceleration

A vehicle's ability to change direction (yaw) is a direct result of the tyres' ability to generate lateral force. The conventional method to increase the yaw rate of a race car is to add tyres that can generate a greater lateral force quicker. However, for an independent 4WD powertrain, torque vectoring can be used to dynamically adjust the yaw rate [39]. This results in a FSAE race car that is nimbler and faster in the corners (remembering that we are considering all other aspects between RWD and 4WD to be irrelevant).

The principle behind torque vectoring is to increase the torque on the outside wheels and decrease the torque on the inside wheels during a corner [40]. In a manner similar to the effect of longitudinal acceleration, a vehicle's weight will shift during cornering, such that there is a greater normal force on the outside tyres than the inside. This creates more lateral grip, allowing more torque to be applied by the outer motors before traction is lost. The aim of torque vectoring is to therefore maximise the force that can be applied by all four wheels, for a corner of any radius, without losing traction.

Figure 2.10 shows the three main stages of a corner with a constant radius. On turn-in, the driver will turn the steering wheel in the direction of the corner and the torque vector control will amplify the yaw rate by applying positive torque to the outside wheels and braking torque to the inside. When the car is in steady-state around the corner, the yaw rate remains constant, such that the radius of the path taken by the car remains constant. At this point, the torque applied is only enough to rotate the wheels at the correct speed (balanced between the wheels to minimise the potential loss of traction). Upon exiting the corner, the driver will turn out of the corner and the torque to the motors will be the inverse of turn-in. The torque to the outside wheels will decrease and increase for the inside to reverse the yaw direction.

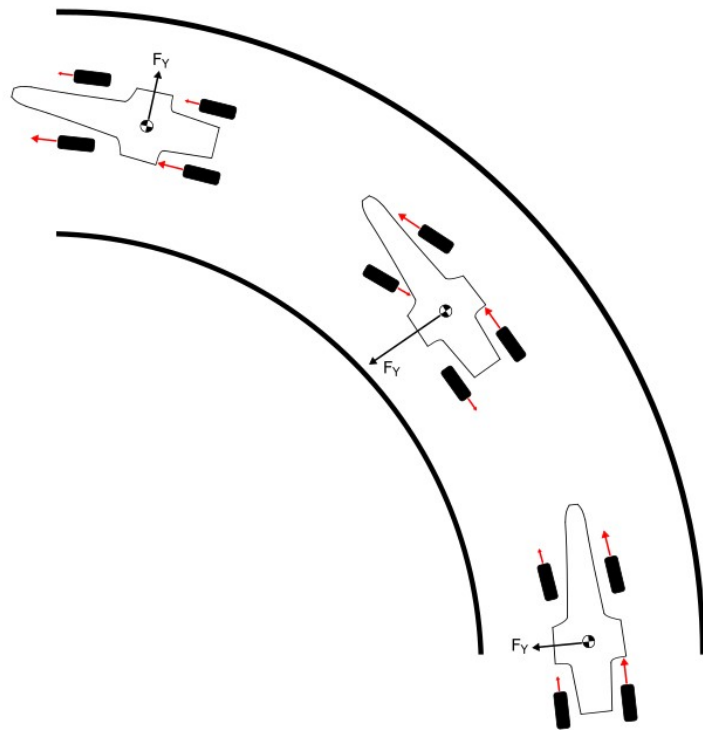


Figure 2.10. Simplified diagram showing implementation of torque vectoring

The aim of traction control is to maximise the available grip from the tyres and prevent the wheels from slipping. When a wheel is slipping, it is not acting to accelerate the car (or decelerate in the case of braking) and is therefore reducing performance. Traction control is conventionally achieved by measuring the wheel speed of an undriven wheel and limiting the power to any wheel that is rotating greater than this reference. However, with a 4WD powertrain all wheels are being driven, therefore any one could be slipping. Most 4WD FSAE teams solve this problem using optical ground speed sensors to determine the speed of the vehicle. An alternative method to determine vehicle speed is to use GPS position and accelerometer sensors as an input to a Kalman filter.

2.4. CONTROLLER AREA NETWORK

Controller Area Network (CAN) is an automotive communication protocol that was developed by Bosch in 1985 in response to the ever-increasing use of electronics in vehicles [41]. CAN is a multi-master system which, unlike the multi-wire point-to-point systems it replaced, only requires a single twisted pair with impedance matching 120Ω terminating resistors at each end. One major benefit of CAN for automotive applications is that it is a differential bus, allowing it to operate in electrically-noisy environments, such as those created by electric powertrains.

A standard CAN message has the format shown by Figure 2.11, where:

- SOF Start-of-Frame, synchronises all nodes in the network
- Identifier Priority of the transmitted message
- RTR Remote Transmission Request
- IDE Identifier Extension, indicates Standard or Extended ID message
- r0 Reserved
- DLC Data Length Code, length of the transmitted data
- Data Message data (0 – 8 bytes)
- CRC Cyclic Redundancy Check, checksum for error detection
- ACK Acknowledge, indicates an error-free transmission
- EOF End-of-Frame

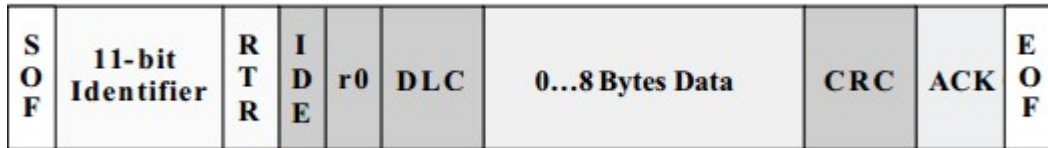


Figure 2.11. Example of standard CAN message [42]

Priority is established on a network using bit-wise arbitration of the message identifiers. The two bit-states of a network are dominant (logic-low) or recessive (logic-high), in which every node sees the same state. In the case where two nodes start transmitting simultaneously, they both transmit the same SOF and remain synchronised until the point at which they transmit conflicting bits. In this situation, the node that transmitted a recessive bit yields to the dominant node and ceases transmission. This means the node with the lowest decimal identifier will have the highest priority, as it contains the most dominant bits.

Figure 2.12 illustrates the physical layer of a CAN network. Each node consists of a microcontroller, CAN controller and CAN transceiver. As previously mentioned, all nodes in a network see the same message being transmitted. This gives the advantage of a single node, for example interfacing a temperature sensor, to broadcast its message and for multiple nodes to receive the measurement simultaneously, for example a fan control unit and a datalogger. Masks and filters can be set in the CAN controllers to ignore messages that are not of interest, reducing the need for additional processing power from the corresponding microcontroller.

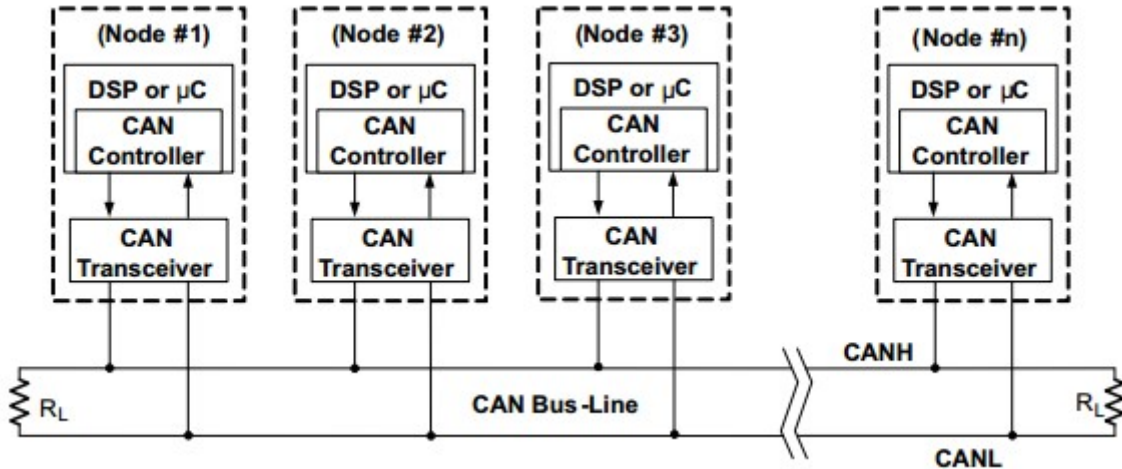


Figure 2.12. Diagram of CAN bus physical layer [42]

2.5. ELECTROCHEMICAL CELL THEORY

A battery consists of two electrodes (anode and cathode) which are electrically insulated from one another by an ion-conductive separator and electrolyte [43]. Electrical energy is stored and released via a chemical reaction of the electrolyte with the cathode (highest potential) and anode (lowest potential); resulting in the transfer of positively charged ions through the electrolyte, and electrons through an electrical circuit. By varying the material used to create the anode, cathode and electrolyte (referred to as the cell chemistry), the performance characteristics of a battery cell can be adjusted.

To compare the relative performance of different battery cell chemistries, various terms have been defined. Whilst these include characteristics such as cycle life and maintenance requirements, there are four terms that directly relate to the suitability of a cell chemistry to an electric FSAE car: specific energy, specific power, energy density and power density. Specific energy (gravimetric energy density) and specific power (gravimetric power density) define the cell's energy capacity and peak output power per unit mass. Similarly, the energy density and power density of a battery cell define the capacity and peak power per unit volume. With regards to vehicle performance, specific power directly influences vehicle acceleration, whilst specific energy influences range.

In an ideal scenario, a cell's chemistry would maximise both power and capacity. However, as explained later in Chapter 4, the reality of the situation requires a balance to be found dependent on vehicle application. Commercial electric vehicles are commonly compared by customers based upon range, and manufacturers tend to select a chemistry with a greater specific energy. Conversely, the range of an electric Formula SAE race car only needs to be enough to finish an endurance event, therefore allowing dynamic performance to be prioritised by using a chemistry with a greater specific power.

Table 2.2 shows that nickel-metal hydride (NiMH) and lithium-ion (Li-ion) are the favoured cell chemistries of hybrid and electric vehicle manufacturers. When electric and hybrid vehicles began to make an appearance on the commercial market, NiMH was the preferred option as it was a more mature battery technology. However, NiMH batteries have both a lower specific energy and specific power rating than lithium-ion equivalents, and thus, modern electric vehicles utilise lithium-ion tractive packs.

Table 2.2. Battery technology used by selected hybrid and electric vehicle manufacturers [43] [44]

Manufacturer	Country	Vehicle Model	Battery Technology
BMW	Germany	X6	NiMH
		i3	Li-ion (LMO ¹¹ / NMC ¹²)
		i8	Li-ion (NMC)
Chevy	USA	Volt	Li-ion (NMC)
Daimler-Benz	Germany	S400	NiMH
Honda	Japan	Civic	NiMH
Nissan	Japan	Leaf	Li-ion (LMO)
Tesla	USA	Roadster	Li-ion (NCA ¹³)
		Model S	Li-ion (NCA)
		Model X	Li-ion (NCA)
Toyota	Japan	Prius	NiMH

The term lithium-ion battery refers to a group of cell chemistries that use the chemical reaction of lithium to store electrical energy, as shown by the half-cell equation of Equation (2.16). In the case of most lithium based chemistries, the anode is made from graphite, and the cathode material is changed to alter the battery's performance [43]. Table 2.3 is a summary of the most common lithium-based chemistries used in the electric vehicle market. It should be noted that the performance values stated are an estimation, and that actual performance varies dependent on manufacturer. In the case of the specific energy and power, the stated values assume ideal chemical reactions and are therefore higher than reality.



¹¹ Lithium Manganese Oxide

¹² Lithium Nickel Manganese Cobalt Oxide

¹³ Lithium Nickel Cobalt Aluminium Oxide

Table 2.3. Summary of lithium-ion cell chemistries [43] [45] [46] [47]

Chemistry	Nominal Cell Voltage (V)	Specific Energy (Wh/kg)	Specific Power (W/kg)	Cycle Life (cycles)
LiCoO ₄ (LCO)	3.6	400 – 500	300 – 400	500 – 1000
LiMn ₂ O ₄ (LMO)	3.7	410 – 490	400 – 500	300 – 700
LiFePO ₄ (LFP)	3.6	520 – 590	2000 – 3000	1000 – 2000
LiNiMnCoO ₂ (NMC)	3.3	610 – 650	1000 – 2000	1000 – 2000
LiNiCoAlO ₂ (NCA)	3.6	680 – 760	1500 - 2500	500

The most common enclosure types used in electric vehicles are cylindrical, prismatic and pouch (Figure 2.13). Whilst the internal chemistry of the cells remains consistent across the packaging options, the relative benefits and shortfalls of each cell type dictate their application.



Figure 2.13. Examples of pouch (a), cylindrical (b) and prismatic (b) cell enclosures

Cylindrical cells are the industry standard for lithium-ion batteries. The electrodes and separator are wound in a spiral pattern to maximise the surface area available to the chemical reaction, and are contained within a steel can. This construction allows cylindrical cells to be mass produced at a fraction of the cost of prismatic and pouch cells, whilst having similar energy density properties. The most common lithium-ion cylindrical size is the 18650 (18 mm diameter, 65 mm length), which is used by Tesla Motors to construct their tractive packs.

Prismatic cells were created in response to the need for thinner batteries. This is achieved by layering the electrodes and separator into a rectangular casing. The enclosure material of a prismatic cell is usually a strong plastic to apply consistent pressure on the internal layers. Manufacturers often incorporate mounting structures into this enclosure which ultimately reduces the complexity of packaging multiple cells together. The consequence, however, is increased manufacturing cost and a lower energy density due to the added enclosure material.

Pouch cells are considered the most energy dense enclosure option. They are constructed using the same layering technique as prismatic cells, but are sealed within a lightweight bag. The electrolyte of a prismatic cell is typically gelatinous, and often referred to as a Lithium Polymer (LiPo) cell. Pouch cells are considered to have the highest energy density of the discussed enclosure types; however, they require more complex mounting structures to prevent swelling under load.

2.6. ACCUMULATOR MANAGEMENT SYSTEM THEORY

An Accumulator Management System¹⁴ (AMS) is used to ensure batteries remain within their operational limits. At their most basic level, an AMS will measure the voltage of each parallel group of cells in an accumulator¹⁵, and declare a fault if an under or overvoltage condition is detected. In addition, an AMS will also measure the temperature of the cells; however, in the case of most commercial AMS products, this is a global temperature and not cell specific.

When a series string of cells is charged, their individual voltages are never equal, due to natural imperfections that affect a cell's ability to accept charge. There is therefore a risk that the voltage of a cell will exceed its maximum limit whilst the remaining cells are only partially charged. To counter this, accumulator management systems use cell balancing resistors to dissipate energy stored by cells that have a voltage higher than a given threshold. Effective cell balancing results in the voltage of each cell increasing proportionally to one another.

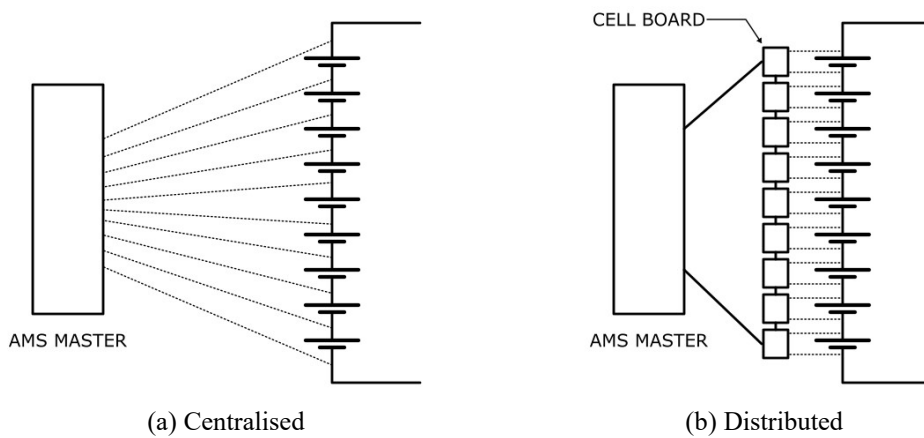


Figure 2.14. Diagram of centralised (a) and distributed (b) AMS topologies

Accumulator Management Systems generally fall under one of two topologies. Centralised management systems (Figure 2.14(a)) consist of a single master unit, which measures the voltage of every cell (or single group of parallel cells). Conversely, a distributed AMS (Figure 2.14(b)) consists of individual circuit boards that interface with each parallel cell, whereupon the boards are controlled by a master

¹⁴ Referred to as a Battery Management System (BMS) outside of Formula SAE.

¹⁵ Formula SAE allows electrical energy to be stored in either batteries or super-capacitors. An accumulator is defined as the cells or capacitors used to store energy for the tractive system, along with the necessary monitoring electronics.

unit. The relative benefits of each topology can be identified based upon the size and complexity of the tractive battery the system is protecting. Centralised systems are ideal for accumulators with a low number of series cells; in other words, less connections to be made to the central unit. Distributed systems are more suited to accumulators with a higher voltage (more cells in series). Galvanic isolation between the cell boards and master unit ensure that the measured voltages are contained to each board, and will not exceed the maximum potential of a single cell.

A centralised-slave topology (Figure 2.15) is a variation of the centralised topology; in which multiple centralised BMS nodes are used to manage groups of cells, and are all controlled by a main unit. This has the advantage, over a conventional centralised topology, of localising the cell measurement wires and therefore voltage potentials.

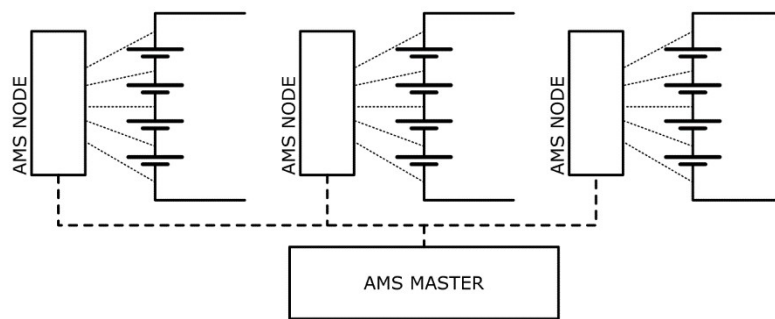


Figure 2.15. Diagram of centralised-slave AMS topology variation

2.7. FUSE THEORY

Fuses are current-sensitive devices used as overcurrent protection for electrical circuits. Fuses are graded based upon their I^2t rating, that is, the thermal energy resulting from current flow. As such, fuses have a non-linear behaviour, as shown by the time-current curves in Appendix B. The time-current curve gives an indication of the time taken to break a circuit for a certain current. For circuits with multiple downstream fuses, the time-current curves can be used to grade the fuses against one another to prevent multiple fuses from rupturing simultaneously.

Fuses are characterised by a few important parameters, which must be considered when selecting a fuse:

- Current Rating: The current rating of a fuse is the maximum current a fuse can carry continuously (at the rated temperature). As fuses are dependent on temperature, changes in ambient temperature affect their behaviour. To counter this, the current rating of a fuse should be re-rated according to the expected ambient temperature of the circuit.
- Voltage Rating: A fuse will behave as expected up to its maximum rated voltage. Exceeding the rated voltage creates the risk of arcing across a ruptured fuse, which maintains circuit

continuity. Voltage ratings are specified for ac or dc circuits, whereby the ac voltage rating is generally higher than that of dc.

- **Interrupt Rating:** The interrupt rating specifies the maximum overload current a fuse can break at its rated voltage. A fuse can be expected to receive a fault current many times greater than its rated current in the event of a short circuit. Provided the fault current is less than the interrupt rating of the fuse, the fault will be interrupted without external damage to the fuse (for example the fuse body exploding).

The Formula SAE rules require the batteries in the accumulator to be protected by a tractive fuse (EV3.3.2). The selection of this fuse will be discussed in Section 4.3.

2.8. ACCUMULATOR ISOLATION RELAY THEORY

As per EV3.5.1 of the Formula SAE rules, each accumulator must have at least two accumulator isolation relays (AIRs). An AIR is a normally-open contactor that is controlled by the vehicle's shutdown circuit (discussed further in Chapter 5). The purpose of the AIRs is to disconnect both poles of the tractive battery, such that no high-voltage is present on the output of the accumulator. An AIR is selected upon its rated voltage, continuous current capability and interrupt rating. The interrupt rating of an AIR implies the maximum power in the circuit that can be broken.

2.9. PRECHARGE & DISCHARGE THEORY

The inverter topology discussed earlier (Figure 2.3) has a capacitor at the tractive input to filter the high frequency switching noise generated. This capacitance, referred to from here onwards as the *intermediate capacitance*, causes two problems when connected to a dc source. Figure 2.16 shows a simplified diagram of the tractive system in UCM16.

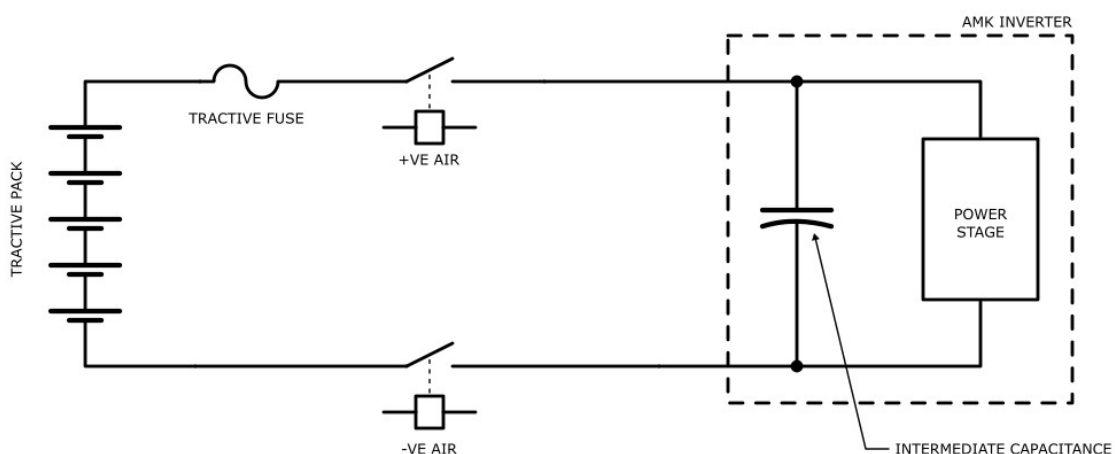


Figure 2.16. Simplified diagram of UCM16 tractive system

Consider first the case where the AIRs are closed and the circuit is completed. The AMK inverter does not allow power transfer until its intermediate capacitor is charged, therefore the current through the charging capacitor can be determined by its natural response, as shown by (2.17) [48]

$$i_C = \frac{V_S (1 - e^{\frac{-t}{RC}})}{R} \quad (2.17)$$

where, i_C is the capacitor current, V_S is the voltage of the accumulator, t is the time, R is the series resistance of the accumulator and intermediate capacitor, and C is the intermediate capacitance. When the AIRs are closed ($t = 0$), the minimal series resistance of the circuit causes a very large initial current to flow through the capacitor. Whilst this will cause the tractive fuse to rupture, protecting the circuit, it means the vehicle cannot drive.

The solution is to precharge the intermediate capacitor through a resistance large enough to limit the peak charging current to an appropriately low value. Figure 2.17 shows the inclusion of a precharge circuit to the previous tractive system diagram (Figure 2.16). When the vehicle is precharging, the precharge relay and negative AIR are closed, such that the series resistance is predominantly that of the precharge resistor. Once the intermediate capacitor has been charged to an acceptable voltage, defined as within 90% of the accumulator voltage by the FSAE rules (EV4.11.1), the precharge relay opens and the positive AIR closes. As the intermediate capacitance voltage is much closer to the tractive pack voltage, the resulting peak current is at an appropriately low value.

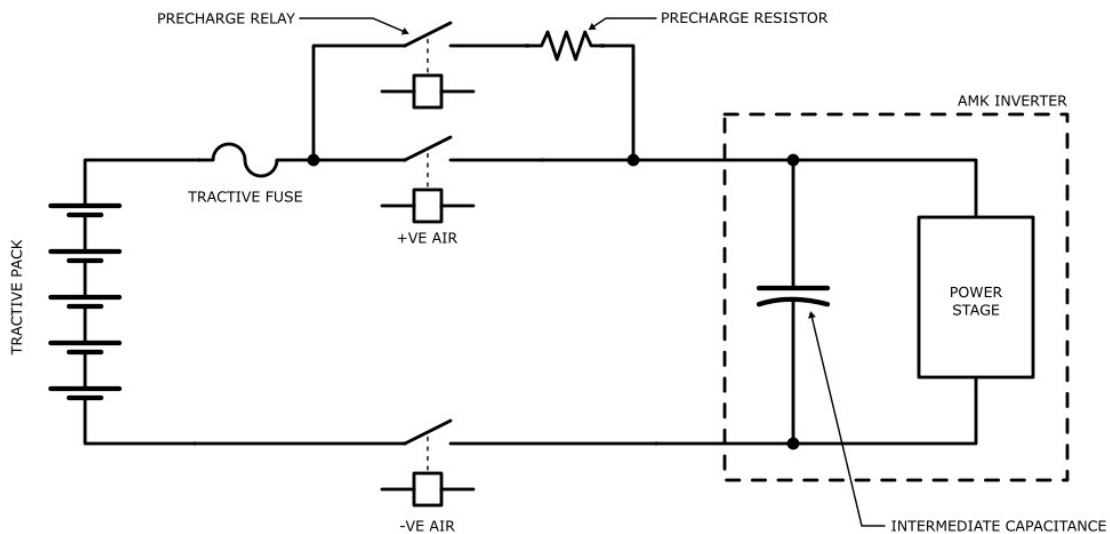


Figure 2.17. Diagram of tractive system with precharge circuit

Consider now the case where the vehicle has been driving and both AIRs are opened (either by the driver or a safety system), and the accumulator is disconnected from the inverter. The intermediate capacitor will remain charged with a potentially lethal amount of stored electrical energy. Although the capacitor will slowly discharge, the time taken is unacceptable in the event of an emergency, or when the driver wants to safely exit the vehicle.

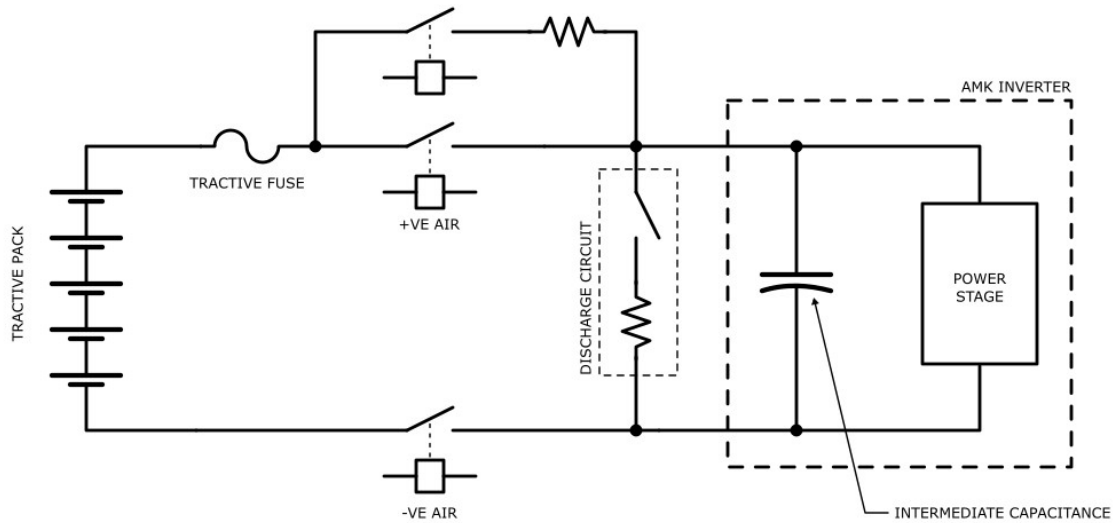


Figure 2.18. Diagram of tractive system with precharge and discharge circuits

A discharge circuit is used to dissipate the stored energy by switching a parallel resistance across the intermediate capacitor. Figure 2.18 shows the inclusion of a discharge circuit to the tractive system diagram. Two factors influence the rate at which the capacitor can be discharged. Firstly, the FSAE rules require the voltage of the capacitor to fall below 60 Vdc within five seconds of the AIRs opening (EV5.1.3). Secondly, the maximum discharge current of the intermediate capacitor must not be exceeded. The current through the discharging capacitor can be calculated using Equation (2.18).

$$i_C = \frac{V_S \left(e^{\frac{-t}{RC}} \right)}{R} \quad (2.18)$$

2.10. CHAPTER SUMMARY

This chapter introduced important theory related to electric vehicles and their application in motorsport. The differences between induction and permanent-magnet synchronous motors were detailed. It was determined that PMSM motors were more suitable for a motorsport application due to their greater torque and power density, and ability to be configured in a 4WD drivetrain configuration. Following this, a three-phase full-bridge inverter topology was introduced, and how reference frame transformations are used to simplify motor control.

The remaining sections of this chapter were dedicated to electrochemical cell theory and managing the energy in the tractive system. A summary was provided of the most common battery cell chemistries, along with the three most common enclosure types. The importance of precharging and discharging the intermediate capacitance of the inverter was then explained.

CHAPTER 3

ELECTRIC POWERTRAIN

The powertrain is the core element of a race car. Whether internal combustion or electric, the goal of a powertrain is to produce the most power from a package with as little mass and loss as possible. Traditionally, race cars use internal combustion engines, in which the combustion of a mixture of fuel and air generates motive force. However, the re-introduction of electric motors into the automotive industry has allowed motorsport engineers to exploit the benefits of an electric powertrain. This chapter discusses the selection process for UCM16's 4WD electric powertrain.

3.1. AMK FORMULA STUDENT ELECTRIC RACING KIT

Selecting the electric powertrain for UCM16 was the first major design decision made as it defines the core requirements for the mechanical and electrical systems. The Formula Student Electric (FSE) Racing Kit by AMK was the only package considered to any notable degree. The FSE Racing Kit is a complete system that has been tailored to suit FSAE teams, and includes:

- An AMKASYN KW26-S5-FSE-4Q Inverter
- Four DD5-14-10-POW synchronous servo motors
- AMK AIPER Pro start-up software
- A 2-day training course at AMK's Headquarters in Kirchheim, Germany
- 100 hours of engineering support

In addition to a 25% sponsorship discount, there were two major benefits of using the FSE Racing Kit, opposed to an alternative powertrain package. Firstly, the kit comes as a complete product in which the motors and inverters have guaranteed compatibility. It is common for different inverter and motor manufacturers to develop their products to work together; for example, an Enstroj Emrax motor controlled by a Unitek Bamocar inverter¹⁶. However, as each manufacturer develops their products further, there is a chance that compatibility issues may arise. Due to the short timeframe allocated to

¹⁶ This motor-inverter combination is the preferred choice of electric vehicle teams at the Formula SAE Australasian competition (refer to Appendix A).

developing UCM16, any time spent fixing compatibility issues would be unacceptable, and therefore avoided with the FSE Racing Kit.

The second benefit is the suitability of the package to Formula SAE. AMK powertrains have been used by multiple FSAE teams worldwide. The most notable are Formula Student Team Delft and GreenTeam Uni Stuttgart who are currently 2nd and 6th respectively in the FSE world ranking list [3]. At the time when the powertrain was being selected, GreenTeam Uni Stuttgart had recently set the world record for the fastest accelerating electric car [49], thereby proving the FSE Racing Kit had the performance desired by the team.

3.1.1. MOTOR DESCRIPTION

The DD5-14-10-POW (pictured in Figure 3.1) is a 10-pole permanent-magnet synchronous servo motor¹⁷. The key specifications (from the datasheet in Appendix C) of the motor are listed in Table 3.1.

Table 3.1. DD5-14-10-POW motor specifications

Mass	3.55 kg
Rated Torque	9.8 Nm
Rated Power	12.3 kW
Rated Speed	12,000 rpm
Maximum Speed	20,000 rpm
Rated Voltage	350 V _{rms}
Rated Current	41 A _{rms}
Maximum Current (for 1.24 s)	100 A _{rms}

The DD5 motor is supplied from AMK with a 300 mm shielded three-phase cable that is hard-wired to the motor windings. Motor rotor position is measured by a digital encoder appended to the rear of the main body that communicates to the inverter using an M12 connector. The temperature of the motor windings is measured by a KTY thermistor, which is also sent to the inverter via the M12 connector. The motors are cooled via thermal conduction through the aluminium housing. To increase heat transfer, AMK recommended the use of a water-cooled jacket.

¹⁷ A servo motor is any motor that has rotor position sensing and control.



Figure 3.1. AMK DD5-14-10-POW motor

Figure 3.2 is an extract from the datasheet showing the performance curves of the motor. The orange curves represent the continuous torque and power in each graph respectively, whilst the blue curves represent the peak performance (limited by the inverter to a maximum of 1.24 seconds). The dashed curves represent the performance of the motor with field-weakening, where the inverter injects a negative magnetisation current to oppose and reduce the magnetic field strength of the rotor [50]. Referring to Equation (2.7), a reduced magnetic field strength allows the angular velocity of the motor to be increased for the same induced back EMF.

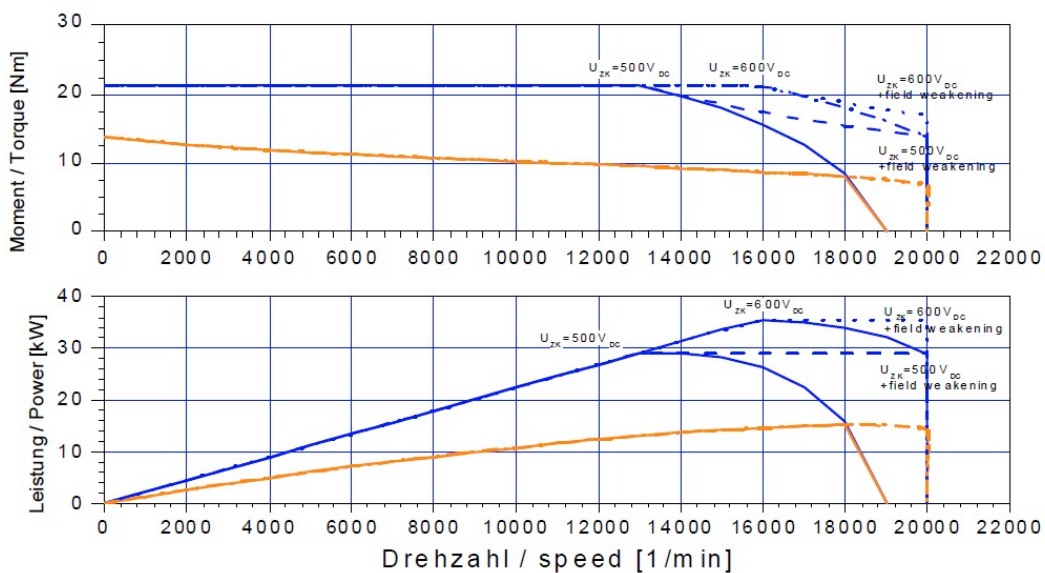


Figure 3.2. DD5-14-10-POW motor performance curves [50]

The performance curves in Figure 3.2 are only shown for a supply voltage of 600 Vdc and 500 Vdc. Since the powertrain is supplied by the tractive pack, the voltage will reduce as the state of charge depletes. This not only reduces the maximum speed of the motor (assuming no field weakening) but also reduces the output power of the motor. The graphs of Figure 3.3 and Figure 3.4 show the performance curves adjusted for differing supply voltages. This was achieved by scaling the curves based upon their theoretical no-load speed using Equation (3.1), and then recalculating the output power using Equation (3.2).

$$\omega_{no-load,B} = \frac{V_B}{V_A} \omega_{no-load,A} \quad (3.1)$$

$$P = \tau \times \omega \quad (3.2)$$

As shown by the adjusted curves, the peak output power of the motor is significantly reduced when the supply voltage is decreased. The peak output power at 300 Vdc is 18.8 kW, which is 53% of the peak power at 600 Vdc (35.2 kW). However, the maximum continuous power output (11 kW) is only 81% of the maximum continuous power at 600 Vdc (13.6 kW). The low-speed torque of the motor is not affected by the supply voltage, and will therefore allow the vehicle to accelerate at the same theoretical rate regardless of battery state of charge. It can be seen in Figure 3.4, however, that the characteristic (knee-point) speed of the motor reduces proportionally with supply voltage, at which point the torque decreases dramatically.

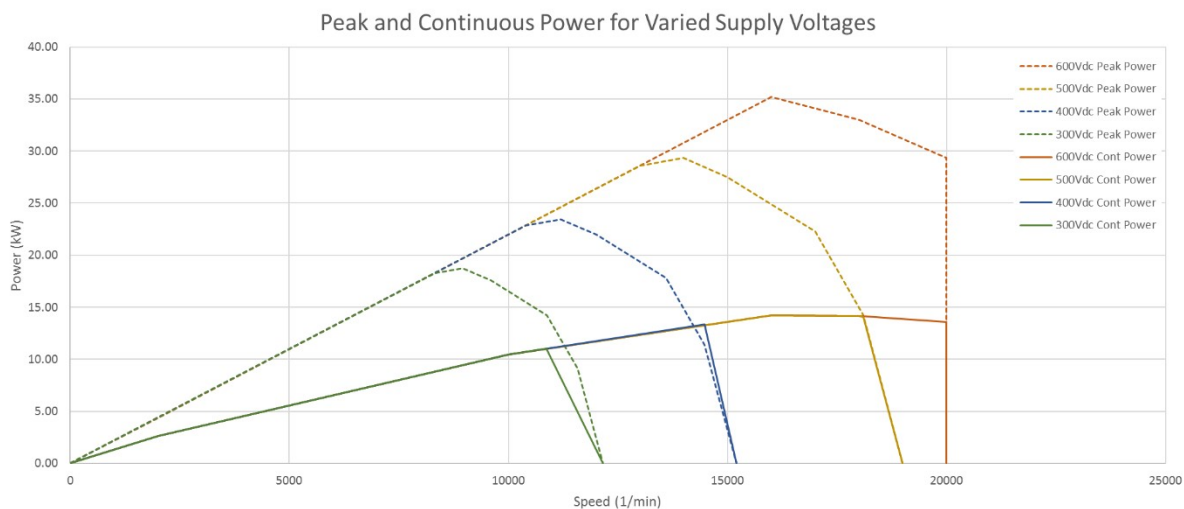


Figure 3.3. Adjusted peak and continuous power curves for DD5-14-10-POW motor

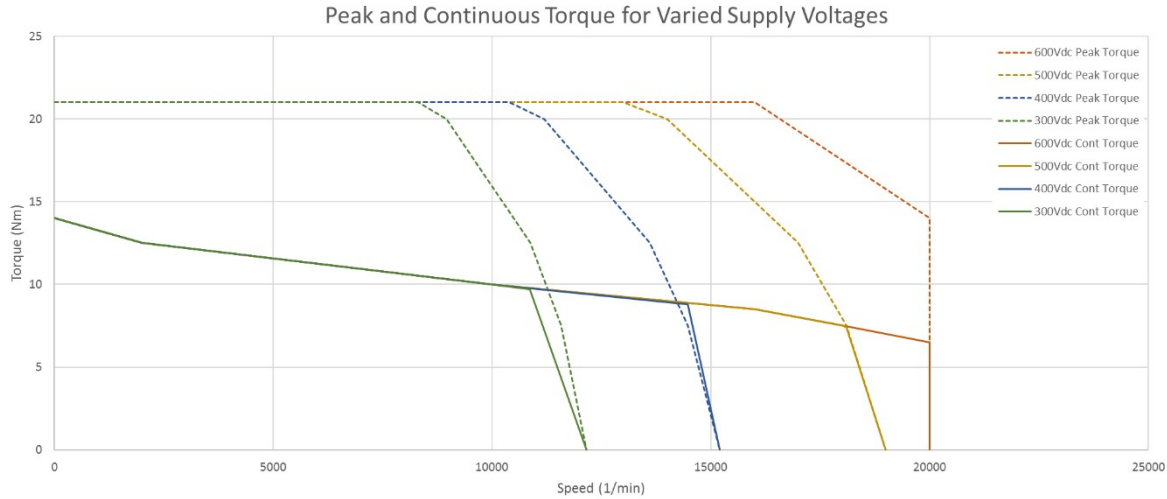


Figure 3.4. Adjusted peak and continuous torque curves for DD5-14-10-POW motor

A comparison was made between four DD5 motors, in a 4WD powertrain, and a single Emrax 228, in a RWD powertrain, to see how the AMK system would compare to the expected electric race cars at the Australasian FSAE competition. The Emrax 228 motor has a maximum speed of 5000 rpm [51], which is considerably lower than that of the DD5 motors. To provide an approximate comparison, the maximum speeds of the motors were matched by specifying gear ratios to be used during the simulation.

The final gear ratio of the single-stage planetary gearbox for UCM16 was designed to be 1:11. This was the maximum ratio that could be housed within the geometric confines of the suspension and wheel assembly. This gear ratio reduces the maximum output speed of the DD5 motors to 1818 rpm at the wheels (or 150 km/h ground speed with 10" Hoosier tyres). To match this, the Emrax motor was simulated with a gear ratio of 1:2.75.

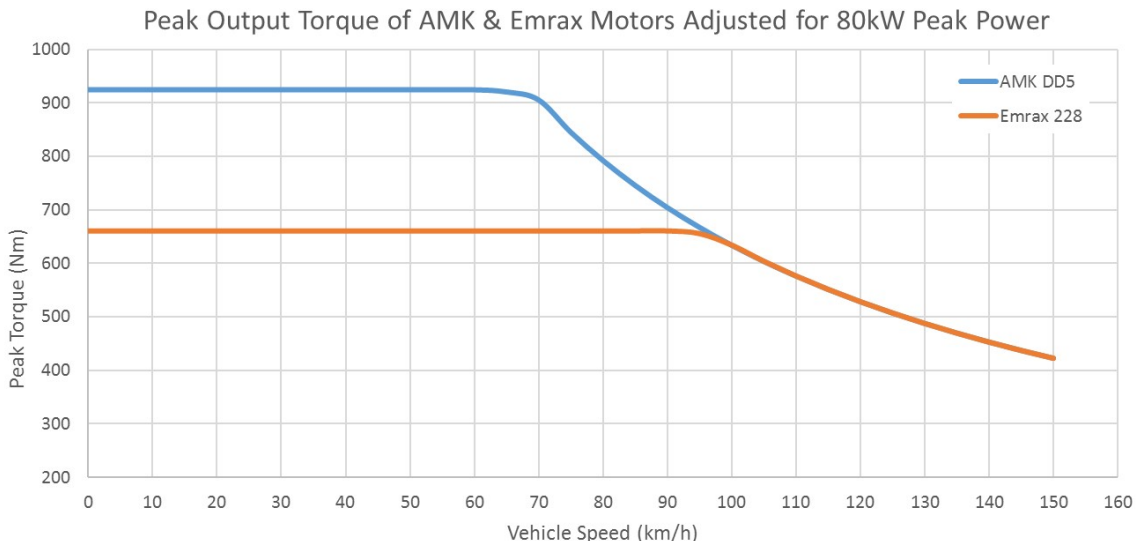


Figure 3.5. Peak output torque comparison of AMK & Emrax motors adjusted for 80 kW peak power

Motor power is not a valid method of comparison between the motors as the FSAE rules prevent the powertrain from drawing greater than 80 kW from the accumulator (EV2.2.1). Instead, the motors were compared on their peak torque output, which was adjusted to prevent more than 80 kW power draw. Note that the comparison ignored the efficiency of the motors (as they are very similar), and assumed the losses in the associated electronics and transmission to be negligible. The results of Figure 3.5 show the 4WD AMK powertrain to have a peak starting torque that is 40% greater than the Emrax motor. It can also be stated that the AMK powertrain provides a greater torque than the Emrax motor until the point at which both powertrains become power limited.

In terms of vehicle performance, a race car with a 4WD AMK powertrain will have a greater rate of acceleration than a similar car powered by an Emrax 228. Although four DD5 motors weigh 15% more than an Emrax 228 (14.2 kg compared to 12.3 kg [51] respectively), for such a small overall vehicle weight difference¹⁸ it can be assumed that the increased grip limitations of a RWD car, over a 4WD car, significantly favour the AMK powertrain for performance.

3.1.2. INVERTER DESCRIPTION

The AMKASYN KW26-S5-FSE-4Q inverter is a quad-inverter unit with integrated drive controllers, which are mounted to a liquid-cooled cooling plate. Figure 3.6 is a CAD model of the KW26-S5-FSE-4Q inverter showing the assembled components, and the key specifications are summarised in Table 3.2 [50]. From here onwards, the KW26-S5-FSE-4Q will be referred to as the *inverter*, and a single inverter within the assembly will be referred to as a *sub-inverter*.

The main components (labelled in Figure 3.6) are as follows:

- C1, C2, C3, C4 – The KW-R06 controller cards for each sub-inverter. The controller cards on each side of the liquid cooling plate (i.e. C1, C2 and C3, C4) share the same CAN network and low voltage power supply.
- P1, P2, P3, P4 – The power electronic circuits for each sub-inverter. Each circuit uses six insulated-gate bipolar transistors (IGBT), configured in the topology described in Section 2.2, and have an input capacitance of 75 μF .
- SL – The supply and logic board for each half of the inverter (only the supply board for I1 and I2 is shown). Each sub-inverter must be supplied with 24 Vdc, and have a maximum current draw of 500 mA.
- CB – The transverse board for each half of the inverter, which is the physical connection between the corresponding controller cards.

¹⁸ Assuming an arbitrary base vehicle mass of 220 kg (based on the mass of electric FSAE cars at FSAE-A), the difference in mass between the two powertrain configurations equates to 1% of the overall vehicle mass.

- I1, I2, I3, I4 - The assembly of the controller card and power electronics for each sub-inverter.

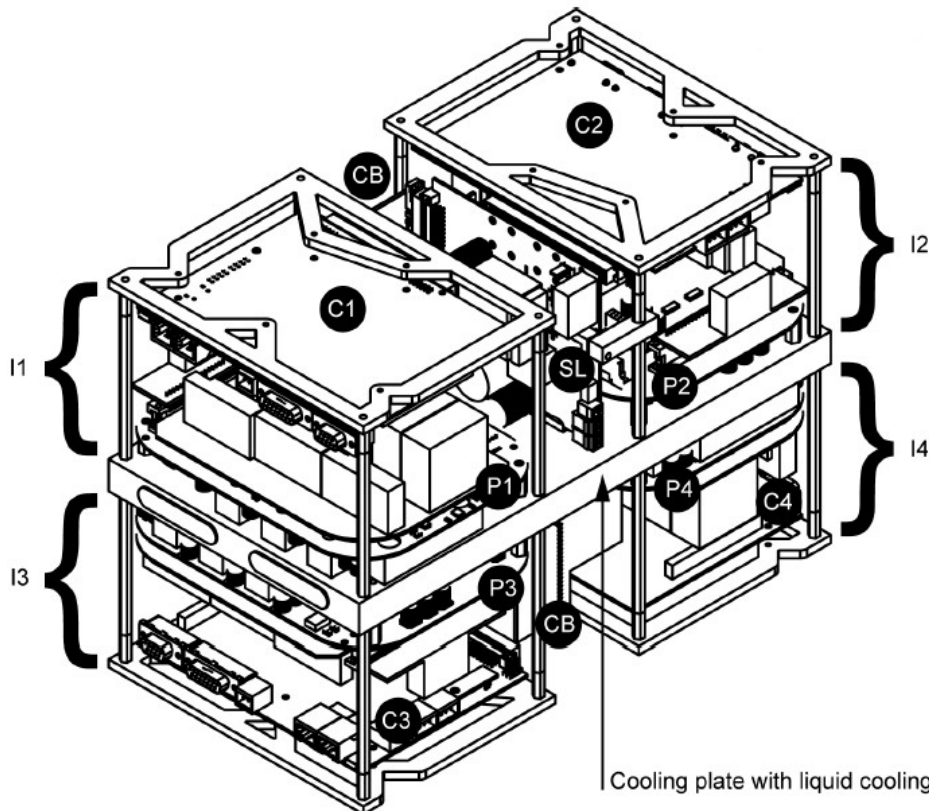


Figure 3.6. CAD model of KW26-S5-FSE-4Q inverter [49]

Table 3.2. KW26-S5-FSE-4Q inverter specifications (per sub-inverter)

Input voltage range	250 Vdc – 720 Vdc
Input current (for HV = 540 Vdc)	48 A
Control method	PWM, Field-Oriented Control
Switching frequency	8 kHz
Output voltage range (HV = 250 – 720 Vdc)	160 – 490 Vac (sinusoidal output current)
Rated output power	26 KVA
Rated output current	43 A
Peak output current	105 A (for 10 s)
Efficiency	Approx. 98%

Each sub-inverter is characterised by its own set of parameters that are categorised using unique identification numbers. The parameters are based on the SERCOS (Serial Real-time Communication System) standard for interfacing industrial control and drive systems, and can only be configured using AMK's proprietary software AIPEX Pro. The motor parameters are automatically uploaded to the inverter via the digital encoder when powered. However, the parameters of the controller card must be

configured manually. AMK have simplified the number of parameters to be set (of which there are over 500 for the KW-R06) to less than 25 for an FSAE application. Table 3.3 details the most important of these parameters in terms of vehicle setup and performance adjustment.

Table 3.3. Key parameters of KW-R06 controller card

Parameter ID	Parameter Description	Default FSE Value
ID34023	‘Bus Address Participant’ – the CAN node number of the sub-inverter	1
ID34024	‘Bus Transmit Rate’ – transmit rate for CAN network	1000 (1 Mbps)
ID32798 - 3	Maximum battery voltage (V)	720
ID32798 - 4	Minimum battery voltage (V)	250
ID32798 - 5	Inverter temperature at which full torque is available (0.1 °C)	500
ID32798 - 6	Inverter temperature at which no torque is available (0.1 °C)	600
ID32798 - 8	Power supply (IGBT) temperature at which full torque is available (0.1 °C)	1150
ID32798 - 9	Power supply (IGBT) temperature at which no torque is available (0.1 °C)	1250
ID32798 - 11	Motor temperature at which full torque is available (0.1 °C)	1250
ID32798 - 12	Motor temperature at which no torque is available (0.1 °C)	1400
ID32837	‘DC Bus Voltage Monitoring’ – the minimum voltage required to activate the motor driver (V)	250
ID38	‘Positive Velocity Limit’ – maximum velocity that can be requested from the vehicle controller (rpm)	5000
ID39	‘Negative Velocity Limit’ – minimum velocity that can be requested from the vehicle controller (rpm)	-5000
ID82	‘Positive Torque Limit’ – maximum torque that can be requested from the vehicle controller ($0.1\%M_N^{19}$)	120
ID83	‘Negative Torque Limit’ – minimum torque that can be requested from the vehicle controller ($0.1\%M_N$)	-120

The Bus Address Participant (ID34023) is used to calculate the 11-bit identifiers of the three CAN messages used for motor control and data transmission (see Appendix D). Each motor and sub-inverter combination is controlled by a single message called *AMK Setpoints*, which is sent by the vehicle control unit. In return, the sub-inverter periodically transmits status information, for example motor speed and device temperatures, in two messages called *AMK Actual Values 1* and *AMK Actual Values 2*. The

¹⁹ M_N is the rated torque of the motor

identifier of a message is calculated in hexadecimal by adding the Bus Address Participant to the message's base address. Figure 3.7 is an interface diagram for the inverter with the vehicle control unit, and shows the message direction and associated base address. As an example, the *AMK Setpoints* message identifier for *Inverter 2* is 0x185 (0x183 + 0x002). It is important to note that the *AMK Setpoints* CAN message must be sent with a period less than 50 ms. If exceeded, the sub-inverter will generate an error and set the motor into a free-wheeling state.

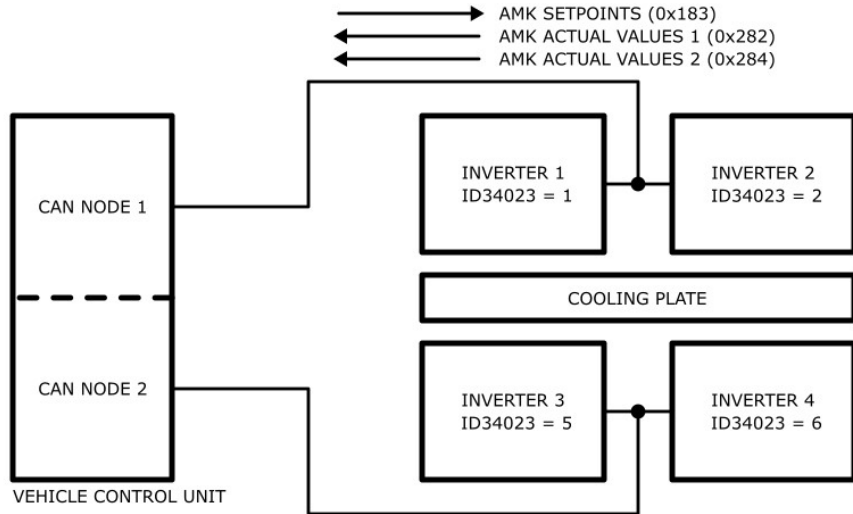


Figure 3.7. CAN network interface diagram for KW26-S5-FSE-4Q inverter

The motors can operate at torque greater than their nominal torque provided the operating limits are adhered to. In the case where the limits are exceeded, the inverter automatically reduces the motor torque, as shown by Figure 3.8. Derating is based upon the temperature parameters of Table 3.3 (ID32798-5 through ID32798-12) and the current integral of the motor and inverter. Figure 3.8 shows that if the limits continue to be exceeded, the drive will be shut down; and must therefore be avoided at all costs during a FSAE event.

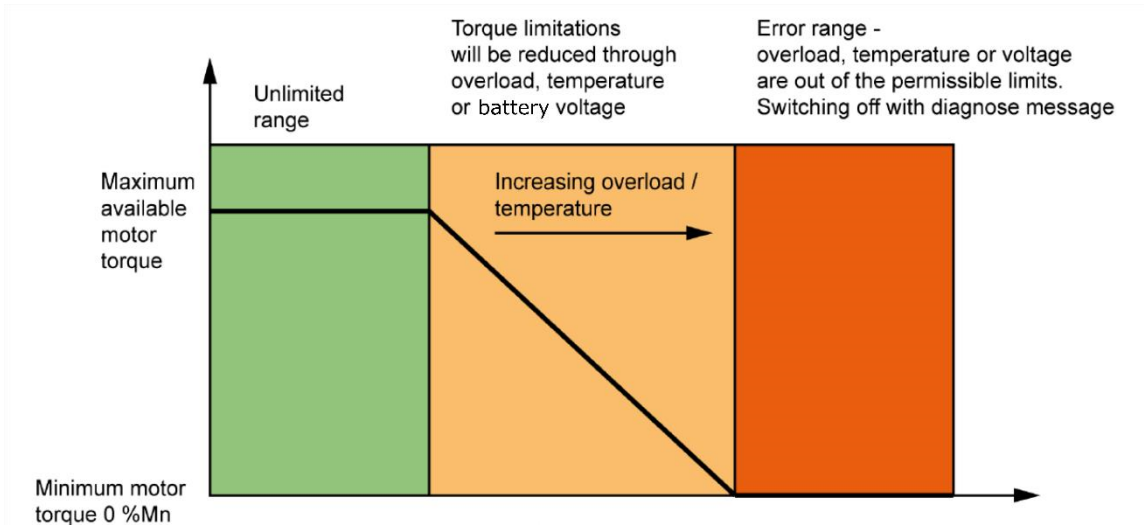


Figure 3.8. Graphical representation of inverter derating feature [50]

3.1.3. MOTOR CONTROL

The inverter controls the motor in a speed-control operating mode. According to AMK, this has the advantage of allowing the motor speed and torque to be dynamically limited. However, speed control is inherently unnatural to a driver as conventional cars are torque controlled. In a car that is speed controlled, the accelerator pedal is proportional to the speed of the car. For a torque controlled car, the accelerator is proportional to the torque or, in other words, the rate of acceleration. Consider the case where a car is accelerating to a constant velocity. In a torque controlled car, the natural response of the driver would be to reduce the rate of acceleration, by lifting the accelerator pedal, as they approached the desired velocity. Doing this in a speed controlled car, however, would result in the car slowing down. To drive a speed controlled car with racing precision, a driver would have to relearn the fundamentals of driving. In the case of UCM, which has many experienced drivers, this was not an option.

To rotate a motor rotor, the speed controller requires the desired velocity and the maximum torque that can be applied; which are set using *AMK Setpoints*. Table 3.4 describes the combination of speed and torque setpoints required to achieve a certain driving outcome. To convert the control of the car, so it appears to be torque controlled from the driver's perspective, the target velocity is set to the maximum speed of the motor (depending on the current tractive voltage) and the positive torque is controlled by the accelerator pedal.

Table 3.4. Driving mode control requirements

Driving Mode	CAN Variable Requirement
Forward Acceleration	AMK_TargetVelocity = required positive speed
	AMK_TorqueLimitPositiv = required acceleration torque
	AMK_TorqueLimitNegativ = 0
Coasting	AMK_TargetVelocity = any speed
	AMK_TorqueLimitPositiv = 0
	AMK_TorqueLimitNegativ = 0
Motor Braking	AMK_TargetVelocity = 0
	AMK_TorqueLimitPositiv = 0
	AMK_TorqueLimitNegativ = required deceleration torque (-ve)

3.2. INITIAL SYSTEM DEVELOPMENT

At the beginning of March (2016) the decision was made to attend the AMK training course in Germany. As this was somewhat last minute, it gave only two weeks to develop a CAN controller to use on AMK's test rig. The CAN controller gave the opportunity to test the idea of developing a custom vehicle control unit for UCM16, and proved successful at the training course. Once back in New Zealand, the controller was used extensively in the development of the drive software and preliminary gearbox design.

3.2.1. CAN CONTROLLER

The controller consisted of two parts, an STM32F4 Nucleo-144 development board and a custom PCB (schematic detailed in Appendix E). The PCB was designed with three isolated CAN bus nodes, which would replicate the two CAN networks required to interface with the inverter and a third network for the remaining vehicle systems. Since the majority of the STM32 microcontroller range only include two CAN controllers, an MCP2515 stand-alone SPI CAN controller was added to the third node. Three potentiometers and push buttons were also added to the PCB as general purpose inputs. Figure 3.9 shows the final assembly of the PCB.

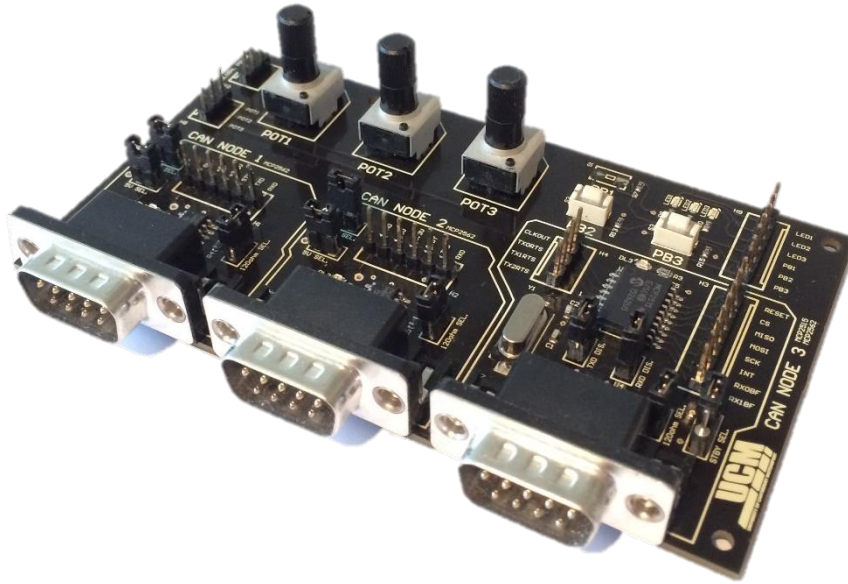


Figure 3.9. Assembled CAN Controller PCB

3.2.2. DYNAMOMETER TESTING RIG

A test rig (Figure 3.10) was constructed in the UCM workshop for testing a prototype planetary gearbox. The inverter was contained within a perforated steel box to reduce EMI radiation, and was supplied by a three-phase, 15 kW Chroma 62150H-1000S programmable dc power supply. To provide dynamic loading, the output shaft of the planetary gearbox was connected to a Dynapack DAQ2 dynamometer via a 1:1 gear ratio chain drive. A flywheel was connected to the dynamometer driveshaft to replicate the rotational inertia that would be expected from a production car (a requirement of the dynamometer).



Figure 3.10. Images of dynamometer test rig

The inverter is supplied by AMK as a blank unit, with only a few flying leads, and must be completely rewired to suit the application. The wiring for the testing rig was relatively simple and will therefore not be discussed in this section. Rather, the more complex wiring of the inverter for use in UCM16 is discussed in Chapter 6. In terms of controlling the single motor and sub-inverter, a testing program was executed on the STM32 Nucleo-144 development board and interfaced with the inverter via the CAN controller PCB. In turn, the development board interfaced with a laptop via UART (universal asynchronous receiver/transmitter) communication, which was running a control and datalogging interface (described below). A basic switchboard was constructed on Veroboard to enable the digital interlocks of the inverter and provide an emergency shutdown point.

The prototype gearbox was tested using three profiles:

Profile A: Motor speed ramped between 500 and 6300 rpm every 5 seconds with the dynamometer set to provide a constant load. This replicated the constant acceleration and deceleration expected on a Formula SAE track.

Profile B: Dynamometer set to maintain a constant speed of 3000 rpm. Every 30 seconds, the motor would pulse to 150% of its rated torque for 30 seconds, causing the dynamometer to increase its load. This tested the gearbox's ability to handle the sudden loading from the motor during hard acceleration, and can be considered a more intense version of Profile A.

Profile C: The motor accelerates to 15,000 rpm in 10 seconds and holds indefinitely. This tested the high-speed performance of the gearbox.

The speed and torque limits of the three profiles were found empirically. Although the Chroma dc power supply was rated for 15 kW, the output current was limited to 15 A. This limited the maximum output power to only 9 kW when the system was tested at 600 Vdc. The rate at which the motor accelerated was also important as it affected the dynamic response of the dynamometer. The response time of the dynamometer to a large input change from the motor was not fast enough and would cause the load to oscillate. This in turn caused the motor power draw to oscillate and trip the protection on the Chroma dc supply. A trial and error solution was therefore implemented to find the maximum operating speed and rate of acceleration that could be consistently tested. These varied depending on the profile being tested.

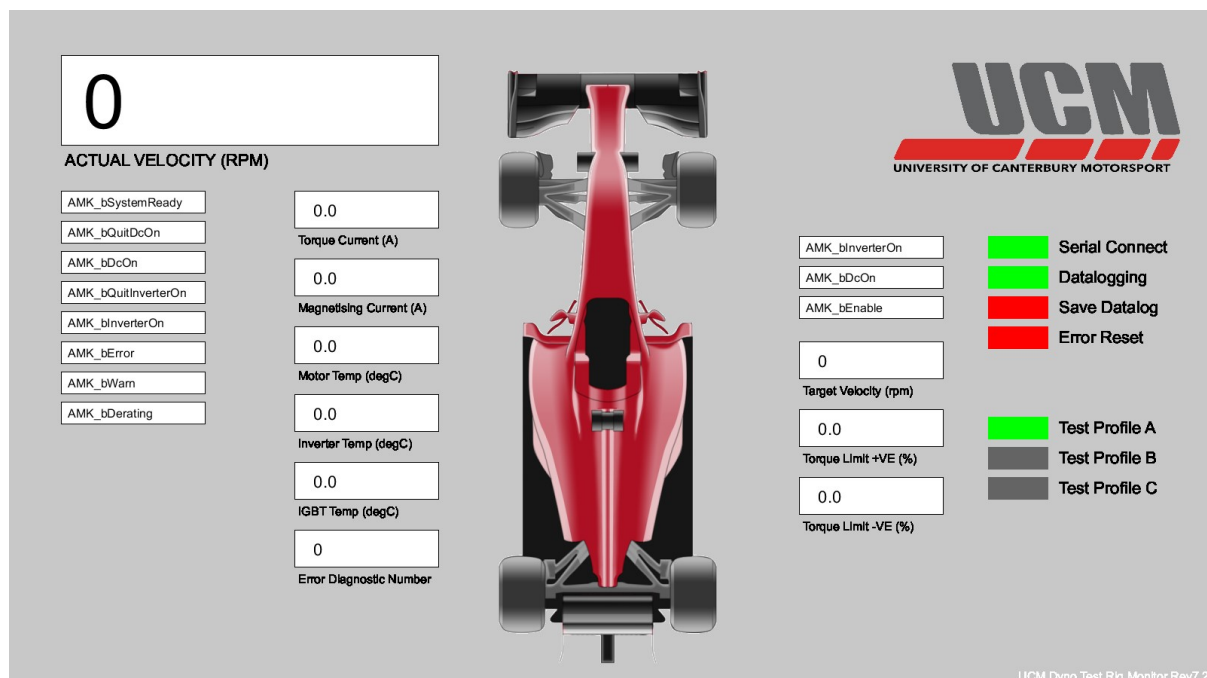


Figure 3.11. Screenshot of datalogger application created for dynamometer test rig

A control dashboard and datalogging Java application was written using Processing as a control dashboard and datalogger for the test rig. The application was run on a laptop and communicated to the STM32 microcontroller via a USB-serial (UART) connection. This allowed data to be transmitted via CAN from the inverter to the STM32 and displayed in real-time to the operator of the test rig, whilst also being logged every second into a CSV file. Figure 3.11 is a screenshot of the application window.

Over 50 hours of testing was conducted within a week-long period. Profiles A and B were primarily tested, with a duration of approximately 20 minutes each. The reason for focussing on these profiles was because they represented the most common conditions expected of a Formula SAE race car. Whilst the high-speed performance of the gearbox needed to be confirmed, Profile C was only tested five times with a duration no longer than two minutes after the motor was at maximum speed.

Figure 3.12 is a graphical example of the data collected for a Profile B test. The most important point to note is that the temperatures of the motor, IGBTs and cooling plate were asymptotical, indicating that the preliminary cooling system was effective for a single motor. The large peaks in motor velocity (red trace) were a result of the motor rapidly accelerating and then oscillating, whilst the system controlling the dynamometer's hydraulic resistance stabilised.

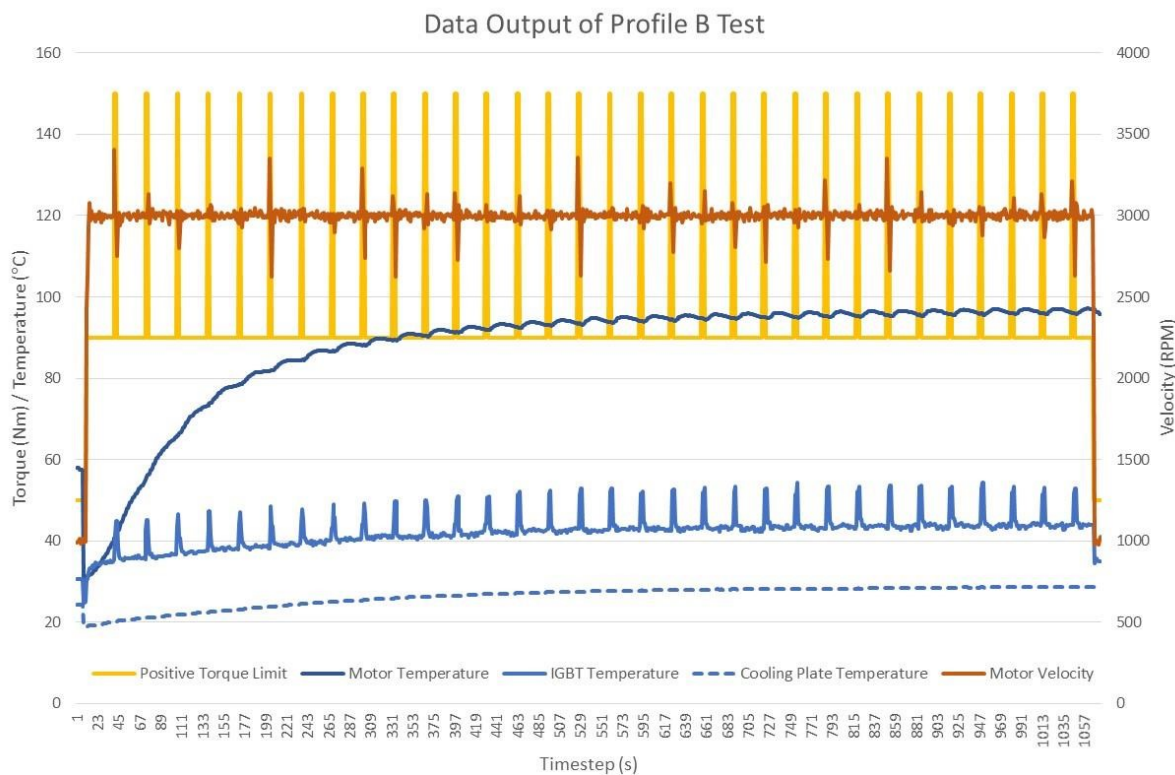


Figure 3.12. Example data output of Profile B test

3.2.3. INITIAL VEHICLE CONTROL UNIT DESIGN

Similar to an Engine Control Unit (ECU) in an internal-combustion vehicle, a Vehicle Control Unit (VCU) is used to control an electric vehicle. A common analogy is to refer to a VCU (or ECU) as the brain of a vehicle, which controls all operations and processes. However, the number of self-controlling sub-systems (for example the accumulator, which can operate almost entirely without external control input) within UCM16 means this is not a clear comparison. Rather, the VCU should be considered as the electronic interface between the driver and the powertrain, with a secondary purpose of checking the sub-systems are operating correctly.

The decision was made to develop a custom VCU for UCM16 in-house, as opposed to an off-the-shelf solution. The main justification was design flexibility, whereby the VCU would be designed to suit the specific needs of the race car. The VCU hardware was designed by an undergraduate electrical engineering student as part of a final year project. The software was a collaboration between the author and another final year electrical engineering student²⁰. The specifications of the VCU, dictated by the author, were as follows:

- STM32 M-Cortex series microcontroller (an STMF746ZG MCU was selected)
- Three CAN bus peripherals (two using the F7's in-built CAN controllers, the final using an MCP2515 stand-alone SPI CAN controller)
- Six analog inputs (used for throttle position, brake pressure, steering angle and temperature measurements)
- Ten digital inputs (used for binary signals such as pushbutton inputs)
- Nine high and low-side MOSFET switches (used for solid state switching control)

²⁰ From here onwards in this thesis it is acknowledged that all software development related to the VCU was a close collaboration, as it is impossible to distinguish individual elements.

3.3. CHAPTER SUMMARY

Chapter 3 provided an in-depth evaluation of UCM16’s electric powertrain. Firstly, the AMK Formula Student Electric Racing Kit was introduced as a complete off-the-shelf four-wheel drive powertrain unit. Selecting a predetermined system was extremely beneficial as it reduced the potential risk of cross-manufacturer incompatibility, and meant the powertrain would be developed from a proven platform. The second section of this chapter discussed the preliminary powertrain testing, which doubled as testing for the prototype planetary gearbox. A custom CAN transceiver PCB was developed, which was used to interface between an STM32 development board and the AMK inverter. A Java application was also created to both control the dynamometer testing rig, and log the data output of the inverter. Finally, the concept for a custom vehicle control unit was introduced, and specifications documented.

The following chapter (Chapter 4) focusses on UCM16’s accumulator and energy management systems. An accumulator is the FSAE term given to the tractive battery and monitoring control systems. Since the maximum voltage of the inverter was not a limitation on the accumulator voltage, the powertrain and accumulator were designed concurrently. Had this not been the case, the accumulator would have been designed after the powertrain had been determined. In addition to the accumulator design, the precharge, discharge²¹ and safety isolation PCB designs will be discussed.

²¹ Although not contained within the accumulator, the discharge circuit is a direct compliment to the precharge circuit, and is therefore included in this chapter.

CHAPTER 4

ACCUMULATOR & ENERGY MANAGEMENT

Movement cannot be achieved without energy. In the case of an electric race car, this energy is stored within the accumulator; a complex assembly of high voltage tractive battery modules, protection systems and monitoring electronics. The proximity of both high and low voltage electronics introduced a significant challenge at both board-level and during the final assembly. In this chapter, the design and integration of the tractive battery, cell monitoring system, energy management circuits and signal isolation circuits will be discussed.

4.1. BATTERY CONCEPT DESIGNS

This section details the three concepts for the batteries and associated module designs for UCM16's accumulator. The concepts were completed by the author with the intention that a mechanical engineering student would continue with the associated mechanical aspects of the design. All three concepts have been included to show the linkages between each iteration, and how elements from each concept were combined into the final design.

4.1.1. CAPACITY AND POWER REQUIREMENTS

The FSAE rules prevent multiple accumulators of differing capacities to be used (EV3.2.2), which restricts the use of a lighter accumulator for the less energy-intensive events. The capacity of an accumulator must therefore be large enough to complete the 22 km endurance event.

The initial attempt to determine the required accumulator capacity was made using Optimum Lap. Optimum Lap is a free-to-use lap simulation software package developed by Optimum G, which simplifies the characteristics of a vehicle into only ten parameters [52]. A vehicle model of UCM16 was created based on the expected metrics of the car. The vehicle model is detailed in Appendix F. Since Optimum Lap was initially developed for internal combustion race cars, and then modified to include electric vehicles, there was no way to incorporate the peak and continuous torque capabilities

of the AMK motors simultaneously. The powertrain of the simulated car was therefore configured to neglect any temperature related limitations by assuming the peak output of the motors was limited to 80 kW (see Motor Output Performance Curves in Appendix F). The expected implication of simplifying the simulation model was that the vehicle would be able to achieve maximum acceleration at any point on the track, consequently decreasing lap time and increasing energy consumption. In reality, the ability to achieve maximum acceleration (i.e. peak torque from the motors) is dependent on cooling and previous motor usage. It was therefore anticipated that the simulation results would be an overestimation of vehicle performance. The vehicle model was simulated using a track model of the 2011 FSAE-A Endurance event, which was downloaded from the Optimum G database. A layout of the track is documented in Appendix F.

Whilst conducting simulations, it was observed that Optimum Lap does not behave as expected when the “engine” parameters have maximum torque at zero speed. Figure 4.1 is a screenshot of the calculated performance metrics, and shows the simulated time to accelerate from 0 – 100 km/h to be 52816.91 s (14.6 hours). In comparison, Figure 4.2, which shows the simulated speed and power of the car over one lap of the endurance track, indicates the acceleration was as expected. As a further example of the unexpected results, the simulated power trace of Figure 4.2 shows the power exceeded the 80 kW maximum limit specified in the motor parametrisation.

Performance Metrics

Metric	Value
Top Speed	112.04 km/h
Time for 0 to 100 km/h	52816.91 s
Time for 100 to 0 km/h	1 s
Lateral Acceleration - Skidpad 50 m	19.37 m/s ²

Figure 4.1. Performance metrics of UCM16 calculated by Optimum Lap

Despite the apparent errors in the simulation, the energy consumption was calculated to be 0.44 kWh per lap. At 788 m per lap, this equates to 12.32 kWh for the entire endurance event. To provide context, the accumulator of Formula Student Team Delft’s DUT16 race car has a capacity of 7.4 kWh. In a design presentation, it was stated that this is sufficient to complete approximately two thirds of the endurance event and full race pace [53], whereby the remaining energy is recovered through regenerative braking. Based on this assumption their total energy expenditure was calculated to be approximately 11.1 kWh for the endurance event; which is within 10% of the Optimum Lap simulation result. Assuming a similar rate of regeneration, UCM16’s accumulator capacity needed to be approximately 8.5 kWh.

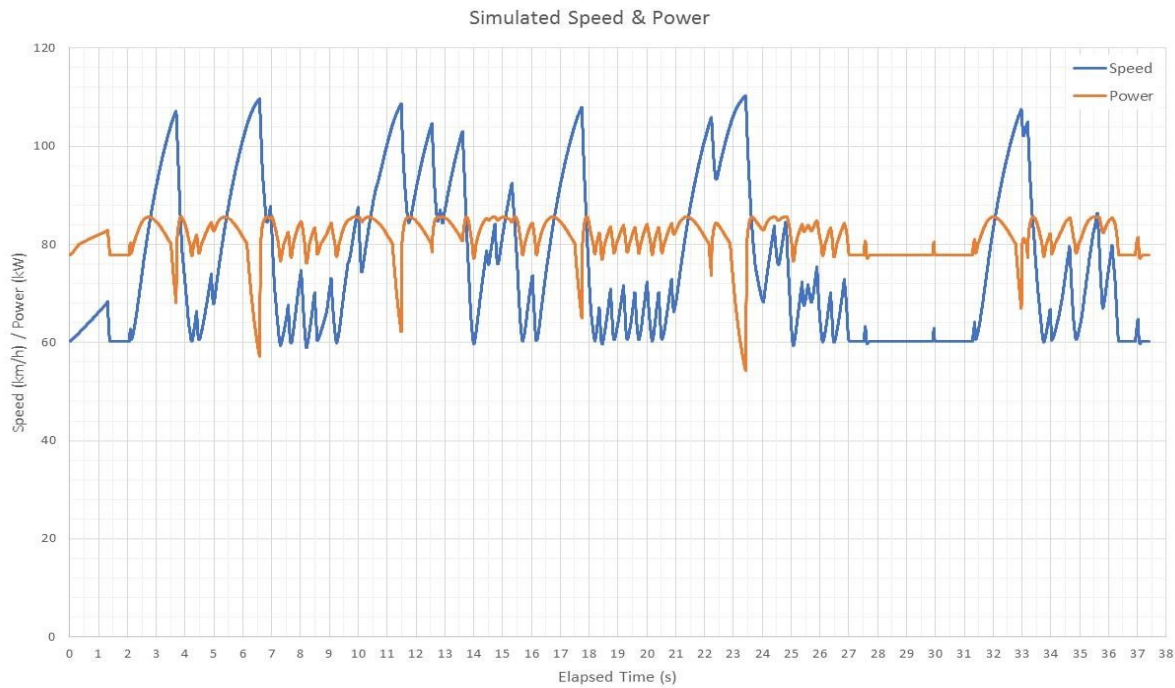


Figure 4.2. Simulated speed and power against elapsed time for 2011 FSAE-A endurance track

Based upon the average accumulator capacity of the researched Formula SAE teams (Appendix A), which was calculated to be 6.6 kWh, the desired capacity of UCM16's accumulator was chosen to be 8 – 8.5 kWh. This accommodated a 20% factor of safety over the calculated average; with the justification that it is better to over-specify the accumulator's capacity and remove cells later if required. This also ensured there would be sufficient capacity in the accumulator to not discharge the cells below 10% state of charge, which is considered the limit for good battery lifespan.

It was hoped that the Optimum Lap simulation would give an indication of the average power of the race car. Using this, the discharge capabilities of the accumulator could have been accurately specified, such that the car would not be power supply limited. This was not possible. As an alternative, the continuous output power of the accumulator was specified to be at least 54 kW, which is the maximum continuous power rating of the four AMK motors.

4.1.2. DESIGN CONSTRAINTS

The following list is a summary of the Formula SAE rules that directly impacted the initial concept design of the accumulator:

- The tractive voltage cannot exceed 600 Vdc (EV1.1.2).
- The accumulator must consist of separable modules with a maximum voltage less than 120 Vdc, and a maximum energy content no greater than 6 MJ (EV3.3.3).
- The mass of each module must not exceed 15 kg (EV3.4.6 clause e).

- Each pole of a module must be separable by maintenance plugs that are positive locking, and do not require the use of tools (EV3.3.3).
- Modules must be insulated from one another by a suitable electrical insulator (EV3.3.4).
- The temperature of at least 30% of the cells must be measured, if using a lithium based chemistry (EV3.6.6).
- The cell temperature must be measured at the negative terminal of the cell. The sensor must be either in direct contact with the terminal, or within 10 mm on the busbar (EV3.6.3).

Following the success of UCM15 in the skid-pad event at the 2015 FSAE-A competition, the preference of the team was to maintain as much of the suspension layout as possible on UCM16. As such, the rear dimensions of the chassis were fixed, and the maximum dimensions allocated to the accumulator were 300 mm (width) x 700 mm (length) x 270 mm (height).

4.1.3. INITIAL BATTERY IDENTIFICATION

The research of other electric Formula SAE cars (Appendix A) indicated a common trend in the use of lithium-ion pouch cells. Lithium-ion chemistry is the obvious choice for a high-performance race car. The use of pouch cells, over cylindrical or prismatic enclosures, can be accredited to energy density and ease of installation. In the interest of preventing an unnecessary overcomplication of the team's first electric car, pouch cells were chosen as the preference for the accumulator.

Table 4.1 lists the lithium-ion pouch cell manufacturers that were contacted for product information and potential sponsorship. Of these manufacturers, only A123, Melasta and Xalt Energy responded. Xalt Energy, despite being the battery supplier for the FIA Formula E racing series, would not supply the team with cells as their commercial interests were with larger applications.

Table 4.1. Contacted lithium-ion pouch cell manufacturers

Manufacturer	Battery Chemistry
A123	LFP
EiG	Li ₄ Ti ₅ O ₁₂ (Lithium Titanate - LTO)
Kokam	NMC, NMC + LFP (hybrid)
Melasta	LCO
Powerstream ²²	LCO, LMO, LFP, NMC, NCA
Targray	LCO, LMO, LFP, NMC, NCA (made to order)
Valence	LiFeMgPO ₄ (LFP with magnesium active material)
Xalt Energy	NMC

²² Whilst not actually a battery manufacturer, Powerstream act as a supplier to numerous smaller manufacturers.

4.1.4. AMS SELECTION

The AMS was selected in the early stages of concept design, as it directly influences the physical layout of a battery module. Whilst there was the option to design a custom management system in-house, preference was made towards an off-the-shelf solution to reduce the overall design complexity. Based upon the recommendations of Formula SAE teams that have built their own systems, the design process averages a year and was therefore not a viable option for UCM16. Table 4.2 lists the commercial accumulator management systems that were considered.

In a similar case to the battery manufacturers, only half of the AMS manufacturers responded to a request for quotes and product information. This reduced the available products to that of Elithion, Orion and Tritium. One downside of fully centralised topologies is the need for a large heatsink to dissipate the heat generated during the cell balancing process. The physical dimensions of the Orion Extended BMS, which has the potential to balance all 180 cells simultaneously, made it impractical to house within the confines of the concept chassis model. Considering the Elithion and Tritium products have the same functionality in a considerably smaller package, the Extended BMS was excluded.

Ultimately, the Elithion Lithiumate was selected. Its distributed topology was favoured as individual cell boards are less restrictive than a single larger board. Another benefit was the inclusion of a temperature sensor on each board; which, in theory, would satisfy EV3.6.6 regarding cell temperature measurements. The Tritium and Orion Junior systems would require an additional temperature monitoring system, thus adding unwanted design time and complexity.

Table 4.2. Summary of considered Accumulator Management Systems

Manufacturer	Model	Topology	Measured Cells (per unit ²³⁾	Temperature Inputs (per unit ²³⁾	Max System Voltage (Vdc)	Comms Protocols
Elektromotus	Emus	Distributed	1	0	1000	CAN, Serial
Elithion	Lithiumate Pro	Distributed	1	1	1000	CAN, Serial
Lithium Balance	LiBAL s-BMS	Centralised-slave	8	2	1000	CAN
Manzanita Micro	MK3x8	Centralised-slave	8	1	1000	RegBus ²⁴
	MK3x12LD	Centralised-slave	12	6	1000	RegBus ²⁴
Orion	BMS (Extended)	Centralised	180	4	900	CAN
	BMS (Junior) ²⁵	Centralised	16	3	60	CAN
Tritium	IQ BMS	Centralised-slave	8	1	1000	CAN

²³ A *unit* is considered the entire system for a centralised topology, a node for a centralised-slave, and a cell board for a distributed topology.

²⁴ Proprietary communication protocol developed by Manzanita Micro.

²⁵ Researched with the intention of connecting multiple units to form a centralised-slave system.

4.1.5. CONCEPT 1: A123 POUCH CELLS

Batteries from A123 were considered for the first module concept as there was adequate information available at the time of design²⁶, including a detailed application report on designing battery packs. A123 manufacture two LFP pouch cells, the 14 Ah *AHP14M1Ultra-A*, and the 20 Ah *AMP20M1HD-A*. However, at the time of enquiry, only the AMP20M1HD-A cells were available through a supplier recommended by A123. Table 4.3 summarises the cell specifications.

Table 4.3. Specifications of A123 AMP20M1HD-A LFP cell [54]

Nominal Capacity	20 Ah
Minimum Capacity	19.5 Ah
Nominal Voltage	3.3 V
Voltage Range	2.0 – 3.6 V
Maximum Continuous Discharge Current	200 A
Pulse Discharge Current (10 s duration)	600 A
Operating Temperature Range	-30 °C – +60 °C
Dimensions (Thickness x Width x Height)	7.25 x 160 x 227 mm
Weight	495 g
Specific Power (nominal)	2400 W/kg
Specific Energy (nominal)	131 Wh/kg
Energy Density (nominal)	247 Wh/L

Initial calculations (Equations (4.1) and (4.2)) showed that 166 cells were required in series to maximise the accumulator voltage; however, this would result in a nominal capacity of 11 kWh, which far exceeded the specified design capacity. Considering such a pack would have a mass of 82 kg, the number of cells had to be reduced to achieve the desired capacity (8 – 8.5 kWh).

$$\text{No. Series Cells} = \frac{V_{\text{tractive,max}}}{V_{\text{cell,max}}} = \frac{600 \text{ V}}{3.6 \text{ V}} = 166.7 \text{ cells} \quad (4.1)$$

$$\text{Capacity}_{\text{nom}} = V_{\text{pack,nom}} \times C_{\text{nom}} = (3.3 \text{ V} \times 166)20 \text{ Ah} = 11.0 \text{ kWh} \quad (4.2)$$

An Excel tool (Tool 1 of Appendix G) was created to calculate the tractive voltage, capacity, mass and discharge capabilities for accumulators with a series cell configuration that ranged from 100 to 166 cells. From this, it was found that the minimum capacity of an accumulator with a cell range between 124 to 132 would achieve the stated design capacity. The continuous output power of a series string in this range is approximately 80 kW, therefore there was no need to add parallel cells.

²⁶ Initially, Melasta were not very cooperative in providing product information.

Having found the appropriate range, a second Excel tool (Tool 2 of Appendix G) was used to determine the appropriate module configurations. Each accumulator was further simulated by dividing the cells equally into modules, where the number of modules ranged from one to eight. The voltage and energy content of each module was then calculated. The criteria for a valid module was defined as an equal number of cells, a voltage less than 120 Vdc, and an energy content less than 6 MJ. Table 4.4 is a summary of the valid module configurations, whereby the 126 cell, six-module configuration was selected as it has the least number of cells and module requirements.

Table 4.4. Summary of valid A123 module configurations

Total Cells	Nominal Capacity (kWh)	Mass (kg)	No. of Modules	Max Voltage per Module (V)	Max Energy per Module (MJ)
126	8.32	62.37	6	75.6	5.44
			7	64.8	4.67
128	8.45	63.36	8	57.6	4.15
132	8.71	65.34	6	79.2	5.70

Concept design using the A123 cells was halted once it was discovered the cells could not be configured within the physical constraints put in place by the chassis and suspension design teams. AMP20M1HD-A cells have a vent at the top corner of the cell, in the event that the electrolyte decomposes and causes pressure to build within the cell [54]. As such, it is recommended that the cells are configured vertically in a battery pack. Due to width constraints (300 mm), two AMP20M1HD-A cells could not be placed next to each other (320 mm). Therefore, the cells would have had to be packaged face to face, as demonstrated by Figure 4.3. However, this would have resulted in a length of 913.5 mm. This length was purely attributed to the cells, and did not consider any tolerances or module separation. Allowing for adequate tolerance, the battery compartment of the accumulator would have been approximately 200 mm (width) x 950 mm (length) x 250 mm (height), and deemed too long by the chassis design team.

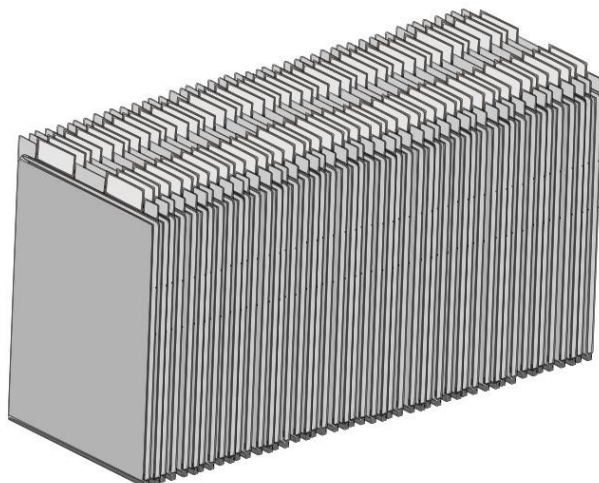


Figure 4.3. Diagram of A123 face-to-face alignment

4.1.6. CONCEPT 2: MELASTA POUCH CELLS

Having determined the A123 concept to be unsuitable, Melasta cells were next considered. Melasta cells have a lithium cobalt oxide (LCO) chemistry with a polymer electrolyte (LiPo), and have a maximum cell voltage of 4.2 V. To maximise the pack voltage to 596.4 Vdc, 142 cells were required in series. Melasta provided an Excel spreadsheet containing the basic product information for all 720 of their cell models. Despite there being several duplicates, where the only difference was cell tab length, an Excel macro was developed to process the list and pick the possible cell models and configurations.

Prior to implementing the macro, the nominal capacity of each cell in the list was calculated for an X p142s tractive pack, where X denotes the number of parallel strings between 1 and 10. This produced a matrix of all the accumulator capacities that could realistically be achieved using Melasta cells. The maximum number of parallel strings was limited to 10 to reduce the time taken to process the list, and as a consideration to system reliability. The more cells there are in a pack, the more cell-to-cell connections, and therefore the more points of failure.

The code for the macro is documented in Appendix H. It works by comparing each parallel configuration for each cell model against two criteria. Firstly, the total capacity must be within the range of 8 to 8.5 kWh. Secondly, the maximum continuous discharge power must be greater than 54 kW. If these criteria are met, the macro copies the cell data into a separate worksheet and calculates the mass and volume of the configuration. Running the macro on the 2015 list provided by Melasta successfully reduced the number of cell models to 130, which were then sorted by minimum capacity and total mass. An extract of the top 30 filtered cells is documented in Appendix H.

According to the filtered results, the lightest solution was a 43.45 kg pack consisting of 1278 1700 mAh SLPB6743060 cells in a 9p142s configuration. However, based upon the intention to reduce the number of cells in parallel, the final solution was chosen to be a 2p142s pack using either the SLPB7864155 or SLPB7664155 cell models (which are identical except for cell tab length). Table 4.5 shows the comparison of accumulators using the two Melasta cell models, as well as a comparison to the previous A123 accumulator concept. Whilst the SLPB6743060 cells give a greater specific energy, the remaining parameters are in favour of the SLPB7864155 cells.

Table 4.5. Comparison of accumulator parameters between Melasta and A123 cells

	Mass (kg)	Specific Energy (Wh/kg)	Specific Power (Cont.) (W/kg)	Energy Density (Wh/L)	Power Density (Cont.) (W/L)
SLPB6743060	43.45	185.0	1480.1	365.5	2923.2
SLPB7864155 / SLPB7664155	47.71	176.27	2643.1	400.5	6004.8
A123, 126s1p	62.37	133.3	1333.3	250.8	2506.5

Table 4.6 is a summary of the SLPB7864155 and SLPB7664155 cell specifications. For reasons explained later in this section, the SLPB7664155 cells were chosen as they have a tab length of 30 mm, compared to 10 mm.

Table 4.6. Specifications of SLPB7864155 / SLPB7664155 cells [55]

Nominal Capacity	8.0 Ah
Nominal Voltage	3.7 V
Voltage Range	3.0 – 4.2 V
Maximum Continuous Discharge Current	120 A
Pulse Discharge Current (2 s duration)	160 A
Internal Resistance	< 2.0 mΩ
Operating Temperature Range	-20 °C – +60 °C
Dimensions (Thickness x Width x Height)	7.5 x 63.5 x 155.5 mm
Weight	168 g
Specific Power	4000 W/kg
Specific Energy	200 Wh/kg

Numerous module configurations were considered, by blocking groups of cells in SolidWorks, to find the optimal layout within the dimensional restraints. It was found that the best method for packaging cell modules was to align the cells face-to-face, perpendicular to the longitudinal axis of the accumulator. Figure 4.4 demonstrates the two module layouts that resulted from this method, along with appropriate dimensions. The dimensions included an estimation of module wall thicknesses and spacing between each module. The overall height was estimated the same for both layouts (approximately 250 mm). The layouts were presented to the chassis design team and the 8-module design was selected.

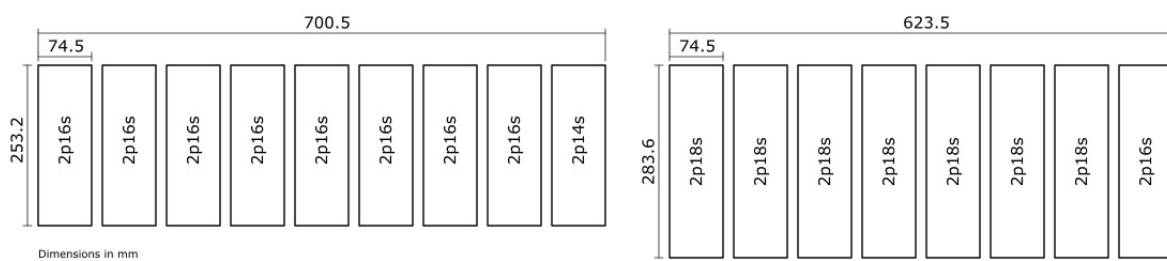


Figure 4.4. Diagram of Module Layouts Considered

In total, the module design was iterated seven times throughout the design process. In the aim of condensing this process, only the final iteration will be discussed in this thesis. Figure 4.5 is a screenshot of the final CAD module concept. At the request of the project supervisor, the 2p18s modules were halved to a 2p9s configuration, such that the maximum module voltage became 37.8 Vdc, with a maximum energy content of 2.2 MJ.

The module frame is made from laser-cut FR-4 glass-reinforced epoxy laminate sheets that slot together. FR-4 was selected as it is a UL94-V0 rated material, implying it will not burn for longer than 10 seconds if ignited [56]. FR-4 also provides the electrical insulator requirement of EV3.3.4. The ideology behind the frame construction was that the cells could be connected using an assembly rig prior to being enclosed by the FR-4 panels. In doing so, the personnel assembling a module are not restricted and have full access to the cells.

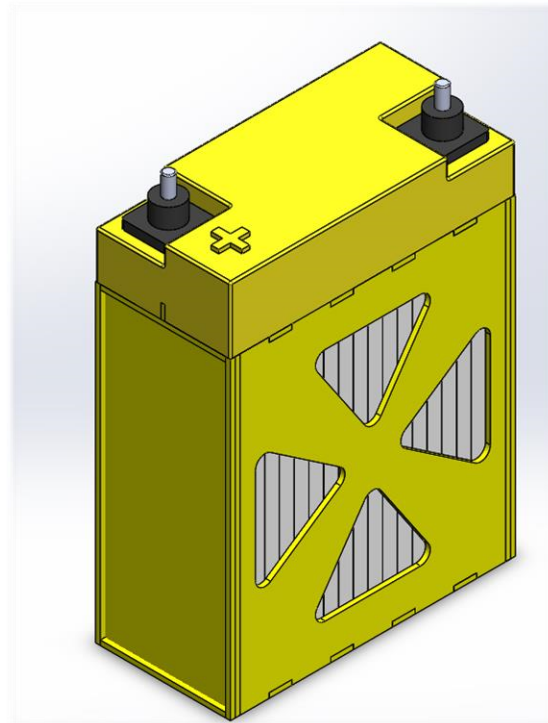


Figure 4.5. CAD model of 2p9s Melasta module concept

Figure 4.6 shows an exploded view of the CAD model, along with the internal components of the module. Research into Formula SAE battery packs indicated the two common methods for connecting pouch cells were laser welding or clamping. Laser welding is the industry standard for connecting pouch cells. However, this firstly requires the use of expensive welding equipment and, secondly, creates a permanent connection that cannot be undone if a cell needs to be replaced. Of the Formula SAE teams that laser weld their accumulators, the majority rely on external sponsors who have the correct equipment. Clamping, on the other hand, requires no specialist equipment and allows cells to be replaced easily in the case of cell failure.

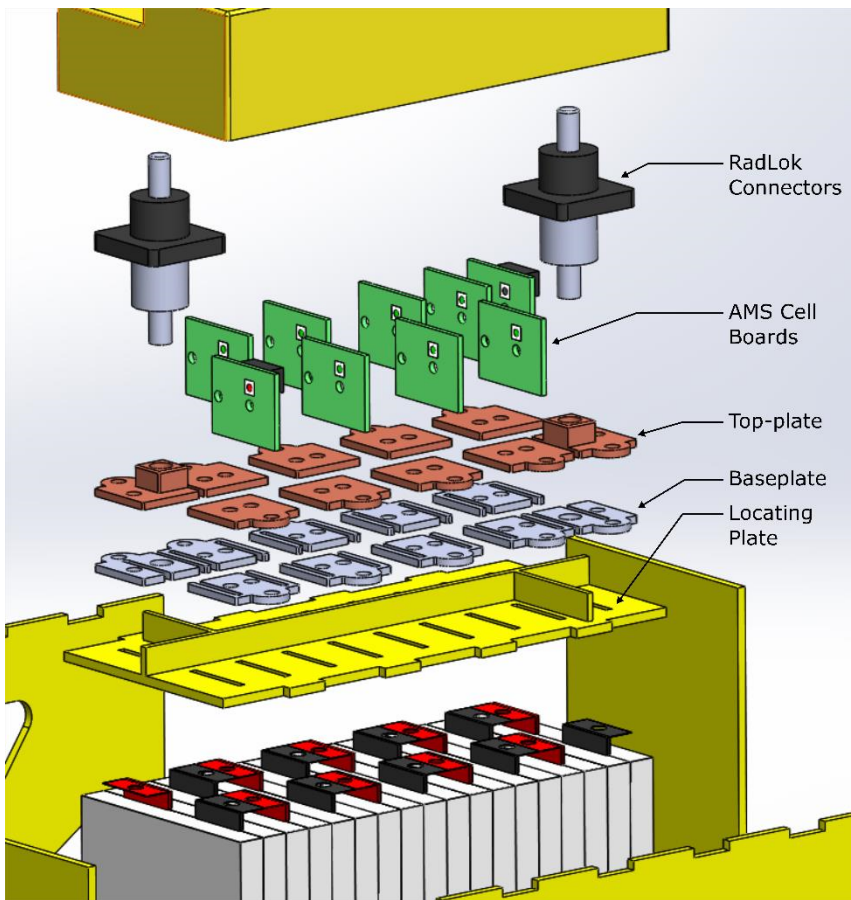


Figure 4.6. Exploded CAD model showing components of 2p9s module concept

The cells are clamped using a three-piece system. The tabs of each cell are slotted through an FR-4 locating plate that sits on top of the cell bodies. The tabs are then folded over a metallic baseplate, such that they overlap, and are then clamped by a top-plate. It was intended for the holes in the baseplate to be threaded such that the compression is maintained using screws (not modelled in the CAD diagrams). The baseplates were modelled as a U-shape to promote the correct folding of the cell tabs. Clamping the cells using this method was only possible with the longer tab length of the SLPB7664155 cell.

As shown by Figure 4.8, the AMS cell boards were to be located directly above the clamping plates. In doing so, each on-board temperature sensor was within 10mm of the negative terminal of a cell, and therefore compliant with EV3.6.3. An auxiliary connector, which was not modelled, would have been used to connect the cell board string to the AMS master controller, located at the front of the accumulator.

Figure 4.7 shows the final assembly of the battery compartment for the Melasta accumulator concept. Amphenol RadLok connectors were selected as the maintenance plugs for the modules, whereby jumper cables were to be used to connect the modules together. Whilst numerous teams design their own specific maintenance plugs, an off-the-shelf solution was favoured for its simplicity.

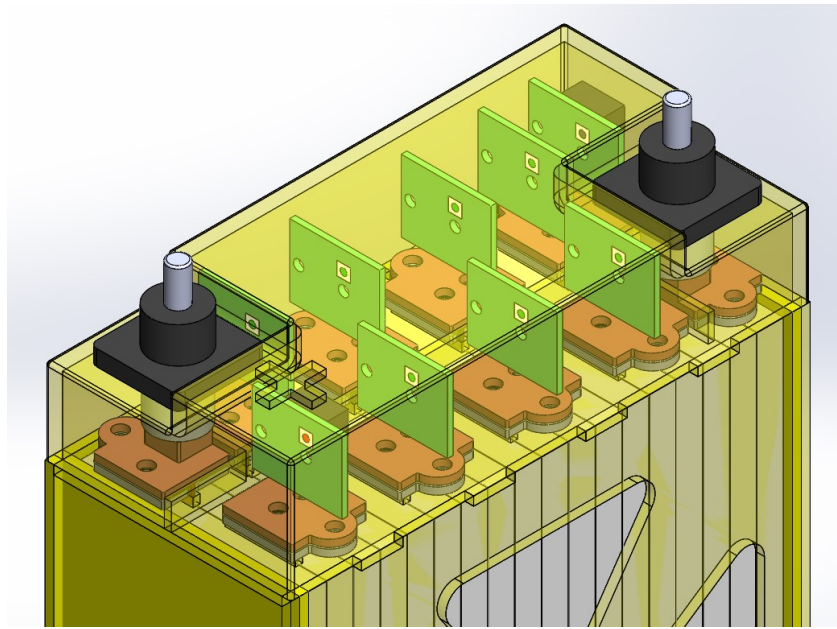


Figure 4.8. CAD model showing internal view of 2p9s module concept

A quote was provided by Melasta for 300 SPLB7664155 cells at a unit price of US\$38.72 each. With the inclusion of shipping and a 15% sponsorship discount, the total cost was US\$10,518. However, at somewhat the last minute, an executive decision was made by the team's faculty advisor that UCM16 should use 18650 cells. As such, the concept design for the Melasta cells, which took two months to complete, was disregarded; a testament to the idea that major decisions made later in a product's development are expensive. In the case of Formula SAE, time is the most valuable resource. As described in the following section, an accumulator consisting of 18650 cells is considerably cheaper; however, this decision created a knock-on effect that delayed the progress of the remaining vehicle design.

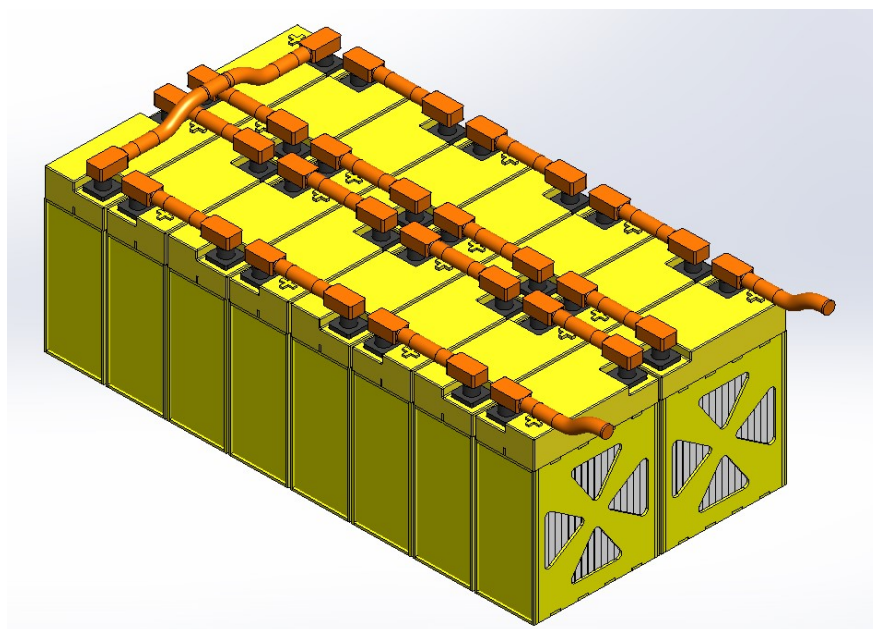


Figure 4.7. Final assembly of Melasta accumulator concept

4.1.7. CONCEPT 3: 18650 CELLS

18650 cells were not initially considered for UCM16's accumulator for two main reasons. Firstly, there were no documented cases of Formula SAE teams using 18650 cells for their electric race cars. In comparison, there were detailed reports of pouch cells (including Melasta) being used by the top-ranked electric teams. Secondly, the industry recommended method for connecting cylindrical cells is by welding; whether it be ultrasonic, laser or resistance welding [57]. Soldering cells is prohibited by the Formula SAE rules (EV3.3.7). As was the case for pouch cells, welding 18650 cells requires specialist battery welding equipment that costs upwards of NZ\$5,000²⁷.

Table 4.7 lists the 18650 cells that were investigated for use in UCM16. There is an inversely-proportional relationship between the nominal capacity and maximum continuous discharge capabilities of a cell; therefore, a two-stage selection process was used to find the best solution. All the cells have the same maximum operating voltage of $4.2\text{ V} \pm 0.05\text{ V}$. Assuming every cell is at its absolute maximum voltage (4.25 V), no more than 141 cells could be connected in series, giving a typical maximum pack voltage of 592.2 Vdc. Based upon this, the first selection stage was to calculate the number of parallel strings required to achieve the desired 8 – 8.5 kWh capacity at nominal pack voltage (507.6 Vdc). The second stage was to then determine if the pack configuration had the capability to continuously output the 54 kW requirement. The results of these calculations are documented in Table 4.8.

Table 4.7. Summary of 18650 cells considered

Manufacturer	Model	Chemistry	Nominal Capacity (mAh)	Max Cont. Discharge Current (A)	Mass (g)
A123	APR18650M1A	LFP	1100	30	39.0
LG	HB2	NMC	1500	30	42.9
	HD2	NMC	2000	25	44.8
Panasonic	NCR18650A	LCO	3100	6.2	44.7
	NCR18650B	LCO	3400	4.9	45.9
Samsung SDI	INR18650-15M	NCA	1500	23	41.9
	INR18650-20R	NCA	2000	22	42.5
	INR18650-25R5	NCA	2500	20	43.7
Sanyo	UR18650E	NMC	2100	10	44.6
	UR18650SAX	LCO	1350	25	43.9
Sony	VTC3	NCA	1600	30	44.7
	VTC4	NMC	2100	30	45.3
	VTC5	NMC	2600	20	44.1

²⁷ Realistically, for the number of cells that needed to be welded, a quality battery welder would cost in the region of NZ\$80,000.

Table 4.8. Results of two-stage selection process for 18650 cells

Cell Model	Number of Cells	Configuration	Total Capacity (kWh)	Continuous Discharge Power (kW)	Total Mass (kg)
APR18650M1A	2115	15p141s	8.38	228.4	90.7
HB2	1551	11p141s	8.37	167.5	66.5
HD2	1128	8p141s	8.12	101.5	50.5
NCR18650A	846	6p141s	9.44	18.9	37.8
NCR18650B	705	5p141s	8.63	12.4	32.4
INR18650-15M	1551	11p141s	8.38	128.4	65.0
INR18650-20R	1128	8p141s	8.12	89.3	47.9
INR18650-25R5	987	7p141s	8.88	71.1	43.1
UR18650E	1128	8p141s	8.53	40.6	50.3
UR18650SAX	1692	12p141s	8.22	152.3	74.3
VTC3	1410	10p141s	8.12	152.3	63.0
VTC4	1128	8p141s	8.53	121.8	51.1
VTC5	987	7p141s	9.24	71.1	43.5

The INR18650-25R5 pack was the lightest pack that met the two criteria. However, the VTC5 pack would have 12% more capacity for only a 1% increase in mass, therefore implying it to be the better solution. That being said, the Samsung cells were selected on the basis that it was almost impossible to source legitimate Sony VTC5 cells at the time, due to an influx of counterfeit cells on the market. Table 4.9 lists the specifications of the INR18650-25R5 cells.

Table 4.9. Specifications of Samsung INR18650-25R5 cells [58]

Nominal Capacity	2500 mAh
Nominal Voltage	3.6 V
Voltage Range	2.5 – 4.2 V
Maximum Continuous Discharge Current	20 A
Pulse Discharge Current (1 s duration)	100 A
Internal Resistance	$\leq 18.0 \text{ m}\Omega$
Operating Temperature Range	-20 °C – +75 °C
Dimensions (Height x Diameter)	64.85 x 18.33 mm

From Equations (4.3) and (4.4) the 7p141s accumulator must be divided into a minimum of seven modules to be rule compliant. This would therefore imply 20.14 cells per module; or, realistically, six 7p20s modules with a single 7p21s module. However, since the Elithion Lithiumate AMS has a maximum string length of 16 cell boards per bank, and a recommended string length of at least 8 cells per bank, the more appropriate module configuration was found to be seven 7p18s modules and a single 7p15s module, with two equal banks per module.

$$Modules_{min,voltage} = \frac{V_{max,7p141s}}{V_{max,module}} = \frac{592.2 \text{ V}}{120 \text{ V}} = 4.935 \quad (4.3)$$

$$Modules_{min,capacity} = \frac{C_{max,7p141s}}{C_{max,module}} = \frac{37.3 \text{ MJ}}{6 \text{ MJ}} = 6.22 \quad (4.4)$$

Figure 4.9 shows the final concept design for a 7p18s module using Samsung INR18650-25R5 cells. The cells are retained within the module using two laser-cut nylon sheets, which in-turn form the main structure of the module. The design aimed to incorporate the RadLok connectors into the overall profile of the module to create a more rectangular shape; hence the top two rows are off-centre to the rest of the module. It was intended for the entire module to be enclosed in ITW Formex, which is a scorable electrical insulator that meets the UL94-V0 flame retardant standard.

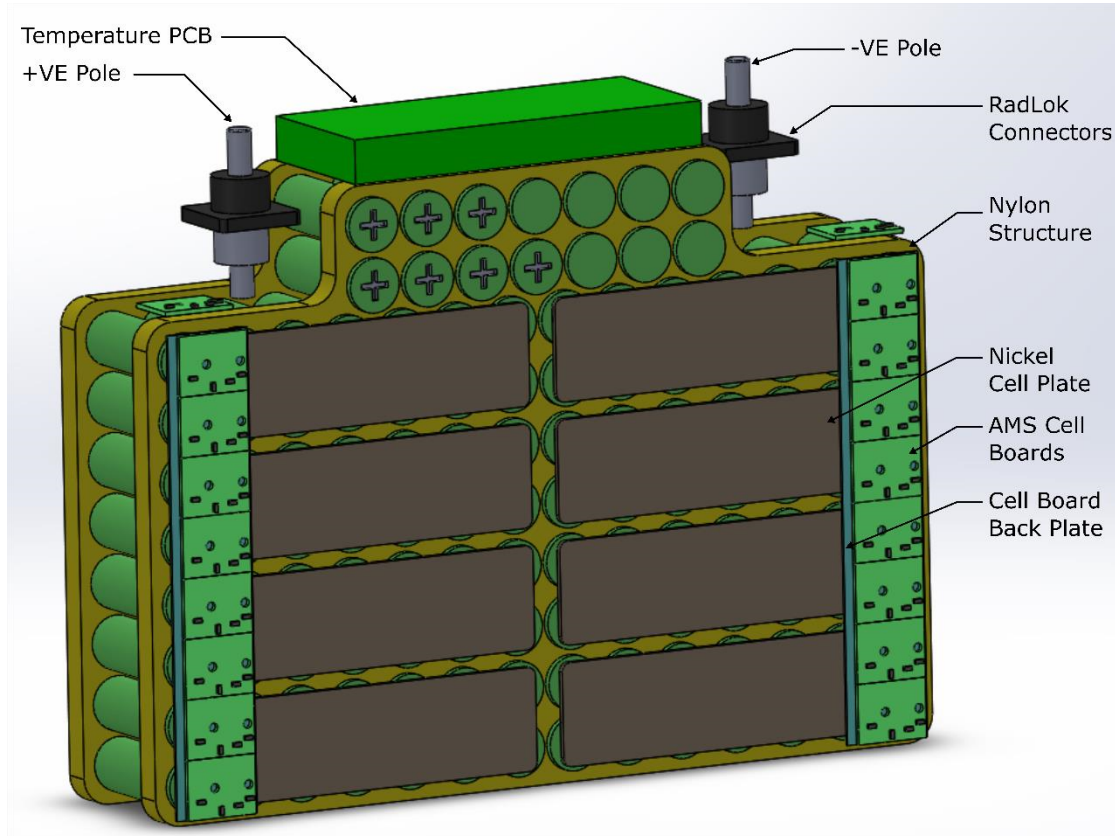


Figure 4.9. CAD model of 7p18s 18650 module concept

The cell polarities are alternated such that the tractive power path follows a U-shape through the module. Excluding the top two rows, each row half is one group of seven parallel cells. The nickel plates are then used to connect each parallel group to the adjacent group in the series string. As shown by Figure 4.10, the two halves of the module are connected by a nickel plate that spans the width of the module. The front face of the top two groups of cells form the positive and negative poles. In the case of the positive pole, the top-left group of cells (Figure 4.9), which have their positive terminal aligned with the front face of the module, are connected²⁸ to the left RadLok connector.

The ninth irregular module was reduced from a 7p15s configuration to a 7p14s configuration. In doing so, the module could use the same design format as the larger 7p18s module, whereby only two full rows of cells needed to be removed. This meant the only dimensional difference between the two module types was height. The effect of removing the 13th string was minimal with respect to the overall accumulator. The nominal capacity was reduced by 0.8%, and the peak tractive voltage was reduced by 4.2 V to 588 Vdc.

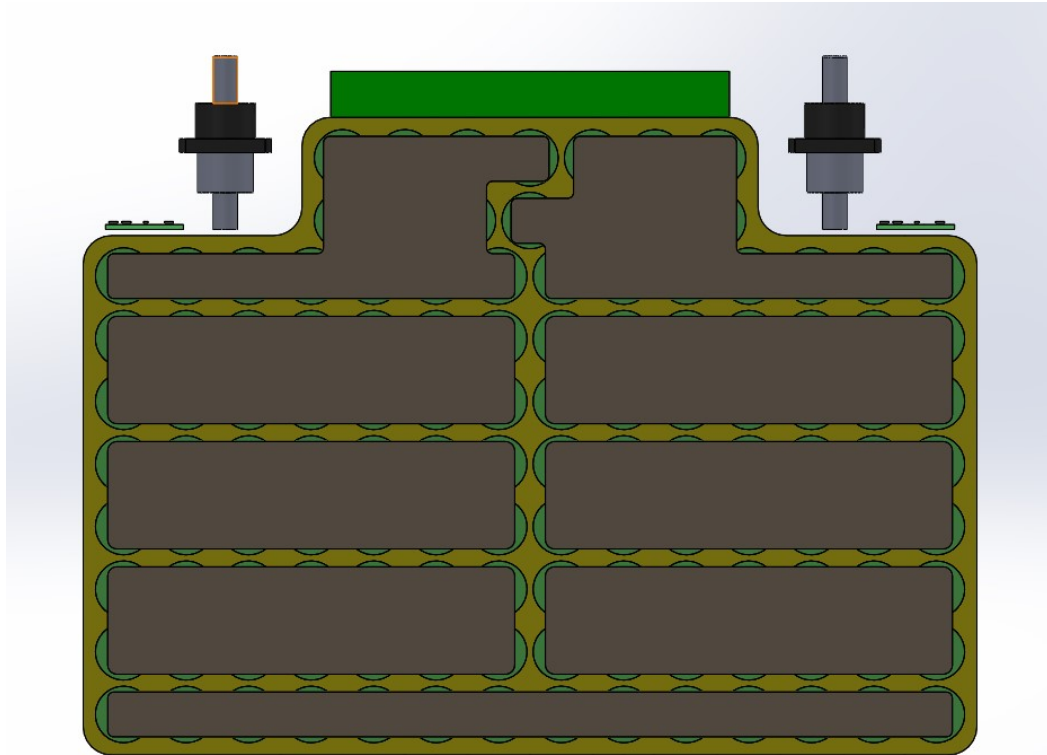


Figure 4.10. Rear-view of 7p18s 18650 module concept

The AMS cell boards were originally located on either end of the module, however this severely impeded the lateral air flow intended for cooling the modules. The solution was to place the boards on the front face and use longer wires to measure the cell voltages on the opposing face. For ease of

²⁸ Connection plate not shown in the CAD model.

application, the cell boards on each half of the module were separated into individual banks; resulting in all 16 banks of the Elithion Lithiumate being used.

The major disadvantage of changing from Melasta pouch cells to 18650 cells was that the temperature sensors on each cell board only measured 12.6% of the total cells; considerably less than the minimum 30% requirement. As such, a temperature monitoring system needed to be designed as an amendment to the Elithion AMS. This task was given to an electrical engineering undergraduate student, with the following specifications:

- The temperature monitoring system must not exceed the dimensions allocated on the top of each module (see Figure 4.9).
- The system must interface with the Accumulator Isolation PCB (see later section) via CAN and a dedicated fault hard-line.
- The system must identify individual cells (or small groups) with abnormal temperatures.

18650 cells have a considerably greater internal resistance than pouch cells, and therefore dissipate more heat when under load. Assuming the maximum stated internal resistance of 18 mΩ, each group of 7 parallel cells can be modelled as a single 2.57 mΩ resistance. Since the power results from the Optimum Lap simulation could not be trusted, a worst-case scenario was investigated, in which the accumulator is discharged continuously at 100 A (approximately 50 kW at nominal voltage). As shown by Equations (4.5) through (4.7), the total power dissipated as heat is 3.6 kW. When compared to the Melasta concept design (1.64 kW), this is an increase of 220%. Whilst it must be noted that UCM16 would not be operating at this power output continuously, the results show the relative difference between the two accumulator designs, and highlight the need for a substantially larger cooling system.

$$P_{7p18s \text{ module}} = i^2R = (100A)^2(18 \times 2.57 \text{ m}\Omega) = 462.6 \text{ W} \quad (4.5)$$

$$P_{7p14s \text{ module}} = i^2R = (100A)^2(14 \times 2.57 \text{ m}\Omega) = 359.8 \text{ W} \quad (4.6)$$

$$P_{7p140s \text{ accumulator}} = 7P_{7p18s} + P_{7p14s} = 3.60 \text{ kW} \quad (4.7)$$

At a per unit price of US\$3.39, the INR18650-25R5 accumulator had a total cell cost of US\$3,322; which was 60% cheaper than the proposed Melasta concept. However, finding a reliable supplier for the cells proved extremely difficult, and the associated lead times further delayed the development of the accumulator and race car. These issues will be addressed in later chapters of this thesis.

4.2. ACCUMULATOR ISOLATION RELAY SELECTION

Table 4.10 shows the contactors that were investigated for use in the accumulator. The LEV100 was selected as it was the smallest and lightest contactor considered that had the capability to open the poles of the accumulator under load. Assuming the worst-case scenario, the tractive current for a fully depleted accumulator (350 Vdc) being discharged at the full 80 kW power limit is 229 A. As this is considerably less than the interrupt rating of the LEV100, it can be confirmed that the accumulator will be safely disconnected from the car if the shutdown circuit is activated.

Table 4.10. Summary of considered Accumulator Isolation Relays

Manufacturer	Model	Max Voltage Rating (Vdc)	Continuous Current Rating (A)	Interrupt Rating (at 600 Vdc) (A)	Internal Coil Suppression
Gigavac	GX12	800	350	225	Yes
	GX14	800	400	350	Yes
	GX23	800	400	350	Yes
	GXSA15	800	400	350	Yes
	P105	1200	50	20	No
TE Connectivity	LEV100	900	100 ²⁹	500	No
	LEV200	900	500	1000	Yes

4.3. TRACTIVE FUSE SELECTION

The primary purpose of the tractive fuse is to protect the accumulator from a fault in the vehicle's tractive system. Below is a summary of the Formula SAE rules that apply to the fuse selection process:

- The continuous current rating of a fuse must not be greater than the continuous current rating of any electrical component it protects (EV6.1.1).
- A fuse must be rated for the highest voltage expected. DC rated fuses must be used to protect dc circuits (EV6.1.2).
- A fuse must have an interrupt rating greater than the theoretical short circuit current of the system it protects (EV6.1.3).

From the overview of the continuous current ratings of the main components in the tractive system (Table 4.11), the tractive fuse must have a current rating no greater than 100 A. As mentioned in the fusing theory section, it is common practice to re-rate a fuse based on temperature. In the expected ambient temperatures of Australia, the tractive fuse would be rated greater than 100 A. However, as

²⁹ 200 A for a 3-minute duration

there is no mention of temperature compensation in the Formula SAE rules, it was decided that the value stated on the fuse should be used over the operational temperature range.

Table 4.11. Overview of continuous current ratings in tractive system

Component	Max Continuous Current Rating (A)
Tractive Pack (7p140s)	140 A
LEV100 AIR	100 A
RadLok Module Connector (Size 5.7)	120 A
FSE Racing Kit (limited by 10 mm ² Radox HV cable)	150 A

The theoretical short circuit current was calculated based upon the internal resistance of the 18650 cells. As shown by Figure 4.11, the tractive system can be simplified to a resistor circuit when under fault conditions. The resistance of this circuit is a contribution of the internal resistance of the battery, and the resistance of the conductors. Assuming the resistance of the conductors is negligible, the minimum fault current at maximum tractive voltage was calculated to be 1.63 kA.

$$I_{Fault,min} = \frac{V_{max}}{R_{i,7p140s}} = \frac{588 V}{359.8 m\Omega} = 1.63 kA \quad (4.8)$$

Note that this is the minimum as it uses the maximum internal resistance stated in the INR18650-25R5 datasheet. Realistically, the fault current would be expected to be significantly greater; however, this cannot be confirmed without measuring the internal resistance of each cell in the accumulator, which is dynamic. For the sake of providing a list of quantifiable specifications, the required interrupt rating was set at 1.63 kA, with the presumption that a fuse with a substantially greater rating be selected.

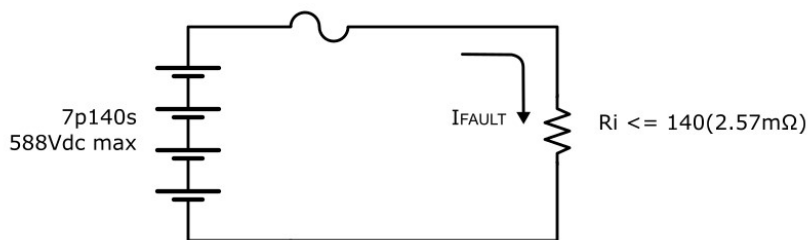


Figure 4.11. Simplified diagram of tractive system under short circuit conditions

The final consideration to be made prior to selecting the tractive fuse was the peak no-blow current. The no-blow current is an estimate as to whether the fuse will rupture under the peak expected load from the motors. Assuming the worst-case scenario, the fuse must handle a peak current of 230 A for a duration of two seconds. This equates to 80 kW at minimum tractive voltage for twice the pulse duration of the AMK motors. Whilst somewhat arbitrary, this specification attempted to define the fuse such that it would not hinder the performance of the race car.

Table 4.12. Summary of considered 100 A rated tractive fuses

Manufacturer	Series	Voltage Rating (Vdc)	DC Interrupt Rating (kA)	Melt Time at 230 A (s)	Dimensions (Length x Diamter) (mm)
Cooper-Bussmann	PVS-R	600	10	150	200.0 x 34.0
Littelfuse	L70S	650	20	70	111.1 x 31.0
	SPFJ	1000	20	200	146.1 x 28.3
Mersen	Protistor	660	50	100	60.3 x 27.0
	HP6J	600	10	100	117 x 27.0

Based on the summary of Table 4.12, the best option was the 66 Vdc Protistor fuse as it meets all of the defined requirements in the smallest form-factor. However, since Mersen never replied to numerous emails requesting for a quote, the Littelfuse L70S fuse was selected as the second-best option.

4.4. PRECHARGE PCB DESIGN

The Precharge PCB was designed to precharge the inverter's intermediate capacitor when the tractive system is activated. The FSAE rules list three rules which directly influence the design of the circuit. A summary of these rules is listed below:

1. The intermediate capacitor must be charged to within 90% of the accumulator voltage before the positive AIR is closed (EV4.11.1).
2. Any precharge circuitry must be supplied directly from the shutdown circuit (EV4.11.2).
3. The positive AIR can be closed after a conservatively calculated time. Feedback via measuring the intermediate capacitor voltage is not required (EV4.11.3).

The full schematics for the Precharge PCB are documented in Appendix I. The following sections discuss the individual design elements. To future proof the design, calculations assumed the tractive voltage to be 600 Vdc, which is the maximum voltage allowed in the FSAE competition.

4.4.1. PRECHARGE RESISTOR SELECTION

The pulse energy rating of a resistor indicates the maximum amount of energy that can be absorbed within a certain period. The pulse energy of the intermediate capacitor was calculated to be 54 J using (4.9).

$$E_{PULSE} = \frac{1}{2} CV^2 = \frac{1}{2} (300 \mu F)(600 V)^2 = 54 J \quad (4.9)$$

It was decided upfront that two smaller resistors in series allowed for more flexible packaging options than a single larger resistor, therefore requiring each resistor to have a pulse energy rating greater than

27 J. The pulse energy ratings of the TE Connectivity HS Series power resistors³⁰ restricted the use of any series lower than the HSC100 [59], which was selected as the smallest and lightest option.

To protect the design, a worst-case scenario of the precharge resistance becoming connected to the negative pole of the accumulator was considered. Based on this, the minimum resistance of each resistor (that would not exceed the power limit) was calculated to be 900 Ω, as shown by (4.10).

$$R_{MIN} \geq \frac{V^2}{P} = \frac{(600 V/2)^2}{100 W} = 900 \Omega \quad (4.10)$$

Product availability resulted in two 1 kΩ HSC100 resistors being selected. The pulse energy rating of a 1 kΩ HSC100 is 50 J, which exceeded the previously calculated requirement. The maximum working voltage (1.9 kV) was also suitable. Using Equation (2.17), the maximum precharge current was calculated to be 300 mA.

4.4.2. PRECHARGE RELAY SELECTION

The precharge relay was required to be normally open, rated for 600 Vdc and switch greater than 300 mA. Using these requirements, a Standex-Meder LI12-1A85 was selected. The LI12-1A85 has a voltage rating of 1000 Vdc and a maximum switching current of 1 A.

4.4.3. PRECHARGE FUSE SELECTION

When selecting the precharge fuse, EV6.1.1 became an issue for concern. It was not made clear, regardless of a rules clarification from the FSAE-A committee, how the constant current of a transient circuit could be determined. Using the worst-case scenario where the precharge circuit is connected indefinitely to the negative pole of the accumulator, the constant current rating of each precharge resistor was calculated to be 316 mA, as shown by (4.11).

$$i_{cont} = \sqrt{\frac{P_{rated}}{R}} = \sqrt{\frac{100 W}{1 k\Omega}} = 0.316 A \quad (4.11)$$

As with the tractive fuse selection, the precharge fuse required an interrupt rating greater than 1.63 kA and a voltage rating greater than 600 Vdc. These requirements reduced the applicable Littelfuse fuse range to one of two options, the 508 (316 mA) and KLKD (0.3 A) series. The KLKD series was selected because it is fast acting, and therefore has a greater chance of interrupting a fault before the main tractive fuse.

³⁰ Type HS Series was selected due to its product availability and datasheet completeness.

4.4.4. CONTROL SCHEME

Although not required by the FSAE rules, it was decided that voltage feedback should be included in the control scheme. Referring to Figure 2.17, if only a timer is used to control the precharge process, a fault could occur if the precharge fuse were to fail prematurely and the positive AIR closed onto a partially-charged intermediate capacitor. To prevent this, the control scheme was designed to have a timer and a differential voltage measurement that would ensure the intermediate capacitor is charged to 90% of the accumulator voltage.

Figure 4.12 is a logic diagram for the control scheme; in which V_{BAT} and V_{CAP} are the accumulator and capacitor voltage measurements respectively, and T is a timing circuit. Control output X denotes the driver signal for the precharge relay, whilst Y denotes the driver for the positive AIR. The first comparator is used to check that the voltage measured is above 300 Vdc, indicating the precharge fuse is still continuous. The second comparator determines if $V_{CAP} > 0.9V_{BAT}$.

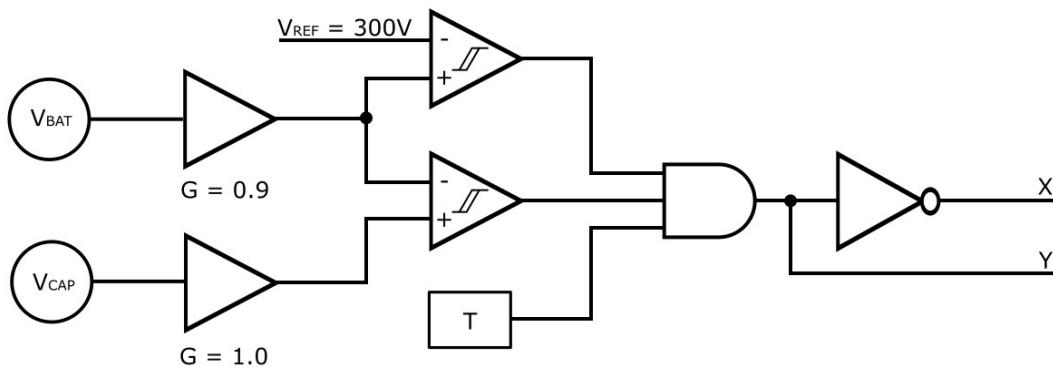


Figure 4.12. Logic diagram of precharge control scheme

Figure 4.13 is a schematic extract illustrating how the tractive voltage is measured. An ACPL-C870 optically isolated voltage sensor is used to measure the tractive voltage whilst maintaining the galvanic isolation between the tractive and low voltage systems. A resistive divider with a gain of 3.3×10^{-3} V/V is used to reduce the tractive voltage to less than 2 V at the input of the sensor. On the low voltage side of the circuit, the tractive voltage is determined by passing the differential output of the ACPL-C870 through a differential amplifier. In the case of the accumulator measurement, a gain of 0.9 V/V is applied in the differential amplifier stage. The tractive side of the ACPL-C870 is powered using a Murata NKE series isolated dc/dc converter.

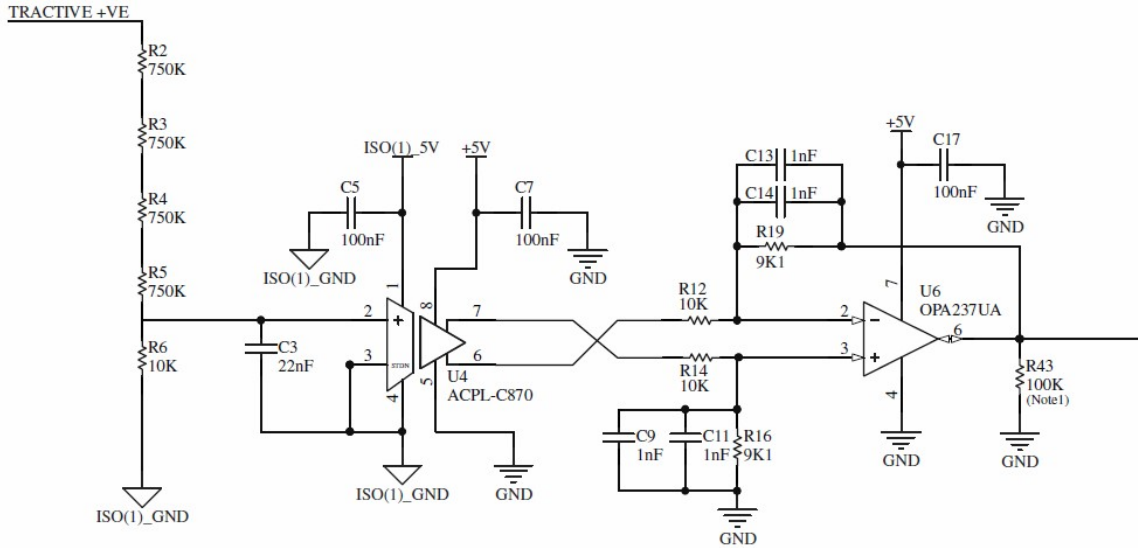


Figure 4.13. Tractive voltage measurement circuit

A capacitor in a RC circuit is considered fully charged after five time constants³¹. This meant the timer circuit required at least a 3 second time delay, which was provided by the circuit shown in Figure 4.14. The timer circuit uses a RC circuit in which the capacitor (C_{25}) voltage is compared against a fixed voltage reference. A normally-closed solid-state relay was included to discharge the timing capacitor rapidly through a resistance (R_{29}), thereby resetting the timer. This removed the case where power to the car is cycled before the timing capacitor has fully discharged, resulting in a shorter time delay. The blocking diode (D_7) ensures the capacitor does not self-power the discharge relay.

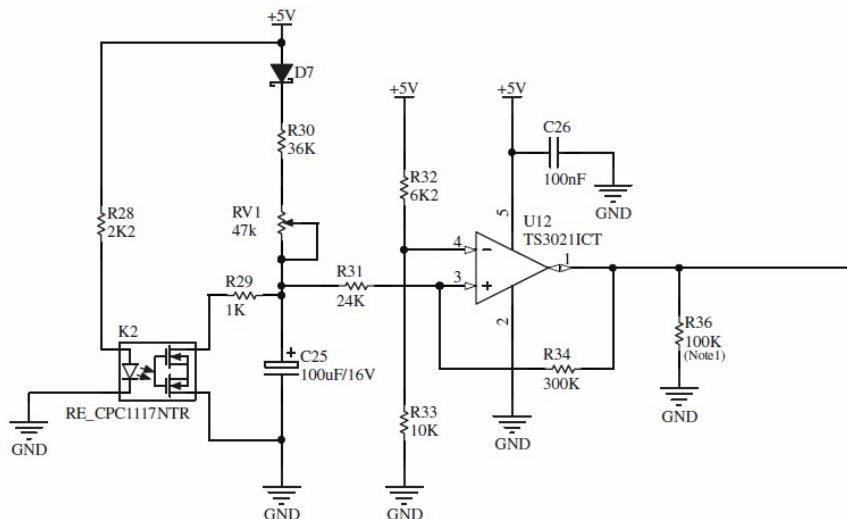


Figure 4.14. Precharge timer circuit

³¹ Time constant, $\tau = R \times C$

4.4.5. RELAY DRIVER & COIL SUPPRESSION

The LEV100 AIRs and precharge relay do not have built-in coil suppression. A relay coil can be loosely modelled as an inductor and an internal resistance. Equation (4.12) shows that when the current through an inductor is switched a voltage is generated that aims to oppose the change in current. In other words, when a relay coil is switched, the voltage will increase until either the energy is dissipated due to parasitic impedance or the switching component fails, causing the relay to remain actuated. This is not an option for the AIRs, which exist to disconnect the accumulator from the tractive system in the event of an emergency.

$$v_L = L \frac{di}{dt} \quad (4.12)$$

The coil suppression circuit was designed for the LEV100 relays and then copied for the precharge relay. Suppression techniques that use a single diode are not advised as they slow down the actuation time of the relay and can reduce the overall lifetime of the device [60]. A diode-Zener method was selected instead, with a Zener voltage equal to 24 Vdc (twice the supply voltage). Figure 4.15 shows the coil suppression circuit across the coil of an AIR. The minimum component ratings were calculated as follows:

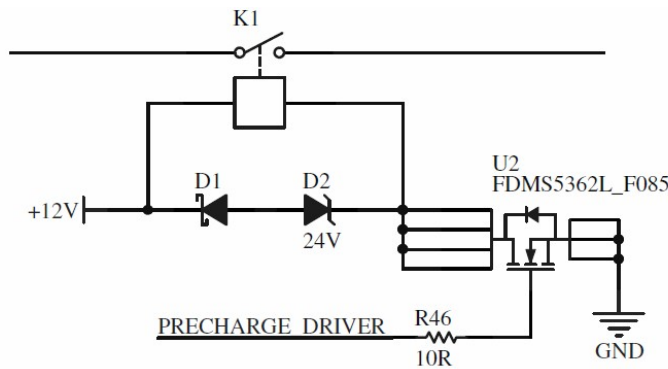


Figure 4.15. AIR coil driver and suppression Circuit

$$I_{COIL} = \frac{V_Z}{R_{COIL}} = \frac{24 V}{26 \Omega} = 0.92 A \quad (4.13)$$

$$P_{ZENER} = V_Z \times I_{COIL} = 22.08 W \quad (4.14)$$

where, I_{COIL} is the current through the relay coil, V_Z is the Zener voltage, R_{COIL} is the resistance of the relay coil, and P_{ZENER} is the power dissipated by the Zener diode.

4.4.6. VOLTAGE INDICATION CIRCUIT

EV3.3.9 requires the accumulator to have a prominent indicator whenever the voltage measured after the AIRs exceeds 60 Vdc. Furthermore, the indicator is required to work if the accumulator is removed from the vehicle (EV3.3.11). This prompted the design to use the tractive voltage as the sole power supply. The voltage indication circuit was included on the same PCB as the precharge circuit and an LED with a fibre-optic light pipe was selected as the indicator. For redundancy, two indicators were included.

Before explaining how the indicator was designed, the effect of the circuit on the greater tractive system must first be identified. Ohm's Law identifies that the voltage drop across a resistance is proportional to the current flow through it. Adding the voltage indication circuit to the tractive system increases the voltage drop across the precharge resistor, and conversely reduces the voltage across the intermediate capacitor³². Too much load will hence prevent the intermediate capacitor from reaching 90% of the accumulator voltage. The maximum allowable current draw at the minimum accumulator voltage was hence calculated to be 17.5 mA using (4.15).

$$I_{MAX} = \frac{0.1V_{MIN}}{R} = \frac{0.1 \times 350\text{ V}}{2\text{ k}\Omega} = 17.5\text{ mA} \quad (4.15)$$

The full 17.5 mA could not be allocated to the voltage indication circuit because the TSAL³³ detection circuit (discussed in Section 5.3) required approximately 5 mA. A limit of 10 mA was therefore allocated to the indication circuit, providing a small factor of safety. To ensure the brightness of the LED remained constant over the full voltage range of the accumulator, a constant current source using a depletion-mode MOSFET was designed (shown in Figure 4.16).

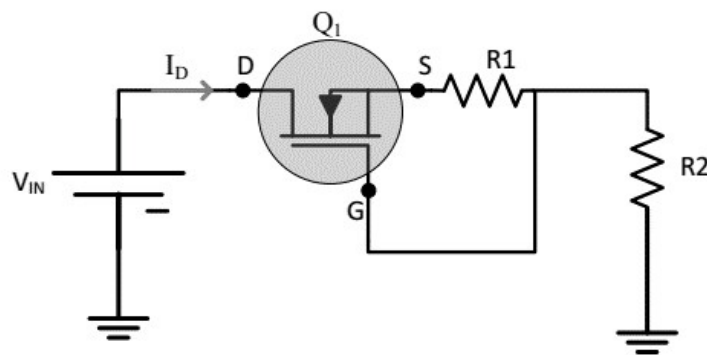


Figure 4.16. Depletion MOSFET constant current source [60]

Depletion MOSFETs are conducting when the gate-source voltage (V_{GS}) is greater than the negative gate-source threshold voltage ($V_{GS(TH)}$). By biasing a depletion MOSFET into its linear operating range

³² Kirchhoff's Voltage Law

³³ Tractive System Activation Light

using a negative feedback circuit, the current through the MOSFET can be controlled. The drain current through a depletion MOSFET is given by (4.16) [61]

$$I_D = I_{DSS} \left(1 - \frac{V_{GS}}{V_{GS(TH)}} \right)^2 \quad (4.16)$$

where, I_D is the drain current and I_{DSS} is the on-state drain current at $V_{GS} = 0$ V. In the constant current source of Figure 4.16 the gate-source voltage is equal to the voltage across R_1 . Equation (4.17) can be substituted into (4.16) and rearranged for (4.18), which calculates the resistance of R_1 for a desired current.

$$V_{GS} = -I_D R_1 \quad (4.17)$$

$$R_1 = \frac{V_{GS(TH)}}{I_D} \left(\sqrt{\frac{I_D}{I_{DSS}}} - 1 \right) \quad (4.18)$$

Super-bright orange LEDs manufactured by Kingbright with a Bivar SMFLP light pipe were selected. The Kingbright LEDs were found to have the greatest light intensity for an LED under 5 mA (525 mcd at $I_F = 4$ mA [63]) and allowed two indicators to operate within the 10 mA allowance. Figure 4.17 is the circuit for the voltage indicator. A 56 V Zener diode is used to switch the circuit when the tractive voltage exceeds 56 Vdc. The power dissipation of the depletion MOSFET was calculated to be 2.17 W, therefore a DN2470 N-Channel depletion MOSFET with an external heatsink was selected. The biasing resistance was calculated to be 440Ω using Equation (4.18). Two 220Ω RC1206 resistors were chosen to ensure the breakdown voltage of the components was not exceeded.

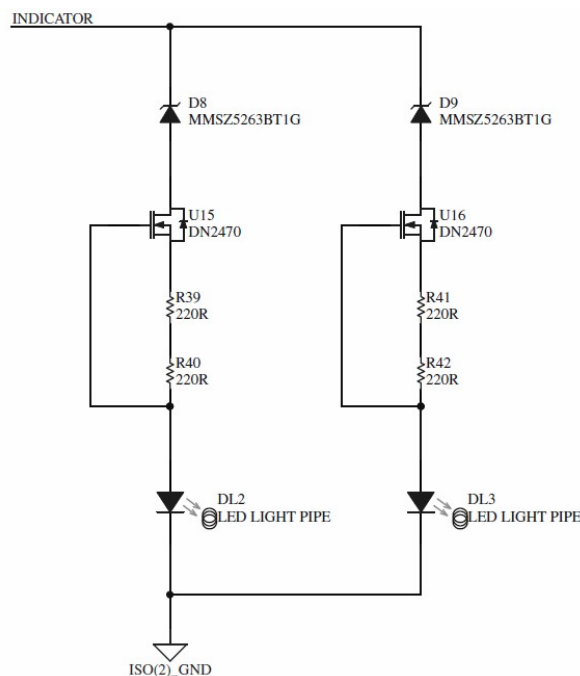
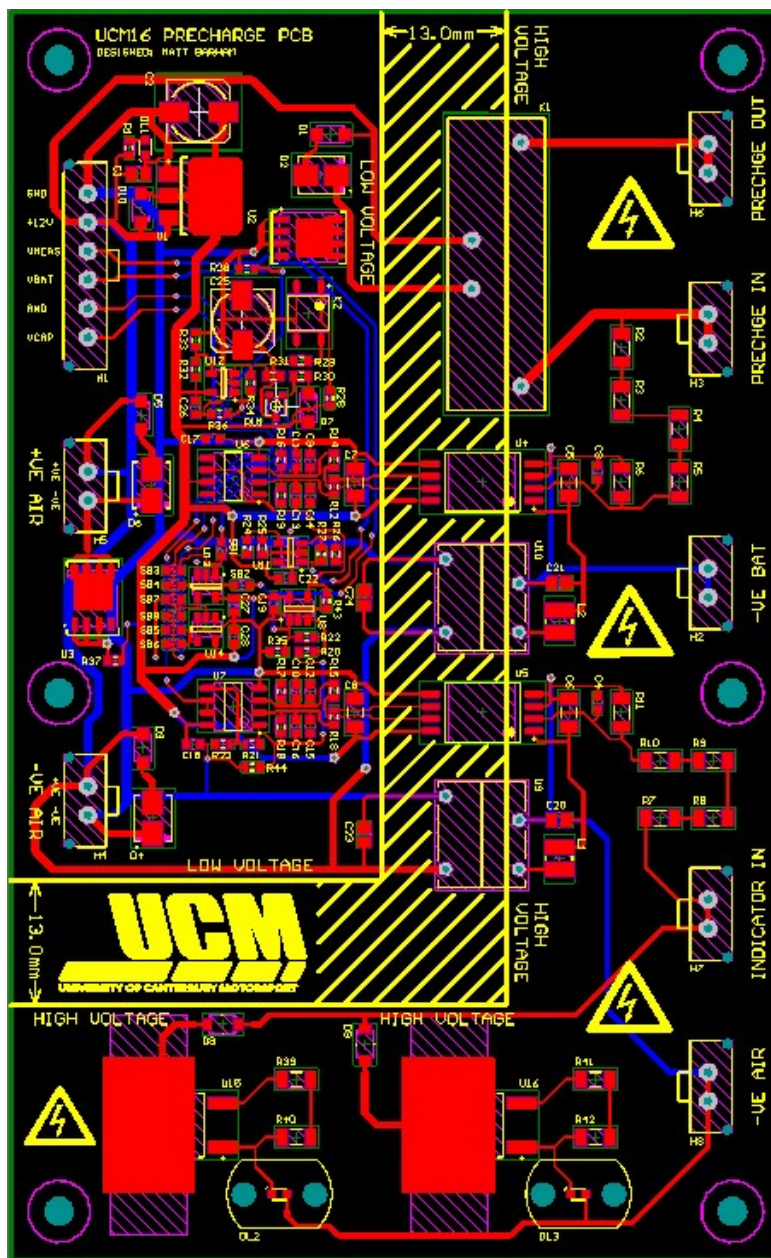


Figure 4.17. Voltage indication circuit schematic

4.4.7. PCB DESIGN

Figure 4.18 is a screenshot of the 130 x 80 mm, 2-layer precharge PCB. The board is separated into two sections, the low voltage control electronics and the high voltage power circuitry. The 13 mm silkscreen region defines the isolation barrier per the spacing requirements of EV4.1.7. It was not intended for the PCB to be conformally coated, which would have reduced the spacing requirement to 4 mm, as size was not considered a restriction during the PCB design. For precaution, high voltage traces with differing potentials were spaced at least 4 mm apart, in the event that the board needed to be coated at the competition. Molex Micro-Fit series connectors were used for all connections to the PCB. The Micro-Fit series has a voltage rating of 600 Vdc and is rated for 5 A per circuit [62].



4.5. DISCHARGE PCB DESIGN

The Discharge PCB was designed to discharge the intermediate capacitor when the shutdown circuit is opened. The full design schematics are documented in Appendix J, for which the notable sections are explained in more detail below. The following is a summary of the FSAE rules that affect the design of the discharge circuit:

1. The circuit must handle the maximum discharge current for at least 15 seconds (EV4.11.4).
2. The discharge circuit must always be active whenever the shutdown circuit is open (EV4.11.5).
3. The discharge circuit must reduce the intermediate capacitor voltage to less than 60 Vdc within 5 seconds (EV5.1.3).

The discharge PCB was designed to be located outside of the accumulator container, after the high voltage disconnect switch (discussed in Chapter 5). The justification for this was to ensure the discharge circuit would always be connected to the intermediate capacitor, regardless of whether the accumulator was connected or not.

4.5.1. HIGH VOLTAGE COMPONENT SELECTION

The design is split into two sections, the high voltage and control circuits. The high voltage element includes the discharge resistors, fuse and switching device. The maximum allowable discharge resistance of 7.2 kΩ was calculated by substituting the formula for capacitor discharge current (Equation (2.18)) into Ohm's Law and rearranging for resistance.

$$R = \frac{-t}{C \ln\left(\frac{V_C}{V_S}\right)} = \frac{-5 \text{ s}}{300 \mu\text{F} \times \ln\left(\frac{60 \text{ V}}{600 \text{ V}}\right)} = 7238 \Omega \quad (4.19)$$

A mirror of the resistor-fuse combination of the precharge circuit was considered to reduce design time. The maximum discharge current was calculated to be 300 mA, using Equation (2.18). The indefinite power dissipation of a single resistor was calculated to be 90 W, which is less than the 100 W rating of an HSC100 resistor. This confirmed the circuit would be rated to handle the maximum discharge current for greater than 15 seconds. Furthermore, the same rated KLKD fuse could be used to protect the discharge circuit, as the continuous current rating remained at 316 mA (as calculated in Section 4.4.3).

$$i_{MAX} = \frac{V_S \left(e^{\frac{-t}{RC}} \right)}{R} = \frac{600 \text{ V} \left(e^{\frac{0 \text{ s}}{(2 \text{ k}\Omega)(300 \mu\text{F})}} \right)}{2 \text{ k}\Omega} = 0.3 \text{ A} \quad (4.20)$$

$$P_{MAX} = i^2 R = (0.3 \text{ A})^2 (2 \text{ k}\Omega) = 90 \text{ W} \quad (4.21)$$

Assuming the switching time of the discharge circuit is negligible, the time taken to fully discharge the intermediate capacitor was calculated to be 3 seconds. By rearranging (4.19), the time taken to discharge to less than 60 Vdc was calculated to be 1.38 seconds.

$$t = -RC \ln\left(\frac{V_c}{V_s}\right) = -(2 \text{ k}\Omega)(300 \mu\text{F}) \ln\left(\frac{60 \text{ V}}{600 \text{ V}}\right) = 1.38 \text{ s} \quad (4.22)$$

EV4.11.5 restricts the switching component of the circuit to be a normally-closed configuration. Two options were considered, a normally-closed relay or a depletion MOSFET. Research concluded that there were very few normally-closed relays with the required switching capability. Relays have a rated switching voltage and current; however, the rated power is not the product of both values, rather a maximum limit of the product. To switch the discharge circuit, a relay would need a rated voltage greater than 600 Vdc, a switching current greater than 0.3 A, and a power rating greater than 180 W. Two products were identified that met this requirement; a Coto 5504-12-1 [63] and a Gigavac G81B [64].

Although these relays were suitable for use in the discharge circuit, each product had its shortcomings. At the time of design³⁴, there were only 21 Coto units worldwide with an eight-week lead-time. Including shipping, the total unit cost was in the range of NZ\$220. Gigavac relays are manufactured to order and had a total cost of NZ\$180. In comparison, the cost of a depletion MOSFET was approximately NZ\$4. Hence, the decision was made to use a MOSFET.

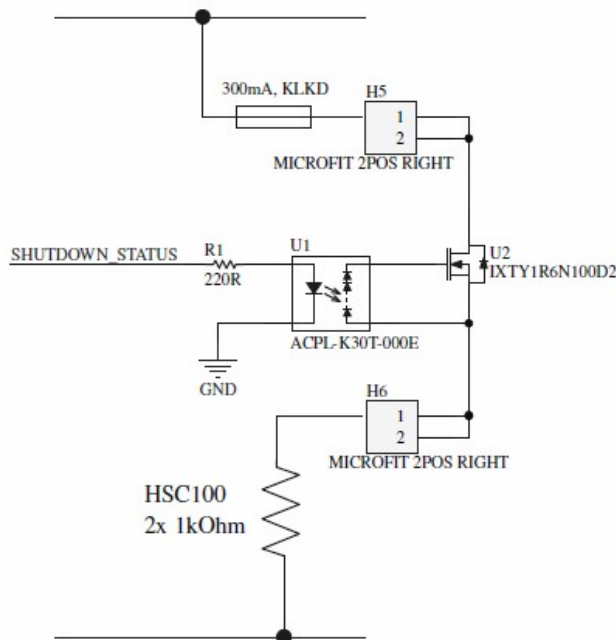


Figure 4.19. High voltage section of discharge circuit

³⁴ April, 2016

Figure 4.19 is a schematic extract of the discharge circuit showing a depletion MOSFET being used as the normally-closed switch. An IXTY1R6N100D2 N-Channel depletion MOSFET was selected because its ratings far exceeded what was required, therefore increasing reliability. The power dissipation of the MOSFET was calculated to be 0.9 W (Equation (4.23)), which is 0.9% of the total package rating. It also confirms that the MOSFET will not affect the circuit's ability to discharge the capacitance indefinitely.

$$P_{U2,MAX} = I_{D,MAX}^2 \times R_{DS(ON),MAX} = (0.3\text{ A})^2 \times 10\Omega = 0.9\text{ W} \quad (4.23)$$

The circuit uses an ACPL-K30T photovoltaic driver to control state of the depletion MOSFET. The ACPL-K30T utilises an LED with a photovoltaic diode array to provide a 7 V open-circuit voltage at the isolated output. The maximum off-voltage³⁵ of the IXTY1R6N100D2 is -4.5 V [65]; therefore, connecting the output as the gate-source voltage allows the discharge current path to be switched dependent on the state of the LED.

4.5.2. CONTROL CIRCUIT DESIGN

It was initially planned for the LED of the MOSFET driver to be controlled directly by the shutdown circuit. However, the final element of the shutdown circuit is the interlock of the HV accumulator connector. To detect if the interlock is open, the LED would need to be controlled by a connection to the shutdown circuit after the interlock. Splitting the shutdown circuit into multiple paths increases the chance that the circuit may become powered unintentionally. Instead, the current flow through the shutdown circuit was used as the control actuator.

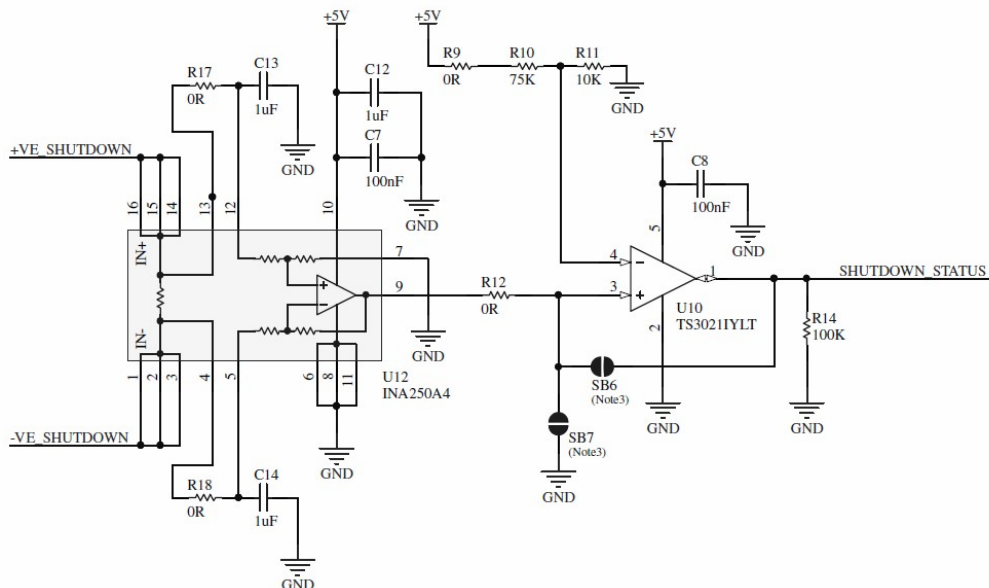


Figure 4.20. Control section of discharge circuit

³⁵ In theory, it is the minimum since the off-voltage is negative, however referring to the maximum is more intuitive.

The circuit shown in Figure 4.20, uses an INA250 current-shunt monitor, connected in series with the shutdown circuit, to measure the current flow. A comparator is connected to the output to convert the analog measurement into a binary output that equates to the status of the shutdown circuit, and is used to drive the ACPL-K30T LED. The coil current of each AIR is 461 mA at 12 Vdc [66] so the comparator threshold was set to 0.6 V, equating to 300 mA for the A4 variant of the INA250.

4.5.3. PCB DESIGN

The discharge PCB was designed in conjunction with the TSAL circuit (Chapter 5). Both circuits were included on the same board to reduce the number of connections required to the tractive circuit. Not only did this reduce the number of failure points, but also constrained the high voltage wiring throughout the vehicle. Figure 4.21 is a screenshot of the final design, and Figure 4.22 an image of the assembled PCB.

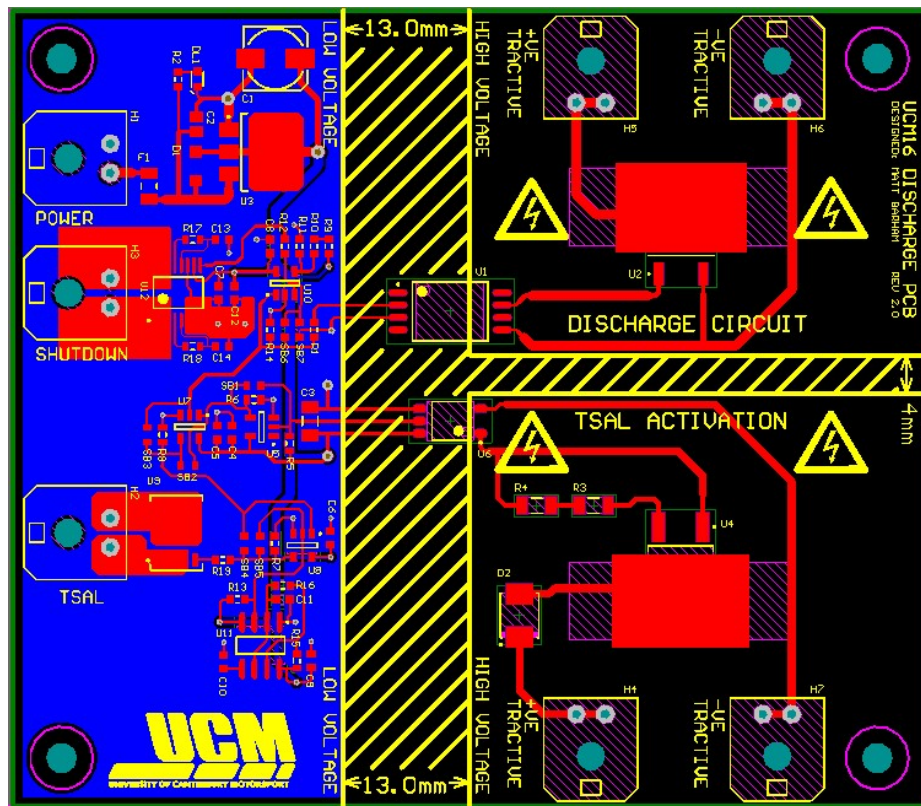


Figure 4.21. Screenshot of Discharge PCB design

The 2-layer PCB is separated into quadrants dependent on whether it is related to the discharge circuit or TSAL. The 13 mm silkscreen barrier defines the on-board galvanic isolation between the low voltage (left) and high voltage (right) areas of the board. The discharge and TSAL related components are then split top to bottom. Only the high voltage quadrants show this separation as a 4 mm silkscreen region, but the barrier can be continued across into the low voltage area of the board. As with the precharge PCB, all high voltage traces of differing potentials are separated from one another by at least 4 mm.

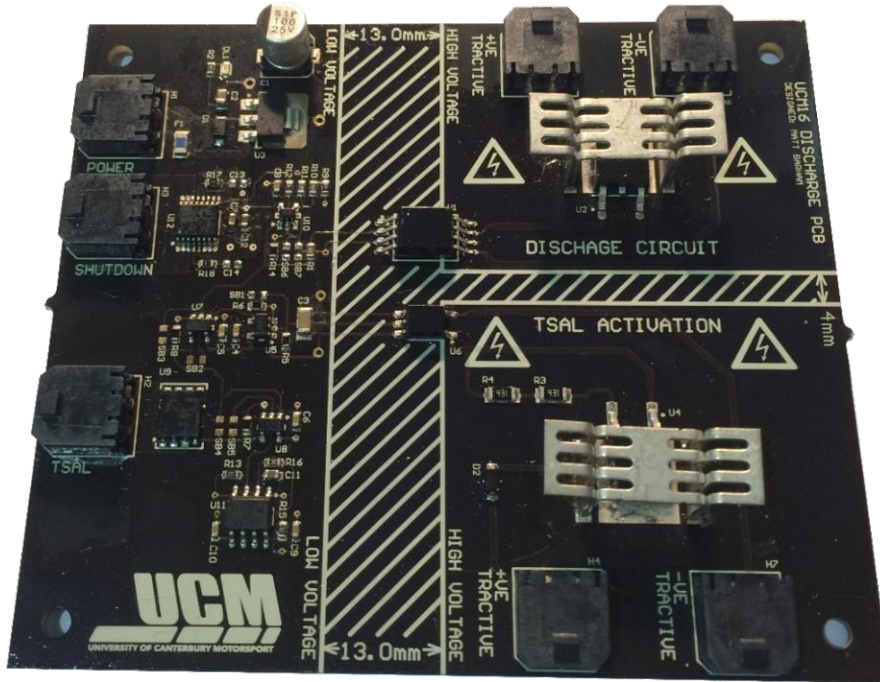


Figure 4.22. Image of assembled Discharge PCB

4.6. PRECHARGE & DISCHARGE BENCH TESTING

Before being connected to the accumulator, the precharge and discharge circuits were bench tested. The Chroma dc power supply was used to simulate the accumulator, whilst the $300 \mu\text{F}$ capacitance of the inverter was replicated using a 2p3s bank of $750 \mu\text{F}$ electrolytic capacitors. The shutdown circuit was powered by a low voltage power supply. A test board was created, to which the precharge and discharge components were attached. Figure 4.23 shows the setup of the bench test and the testing board layout.

The oscilloscope plots shown in Figure 4.24 (Agilent Technologies model DSO-X 3012A) show the results of the bench testing, where Channel 1 (yellow trace) is the tractive voltage (600 Vdc) and Channel 2 (green trace) is the voltage of the intermediate capacitor. Figure 4.24(a) shows a precharge test, in which the capacitor voltage increased to 560 V before the positive AIR was actuated. This equates to 94% of the tractive voltage, hence proving rule compliance. The discontinuity of the tractive voltage at the start of precharge can be accounted by the feedback control of the Chroma power supply.

From the discharge tests (Figure 4.24(b)), it was confirmed that the circuit reduces the capacitor voltage to less than 60 Vdc within the 5 second restriction. Figure 4.24(c) is the result of the shutdown circuit being cycled before the capacitor fully discharged. After each cycle, the positive AIR did not actuate until the timer circuit had elapsed (set to 7 seconds at the time of testing). This proved the timing capacitor reset circuit (explained in Section 4.4.4) was working as expected.

The voltage indication circuits on the Precharge PCB were also tested. Whilst the LEDs illuminated when the tractive voltage exceeded 60 Vdc, they were not considered bright enough (through the light pipe) to act as a sufficient warning indicator. The circuits were therefore updated in the second revision of the Precharge PCB (discussed in Section 6.3.8).

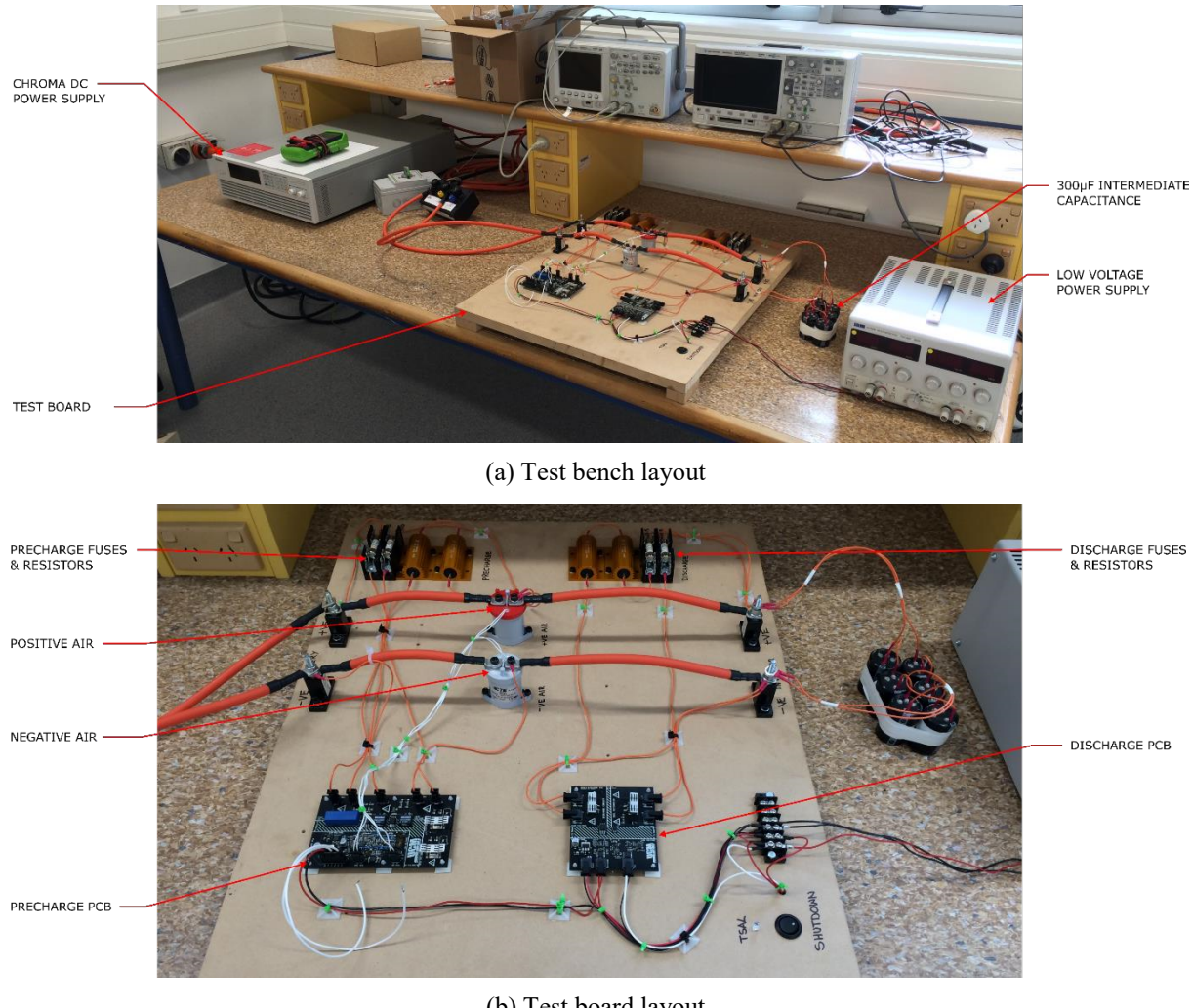
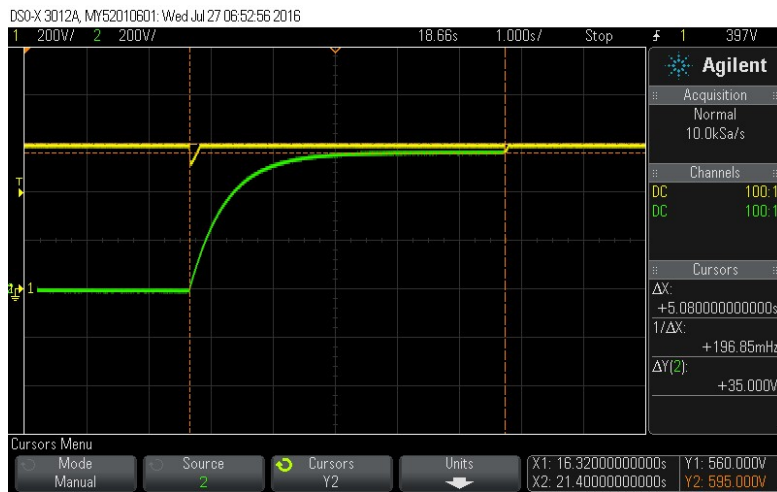
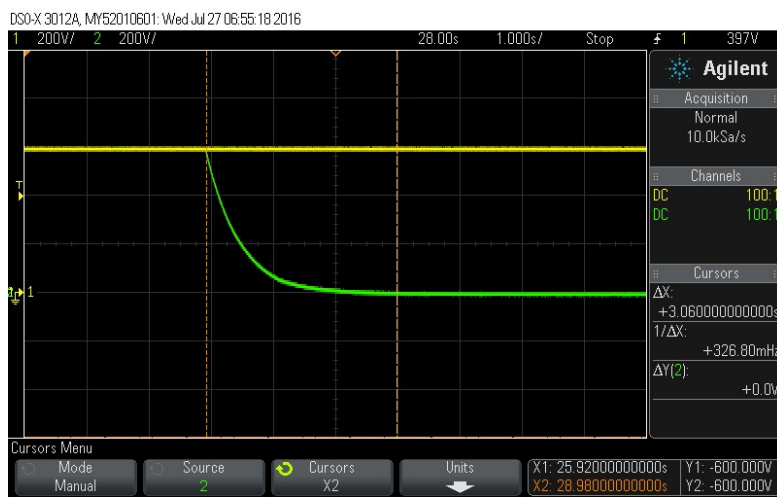


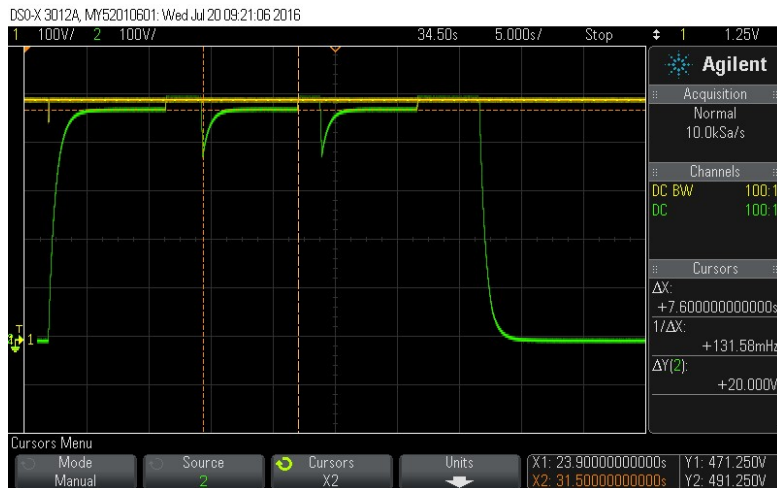
Figure 4.23. Images of precharge and discharge bench testing



(a) Precharge test. Cursors show the duration of precharge to be 5 seconds.



(b) Discharge test. Cursors show the duration of discharge to be 3 seconds.



(c) Precharge cycling test. Cursors show the duration of a precharge (started as an interruption of a discharge) is independent of intermediate capacitor voltage.

Figure 4.24. Oscilloscope plots of precharge and discharge bench tests. Channel 1 shows tractive voltage (V) and Channel 2 shows intermediate capacitor voltage (V).

4.7. ACCUMULATOR ISOLATION PCB

The Accumulator Isolation PCB was initially designed to address EV4.1.4, which states the low voltage systems within the accumulator (i.e. the AMS) must have galvanic isolation for all connections to the outside of the accumulator container. However, the need for a custom temperature monitoring system meant the accumulator isolation PCB was redesigned to be the overall AMS master that incorporated the temperature monitoring system with the Elithion Lithiumate. Figure 4.25 is a simplified diagram of the accumulator isolation PCB acting as the AMS master. The complete schematics are documented in Appendix K.

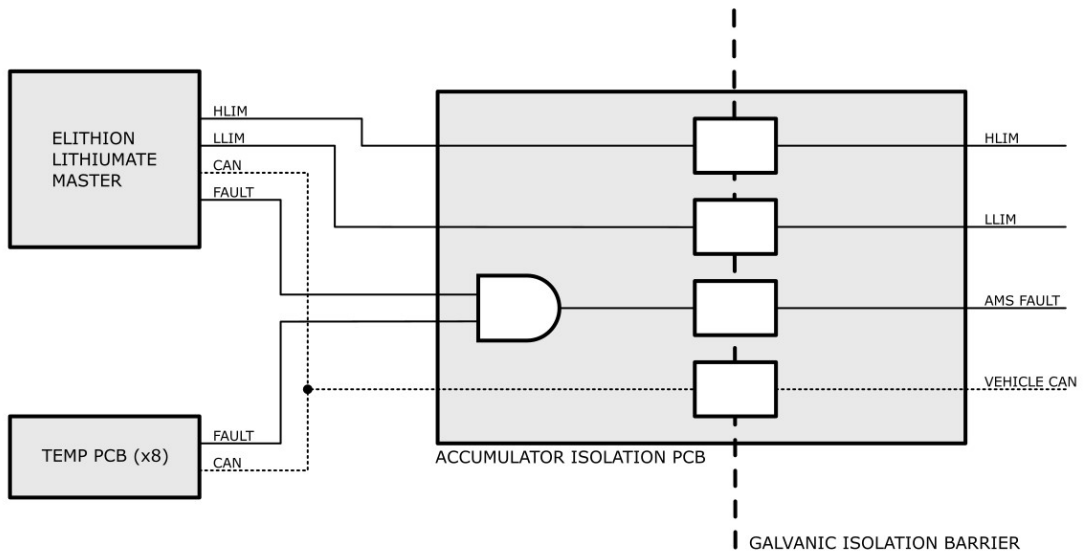


Figure 4.25. Simplified diagram of Accumulator Isolation PCB as AMS master

4.7.1. ISOLATED POWER SUPPLY

An S24SE12002PDFA isolated (1600 V) dc/dc converter was chosen to power the low voltage systems within the accumulator. It was estimated that the total power draw of the low voltage circuits would be a maximum of 1 A; equating to 70% of the converter's output capability. With an input voltage range of 9 – 36 Vdc, the converter is able to maintain a constant 12 V supply to the accumulator over the expected low voltage battery range (10 – 13.5 V).

The Elithion AMS master controller has two power inputs (source and load) which it uses to decipher whether the battery is connected to a charger or not. To prevent the need for two dc/dc converters, the circuit shown in Figure 4.26 was included to switch the isolated supply voltage between the two inputs. The circuit defaults to supply the *Load* input, meaning the accumulator is not charging. Applying 12 V to the *Charger Select* input (a physical pin on the accumulator's low voltage connector) transitions the relay to supply the *Source* input. Galvanic isolation is maintained using a 5000 V_{rms} rated ACPL-K49T optoisolator.

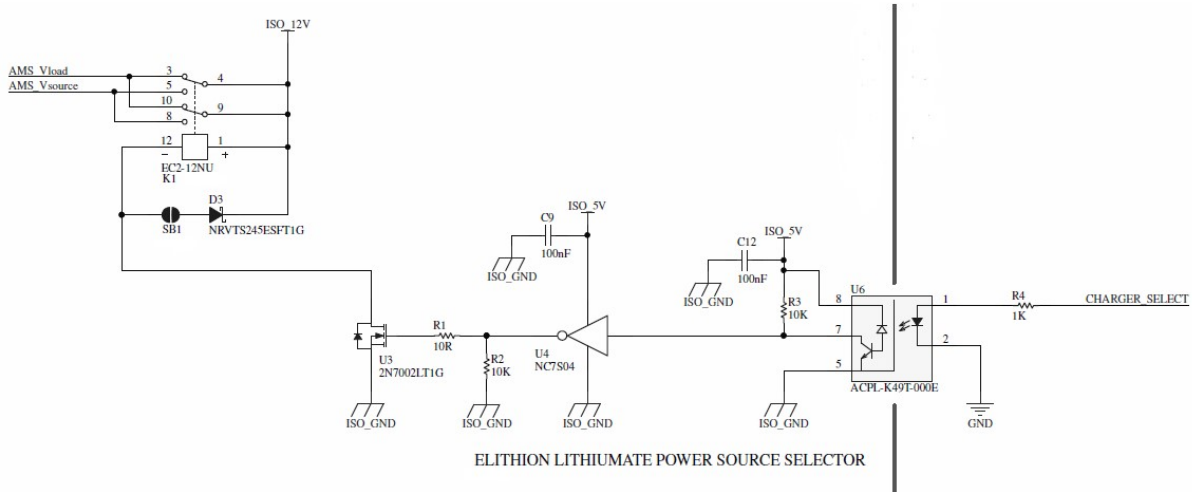


Figure 4.26. Schematic extract of Elithion power source selector circuit

4.7.2. TEMPERATURE MONITORING SYSTEM INTERFACE

Since the accumulator isolation PCB is a crucial part of the vehicle's safety system, the probable failure modes of the components were considered when designing the fault processing circuits. The temperature monitoring PCBs communicate their fault status via CAN and a dedicated hard-line for redundancy; in which logic-high represents a fault³⁶. Figure 4.27 shows the interface circuit for detecting a fault from one of the temperature monitoring PCBs.

A LM2903 dual-package comparator is used to remove any noise from the fault-line by comparing the 12 V input to a fixed 5 V reference voltage. R₈ is a pull-up resistor to ensure the fault-line will become logic-high if the connection is broken. Logic-high was chosen to indicate a fault to counter the effect of the LM2903's open-drain output. It was assumed that the component would fail in the open-circuit configuration, based upon previous experience, which would result in the pull-up resistor (R₂₀) setting the output signal logic-high. All circuits must therefore drive the signal logic-low to indicate no fault.

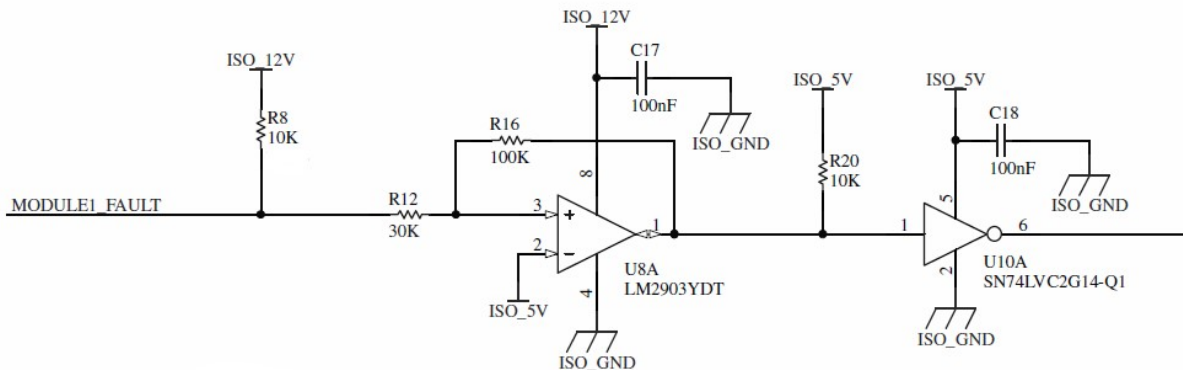


Figure 4.27. Schematic extract of Temperature Monitoring PCB interface circuit

³⁶ Note that a *fault* does not only include an over-temperature cell but also the failure of the PCB.

4.7.3. FAULT SIGNAL ISOLATION

Referring to schematic sheets 3 and 3A of Appendix K, the output signals of the eight temperature interface circuits are combined using quad-input AND gates. The outputs of the AND gates are then combined with the fault status of the Elithion master unit and on-board STM32F105 microcontroller to give the final fault status for the AMS conglomerate; the output stage of which is detailed in Figure 4.28.

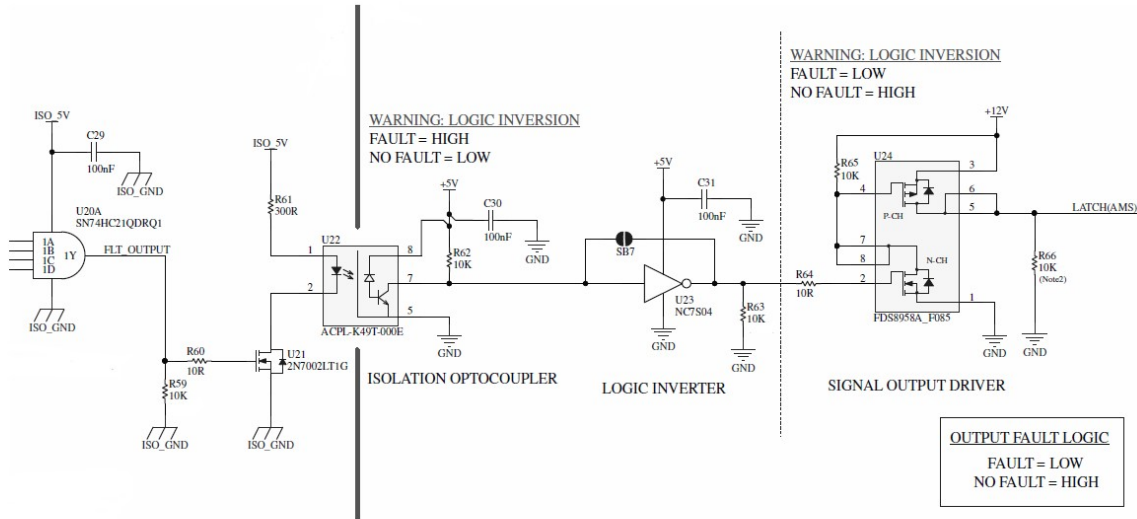


Figure 4.28. Schematic extract of fault signal isolation circuit

Galvanic isolation of the AMS fault status is maintained using an ACPL-K49T optoisolator. The switching logic is such that the optocoupler's LED is constantly illuminated when there is no AMS fault. In doing so, an LED failure is detected automatically as a fault. A dual N-P Channel MOSFET package is used to level-shift the isolated fault signal from 5 V to 12 V, for transmission to the Shutdown PCB (discussed in Section 5.2).

Near-identical circuits to that shown in Figure 4.28 are used to isolate the *HLIM* and *LLIM* signals from the Elithion BMS (see Sheet 5 of Appendix K). *HLIM* is a binary signal that indicates whether the batteries can accept charge, through either regenerative braking or from the charger. *LLIM* indicates if the batteries can no longer discharge. Whilst these signals are also transmitted digitally via CAN, it was decided that they should be incorporated into the general control of the vehicle for redundancy; especially *HLIM*, which is used as a lock-out signal during the charging process (see Section 4.8).

4.7.4. CAN BUS ISOLATION AND STM32F105 MICROCONTROLLER

The CAN network within the accumulator was designed to be a fully-isolated network that would function independently of the vehicle's main CAN network. The accumulator isolation PCB is the gateway between the two networks; or in the case of charging, between the accumulator and charger networks. After considerable research, it was determined that there was no off-the-shelf solution for linking two galvanically isolated CAN networks. Most products researched were intended to only isolate a node from the CAN network, with no further transmission intentions.

The solution was to design a custom CAN repeater, shown in Figure 4.29. The circuit consists of a dual-CAN controller STM32F105 microcontroller, a standard MCP2562 transceiver, and an isolated TJ1052 transceiver. The software used to repeat the CAN messages is relatively simple. Interrupts were used to detect a message on either CAN network, which was then retransmitted on the opposite bus. Preference was made to the vehicle CAN network, over the accumulator network, to ensure the system would respond immediately to an emergency message sent by the VCU, or other such safety system. One benefit of the circuit was that the microcontroller could be used to filter the messages in either direction.

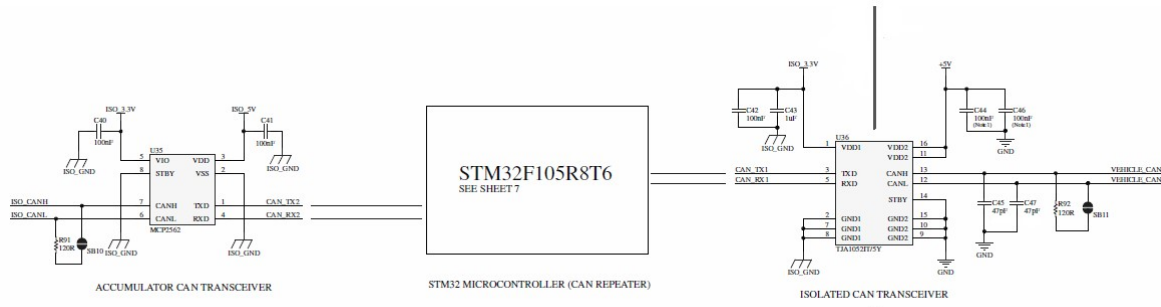


Figure 4.29. Schematic extract of CAN repeater circuit

The STMF105 microcontroller served the dual purpose of also transmitting the state of the precharge circuit over CAN. The precharge PCB outputs four status signals that were intended for debugging purposes. The status labelled *AND* on the PCB silkscreen is a direct connection to the output of the precharging logic circuits. By reading this signal as an input, the accumulator isolation PCB could indicate to the VCU (on the main vehicle CAN network) that the precharge process had been completed. The intention of doing so was to incorporate a software lock-out, where the race car could not drive until precharging was complete. An optocoupler was used to provide galvanic isolation between the precharge and accumulator isolation PCBs, as the dc/dc converter creates a separate ground reference for the accumulator isolation PCB compared with that of the precharge PCB. The circuit is detailed on Sheet 8 of Appendix K.

4.7.5. PCB DESIGN

Due to layout constraints in the front-end of the accumulator, the area allocated to the accumulator isolation PCB was restricted to 100 x 100 mm. To accommodate for mounting structures and CAD inaccuracies, the PCB was designed as a 90 x 90 mm, 4-layer board (Figure 4.30). As the components of the board are all low voltage, the isolation barriers were set at 4 mm. This is the minimum spacing allowed for a *potential* 600 Vdc system per the FSAE rules³⁷, and 1mm greater than the minimum clearance (C_{MIN}) recommended by IPC-2221 for an uncoated 600 V system (calculated using Equation (4.24) [67]). Figure 4.31 shows the fully assembled PCB.

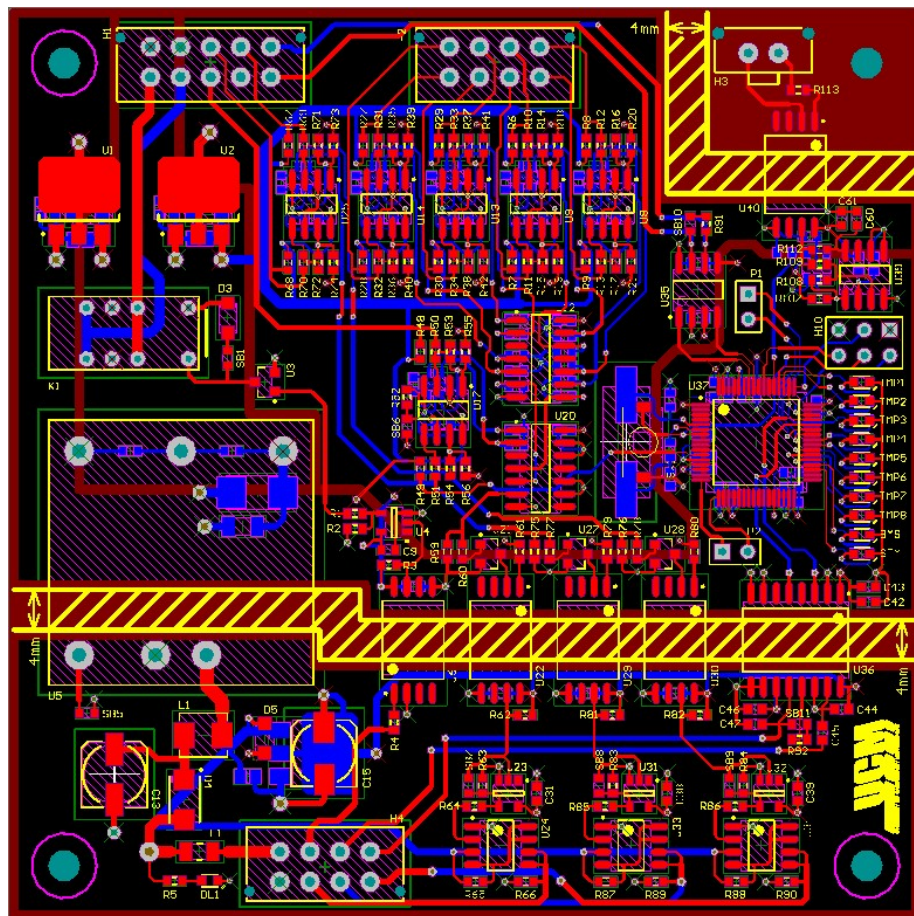


Figure 4.30. Screenshot of Accumulator Isolation PCB design

$$C_{MIN} = 2.5 + 0.005(V - 500) = 2.5 + 0.005(100) = 3 \text{ mm} \quad (4.24)$$

³⁷ The PCB would have to be conformally coated if the spacing was questioned during scrutineering.

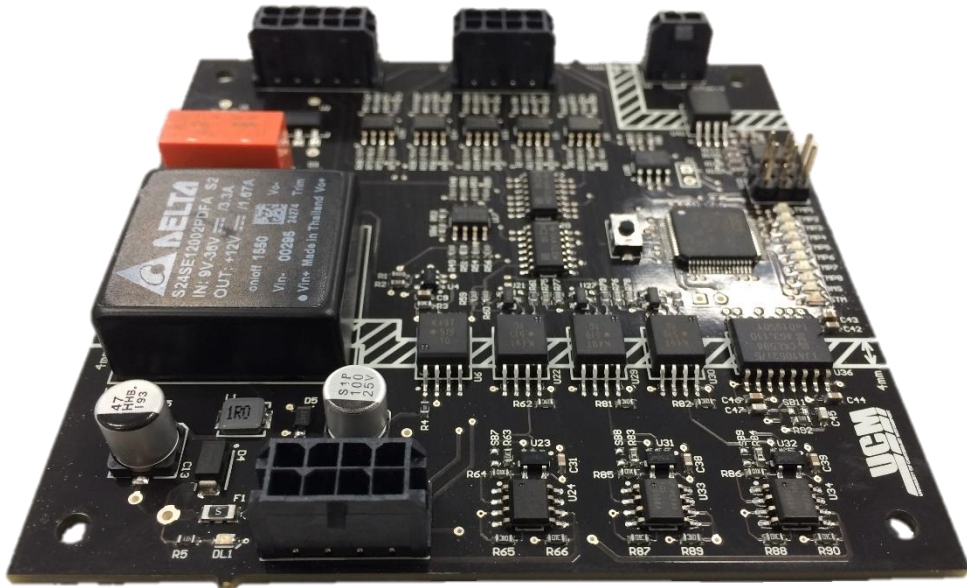


Figure 4.31. Assembled Accumulator Isolation PCB

4.7.6. PCB TESTING

Figure 4.32 shows the rig that was created for testing the accumulator isolation PCB (centre-right of image), and simultaneously confirm the operation of the temperature monitoring PCBs (left-hand boards). The PCBs were spaced on the rig per their actual placement in the accumulator, thus allowing the wiring loom to be made to the correct length. The CAN Controller PCB and corresponding microcontroller development board (right) were used to replicate the CAN network of the race car.

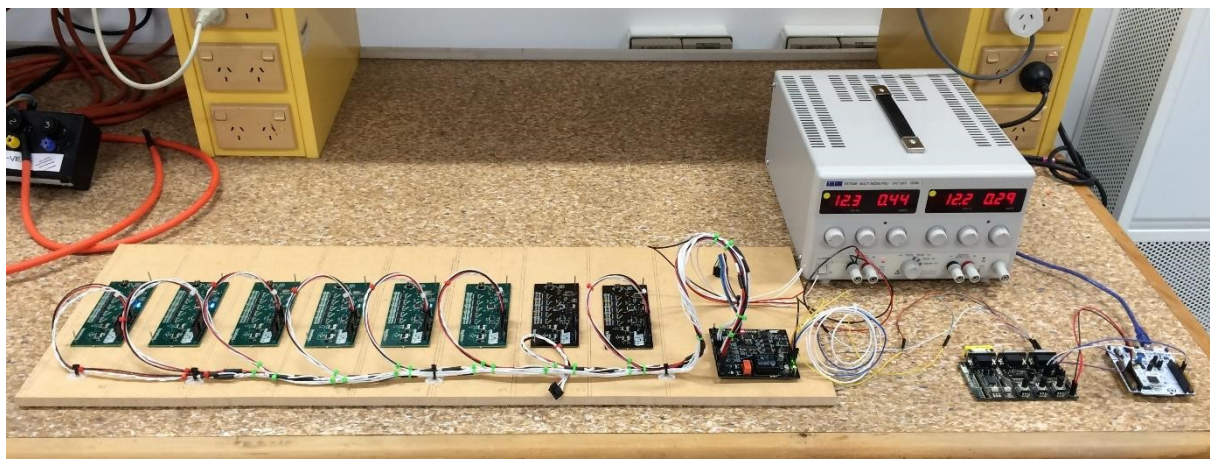


Figure 4.32. Image of Accumulator Isolation PCB testing

Figure 4.33 (Agilent Technologies model DSO5012A) shows an oscilloscope plot of the CAN repeater function of the accumulator isolation PCB. Channel 1 (yellow trace) is a message from one of the temperature monitoring PCBs that has been retransmitted onto the vehicle's CAN network. Channel 2

(green trace) is the original message. The retransmission delay was measured to be 136 μ s, which is negligible with regards to the macro operation of the vehicle. The original message on the isolated accumulator CAN network is noisier than its retransmitted counterpart. This is the result of switching noise from the dc/dc converter being induced onto the CAN lines. The single spike towards the end of the message is the acknowledgement bit of the message. As there are eight transceivers receiving the message, all of which set the acknowledgement bit, the overall effect is a superimposed bit with greater magnitude.



Figure 4.33. Oscilloscope plot of repeated CAN message

4.8. CHARGER SELECTION

Multiple lithium-ion battery charger manufacturers were contacted to find a suitable charging system for the accumulator. Initially, only Current Ways replied with a solution to connect two of their 3 kW 450 Vdc chargers in series. However, just prior to making an order, Current Ways developed a problem in their manufacturing process, resulting in an expected lead-time of 12 weeks. Conveniently, Brusa, who were the preferred charger manufacturer due to their compatibility with the Elithion Lithiumate, replied and an order was placed.

The Brusa NLG514 is a 3.3 kW, 300 – 720 Vdc air-cooled charger that is designed to be an on-board solution for electric vehicles. The main benefit of the NLG514, over many of its competitors, is that the charge process is controlled by the AMS via CAN. This allows the charger to de-rate the charge current as the batteries tend towards being fully charged; as opposed to a direct cut-off, which generally results in a partially-charged tractive pack.

Figure 4.34 shows the low-voltage connection diagram for the NLG514 with the accumulator when charging. The basic configuration was based upon the recommended connection diagram supplied by Elithion [68]. However, the circuit had to be modified to include the accumulator isolation PCB, such that galvanic isolation between the accumulator and the charger is maintained. Pin 3 of the charger (P_{ON}) is used as an enable pin (which must be set logic-high (12 V)) in collaboration with a message over CAN to enable charging. P_{ON} was therefore connected to the isolated HLIM output of the AMS to provide redundancy if an error occurs over CAN; since HLIM will change state when either the batteries are charged or the AMS develops a fault.

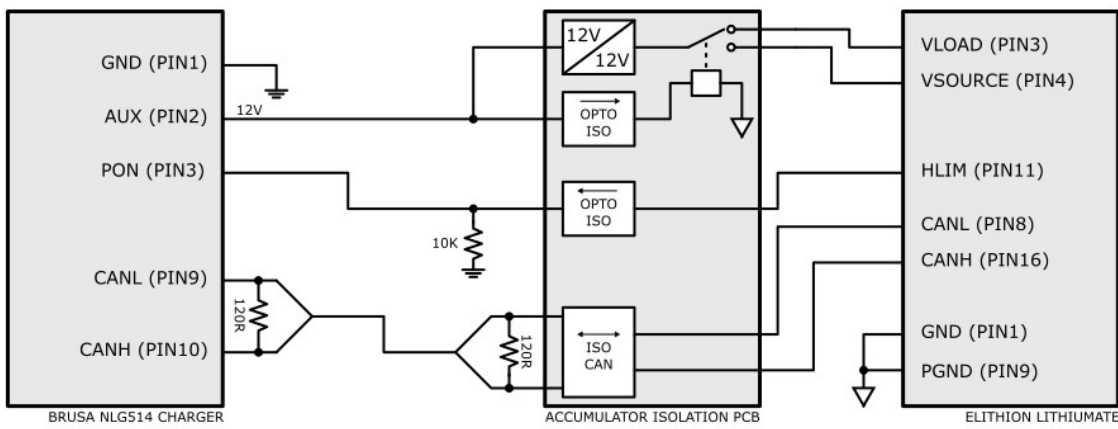


Figure 4.34. Low voltage connection diagram for Brusa NLG514 charger

4.9. ACCUMULATOR ASSEMBLY

This section details the assembly process of UCM16's first accumulator. Whilst the author completed the majority of the electrical design, the physical assembly was the responsibility of an electrical engineering undergraduate student. For completeness, the key topics will be briefly explained. The accumulator testing was a collaborative effort and will therefore be discussed in greater detail.

4.9.1. BATTERY MODULES

Figure 4.35 shows a completed module of Samsung INR18650-25R5 cells, with the exception of the RadLok connectors, Formex cover and complete temperature sensor arrangement (there is one temperature sensor indicated in the image). The design was based on the concept detailed in Section 4.1.7. Whilst it was made very clear by the author that the team should be using a dedicated battery welder for connecting the cells, a home-made resistance welder was used instead to reduce cost. The welder consisted of a microwave transformer with a single turn on the secondary coil, and did not include any form of pulse shaping.

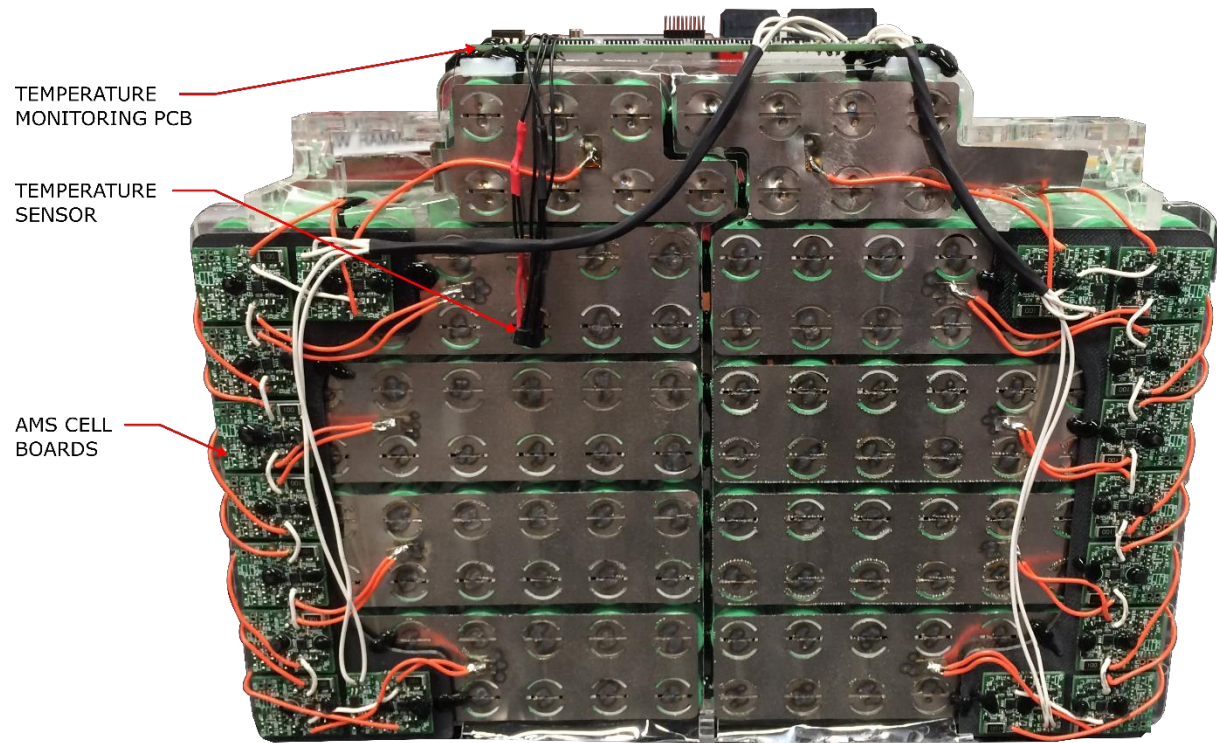


Figure 4.35. Image of assembled INR18650-25R5 module (excluding RadLok connectors and Formex cover)

As a result, the welds were less than satisfactory in most cases, and the uncontrolled pulse caused damage to the internal chemistry of the cells. The home-made welder broke after 90% of the welds had been completed, at which point use of a Miyachi Unitek welder was provided by GreenStage in Auckland. Figure 4.36 is an image of showing the difference between the welds made by the two welders. The top red box indicates welds that were completed by the Miyachi welder, and the bottom box indicates welds by the home-made welder. The two distinct weld points of the Miyachi welder, compared to the multiple distorted welds of the home-made solution, are visible indications of the weld quality. In addition, it was found that a number of the poor welds broke when the modules were being transported to Auckland, implying the weld was “dry” and would have had a high resistance.

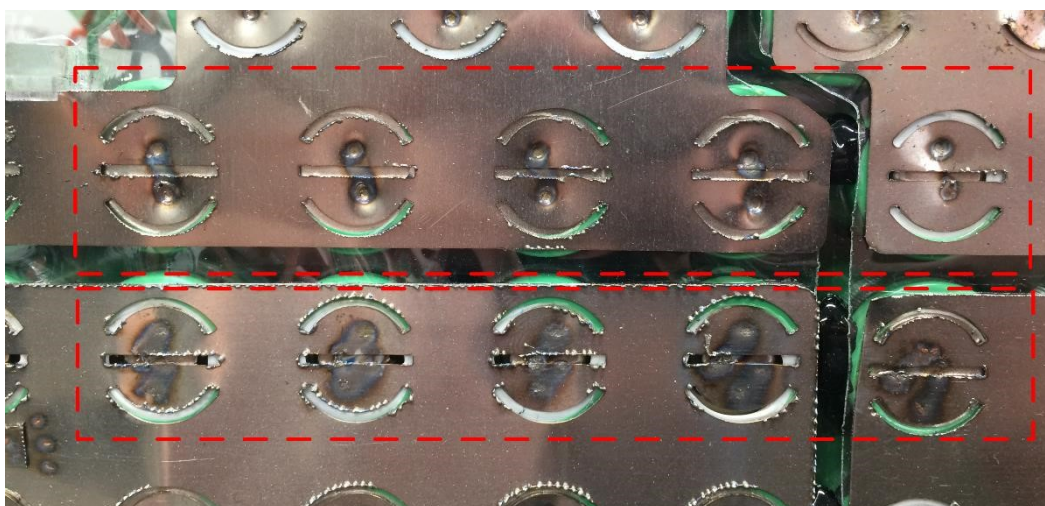


Figure 4.36. Image showing good (top) and poor (bottom) resistance welds

The AMS cell boards were wired external to the module on 3D printed holders to reduce exposure to the cells (Figure 4.37). The 3D printed holders were secured to the module frame using acrylic clips, that doubled as the separation mechanism for the two face plates. There was an issue, however, when the cell measurement wires were added. It was initially planned to have small nickel tabs soldered to the end of the wires, which would then be resistance welded to the main nickel plates. However, the heat from the resistance welder melted the solder when welding the smaller tabs. As such, the measurement wires had to be soldered directly onto the plates. Due to the large surface area acting as a heat sink, this was a very difficult process.

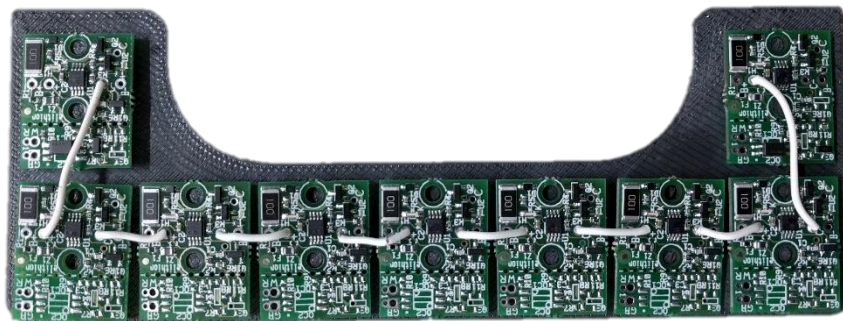


Figure 4.37. Image of AMS cell boards assembled on 3D printed holder

4.9.2. ACCUMULATOR ASSEMBLY

Figure 4.38 shows the overall assembly of the accumulator. It was discovered during the assembly that the CAD model lacked sufficient manufacturing tolerance, and the depth of each battery module was too large to fit within the segments of the accumulator's battery compartment. Consequently, the aluminium dividers had to be removed from the accumulator container. Only six modules could fit within the final assembly, resulting in the peak tractive voltage dropping to 453.6 Vdc.



Figure 4.38. Image of assembled accumulator

The front-end of the accumulator was intended to house the precharge and accumulator isolation PCBs, AIRs, fuses, precharge resistors and the Elithion Lithiumate master unit. However, due to physical constraints, the precharge PCB and associated fuses had to be relocated into the battery compartment. Figure 4.39 shows the assembled front-end of the accumulator.

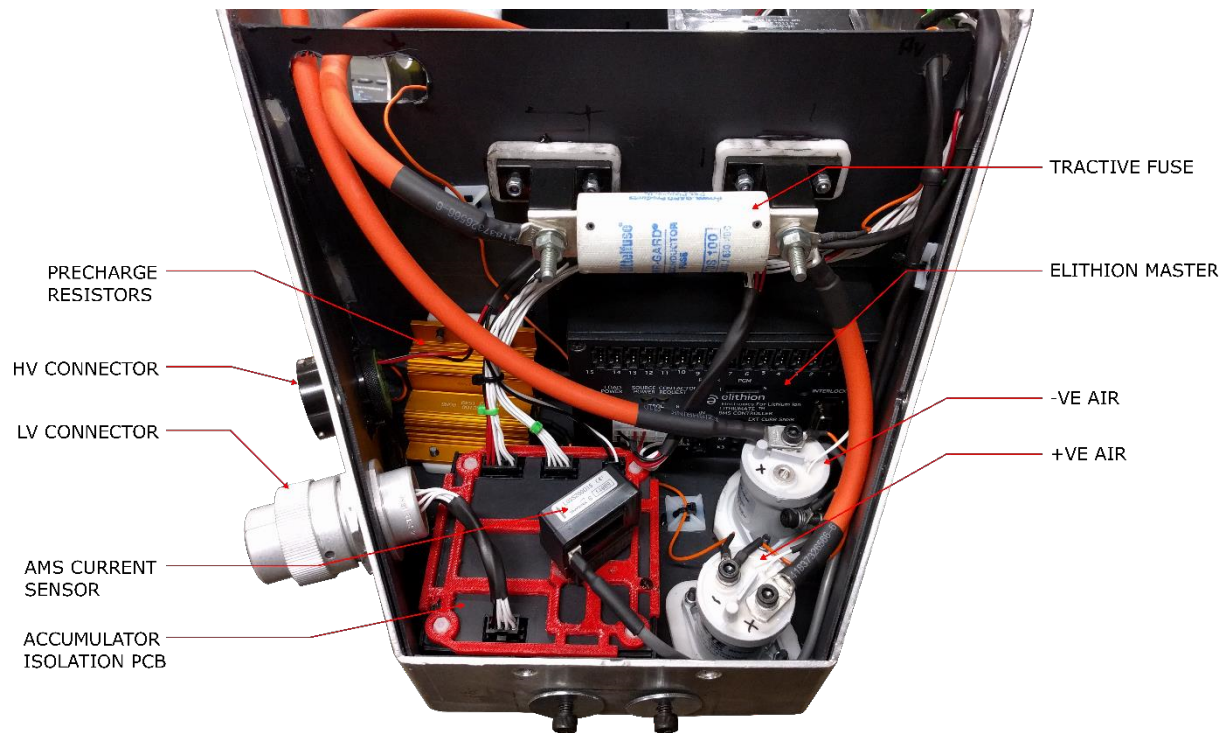


Figure 4.39. Image showing assembled front-end of Accumulator

4.9.3. FINAL ASSEMBLY AND BENCH TESTING

The accumulator was bench tested prior to installation in the car. Initially, the switching of the AIRs was tested without any capacitance connected to the high voltage output. This had the misleading effect of the precharge circuit oscillating between the *precharging* and *precharged* states, whereby the positive AIR and precharge relay would switch rapidly. Figure 4.40 (Agilent Technologies model DSO5012A) is an oscilloscope plot of this occurrence, where Channel 1 (yellow trace) is the voltage after the positive AIR, and Channel 2 (green trace) is the battery voltage. The capture shows the oscillations began after the five second time delay of the precharge circuit, and continued until the circuit was switched off. No capacitance meant the output voltage would drop to zero almost instantaneously, therefore causing the voltage comparison element of the precharge circuit to reactivate the precharge relay. As the power supply to the precharge PCB had not been removed, the timing capacitor remained charged and thus no further time delays were applied.

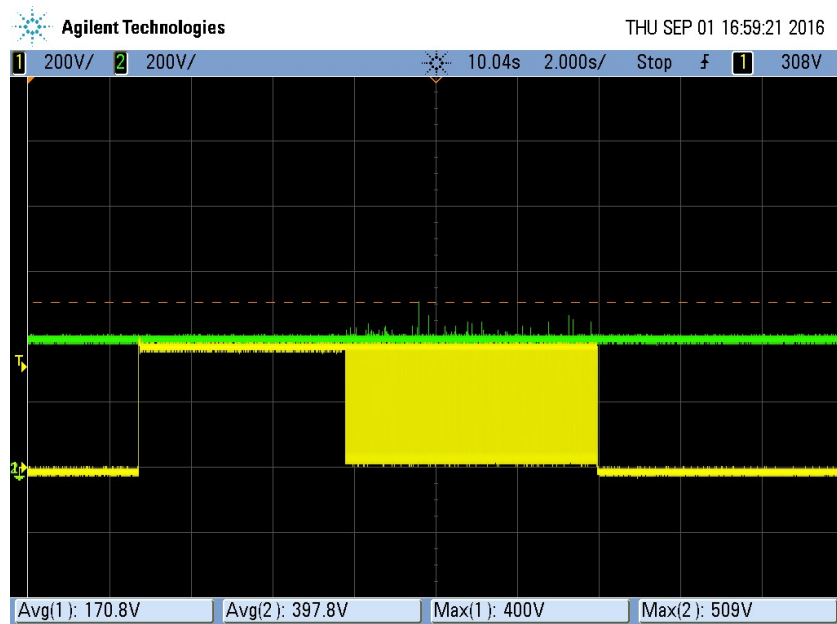


Figure 4.40. Oscilloscope plot of oscillating precharge circuit

Testing the accumulator assembly with the Brusa NLG514 charger (Figure 4.41) confirmed the correct operation of the AMS and accumulator monitoring PCB. However, the start-up procedure had to be altered from what was recommended by Elithion. Due to the start-up time of the dc/dc converter on the accumulator isolation PCB, there is a delay between power-on to the first CAN transmission. As such, the Brusa enters a fault state as it assumes the AMS has not been connected. To resolve this, the low voltage system had to be powered by a separate power supply, such that it could be enabled and stabilised before the Brusa charger was enabled.

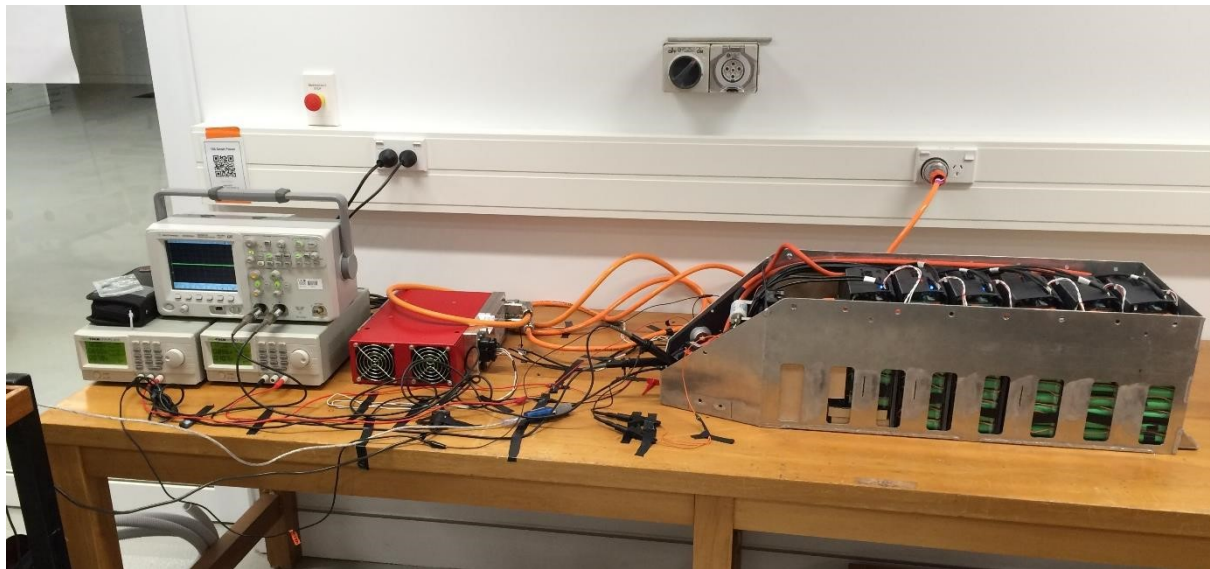


Figure 4.41. Image of first accumulator charge using Brusa NLG514 charger

4.10. CHAPTER SUMMARY

This chapter detailed the selection and design of the high voltage tractive battery modules, protection systems and monitoring electronics that were integrated together to create UCM16's accumulator. The first section identified the requirements of the tractive pack, which included both performance requirements (capacity and power) and physical requirements instigated by other design team members. Following this, three battery module concepts were explained, and how external changes during the design process resulted in the 18650 cell concept being selected.

The later part of Chapter 4 focussed on the design of the printed circuit boards for the precharge, discharge and signal isolation circuitry. Although not included in the accumulator assembly, the discharge circuit is a compliment to the precharge circuit, and was bench-tested with the precharge circuit prior to being installed in the race car. The accumulator isolation PCB was designed as an interface between the low voltage network of UCM16, and the network within the accumulator.

The final section of this chapter showed the assembly of UCM16's accumulator. Dimensional discrepancies between what was modelled in CAD and the manufactured product meant the accumulator was assembled using only six battery modules, reducing the peak tractive voltage to 453.6 Vdc. Further issues also meant the precharge and associated protection fuses were relocated from the front section of the accumulator to the main battery compartment.

The next chapter (Chapter 5) is dedicated entirely to the design of UCM16's electrical safety system. Each of the circuits discussed was designed to independently protect a driver, support engineer or emergency responder from potential electrical hazards; primarily those presented by the high voltage tractive system.

CHAPTER 5

SAFETY SYSTEM DESIGN

Motorsport is inherently dangerous. The primary aim of a design engineer is to extract as much performance from a race car as possible, whilst minimising the risk to the driver, pit crew and emergency personnel. The inclusion of an electric powertrain to the “Formula SAE blueprint” introduced risks that had not been experienced by most UCM team members. For this reason, the safety system of UCM16 was designed to be as comprehensive and reliable as possible. This chapter discusses the design of the Shutdown Circuit, Shutdown PCB and Tractive System Activation Light, and how they are used to mitigate risk exposure.

5.1. SHUTDOWN CIRCUIT

The shutdown circuit is the backbone of the safety system in UCM16. Its purpose is to carry the current of the AIRs, and is therefore used to activate and deactivate the tractive system. At a minimum, rule EV5.1.2 requires the shutdown circuit to include the following:

- 2 Master Switches
- 3 Shutdown Buttons
- Brake-Over-Travel switch
- Insulation Monitoring Device (IMD)
- Inertia crash sensor
- Brake System Plausibility Device (BSPD)
- Accumulator Management System (AMS)
- Hardware interlocks

Each element of the shutdown circuit is connected in series, as shown by Figure 5.1. If any one element is open, the AIRs will open and the tractive system will become disabled. Figure 5.2 is a diagram of the routing path of the Shutdown Circuit in UCM16.

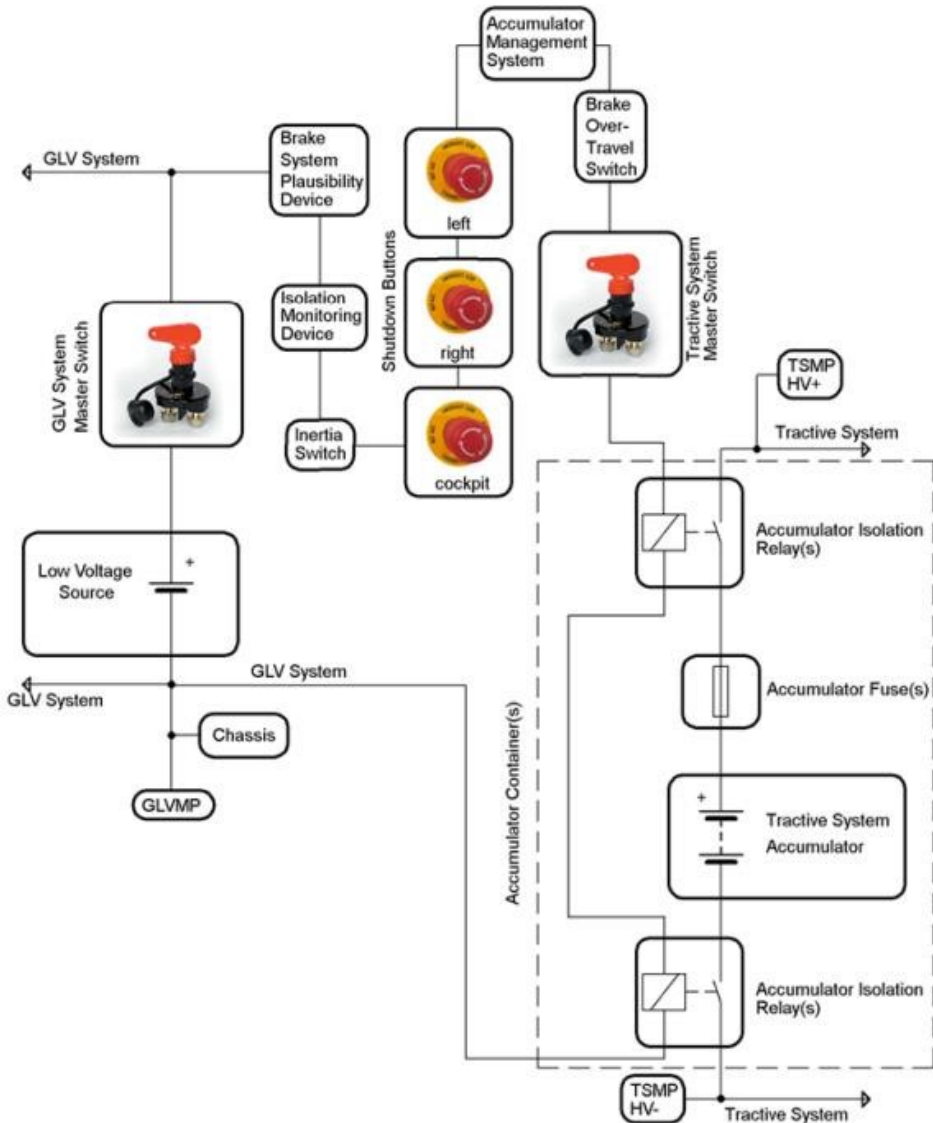
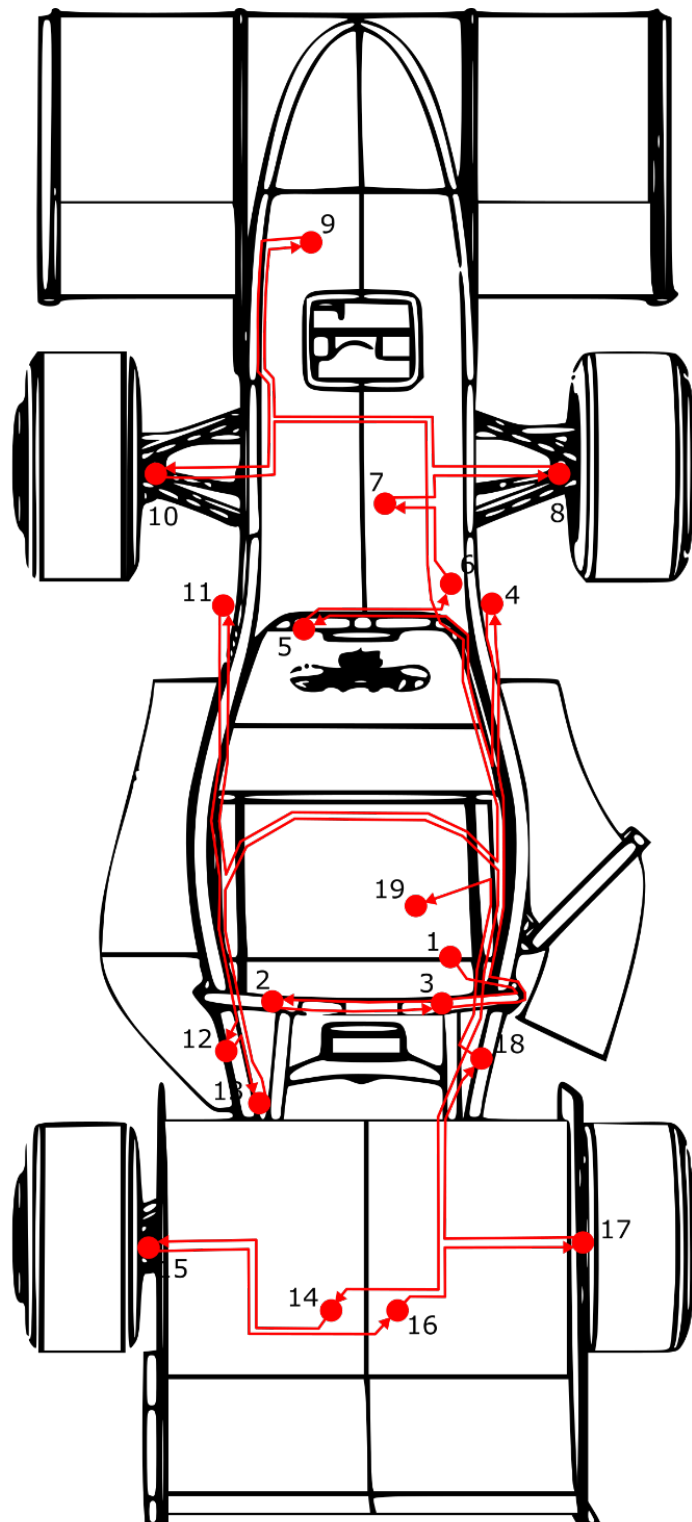


Figure 5.1. Example shutdown circuit diagram [5]

5.1.1. INTERLOCKS

An interlock is a mechanism that makes two or more systems mutually dependent, such that one system cannot change state unless the other systems are in their correct operating states. In doing so, interlocks prevent the occurrence of undesired states. In the case of Formula SAE, interlocks are required for all tractive connectors that can be disconnected without the use of tools (EV3.3.6). When a connector is disconnected, the Shutdown Circuit becomes discontinuous, and cannot activate the now exposed tractive system. Souriau 8STA connectors were used for all tractive connections in UCM16. In addition to the power pin positions, the connectors have four auxiliary pin positions, which were used to create the interlocks.



- | | |
|--|---|
| 1. START | 11. FRONT RIGHT MOTOR CONNECTOR INTERLOCK |
| 2. LEFT ROLLOOPO E-SWITCH | 12. HVD |
| 3. RIGHT ROLLOOPO E-SWITCH | 13. SHUTDOWN PCB |
| 4. FRONT RIGHT MOTOR CONNECTOR INTERLOCK | 14. REAR LEFT MOTOR CONNECTOR INTERLOCK |
| 5. DASHBOARD E-SWITCH | 15. REAR LEFT WHEEL INTERLOCK |
| 6. INERTIA SWITCH | 16. REAR RIGHT MOTOR CONNECTOR INTERLOCK |
| 7. VCU CONTROLLED MOSFET | 17. REAR RIGHT WHEEL INTERLOCK |
| 8. FRONT RIGHT WHEEL INTERLOCK | 18. TRACTIVE SYSTEM MASTER SWITCH |
| 9. BRAKE-OVER-TRAVEL SWITCH | 19. ACCUMULATOR HV CONNECTOR INTERLOCK |
| 10. FRONT LEFT WHEEL INTERLOCK | |

Figure 5.2. Diagram of shutdown circuit routing path and element location

Additional interlocks had to be added to the Shutdown Circuit as a precaution to avoid motor damage. Since the motors are outboard motors (located outside of the protection of the chassis), EV4.2.3 requires interlocks to open the AIRs if the “wheel assembly is damaged or knocked off the car”. The lack of quantification regarding a damaged wheel assembly led to the creation of numerous overcomplicated concepts. For example, one concept considered the use of an accelerometer on each wheel assembly to detect abnormal changes in acceleration associated with a collision.

The visit to Formula Student teams in Germany and the Netherlands, however, showed the simplest mechanism was to use small gauge wire secured to the wheel assembly and chassis, with a purposefully weakened section in between. If the wheel assembly was to experience a large external force, the section would break and thus cause the Shutdown Circuit to become discontinuous. If the motor cable were to become damaged and touch the grounded motor enclosure, it would generate a large current that would be interrupted by the output fuse of the associated sub-inverter. However, replacing the fuse post fault would have almost definitely required the inverter to be fully disassembled, thus increasing the risk of further component damage.



Figure 5.3. Image of rear-left wheel assembly interlock

Figure 5.3 shows the interlock for the rear-left wheel assembly. A loop was added to the 3D printed cooling jackets of the motors for securing the wire. The wire was weakened by inserting a spade connector part way along the outgoing cable. This allowed the interlock to be demonstrated during the FSAE-A technical inspection without physically cutting the wire. The spade connectors were insulated from contact with any part of the suspension, wheel assembly, and motor casing (which were grounded) by heat shrink.

5.1.2. HIGH VOLTAGE DISCONNECT

One element of the Shutdown Circuit which is not indicated on the diagram of Figure 5.1 is the High Voltage Disconnect (HVD). In emergency situations, it must be possible for an untrained individual to remove a dedicated element of the tractive system (for example a fuse or connector) which disconnects at least one pole of the accumulator (EV4.7.1). The HVD was also used a physical lock-out feature for the tractive system. Whenever the car was not in a ready-to-drive state the HVD was in a dedicated enclosure, which only the author had access to.

Figure 5.4 shows the electrical position of the HVD within the tractive system. It is because of the HVD that the Discharge PCB had to be located outside of the accumulator. If the discharge circuit was within the accumulator, and the HVD was removed, there would be no way for the circuit to discharge the intermediate capacitor.

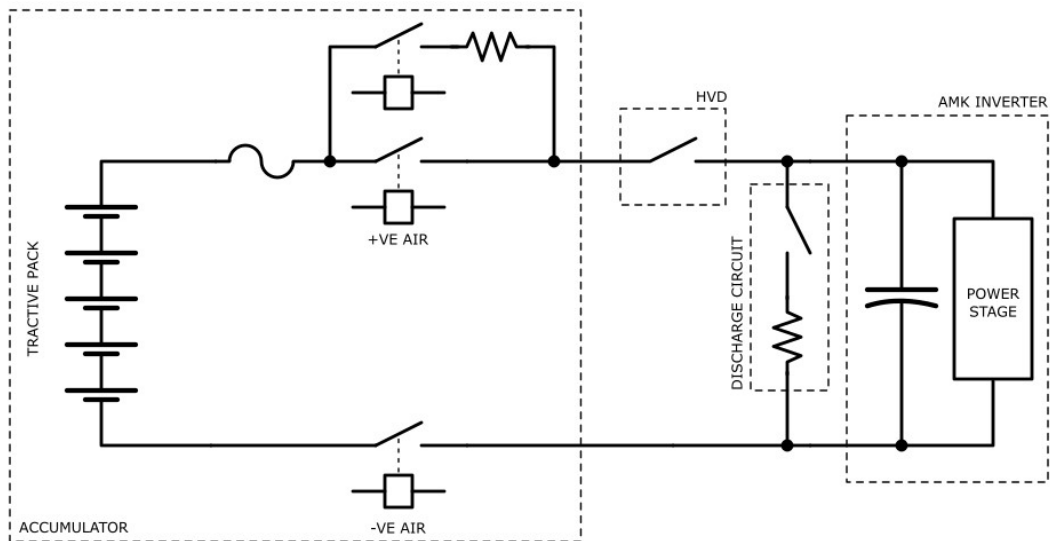
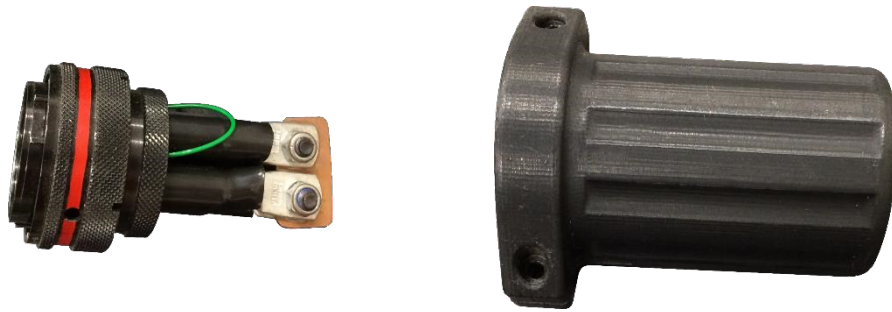


Figure 5.4. Diagram of tractive system with HVD

UCM16's HVD was a Souriau 8STA tractive connector with a continuous connection between the four power positions, as shown by Figure 5.5(a). Since the HVD is a removable element of tractive system, an interlock was added by looping 22 AWG mil-spec wire between two of the auxiliary positions. A handle was 3D printed to enclose the cabling. Figure 5.5(b) shows the final assembly of the HVD in position on UCM16. It should be noted that whilst the concept and electrical design of the HVD was the work of the author, its manufacture was completed by two undergraduate engineering students.



(a) HVD internal (left) and enclosure (right)



(b) HVD mounted on UCM16

Figure 5.5. Images of High Voltage Disconnect

5.2. SHUTDOWN PCB

The Shutdown PCB incorporates the output signals of the AMS and IMD with the BSPD to create a single node that activates (opens) the shutdown circuit. The PCB also has the dual purpose of measuring the tractive current. EV5.1.4 states that, in the event of an AMS, IMD or BSPD fault, the tractive system must remain disabled until manually reset by a person external to the car. A rules clarification concluded that a dedicated reset switch was required, and that the tractive system must remain disabled after the low voltage power has been cycled³⁸. This therefore prompted the need for a memory latch.

³⁸ As an aside, at the 2016 FSAE-A competition the scrutineers said cycling the LV system is in fact sufficient and that the author had been misled by the rules committee. The system developed simply exceeded the minimum safety requirement and maintained rule compliance.

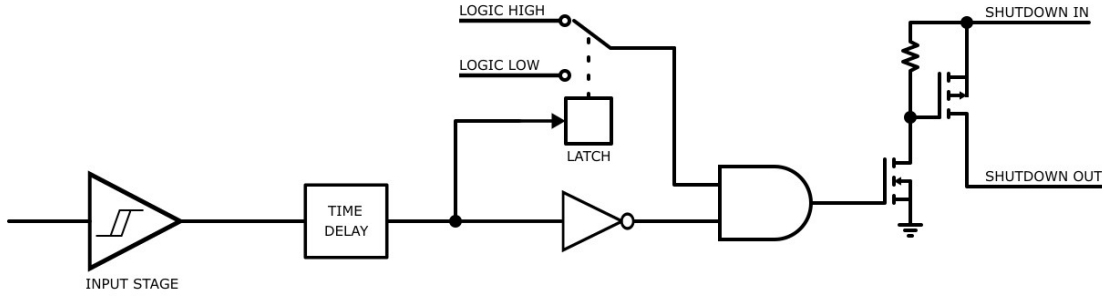


Figure 5.6. Shutdown circuit memory latch & power stage logic diagram

The Shutdown PCB was designed using the same “building block” with an input stage that was altered to suit each application. Figure 5.6 is a logic diagram of the “building block”. The full schematics are documented in Appendix L. In a no-fault case, the output of the time delay block³⁹ is logic-low, and the MOSFET driver signal closes the shutdown circuit. When the input stage detects a fault, the output switches logic-high and the shutdown circuit is opened. The latching relay is also triggered which connects the input of the AND gate to logic-low. This locks the output of the AND gate to logic-low and prevents the shutdown circuit from closing until the latching relay is reset. For the AMS element of the Shutdown PCB, the input stage is a comparator with external hysteresis applied to remove any induced noise.

The powerstage used to open the shutdown circuit consists of an N and P-channel dual-package MOSFET, where the P-Channel MOSFET switches the shutdown circuit and the N-Channel MOSFET forms the gate driver. Three powerstages were included on the Shutdown PCB, such that each fault detection circuit would actuate its own powerstage.

5.2.1. INSULATION MONITORING DEVICE

An Insulation Monitoring Device (IMD) is a protection device that measures the resistance between the tractive and low voltage systems. The principle behind detecting an insulation fault in an electric vehicle is to superimpose a clocked measurement voltage onto the tractive system and then search for the signal in the low voltage system [69]. An Isometer IR155-3204 (Figure 5.7) with a response value of 264.6 kΩ was supplied by Bender as part of a sponsorship agreement. The response value (R_{an}) was calculated based upon the required response of 500 Ω/V (EV5.5.3) for the maximum tractive voltage, as shown by Equation (5.1). The fault status of the IR155-3204 is indicated by a high-side MOSFET switch, in which logic-high indicates no fault. A fault is declared when either the measured insulation resistance is less than a given threshold, or the IMD detects an internal fault.

$$R_{an} = \frac{500 \Omega}{V} \times 529.2 V = 264.6 k\Omega \quad (5.1)$$

³⁹ The same design used in the precharge circuit (Section 4.4.4)



Figure 5.7. Image of Bender Isometer IR155-3204 Insulation Monitoring Device

There were two practical connection points for the IMD; inside the accumulator or after the HVD. Most electric Formula SAE teams install their IMDs within the accumulator to reduce the number of required units. Since an IMD must be active when charging (EV8.3.7), teams such as Academic Motorsports Club Zurich (AMZ)⁴⁰, who only build one accumulator per season, install their IMD inside the accumulator for dual functionality. It was intended for UCM to manufacture at least two accumulators for the FSAE-A competition; therefore, it was more appropriate to install one IMD on the vehicle-side of the tractive system (Figure 5.8), and one with the charger.

Installing the IMD outside of the accumulator is a safer location, with regards to detecting insulation faults. The Isometer IR155-3204 supplied by Bender did not have an undervoltage lock-out feature, which declares a fault unless a predetermined voltage is measured. This meant the IMD would measure the insulation resistance as soon as it was powered. Considering the tractive cables outside of the accumulator (battery and motor cables) are exposed, in comparison to the cabling within the

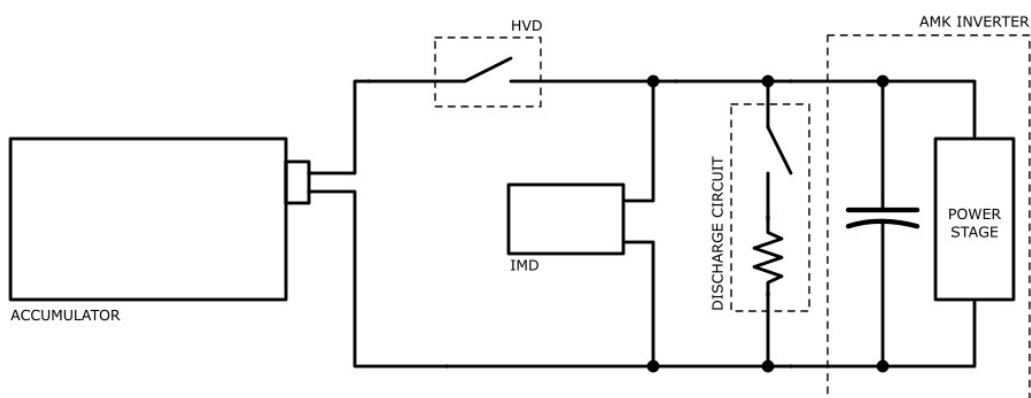


Figure 5.8. Diagram showing location of IMD in tractive system

⁴⁰ The highest team in the 2016 Formula Student Electric ranking

accumulator, there is a considerably higher chance of an insulation failure occurring after the accumulator's high voltage connector. As shown by Figure 5.8, this section has a continuous connection to the IMD. Consequently, if an insulation failure were to occur, it would be detected by the IMD prior to the tractive system activating, causing the circuit described below to disable the vehicle. This precheck could not be accomplished if the IMD was within the accumulator.

Figure 5.9 is a logic diagram of the input stage for the IMD element of the Shutdown PCB. When the IMD powers on, it performs a self-check that takes a maximum of two seconds, in which the output remains logic-low. The D-Latch and associated time delay circuit are used to snapshot the state of the IMD two seconds after power-up, and will lock the circuit in the fault state if the self-check results in a fault. For the IMD circuit, the time delay of the "building block" was set to 2.7 seconds, so as not to prematurely trip. The $2.2\text{ k}\Omega$ pull-down resistor is used to limit the current through the high-side switch and generate a fault if the wire from the Shutdown PCB to the IMD is broken.

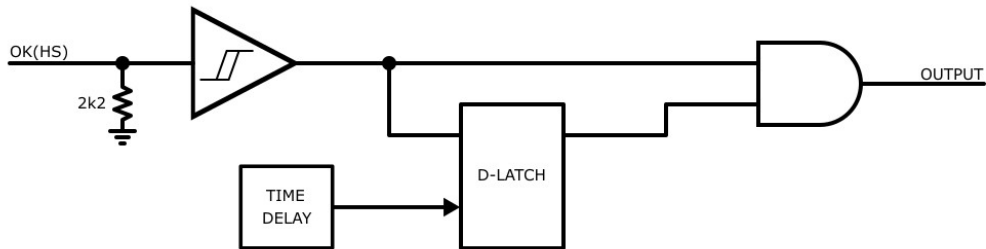


Figure 5.9. Logic diagram of IMD input stage

5.2.2. BRAKE SYSTEM PLAUSIBILITY DEVICE

The Brake System Plausibility Device (BSPD) will open the shutdown circuit if the tractive system is delivering more than 5 kW to the motors, and the car is braking hard for longer than 0.5 seconds (EV5.6). The input stage of the BSPD is split into the brake detection and current measurement circuits. Each circuit provides a binary output that is combined at an AND gate to activate the memory latch circuit. The time delay of the circuit was set to 470 ms.

The brake detection circuit (Figure 5.10) taps into the output of the car's brake pressure sensor, which nominally interfaces with the VCU. A $100\text{ k}\Omega$ pull-up resistor ensures a fault will be generated if the signal wire is broken, and an op amp buffer is used to provide a high input impedance, so as not to distort the brake pressure measurement to the VCU. The definition of "hard braking" is adjusted using the potentiometer. When driving, heat transfer from the brake rotors to the brake fluid causes the resting brake pressure to change significantly. To counter this, the initial brake threshold was set to the maximum pressure that could be actuated when the car is at rest.

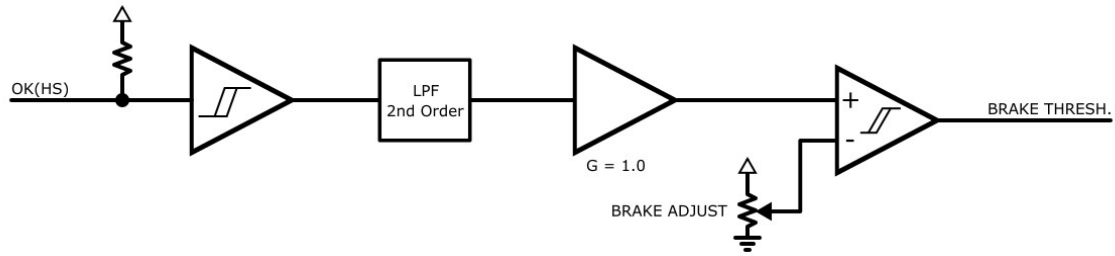


Figure 5.10. BSPD brake detection logic diagram

Figure 5.11 shows the logic diagram for the current measurement circuit. The circuit defines not only the current threshold for the BSPD but also measures the tractive current for use in the vehicle control systems. An LEM HASS 100-S hall-effect current transducer was used to measure the tractive current. Hall effect sensors measure the strength of the magnetic field generated by current flowing through a wire. They are hence susceptible to error due to the electromagnetic interference generated by the inverter (discussed further in Section 6.2.2). The output voltage of the LEM transducer has the following relationship to the current [70],

$$V_{OUT} = V_{REF} + 0.625 \left(\frac{I_P}{I_{PN}} \right) \quad (5.2)$$

where, V_{OUT} is the output voltage, V_{REF} is the output reference voltage, I_P is the measured current, and I_{PN} is the primary nominal RMS current (100 A in the case of the HASS 100-S). It was assumed that the same noise would be induced onto both outputs (common-mode noise), therefore a differential amplifier was used to subtract V_{REF} from V_{OUT} .

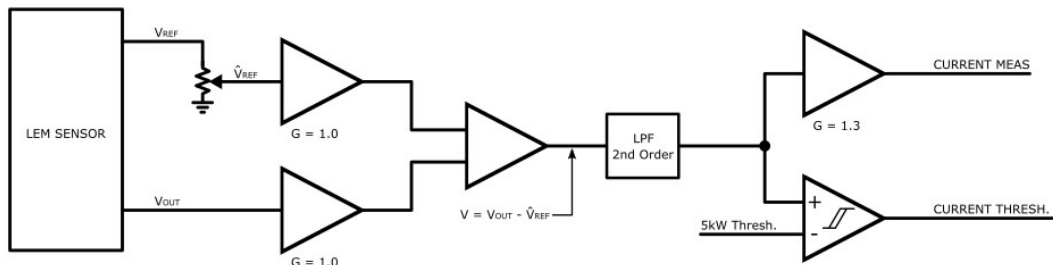


Figure 5.11. BSPD current measurement logic diagram

The full measurement range of the HASS 100-S is ± 300 A; however, the maximum expected current of UCM16 was no more than 200 A. The transfer function of the circuit was therefore adjusted such that the full range of a supervising microcontroller's ADC matched the expected current range. A potentiometer connected to V_{REF} allows the dc offset of the circuit to be adjusted. Using Equation (5.2), an offset of 1.25 V (\hat{V}_{REF}) was required such that a tractive current of -200 A results in a voltage of 0 V at the output of the low pass filter. The subsequent transfer function of the circuit at the output of the

low pass filter is given by Equation (5.3). This was used to set the 5 kW threshold limit for the BSPD circuit and determine the 1.3 V/V gain required to match the ADC measurement range.

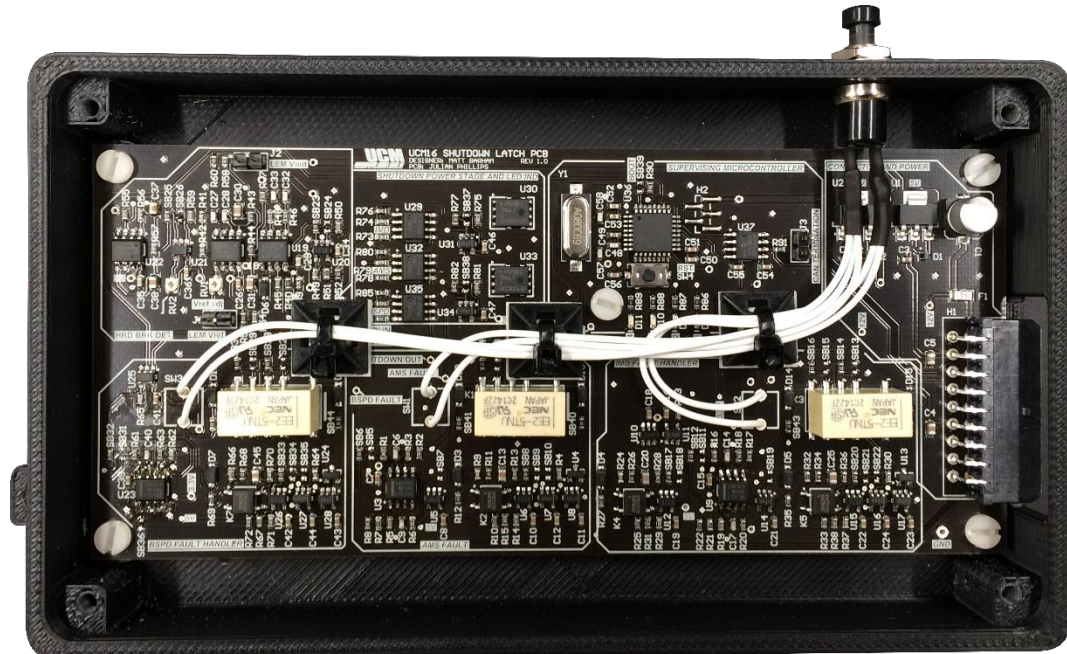
$$V = 0.00625I_P + 1.25 \quad (5.3)$$

5.2.3. SUPERVISING MICROCONTROLLER

An STM32F072 microcontroller was used to read the measured tractive current and then transmit the measurement onto the main CAN network. The microcontroller was also used to supervise fault handling and provide a back-up in the case of a circuit failure. The fault status of the AMS, IMD and BSPD were monitored and sent periodically as a status message. The VCU monitored the status message and, in the event of either a fault or lack of message, would open the shutdown circuit. This therefore meant there were two points at which the circuit would be opened.

5.2.4. PCB DESIGN

The PCB layout was completed by an electronics technician, using schematics created by the author (Appendix L). Figure 5.12 is an image of the assembled PCB in its 3D printed enclosure. The push-button at the top-right of the enclosure was wired in parallel across all three switch positions to reset the latching relays. Due to access restrictions, the push button was later relocated to the rear of the chassis, and connected to the Shutdown PCB using a 2-pole connector.



5.3. TRACTIVE SYSTEM ACTIVATION LIGHT

The Tractive System Activation Light (TSAL) is mounted to the top of the main roll hoop and gives a visual indication when the tractive system is active. The TSAL design is split into two sections; the detection circuit (located on the discharge PCB) and the light itself. The following rules governed the design of the TSAL:

1. The TSAL must be active when either the shutdown circuit is closed or the voltage of the tractive system outside the accumulator container exceeds 60 Vdc (EV4.12.1).
2. The TSAL must be red (EV4.12.2) and flash continuously with a frequency between 2 Hz and 5 Hz (EV4.12.3).
3. The TSAL must be visible from every horizontal direction by a person standing 3 m away, even in bright sunlight (EV4.12.6).

The state of the shutdown circuit was already being monitored by the current-shunt circuit (Section 4.5.2), so only the tractive voltage detection needed to be designed. This was achieved by replicating the constant current source circuit used for the accumulator voltage indicator (Section 4.4.6) and replacing the LED with a TLP2361 optical isolator. The feedback resistance was calculated⁴¹ to be 860 Ω for a 2 mA drain current.

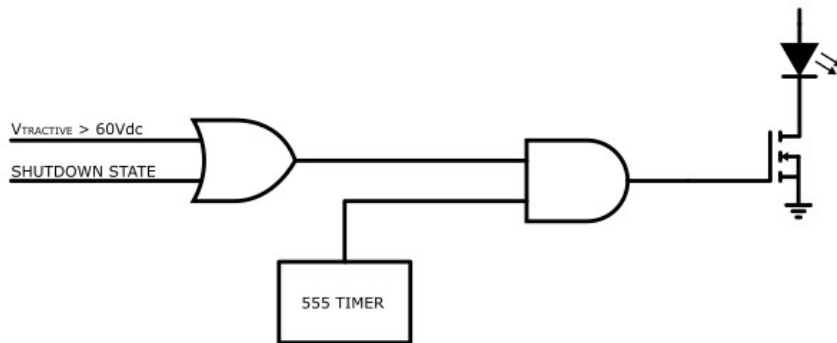


Figure 5.13. Simplified diagram of TSAL driver

Figure 5.13 shows a simplified diagram of the drive circuitry for the TSAL. The two activation conditions are combined by an OR gate, which then activates the output of the AND gate. A 555 timer in an astable configuration is used as a 4 Hz square-wave generator that oscillates the output of the AND gate, and thus flashes the LED light.

The light consists of three parts, two 2-layer PCBs and a 3D printed housing. Each PCB (Figure 5.14) features 24 super-bright Osram surface mount LEDs arranged in a 4s6p lattice. The housing was designed by an undergraduate mechanical engineering student, and was printed with translucent plastic allowing the unit to be sealed around the roll hoop. Figure 5.15 is an image of the final TSAL assembly.

⁴¹ Using Equation (4.18)

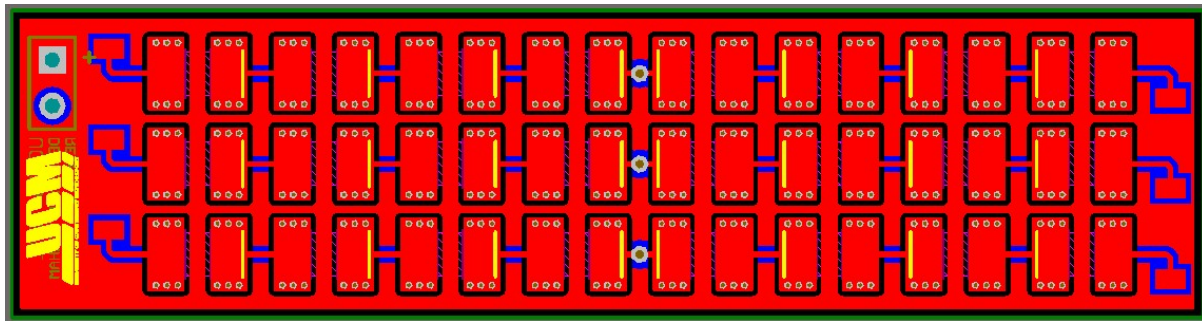


Figure 5.14. Screenshot of TSAL PCB design



Figure 5.15. Image of illuminated TSAL (rear-view) on UCM16

5.4. CHAPTER SUMMARY

Chapter 5 covered the electrical safety systems of UCM16. Firstly, the Shutdown Circuit was discussed. It serves as the main emergency control line, and disconnects the poles of the tractive system if triggered. Trigger points include the emergency stop buttons, VCU and the Shutdown PCB; which processes status inputs from the accumulator management system and insulation monitoring device. Included on the same board is the brake plausibility device and a supervising microcontroller, which has the dual purpose of converting the measured tractive current to CAN.

The final system covered in this chapter was the tractive system activation light, and its control electronics located on the discharge PCB. The TSAL is a visual indication that the shutdown circuit has been enabled, or that the tractive voltage outside of the accumulator has exceeded 60 Vdc.

CHAPTER 6

NEW ZEALAND'S FIRST ELECTRIC FSAE CAR

Engineering is an iterative process that sees designs tested and then refined until they meet their initial specifications. It is uncommon for a new concept to be perfect first-time; and, given the newness of an electric race car, UCM16 was no exception. This chapter is focussed on the assembly (and resulting issues) of the systems detailed in the previous chapters, to create New Zealand's first electric Formula SAE race car.

6.1. PRELIMINARY VEHICLE TESTING

The assembly of the accumulator was very delayed in terms of the overall project plan. It was originally planned to reconfigure the inverter from its single drive state (used for the gearbox testing) directly to 4WD. However, in the final week of July, the request was made to only rewire two of the sub-inverters and run the car in RWD. In doing so it was anticipated that the completion of the accumulator would coincide with the powertrain. This section describes the configuration process and initial commissioning of the RWD powertrain.

6.1.1. RWD INVERTER WIRING

The inverter was housed within a 2-piece carbon fibre enclosure, designed by an undergraduate mechanical engineering student. The first piece of the enclosure was a faceplate that was fixed to the frame of the inverter. The connectors and cable glands were mounted to the faceplate, thus allowing the inverter to be wired with minimal restriction. The second piece was a shroud that slid over the rear of the inverter. Mounting blocks attached to the inverter frame allowed the inverter to be hung from the roof of the chassis.

Figure 6.1 shows the partially completed inverter with the faceplate attached. Due to cost constraints, only two Souriau 8STA connectors were purchased to allow the removal of the rear motors. The tractive cables for the front motors therefore had to be hardwired (Section 6.3.3), with cable glands for protection through the faceplate. The low voltage system used Deutsch HD30 circular connectors.

As both tractive and low voltage systems were present within the inverter enclosure, EV4.1.5 had to be adhered to; which states the systems must be separated by a moisture resistant, UL recognised insulating material with a temperature rating greater than 150 °C. As an alternative, the systems could be separated through air by 30 mm; however, the tight confines of the inverter enclosure made this impractical. The solution was to contain all the wiring with Qualtek Q-150K heat shrink, which is a 150 °C rated flexible tubing with a dielectric strength of 2.5 kV/mm.

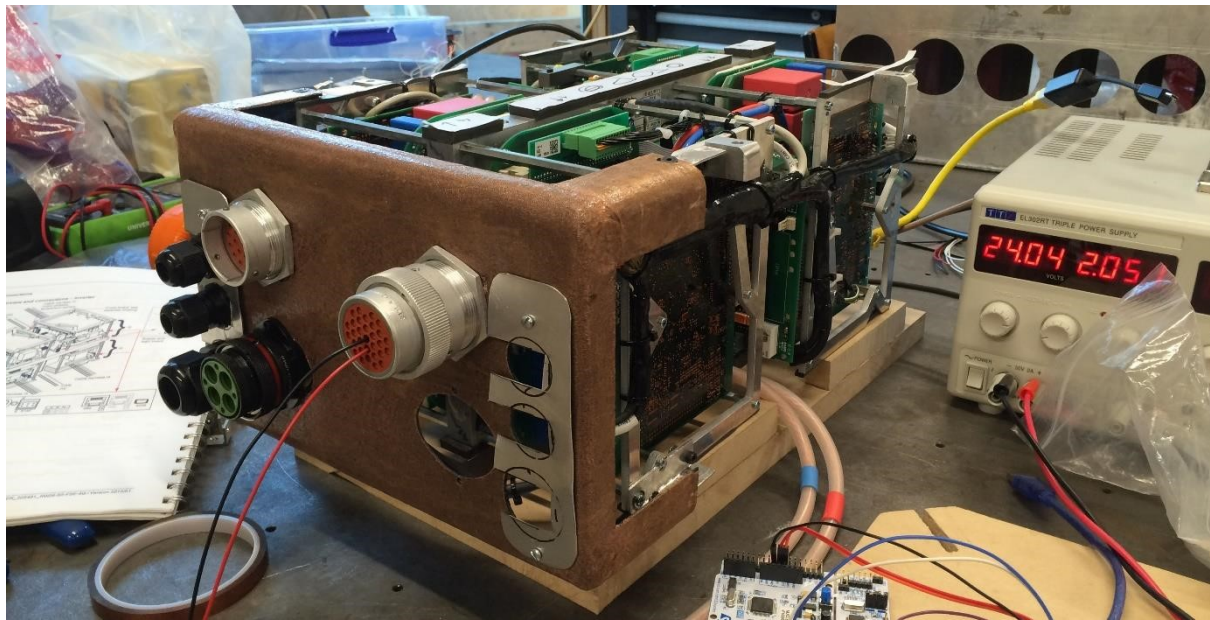


Figure 6.1. Image of inverter being wired for RWD

6.1.2. RWD INVERTER COMMISSIONING WITH VCU

The newly configured inverter was commissioned outside of the chassis, but with the rear motors and gearboxes fully assembled (as shown by Figure 6.2). The Chroma dc power supply was used in place of the incomplete accumulator. Initially the CAN Controller PCB was used to control the motors before the custom VCU was integrated into the system. Since the Nucleo development board used in conjunction with the CAN controller featured an STM32F4 microcontroller, as opposed to the STM32F7 on the VCU, the post-integration commissioning was primarily focussed on transferring the software developed during the dynamometer testing.

At the time of commissioning the inverter, the wiring harness for the car was installed and tested. The harness was concentrically twisted to improve routing flexibility, reduce isolated cable strain, and reduce the frontal area of each branch. The core of the inverter branch (Figure 6.3) was the shielded CAN cables to the VCU.

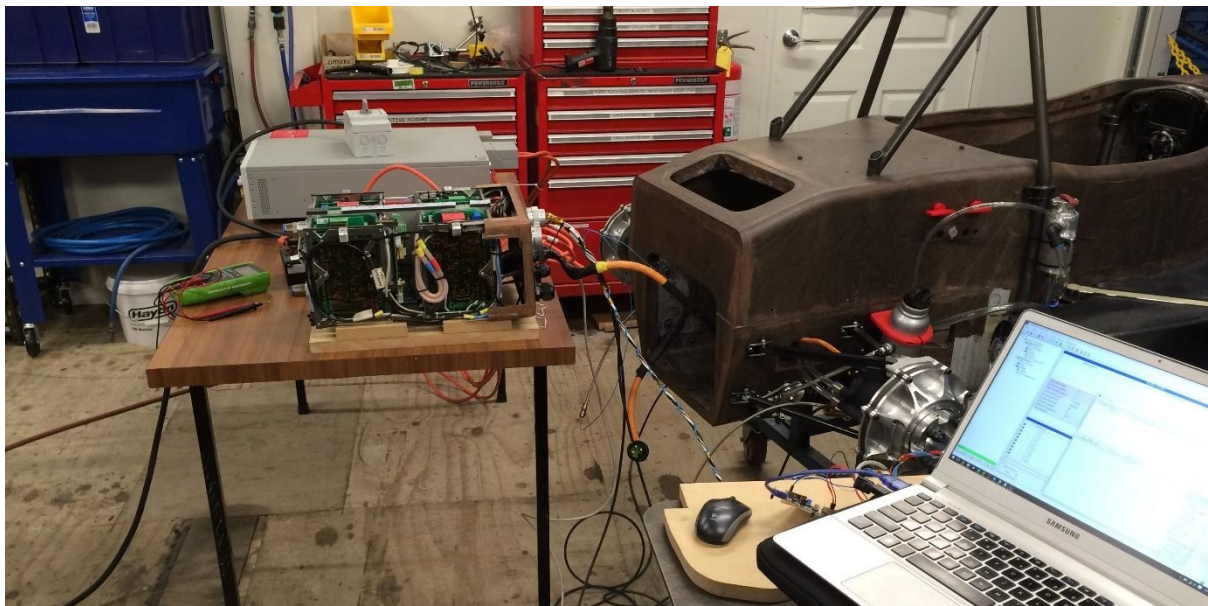


Figure 6.2. Image of stationary powertrain testing



Figure 6.3. Image of concentrically twisted wiring harness for inverter

6.2. RWD TESTING

On the 7th of September 2016, UCM16 drove for the first time under its own power, making it New Zealand's first electric Formula SAE race car. It was a massive motivational boost for the team after the numerous delays and issues faced prior to the car driving. To ease into the shakedown session, the maximum torque that could be requested by the driver was slowly increased for each series of laps; from 30% nominal torque to 100%. As the steering angle sensor had not been installed, the car drove with an equivalent fixed axle mode, meaning the same torque was applied to each rear wheel by its associated motor.



Figure 6.4. Image of the author driving UCM16 on its first drive day

After approximately 15 minutes of driving, the 56 V Zener diode on the discharge PCB failed, prompting the end of the testing session. As it turns out, the diode had been selected with a power rating equal to the calculated heat dissipation, and no factor of safety (a mistake on behalf of the author). As the Zener diode was used in the voltage detection circuit for the TSAL, which had not been installed, it was not fixed until the second revision of the discharge PCB was made. The car remained in its RWD configuration for a month to test the core electrical and mechanical designs. The following is an explanation of the issues uncovered during this testing period.

6.2.1. EMI INTERFERENCE WITH AMS

It was not until the car was driving that the effect of the electromagnetic interference from the inverter could be evaluated. In previous tests, the vehicle components were separated, for example when the inverter was tested outside of the chassis, and the interference did not prevent the system from operating

correctly. However, the proximity of the inverter to the surrounding components, most importantly the accumulator, caused several issues that had to be resolved.

The status of each cell bank is requested once a second by the Elithion Lithiumate. During this update, the cell boards transmit their voltage and temperature measurements using a proprietary serial communication protocol. Despite using shielded cable, it was found that the interference from the inverter distorted the serial communication, thus prompting the master unit to declare a communication failure. If the communication failure persisted for longer than 25 seconds (which was the maximum fault delay that could be programmed) the master unit would declare an AMS fault and the vehicle's shutdown procedure would disable the tractive system.

Analysis of the fault status message, sent by the master unit over CAN, revealed that the communication faults (designated Fault Code 3) occurred immediately when the drive stage of the inverter was enabled. As the message only indicated the status of the whole system, it could not be determined which banks were failing. Furthermore, the inverter and accumulator were an interference fit within the chassis, and it was impossible to remove the lid of the accumulator to probe the communication lines with an oscilloscope. The only diagnostic tool available was Elithion's computer-based graphical user interface. Figure 6.5 is a screenshot of the interface which shows a communication fault occurring on cell bank 7 (red text box with "0" cell boards detected where there should be nine). It was observed that the faults occurred randomly throughout the accumulator; however, they were more common in the two modules directly below the enabled sub-inverters.

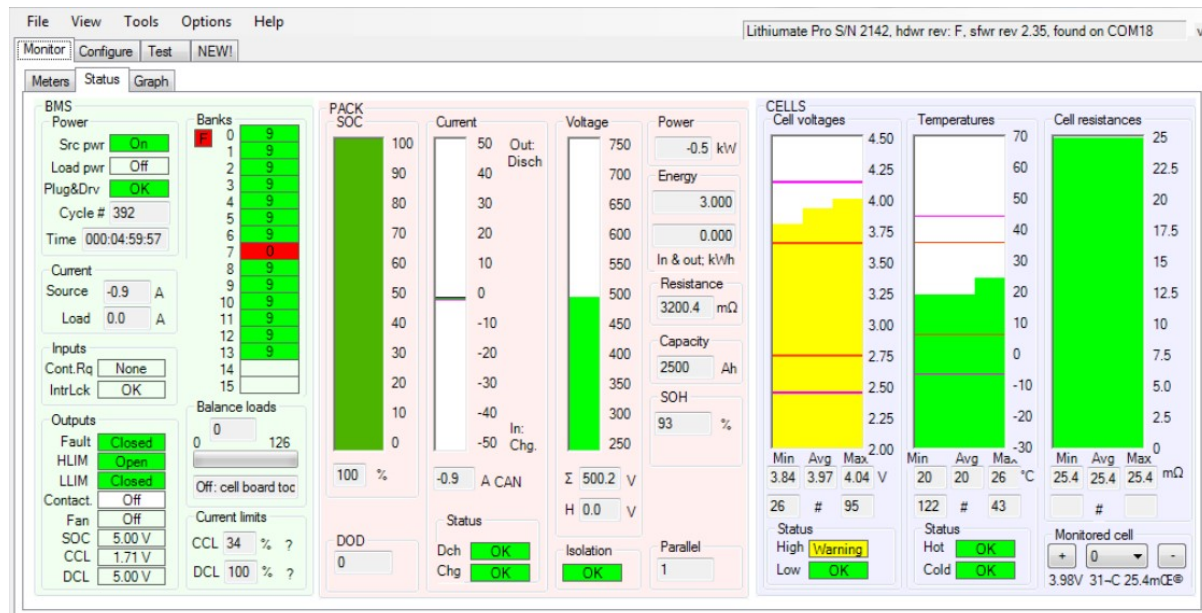


Figure 6.5. Screenshot of Elithion AMS graphical user interface showing a communication fault on cell bank 7 (red box with zero cells detected)

Further testing showed that the rate of communication failures was inversely proportional to the speed of the motors when tested under no load⁴². An attempt was made to quantify this observation; however, the CAN data showed a consistent fault, and recording the observations of the graphical user interface was not feasible. Driving the motors as soon as the inverter was enabled increased the time before an AMS fault was called (in some instances the car would drive for minutes without issue). However, the introduction of tighter corners on the test track resulted in an AMS fault if the driver could not traverse them quickly enough.

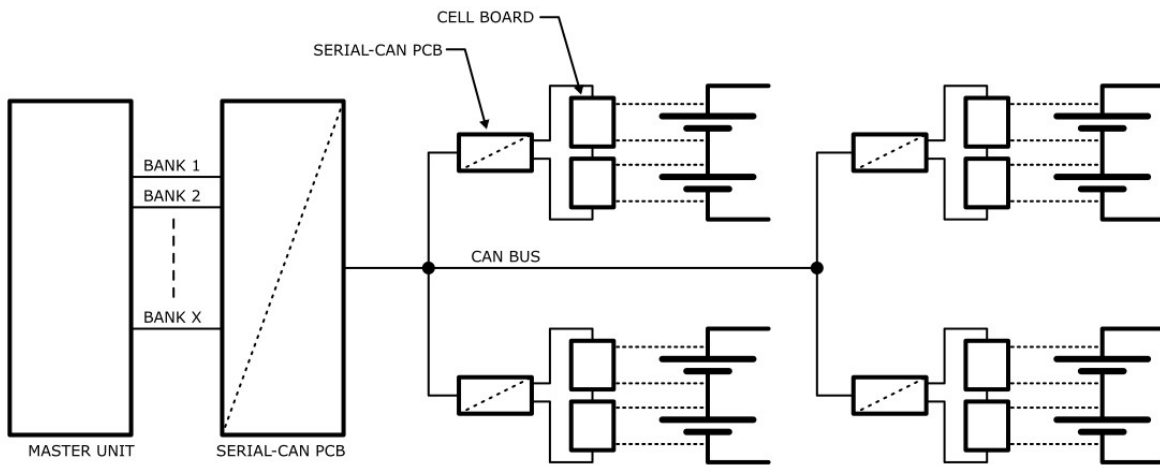


Figure 6.6. Concept diagram of serial-to-CAN interference solution

Two solutions were considered to this problem. The first was to design a bi-directional serial-to-CAN network that would convert the serial messages, from either the cell boards or master unit, to CAN messages for transmission over the length of the accumulator (Figure 6.6). This would have also had the benefit of reducing the communication wiring within the accumulator to a single twisted pair. Figure 6.7 is an oscilloscope plot (Agilent Technologies model DSO-X 2012A) of the CAN bus directly at the low voltage connector of the accumulator when the inverter drives were enabled at standstill. Channel 1 (yellow trace) shows the positive differential component of the CAN messages, and Channel 2 (green trace) the negative. The *CAN bus decode* mode of the oscilloscope (blue overlay at the base of Figure 6.7) shows that the captured messages were transmitted error free, thus suggesting the solution was feasible. An error would be indicated in red.

The major issue with this concept, however, was the considerable amount of design time that would have been dedicated to developing the system. Elithion were not cooperative in providing any details about their proprietary communication, so the first hurdle would have been reverse-engineering the serial protocol. The second hurdle would have been developing the associated electronics to first interface with the Elithion hardware, and then fit within the already restricted confines of the assembled accumulator. For these reasons, a software-based solution was implemented.

⁴² Vehicle raised on a stand with rear wheels unrestricted



Figure 6.7. Oscilloscope plot of CAN bus at the output of the accumulator with inverter drives enabled

The Lithiumate AMS can be controlled by a set of 1500 OBII-PID (On-board Diagnostics Parameter ID) codes, which are sent via CAN. Of these codes, there is a self-defined *special function* that allows the output fault line of the master unit to be cleared. The microcontroller on the accumulator isolation PCB was therefore programmed to send the PID command every second, unless a fault code not corresponding to a communication error was sent in the fault status CAN message. In conjunction, the time delay of the AMS memory latch circuit on the shutdown PCB (refer to Section 5.2) was set to two seconds, thereby preventing the circuit from triggering prior to the fault line being cleared.

The software-based solution was implemented immediately and instantly prevented the AMS from disabling the tractive system due to a communication fault. Whilst it could be said that this solution was not ideal, as it ignored a known fault with the AMS, safe-guards were added to the monitoring software. One of these safe-guards was to monitor the voltages measured by the cell boards. A communication fault would result in the default value of 4.5 V being transmitted. If this default was detected, a counter would be incremented. If exceeded, the PID code would cease transmission, thus allowing an AMS fault to disable the tractive system.

6.2.2. EMI INTERFERENCE WITH CURRENT SENSOR

The Tamura 2SC0200K current sensor supplied by Elithion was extremely susceptible to interference from the inverter; to the point where the AMS assumed the car was drawing in excess of 500 A (in both directions). As with the communication problem, it was not possible to open the accumulator lid to measure the output of the sensor. Instead tests were performed using the LEM HASS 100-S current sensor intended for the shutdown PCB.

The tests were performed with the rear wheels freewheeling, and the accumulator replaced with the Chroma dc power supply. To maintain a consistent baseline, it was attempted to keep the current draw of the inverter at 10 A, based upon the current measurement on the Chroma's digital display. Figure 6.8 is an oscilloscope capture (Agilent Technologies model DSO5012A) of the HASS 100-S output when the sensor was placed at the output of the Chroma, approximately 1 metre away from the inverter. Initial observation indicated four areas of interest, labelled A through D, on the oscilloscope plot of Figure 6.8.

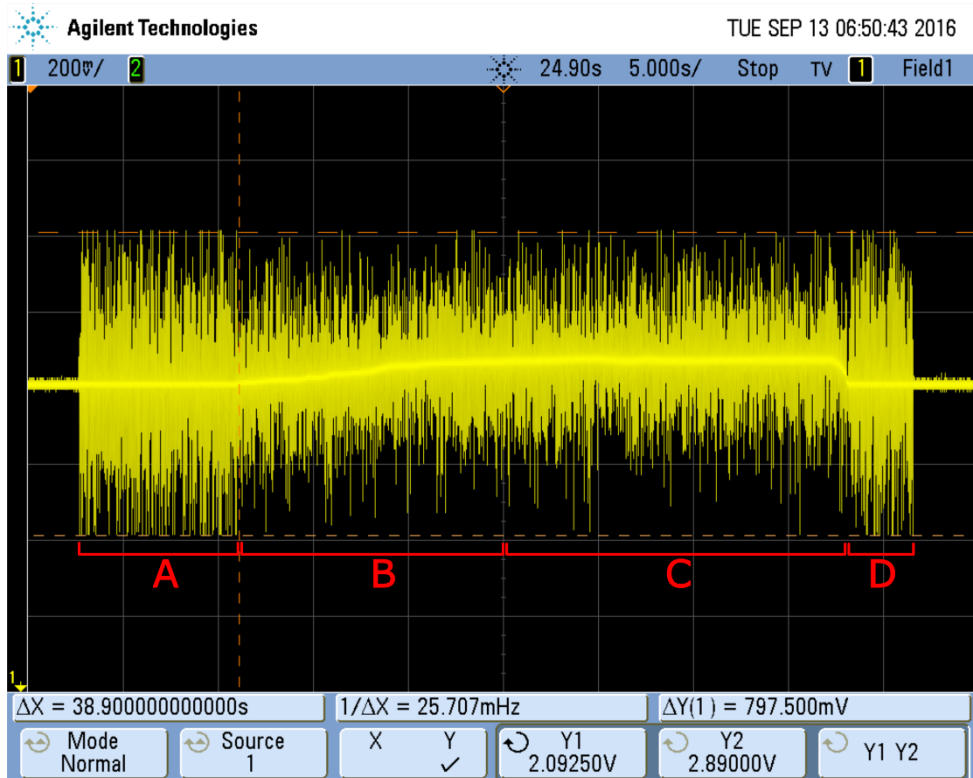


Figure 6.8. Oscilloscope plot of LEM HASS 100-S current sensor placed 1 m away from inverter

The oscilloscope capture was started after the inverter was precharged, whereupon it was waiting for confirmation from the VCU to enable the output drives. Section A is the period when the inverter was enabled but the motors were not rotating. The cursor data shows the measured noise to be 798 mV peak-to-peak. The motors were rotated at the start of Section B, indicated by the rise in voltage offset. The transition between Section A and Section B visually indicates the reduction in EMI from the inverter when the motors are operating. Section C shows the current draw to be relatively constant, and within the region of 10 A. It must be noted that the throttle was controlled by hand and visual feedback from the Chroma's display resulted in small oscillations that could not be avoided. Finally, Section D shows the drop in current as the motors are stopped, at which point the noise reverted to its original magnitude.

The same test was repeated with the HASS sensor placed on the outside surface of the accumulator, to best replicate the interference experienced by the Tamura sensor. Figure 6.9 shows that the magnitude

of noise doubled to approximately 1.4 V peak-to-peak for the motors at standstill, and marginally decreased once rotating.

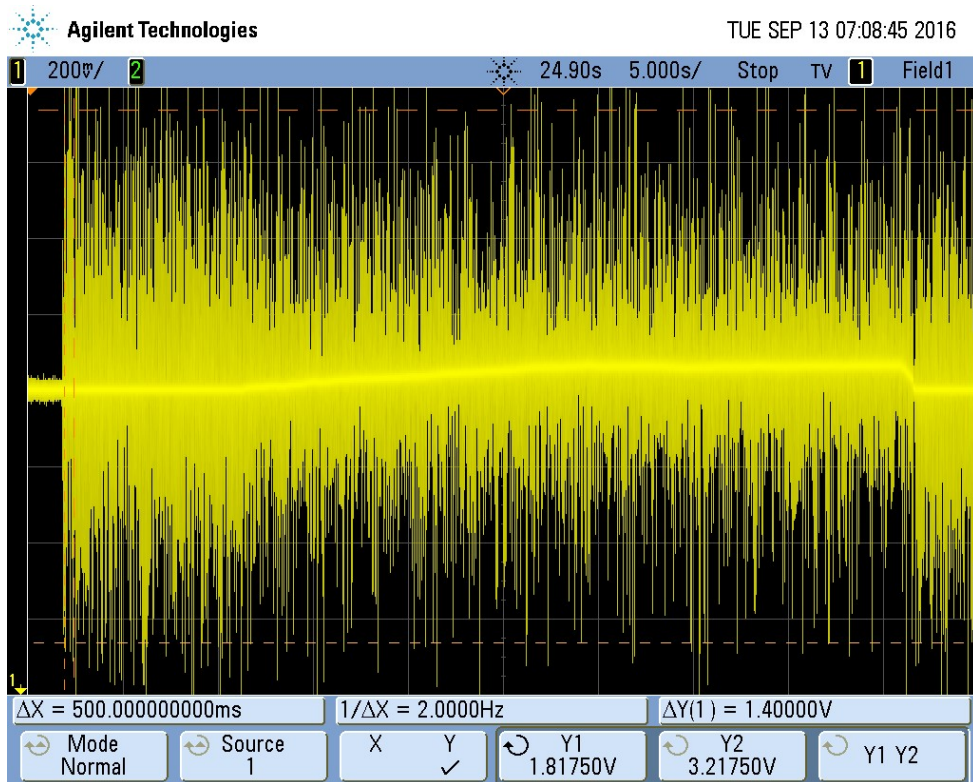


Figure 6.9. Oscilloscope plot of LEM HASS 100-S current sensor placed on accumulator container

The AMS requires an accurate current measurement to calculate the accumulator state of charge. Whilst state of charge can be determined based upon cell voltage, the Lithiumate AMS uses a combination of voltage tracking and Coulomb counting methods to provide an accurate representation. Instead of attempting to filter the output of the Tamura current sensor, the tractive current was measured by the Shutdown PCB and sent to the AMS via CAN.

An active 2nd order low pass filter was created on vero-board to quickly prototype the required cut-off frequency of the filter on the Shutdown PCB. The peaks of the waveform measured in Figure 6.9 were found to have a period of 400 μs ; therefore, equating to a frequency of 2.5 kHz. To fully attenuate the high-frequency component of the waveform, the cut-off frequency of the low pass filter was selected as 2.3 Hz (1000 times less than the frequency of the noise). Figure 6.10 (captured using an Agilent Technologies model DSO-X 2012A oscilloscope) shows the input and output of the low pass filter with a cut-off frequency of 2.3 Hz. The filter reduced the magnitude of noise considerably with a negligible delay in response when the motors were pulsed (shown by the oscillations towards the end of the captured waveforms).

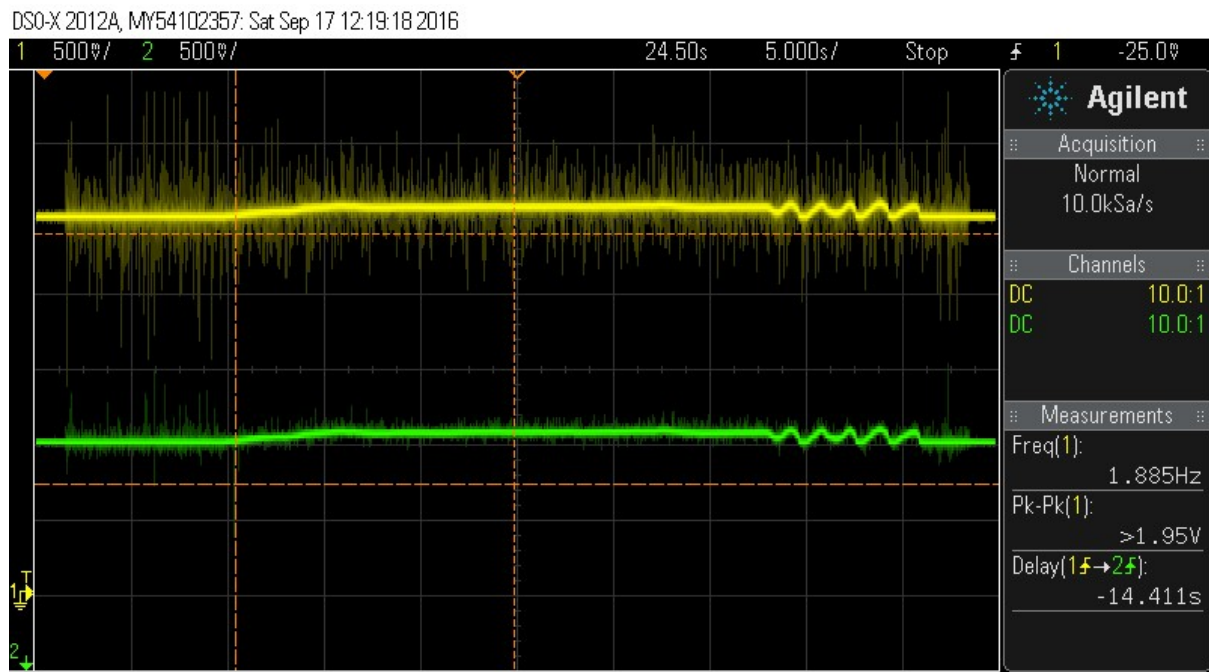


Figure 6.10. Oscilloscope plot showing input (yellow trace) and output (green trace) of 2.3 Hz cut-off LPF

The current sensor calibration was validated by comparing the measured current sent by the Shutdown PCB over CAN with a Digitech QM1563 current clamp. The race car was attached to the dynamometer to provide external loading to the drivetrain, and powered by the accumulator (to exceed the power limitations of the Chroma dc supply). Firstly, the output of the sensor was zeroed for no current draw by adjusting the reference voltage potentiometer on the Shutdown PCB. From there, the throttle was manually adjusted to increase the tractive current in increments of 5 A, based upon the current measured by the Shutdown PCB. At each increment, the output of the current clamp was recorded.

It was not possible to safely measure the tractive current greater than 60 A, as the dynamometer load could not be accurately controlled, causing the testing rig to shake violently. Lack of time meant developing a more robust solution was not feasible. The results were therefore extrapolated to predict the response of the sensor over a 0 – 180 A range, as shown by Figure 6.11. Whilst the extrapolated data indicated the current measurement will deviate from the actual tractive current as it increases, the difference equates to only 1.03% at 180 A. Due to time constraints and more important issues, this was deemed acceptable, and was not worth pursuing further.

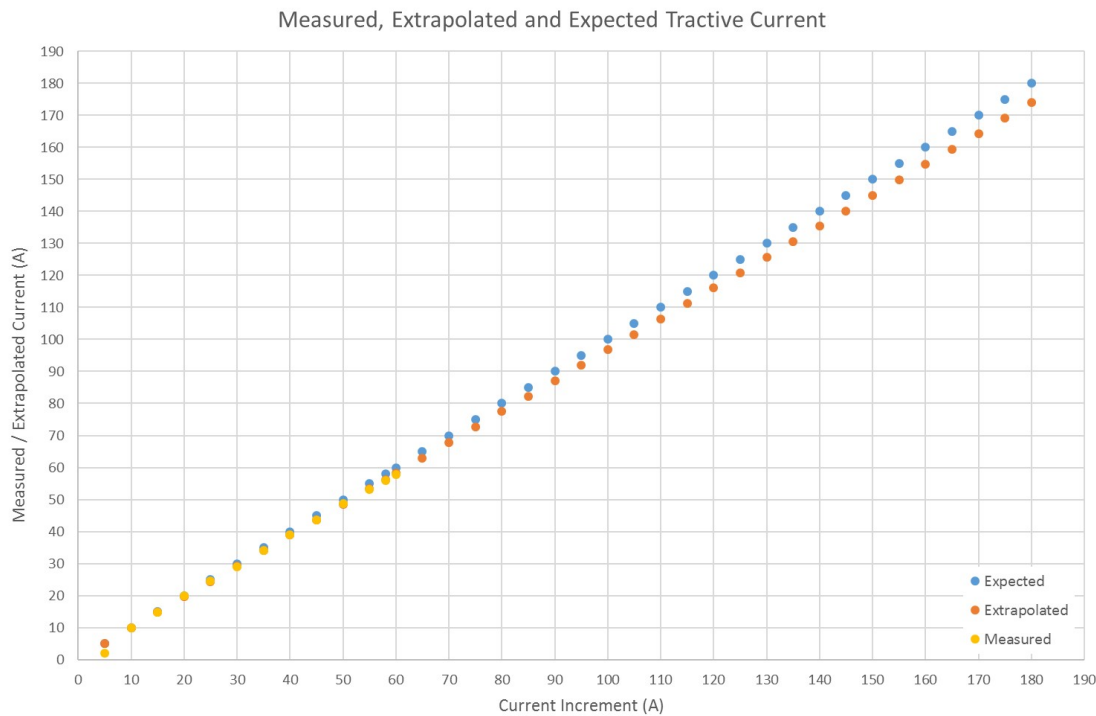


Figure 6.11. Plot of measured, extrapolated and expected tractive current

6.2.3. ACCUMULATOR CONDITION

Over the duration of testing the car in RWD, the accumulator was plagued with individual cells failing and becoming under-voltage when under load, prompting the AMS to declare a fault. A failed cell never fully recovered, and had a resting voltage consistently lower than the average cell voltage of the accumulator. If not addressed, the problem would get to the point where the car would be in a perpetual state of shutdown, and the tractive system could not be enabled. Much of the RWD testing was therefore spent replenishing the accumulator with modules that had the failed cells replaced with brand new cells. Since the cells were in a welded parallel configuration, the entire row had to be replaced, as it was not possible to determine which cells were faulty.

The cells would fail randomly throughout the accumulator and could not be pre-empted. An attempt was made to track the condition of the cells by analysing their rate of change in voltage when charging. The assumption was that a cell which would not accept charge as readily as the surrounding cells had a higher internal resistance, presumably indicating a potential failure. However, this theory was quickly disproved when cells that charged without issue failed under load. The only method of detecting a failed cell, was to pulse the motors when the wheels were unrestricted, and monitor the cell voltages using the Elithion graphical user interface.

Several theories were suggested as to why the cells failed. The most likely were the use of the home-made resistance welder, and the lack of preconditioning. Preconditioning involves gradually charging

and discharging the tractive pack under light loads to allow the batteries to achieve a uniform state of charge. This was neglected when testing the accumulator due to the pressing time constraints of the project. Another theory suggested that the cells were initially faulty from the supplier. However, a random sample of cells were tested prior to the accumulator being assembled, to ensure they performed as expected (based upon the datasheet).

As the car was tested more extensively, the condition of the accumulator became so bad that the modules could not be repaired fast enough. To continue testing, the team was forced to remove modules from the accumulator (without replacing them) and run the car at a lower tractive voltage. Consequently, the increased usage accelerated the rate of failure; eventually leading to the car operating for a maximum of a few minutes (at a very reduced pace) before stopping.

6.2.4. PULSE INJECTION FROM DC/DC CONVERTER

Whilst making amendments to the VCU a large fluctuation was measured on the output of the on-board 5 V regulator, with respect to the chassis ground. The chassis ground point was designated the front right mounting bracket for the accumulator, to which the grounds of all low voltage systems were star-connected. Figure 6.12, shows an oscilloscope plot (Agilent Technologies model DSO-X 2012A) of the measured fluctuation; where Channel 1 (yellow trace) is the 5 V output of the on-board regulator, Channel 2 (green trace) is the ground plane on the VCU PCB, and the pink trace is a mathematical function showing the difference between Channel 1 and Channel 2. The difference between the 5 V and ground planes shows that, whilst there is a very small oscillation, the pulses are in-phase and of equal

DSO-X 2012A, MY54102357: Thu Sep 22 23:37:38 2016



Figure 6.12. Oscilloscope plot showing Measured Disruptions of 5 V (yellow trace) and GND (green trace) planes on VCU PCB

magnitude (common-mode noise). This explains why the VCU continued to operate correctly, since all measurements (for example throttle position) were taken with reference to the local ground potential, and “floated” with the changing ground plane.

The source of the fluctuations was traced back to the Murata UWE-24/3-Q12 isolated dc/dc converter, which supplies the inverter with 24 Vdc. The converter was selected by a final year electrical engineering student, who also designed its application PCB. Through multiple tests, it was determined that the issue was directly related how the converter was wired⁴³, in which the input and output ground connections of the converter were joined. Although this voided the galvanic isolation of the converter, it should not have been an issue as both sides were low voltage. However, connecting the two potentials made the converter unstable and enter a version of its input protection mode, where it would pulse its output.

Since the AMK inverter has an isolated power input stage, along with isolated inputs and outputs (including CAN transceivers), rewiring the dc/dc converter resolved the problem immediately (without the need to reconsider a reference ground between the inverter and VCU).

6.3. TRANSITION TO 4WD

The transition from RWD to 4WD provided the opportunity to make some much needed improvements to the initial electrical design. This section details the improvements, as well as key elements of the final design and build.

6.3.1. VEHICLE CONTROL UNIT REDESIGN

One of the most important revisions that needed to be made was the vehicle control unit. The first revision had significant hardware errors that had been made during the design process, and were not detected until after the PCB had been manufactured. Having a working vehicle also allowed the quantity of each peripheral to be readdressed to reduce size and complexity.

The redesign was a collaboration between the author and an undergraduate electrical engineering student. The pseudo-circuits and reference designs were provided by the author, and the PCB design was completed by the student. Emphasis was placed on making each peripheral multi-purpose with the population (or absence) of components. The following is a brief description of the major design changes made to the VCU (Figure 6.13).

⁴³ To clarify, this was the responsibility of the author.

- The STM32F7 was replaced with an STM32F429ZIT6 microcontroller. Since the F7 was a relatively new microcontroller series, STMicroelectronics only provided the HAL (Hardware Abstraction Layer) code libraries, as opposed to the Standard Peripheral libraries used by the F0, F1 and F4 series. Although the two libraries share similarities, time was wasted learning how to implement functions using the HAL library, that were well known to the author with the Standard Peripheral alternative. In addition, the large majority of online support used only the Standard Peripheral library.
- The MCP2515 stand-alone SPI CAN controller was replaced with an STM32F042 microcontroller and CAN transceiver for the third CAN bus peripheral. There was no support library for the MCP2515, thus requiring a custom library had to be developed (which ultimately became an unnecessary waste of resources). The replacement concept was to use the F0 as a bi-directional CAN to SPI converter for the main F4 microcontroller.
- A current detection circuit identical to that on the Discharge PCB (Figure 4.20), was included to check the continuity status of the Shutdown Circuit. Assuming all interlocks and switches were in their operating position, the VCU was the final controller for the Shutdown Circuit and therefore the tractive system (waiting for the driver to push the activation button). The inclusion of the current detector allowed an additional software-based interlock to be added to check if the Shutdown Circuit was continuous once activated. If the circuit did not become continuous within two seconds, the VCU disabled the tractive system and indicated a warning on the driver display. This feature prevented the risk of a faulty component in the Shutdown Circuit from unexpectedly enabling the tractive system if the driver forgot to disable the circuit when out on track. It was also invaluable for fault-finding if an interlock or switch had not been reset along the Shutdown Circuit.
- A 3-axis accelerometer and 3-axis gyroscope were added in anticipation that they would be used as inputs to the torque vectoring algorithm (Section 7.1.2). Due to time constraints, these were never implemented in the final operation of the vehicle.

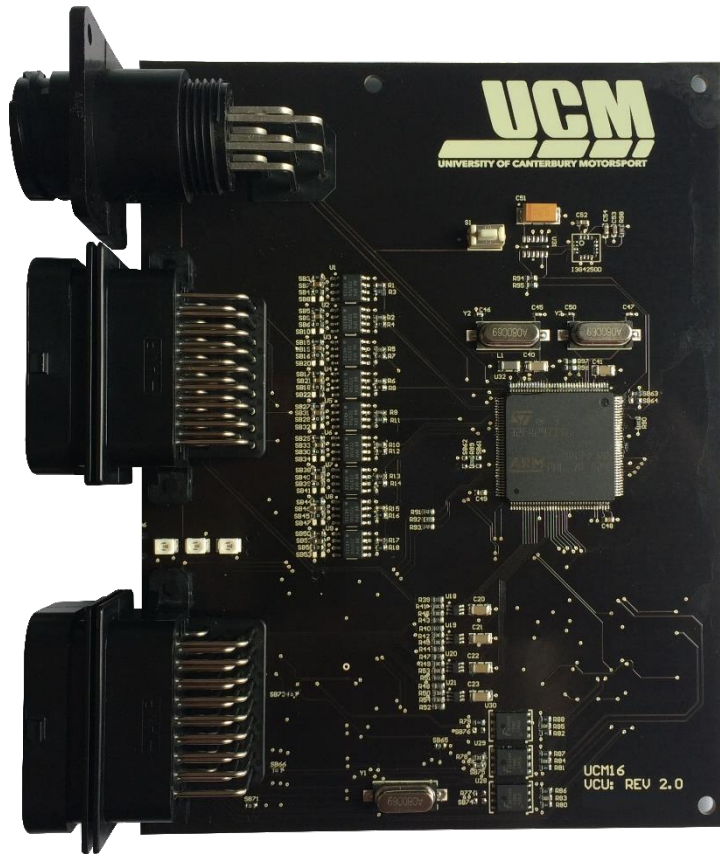


Figure 6.13. Image of assembled VCU PCB (Revision 2)

6.3.2. MOTOR WIRING

Both the front and rear motors had to be wired (rewired in the case of the rear motors) and sealed appropriately. When the rear motors were initially wired, an order of Raychem ATUM heat shrink had not arrived, meaning the motors could not be properly sealed. Figure 6.14 is an image of the individual components required to wire the front left motor. The motors were wired identically, such that the rear motors could be replaced by the front motors if the worst-case scenario occurred, where the car needed to be reconfigured to rear-wheel drive if more than one of the motors failed.

The small diameter of the motor cable meant an unconventional approach had to be taken to accommodate the Souriau 8STA aerospace connector. Firstly, copper sleeves had to be custom-machined to reduce the inner diameter of the power pins for each 4 mm^2 phase of the motor cable. The 8STA connectors were already supplied with copper sleeves, which did not give a sufficient reduction, so the custom sleeves were machined to fit within the supplied sleeves.

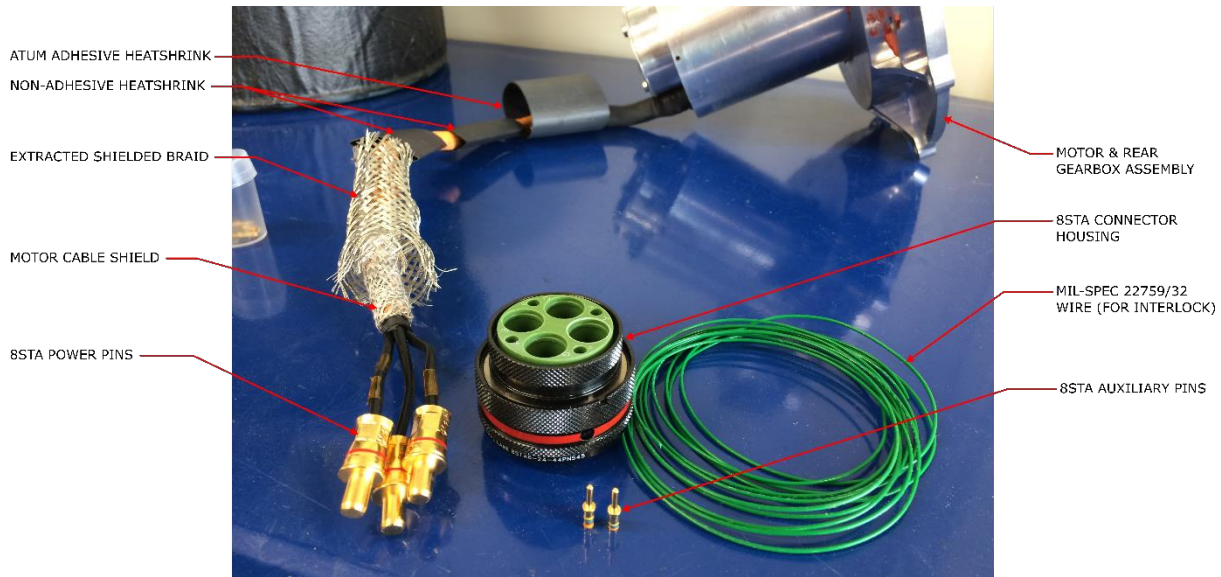


Figure 6.14. Image of individual components for motor wiring

The shield of the motor cable could not be stretched over the rear lip of the 8STA connector. To reduce the radiation of electromagnetic interference the shield must remain continuous from the motor to the inverter. The solution was to extract a section of shield from a larger motor cable and append it to the shield of the motor cable. Figure 6.15 is an image of the assembled shield. High-temperature rated Kapton tape was used to constrict the extracted shield over the perforations on the connector lip, and ensure a connection to the motor cable shield. At this point, the motor connector interlock was installed by creating a small loop between two of the auxiliary positions on the 8STA connector.



Figure 6.15. Image of assembled shield for motor connector

Figure 6.16 shows the final assembly of the motor connector. The lip of the connector was sealed using 40 mm diameter Raychem ATUM heatshrink. ATUM heatshrink is an adhesive heatshrink series manufactured by TE Connectivity with a shrink ratio of 4:1, thus making it ideal for sealing large diameter circular connectors. Through experimentation it was found that the ideal length of unshrunk ATUM was 45 mm. This ensured the heatshrink had enough coverage of the cable assembly post-shrink, whilst remaining short enough that it would not reduce overall flexibility post-connector.



Figure 6.16. Image of assembled motor connector

6.3.3. INVERTER RECONFIGURATION

When the inverter was first configured for RWD testing, it was less time consuming to only use one half of the inverter, as the low voltage wiring is shared for each half. Figure 6.17 shows the left side of the inverter after it was rewired for 4WD (further images are in Appendix M). The orange tractive cable at the bottom of Figure 6.17 is the cable for the front left motor, which is controlled by the rear sub-inverter (left-most sub-inverter). All tractive cabling was contained within clear Q-150K heat shrink; otherwise orange heat shrink would have been required as the outer layer (to indicate the cable is part of the tractive system).

The only connection made between either half of the inverter was the EtherCAT communication cables, which were daisy-chained together between sub-inverters. This meant only one RJ45 cable was required for the AIPEX Pro software to configure all the inverters simultaneously. This increased the usability of the powertrain, as not only did it reduce the time needed to make changes to the sub-inverter parameters, but it allowed the status of all sub-inverters to be diagnosed concurrently.



Figure 6.17. Image of wiring on right side of inverter

The wiring was commissioned in a similar setup to that described previously in Section 6.1.2; only with the new revision of the VCU. Firstly, the Chroma dc power supply (with a current limit of 1 A) was used to power the high voltage wiring to check for short circuits. Following this, the motor wiring was validated incrementally using one of the rear motors and the accumulator. The front motors were also commissioned with their new gearbox assemblies, in which they were run continuously at 1000 rpm for an hour⁴⁴.

Due to the compactness of the chassis, it is not pragmatic to show an image of the inverter mounted in UCM16. Instead, Figure 6.18 shows the location of the inverter (and accumulator) in the CAD model.

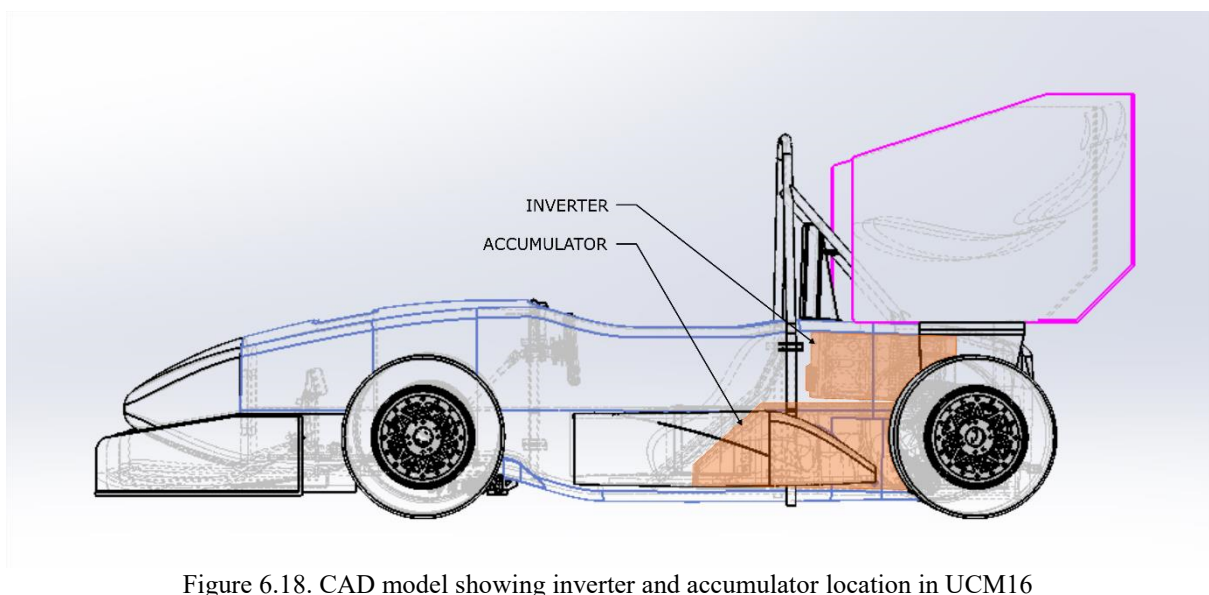


Figure 6.18. CAD model showing inverter and accumulator location in UCM16

⁴⁴ This was the testing procedure given by the gearbox designer.

6.3.4. DC/DC CONVERTER REDESIGN

The Murata UWE dc/dc converter has a maximum capacitive load rating of $1500 \mu\text{F}$ [71], which is equal to the stated capacity of the inverter's low voltage switch mode power supply [50]. However, the inverter datasheet was misinterpreted; in that the capacity refers to the power supply for each half of the inverter (two sub-inverters per half), therefore meaning the total load capacity of the dc/dc converter is $3000 \mu\text{F}$. This mistake was only discovered when the inverter's low voltage systems were tested after being rewired, and the converter pulsed its output.

Fortunately, a single UWE converter could be used if the low voltage systems were enabled in stages. Initially this was achieved by manually delaying the connection of the driver's left low voltage connector upon power up. However, as this required the author to be present at the car this had to be remedied in case the car needed to be restarted on track. The solution was to redesign the dc/dc converter PCB and add a delay to the power supply on the driver's left half of the inverter⁴⁵. The delay had to be implemented to the left half of the inverter because it includes the output driver stage of the daisy-chained EtherCAT communication. Experimentation showed that communication to all the sub-inverters could only be achieved if the output driver was powered last.

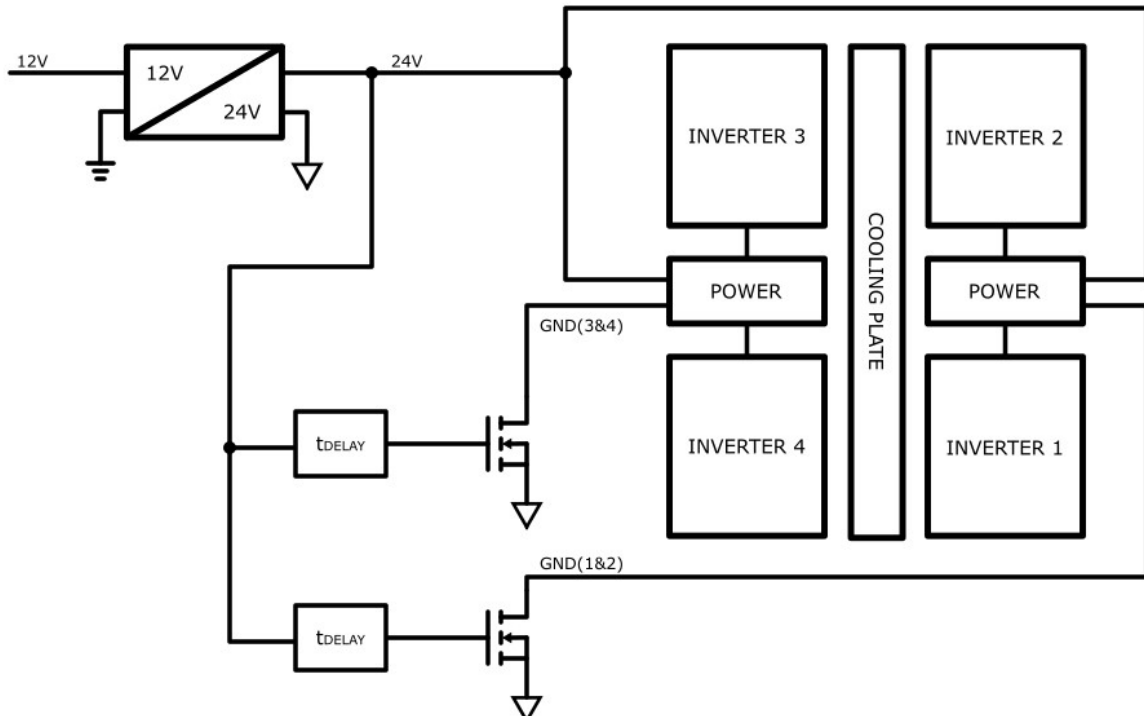


Figure 6.19. Simplified circuit diagram showing dc/dc converter with delayed ground switches

⁴⁵ Whilst this is not the most elegant solution, sourcing a dc/dc converter capable of regulating a $3000 \mu\text{F}$ load (or even a second UWE converter) would have delayed the project's progress further.

The initial dc/dc converter PCB had already been packaged within the chassis when the problem was discovered. Thus, the redesigned PCB had to have the same dimensions as its predecessor. Two identical RC timer circuits (using the same reference design as previously explained PCBs) with N-channel MOSFET switches were appended to the underside of the PCB (see Appendix N for schematic). A simplified diagram of the updated circuit operation is illustrated by Figure 6.19, where the MOSFET switches are used to independently switch the grounds of the inverter power supply. To remove the need for an isolated gate driver, the timer circuits were powered from the 24 Vdc output of the converter using a 24 V to 5 V linear voltage regulator. Figure 6.20 is a screenshot of the PCB for the redesigned dc/dc converter, the final assembly of which was installed and tested once the race car was in Australia.

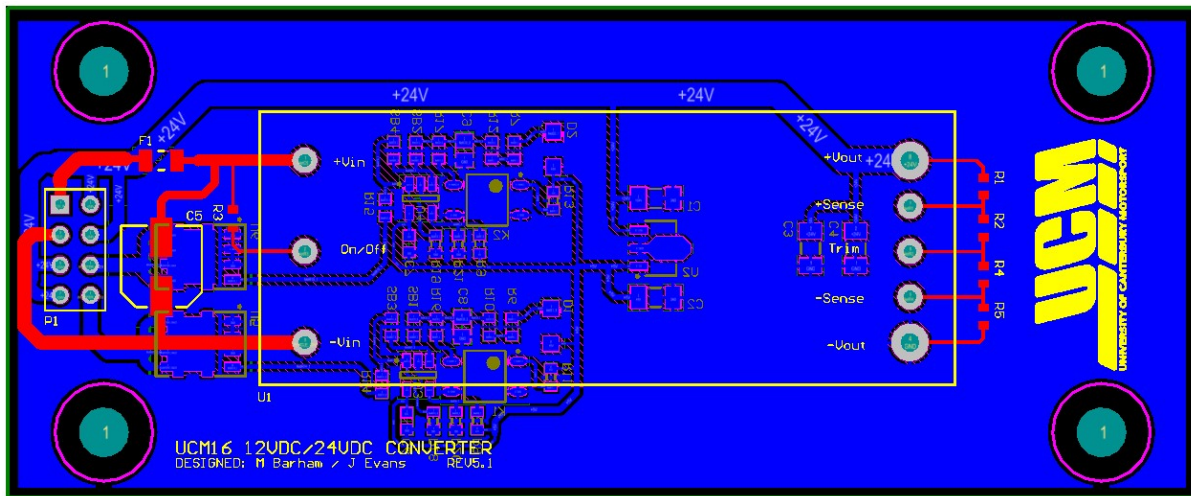


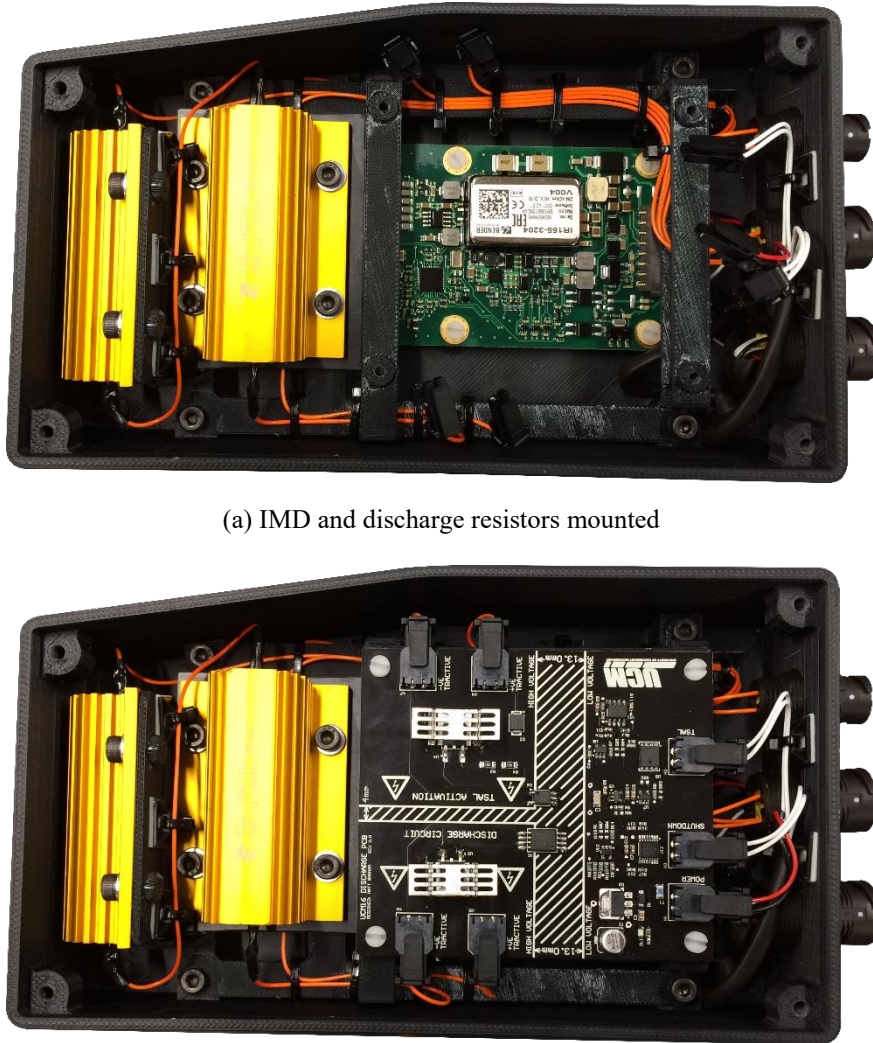
Figure 6.20. Screenshot of redesigned dc/dc converter PCB

6.3.5. DISCHARGE PCB AND IMD REPACKAGING

The intended location for the Discharge PCB and IMD was on the rear bulkhead of the chassis, just above the opening for the accumulator. However, due to the presence of the inverter connectors and cabling in this region, the PCBs were temporarily relocated behind the driver's headrest for RWD testing (the yellow-lid enclosure in Figure 6.4). Due to the risk of having cables carrying tractive voltage outside of the confines of the chassis, the location was revised to the rear-left corner of the chassis.

Figure 6.21 shows the assembly of the circuits within a 3D printed enclosure⁴⁶. The enclosure was designed to allow individual components to be easily replaced, without the need for rewiring. As shown by Figure 6.21(a), the IMD PCB is mounted to the base of the enclosure. The discharge PCB and associated resistors are mounted to a removable tray which is separated from the IMD using laser-cut Formex insulation.

⁴⁶ Enclosure designed by UCM's Lead Powertrain Engineer, assembled by author.



(b) Assembled Discharge PCB and IMD enclosure
Figure 6.21. Images of Discharge PCB and IMD enclosure

6.3.6. ACCUMULATOR REVISION

Following the failure of the first accumulator, a completely new accumulator was manufactured. Since the cause of the cell failure had yet to be identified, an attempt was made to mitigate all potential causes; by sourcing cells from a different supplier, welding the cells using a dedicated battery resistance welder, and preconditioning the cells once assembled. Several mechanical updates were made to the battery modules and layout of the components in the front of the accumulator. These changes will be mentioned briefly for completeness of this thesis; although it should be noted that the author had minimal input with the design.

Figure 6.22 is an image of the updated battery module. The previous frame material (acrylic) was found to be too brittle for its high vibration environment, and was replaced with 5 mm laser-cut nylon. Subtle changes were also made to the previously weak structures used to attach the AMS cell boards and

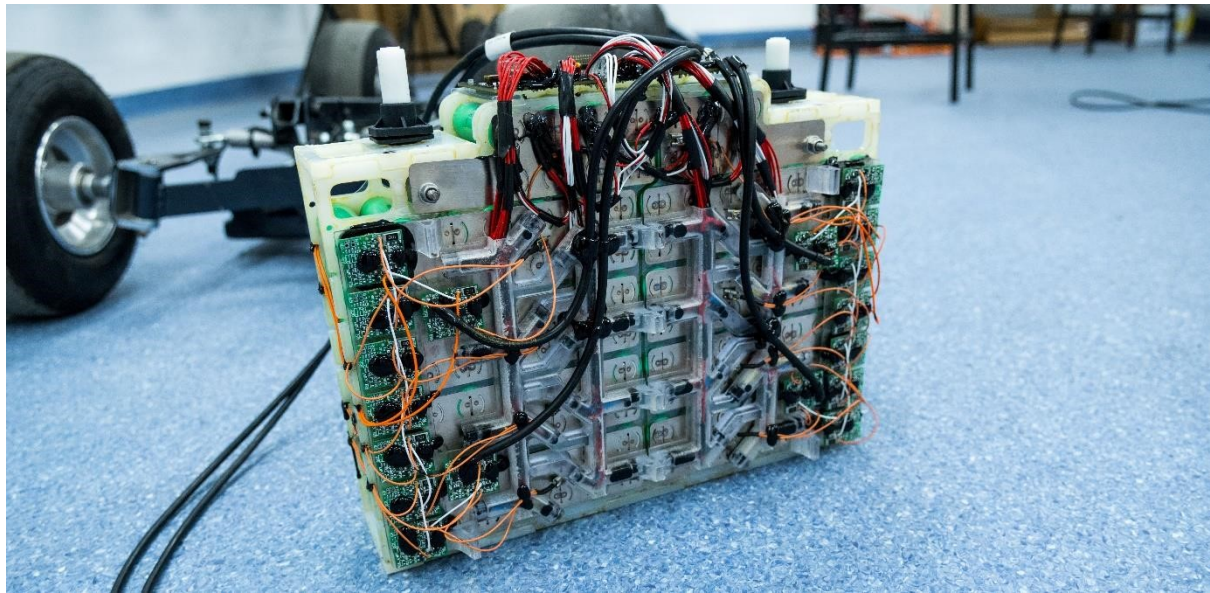


Figure 6.22. Image of revised battery module

Formex insulating cover. Whilst these improvements increased the durability of the modules, they became 5 mm taller (due to the addition of a baseplate), a change not noticed until they were fully assembled. Consequently, the vertical connectors on the Temperature Monitoring PCBs could not fit under the lid of the accumulator, and the cables had to be hard-wired to the PCBs.

Hard-wiring the cables removed the modularity aspect of the battery modules, as the cables had to be cut to a fixed length based on their position in the accumulator. In addition, solder joints are affected significantly more by vibration than a connector assembly, which caused numerous connectivity issues between the AMS cell boards and the master unit⁴⁷ during the early commissioning of the modules. This was eventually mitigated by encapsulating the cable joints with high temperature thermal adhesive.

Figure 6.24 is an image of the final assembly of the revised accumulator. Seven battery modules were successfully fitted, increasing the maximum tractive voltage to 529.2 Vdc (7p126s cell configuration). The layout of the front-end was also updated, and featured a removable 3D printed structure that allowed the components to be wired outside of the accumulator container. Electrically, only one change was made between the previous and current accumulator designs. A review of the continuous current limits of the tractive components indicated the 100 A rated tractive fuse had to be replaced with an 80 A equivalent. This was to remain rule compliant (EV6.1.1) as the current rating of each Souriau 8STA power pin (size 4) is 80 A [72].

The accumulator was preconditioned to preserve the health of the cells. This repeating process involved fully charging the accumulator prior to its first use, and then depleting the pack charge to approximately 80% under a light load. Whilst it would have been advisable to precondition the accumulator in a

⁴⁷ The communication cables for the AMS were hard-wired (intended) to the Temperature Monitoring PCB, which was used as a platform for a connector.

controlled environment using a set resistive load, time constraints meant the process had to be completed in-vehicle; thus, allowing other aspects of the car to be tested simultaneously. The cell voltages were tracked during preconditioning using the AMS's cell voltage histogram (Figure 6.23).



Figure 6.23. Screenshot of Elithion AMS graphical user interface showing histogram of present cell voltages measured by each cell board (right window)



Figure 6.24. Image of revised accumulator assembly

6.3.7. WIRING HARNESS

Transitioning to 4WD required a new low voltage wiring harness to be constructed, as most components changed location within the chassis. The harness was planned by segregating the chassis into regions that required cabling, along with an estimation of length. A cable list was then created which documented the start and end location of each cable; along with cable type and layer position in the concentric twist. Figure 6.26 is a plan-view diagram showing the branch paths of the low voltage loom in UCM16. It should be noted that the Shutdown Circuit wiring has been omitted, as it was previously illustrated in Figure 5.2 (Section 5.1).

The change in location of the Discharge PCB, and addition of the front motors, required the tractive system to be rewired. Figure 6.26 shows the position of the tractive cables in UCM16. Miscommunication between sub-teams meant the HVD had to be located on the left side of the chassis, as there was no longer sufficient space on the right (the HVD's intended location). Since the high voltage on the accumulator was on the right-hand side, the battery cables had to transition across the chassis (behind the driver's seat). Two 10 mm² cables were used per pole of the accumulator to match the output connector of the accumulator.

The junction box (Figure 6.25) houses two posts which are used as a busbars for reducing the 10 mm² tractive cables to 0.32 mm² cables for the Discharge PCB and IMD. The junction box also houses the discharge fuses and tractive current sensor, which is connected to the adjacent Shutdown PCB.

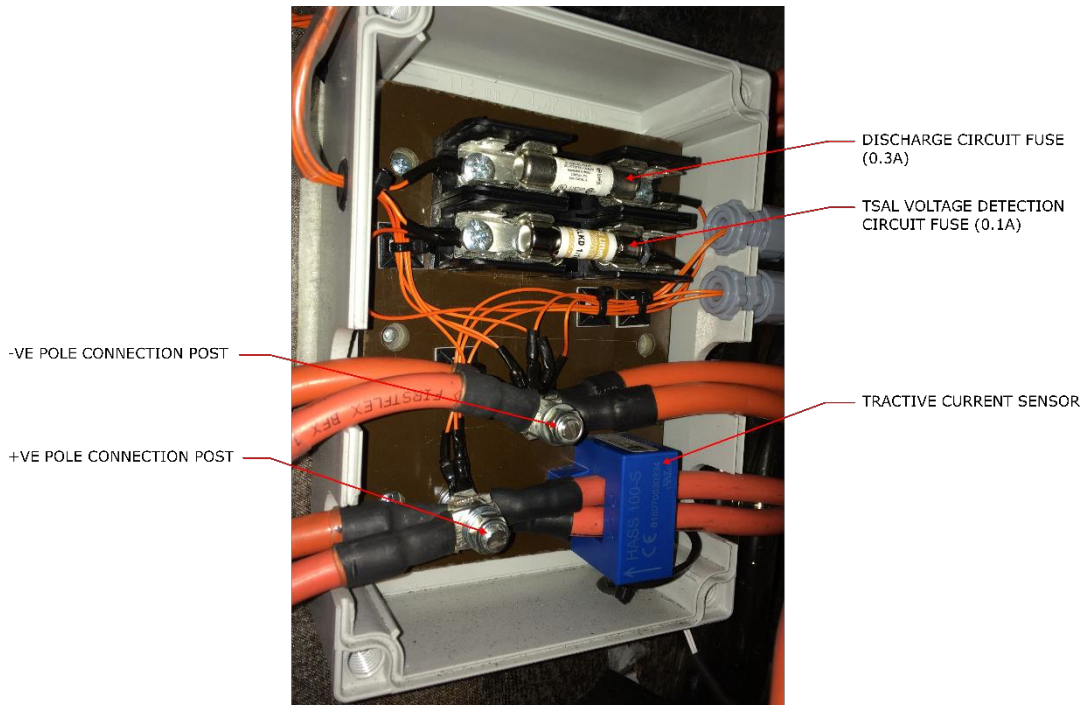


Figure 6.25. Image of junction box mounted in UCM16

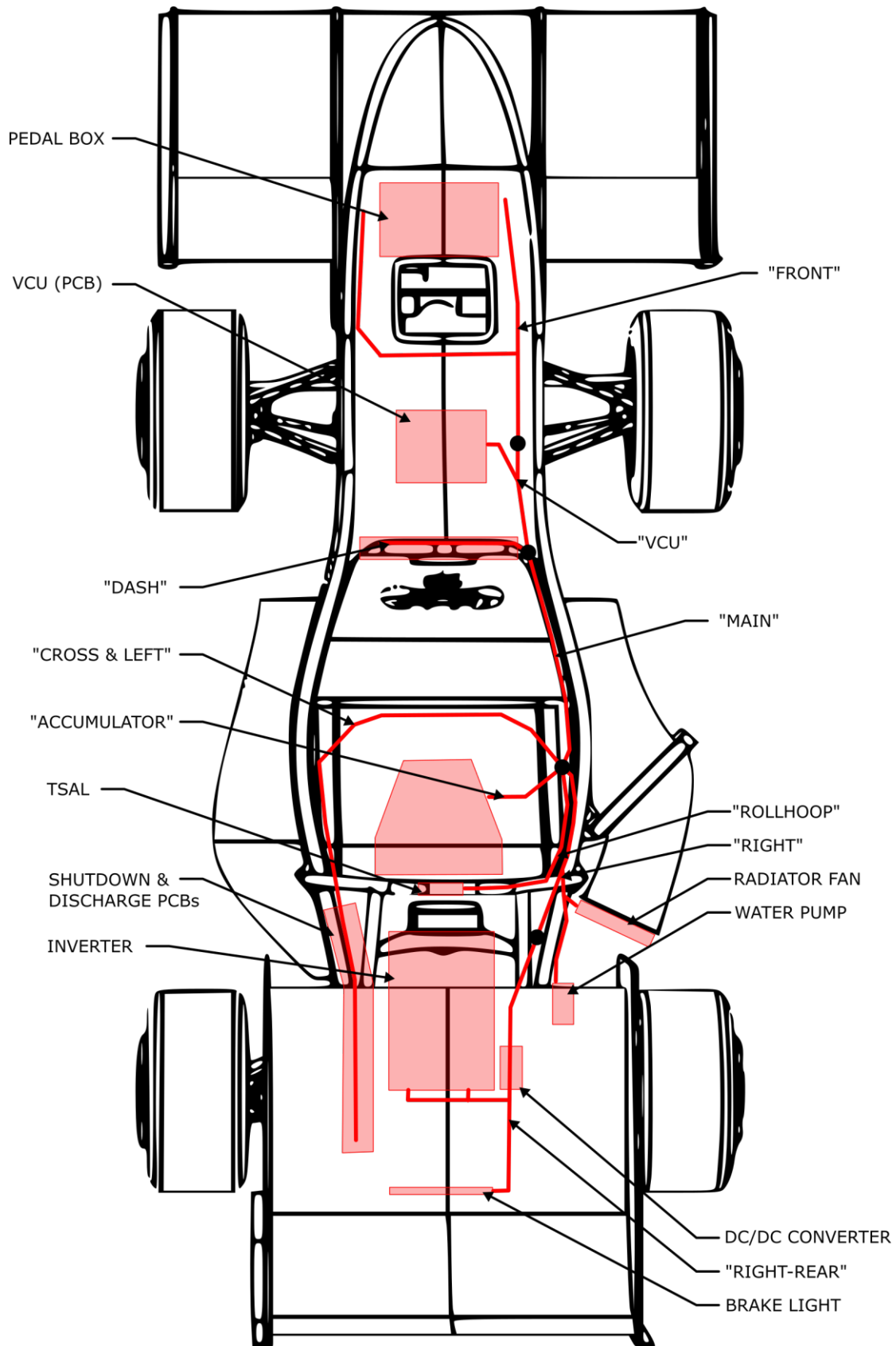


Figure 6.26. Diagram of low voltage routing paths

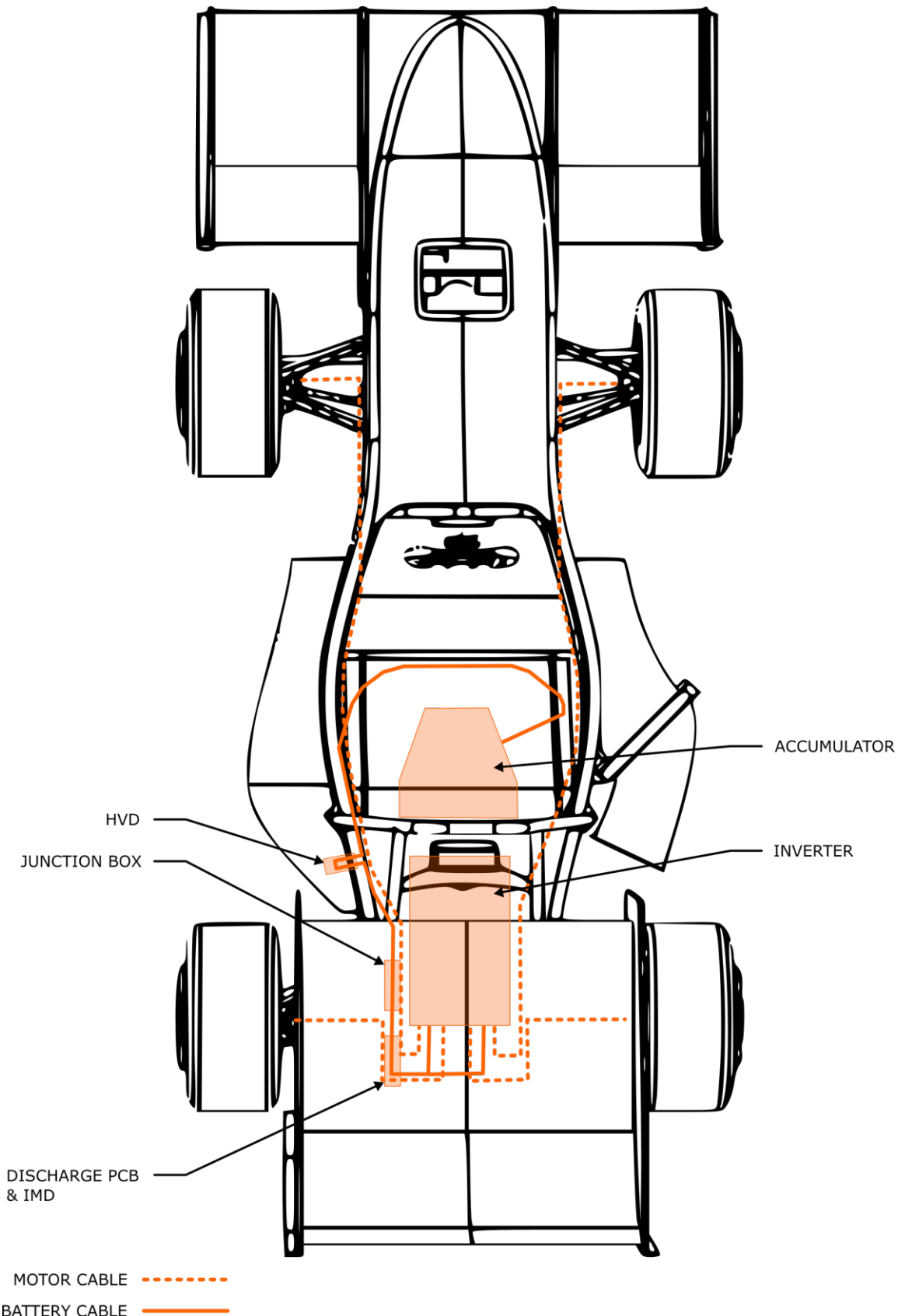


Figure 6.27. Diagram of tractive system routing paths

6.3.8. PRECHARGE PCB REDESIGN

Whilst the first revision of the Precharge PCB successfully precharged the intermediate capacitor throughout the testing sessions, there were a few issues that needed to be fixed prior to the competition in Australia. The schematics for the redesigned Precharge PCB are documented in Appendix O.

A rule clarification with the FSAE-A rules committee indicated that the isolation of the AIRs was sufficient for EV4.1.4⁴⁸, as the location of the barrier is not explicitly stated in the rules. However, a review of the NKE1205 dc/dc converters, used to provide 5 Vdc to the tractive-side components, revealed that the converters are not intended to be the sole source of isolation. A technical note in the NKE datasheet mentions the isolation barrier is intended for transients, and a continuous overvoltage should be avoided [73]. To resolve this, an S24SEI2002PDFA isolated dc/dc converter was included to create an isolation barrier between the low voltage electronics of the Precharge PCB and the Shutdown Circuit. The dc/dc converter circuit is identical to that used on the Accumulator Isolation PCB. The converter was validated using the first revision of the Precharge PCB prior to the design being updated.

The changes made to the accumulator voltage during the RWD testing period highlighted the unnecessary complexity of the precharge control system. The resistor dividers used to compare the voltage of the battery with that of the intermediate capacitor were not exactly equal. Each voltage change required the gains of the operational amplifiers to be adjusted slightly to recalibrate the 90% voltage threshold. Previous Formula SAE experience has shown that anything can go wrong at competition, and the circuit was therefore simplified as a precaution.

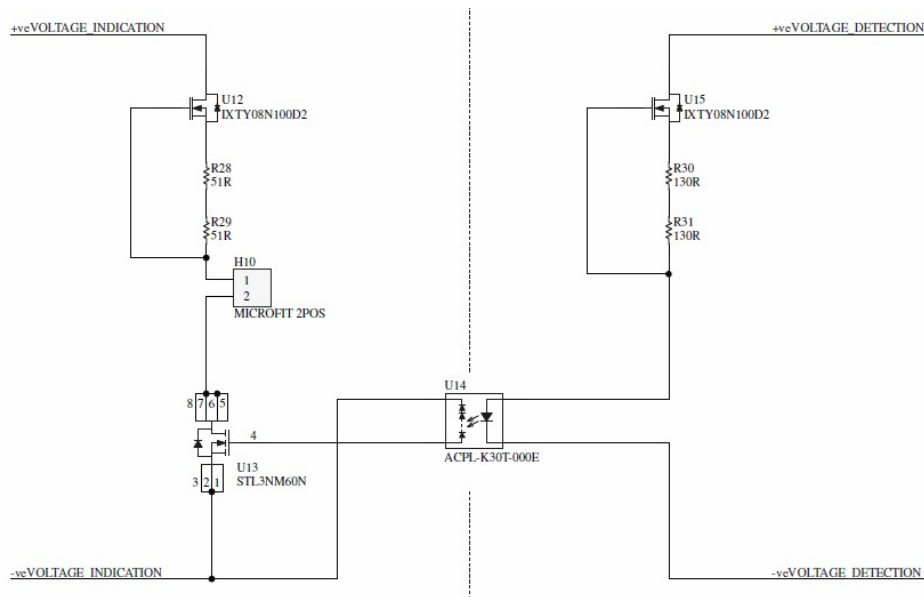


Figure 6.28. Schematic extract of voltage indication circuit redesign

⁴⁸ All low voltage systems in the accumulator container must have galvanic isolation for all connections to the outside of the accumulator container.

The voltage comparison circuit was added to the first revision of the Precharge PCB to counter the case where the precharge fuse blows prior to the intermediate capacitor being successfully charged. The same result can be achieved by only comparing the voltage after the precharge fuse to a fixed reference; in which an open circuit is indicated by a null measurement. As shown by Sheets 2 and 3 of Appendix O, the revised circuit utilised only half of the existing design.

Figure 6.28 shows the updated schematic for the accumulator voltage indicator. Since the previous indicators were deemed too dim, the circuit was redesigned such that an LED (connected to H10) could be powered directly from the battery. This removed the current constraint imposed by the precharge circuit, and allowed a larger range of LEDs to be used. The detection element of the circuit (right side of the isolation barrier in Figure 6.28) uses a depletion MOSFET constant current source to drive the input of an ACPL-K30T isolated gate driver. The ACPL-K30T controls the gate of a 600 V rated N-channel MOSFET (U13), which is used to switch the conduction path for the indicator LED. Current through the LED is regulated using a second constant current source.

Figure 6.29 is an image of the redesigned Precharge PCB. As the updated accumulator had already been assembled with the previous revision of the Precharge PCB, the dimensions and mounting hole locations had to be preserved for cross-compatibility.

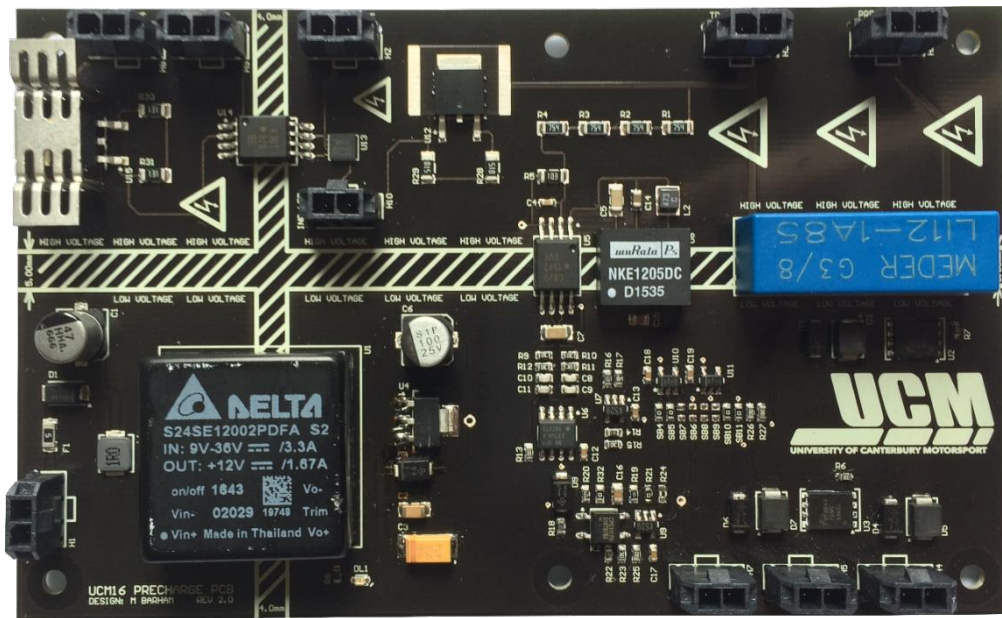


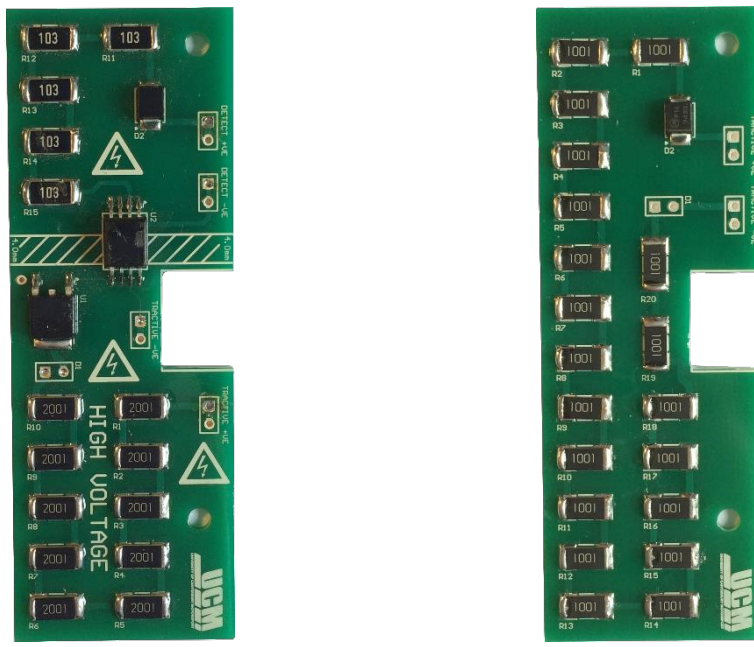
Figure 6.29. Image of redesigned Precharge PCB

The PCB was tested using the same test setup as described in Section 4.6. Whilst the precharge element operated correctly, the N-channel MOSFET in the voltage indication circuit failed when the tractive voltage was cycled (to replicate the driver restarting the car). The tests were conducted on the author's final day in New Zealand before leaving for the competition in Australia, so there was no opportunity

to diagnose the problem. It was, however, suspected that solder bridging underneath the surface-mount component was to blame.

Two voltage indication PCBs were designed and assembled in Australia just prior to the competition to ensure the accumulator remained rule compliant. The PCBs had differing designs for redundancy, as there was no time for prototyping. They were also constrained dimensionally to be no larger than 35 x 95 x 8 mm (width, length, height) to fit over the top of the precharge PCB assembly.

The first design (Figure 6.30(a)) was an amendment to the circuit on the revised precharge PCB (Figure 6.28). The constant current sources were replaced with resistor ladders, thus minimising the height of the PCB. An N-channel MOSFET with a larger footprint was also selected to prevent a similar failure from occurring as before. The second design (Figure 6.30(b)) reverted to powering the indication LED from the tractive system after the positive AIR. It used a single resistor ladder and a 56 V Zener diode to limit the current through the LED. Only the first design was tested in the accumulator as it worked immediately, thus neglecting the need to test the second design. The PCB is shown at the bottom of the accumulator assembly in Figure 6.24 (Section 6.3.6). The schematics for the two designs are documented in Appendix P.



(a) First design

(b) Second design

Figure 6.30. Image of replacement voltage indication PCBs

6.4. CHAPTER SUMMARY

Chapter 6 focussed on the integration of the previously detailed electrical systems into a driveable race car. Since the accumulator was not yet ready, the electric powertrain was commissioned in a rear-wheel drive configuration using a dc power supply.

On the 7th of September, UCM16 drove for the first time, making it New Zealand's first electric Formula SAE race car. The intention to start with a rear-wheel drivetrain accelerated the car's development timeline, allowing other sub-teams to test their designs. Several crucial flaws with the electrical system were unearthed during the month of rear-wheel drive testing. The magnitude of the electromagnetic interference emitted by the inverter was far greater than expected, and resulted in noise being inducted onto the communication lines between the AMS cell boards. Consequently, the tractive system would become disabled after only a short period of driving. This was alleviated by transferring the fault handling functionality to the Accumulator Isolation PCB and Shutdown PCB.

Testing also highlighted the detrimental effect the home-made resistance welder had on the accumulator's lithium-ion cells. As UCM16 was driven more, the number of failed cells increased; the replacement of which expended valuable time and resources. By the end of the month, the accumulator could only power the race car for a maximum of a few minutes at a dramatically reduced pace.

Problems, whether minor or major, were to be expected with such a new concept. The final section of this chapter was dedicated to explaining the revisions made to the electrical systems to convert UCM16 to its intended four-wheel drive configuration. The vehicle control unit, dc/dc converter and precharge PCBs all experienced significant revisions, based on what had been learnt during testing. It was the accumulator, however, that received the largest revision, both mechanically and electrically. A professional resistance welder was used to connect the cells, and the module structure and packaging were refined.

CHAPTER 7

FORMULA SAE-A COMPETITION

UCM16's conversion from rear-wheel to four-wheel drive was completed in the final week of October, thus superseding its previous title to become New Zealand's first four-wheel drive electric race car. To maximise the three weeks available before the car was shipped to Australia, the team tested both during the day and at night (using the time between to make alterations).

The arrival of UCM members in Australia was staggered based upon their responsibilities with the car. The author, along with the sub-team leaders, arrived two weeks prior to the competition; shortly followed by the team's drivers. During the day, the car was tested at numerous locations around Melbourne (Figure 7.1). At night, the final hardware revisions were made (for example the installation of the revised dc/dc converter and precharge PCB), and the car was reviewed for rule compliancy.

This chapter is dedicated to the development of UCM16's vehicle dynamic software (the final amendment to the car) and the car's performance at the 2016 Formula SAE Australasian competition.



Figure 7.1. Pre-competition testing in Melbourne, Australia

7.1. VEHICLE DYNAMICS SOFTWARE DEVELOPMENT

Testing in the two weeks preceding the Formula SAE-A competition saw the greatest improvement to the performance of UCM16. Whilst factors such as an improved aerodynamic design and suspension setup were collaborative to this result, it was likely that the main contributor to improvement was the software controlling the electric powertrain, which was previously underdeveloped with respect to the other systems. The following sections will hence discuss the development of the race car's vehicle dynamic software.

7.1.1. SENSOR MEASUREMENTS USING DIRECT MEMORY ACCESS

During the RWD and initial 4WD test sessions, the throttle sensors were the only measured input from the driver. This was carried out by creating a timer interrupt in the VCU which polled the respective analog to digital (ADC) channels each time it elapsed. Whilst this was the simplest method for measuring analog sensors, the inclusion of the brake and steering angle sensors resulted in the ADC operations taking too long, and causing other interrupts (related to other vehicle functions) to overlap (where an interrupt would be called from within another interrupt prior to the completion of its subroutine).

In almost all cases, the formation of the interrupt overlaps resulted in the throttle's ADC buffer overflowing and generating an error, subsequently disabling the vehicle. However, on one occasion the throttle value was set to its maximum limit, causing all four motors to accelerate to 15,000 rpm as soon as the inverter was enabled. This error occurred when the car was raised on its stand. In response, all software was rewritten (using none of the previous code). A combination of daily amendments and the issue not occurring when the brake and steering angle measurement code was first introduced to the software meant the fault was not immediately detected.

To continue measuring the sensors, Direct Memory Access (DMA) was utilised. DMA is a method that allows an input or output peripheral to store or retrieve information directly from the main memory location, thus bypassing the central processing unit (CPU). An 80 element (`uint16_t`) DMA buffer was created to which measurements from the four sensors are added cyclically every 112 cycles (as shown by the pictorial representation of Figure 7.2). Upon filling the buffer, an interrupt subroutine would calculate the average measurement for each sensor. Completing the subroutine was therefore the only time the CPU was used throughout the measurement process.

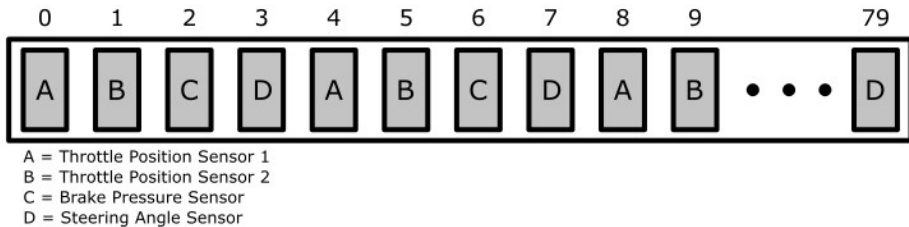


Figure 7.2. Pictorial representation of direct memory access buffer measurement locations

7.1.2. TORQUE VECTORING

The torque vectoring algorithm was based on the parameterisation of UCM16 into three parameters (Figure 7.3) that collectively scale the torque requested by the driver. The longitudinal bias (denoted Y in Figure 7.3) is a static parameter that reduces the torque to both front motors with respect to the rear motors. X_{GLOBAL} is a dynamic lateral bias, based upon steering angle position, that reduces the torque to the inside motors with respect to the outside motors (where “inside” and “outside” refer to the side of the car on the inside or outside of any particular turning curve). Finally, $X_{FRONT-INSIDE}$ is a static parameter that further limits the torque to the front inside wheel, thus accounting for the case where the front inside wheel has the least amount of traction (as mentioned previously in the vehicle dynamic theory of Section 2.3). A process diagram for the torque vectoring algorithm is shown in Figure 7.4.

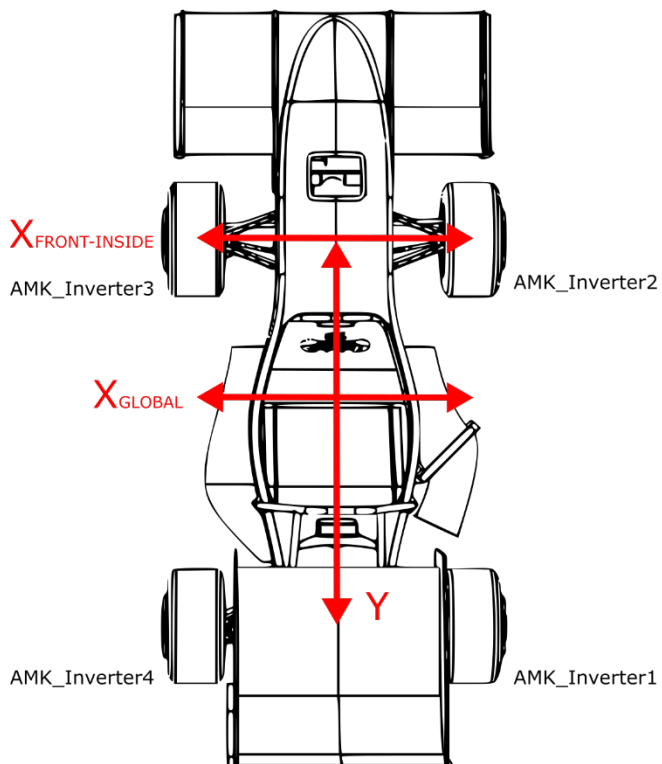


Figure 7.3. Diagram of torque vectoring parameterisation

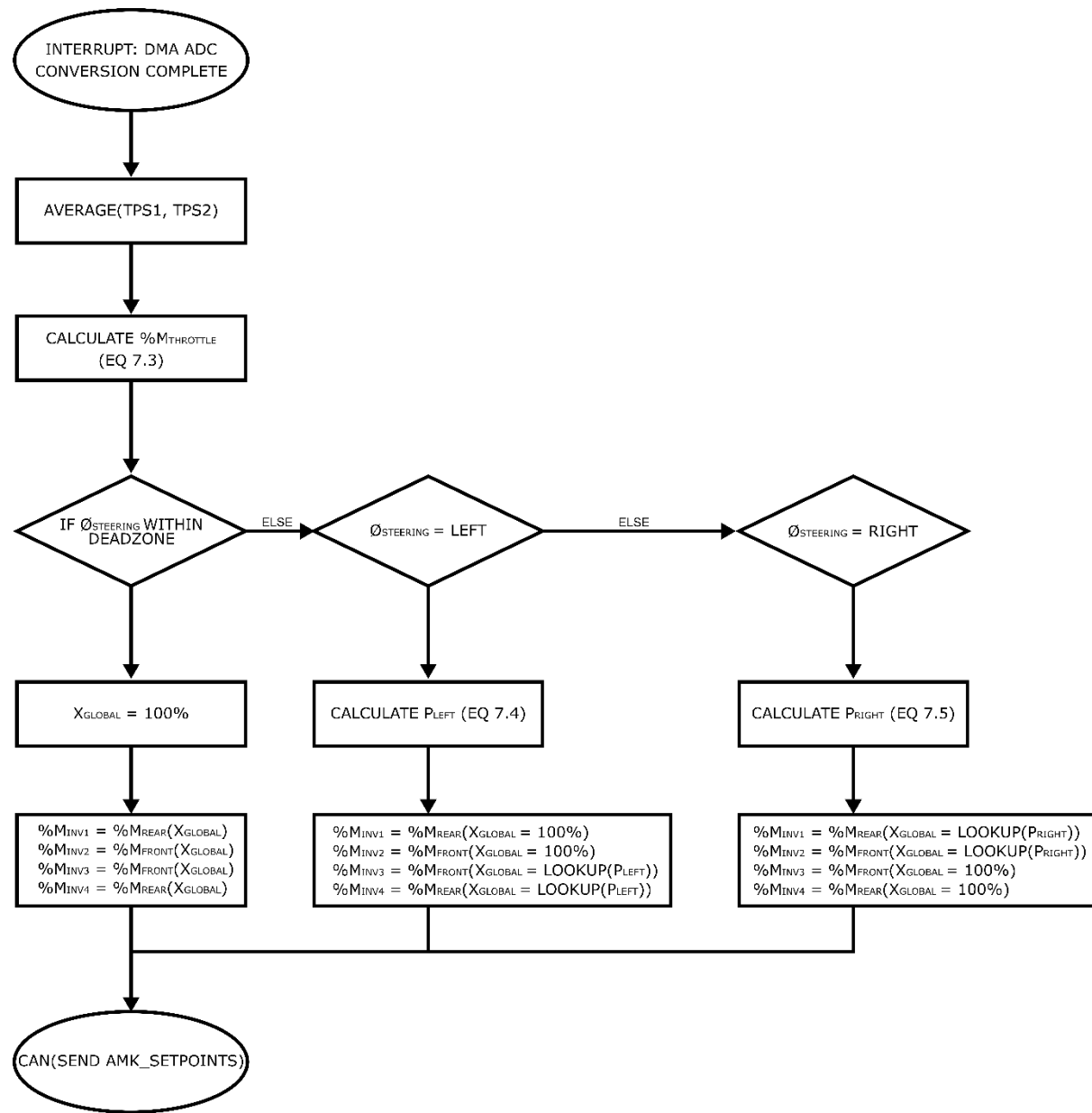


Figure 7.4. Torque vectoring algorithm process diagram

The parameters are defined as percentages (0 – 100%). This allows them to be multiplied together to calculate the required torque limit for a motor, which can then be sent directly to the relevant sub-inverter as a percentage of nominal torque. Equations (7.1) and (7.2) are the base torque calculations for the front and rear motors respectively

$$\%M_{FRONT} = \%M_{THROTTLE} \times Y \times X_{GLOBAL}(\phi_{STEERING}) \times X_{FRONT-INSIDE} \quad (7.1)$$

$$\%M_{REAR} = \%M_{THROTTLE} \times X_{GLOBAL}(\phi_{STEERING}) \quad (7.2)$$

where, $\%M_{FRONT}$ is the requested percentage of nominal torque to a front motor, $\%M_{REAR}$ is the requested percentage of nominal torque to a rear motor, $\%M_{THROTTLE}$ is the throttle position remapped to correspond to a percentage of the maximum torque limit, and $\phi_{STEERING}$ is the steering angle.

The parameterisation is such that, when the vehicle is turning, the requested torque to the rear-outside wheel (which theory suggests has the greatest traction) is equal to the torque requested by the driver using the throttle pedal. It can therefore be said that the torque distribution is relative to the rear-outside motor; with the exception when the vehicle is travelling in a straight path, in which the distribution is relative to both rear motors. This is therefore compliant with EV2.3.12, which states that any torque manipulating algorithm cannot increase the amount of torque beyond that requested by the driver.

Equation (7.3) is the formula used to remap the throttle pedal position in terms of a percentage of nominal motor torque,

$$\%M_{THROTTLE} = \frac{TPS_{DMA_AVERAGE} \times \%M_{MAX}}{TPS_{MAX} - TPS_{DEADZONE}} \quad (7.3)$$

where, $TPS_{DMA_AVERAGE}$ is the average of the measurements stored in the DMA buffer for the two throttle position sensors, $\%M_{MAX}$ is the maximum torque limit, TPS_{MAX} is the maximum position value of the throttle pedal, and $TPS_{DEADZONE}$ is the maximum position value of the throttle dead zone.

The dynamic lateral bias (X_{GLOBAL}) is pre-calculated and entered into the VCU as a single lookup array of 160 elements. Once the algorithm has determined the direction of the vehicle, the measured steering angle is modulated and used as a pointer location for the array. The lookup array is configured such that the zero-position entry corresponds to no steering input, and the final entry corresponds to full lock in the identified direction. An adjustable dead zone was also included about the central steering position to expand the range considered to have no steering input.

The steering angle sensor was a linear potentiometer connected to the right side of the steering rack. This meant the measurements were offset (a measurement close to zero corresponded to full lock right) and had to be adjusted in software. Equations (7.4) and (7.5) are the formulae used to find the array pointer value for turning left (P_{LEFT}) and right (P_{RIGHT}) respectively,

$$P_{LEFT} = \frac{\phi_{STEERING_DMA_AVE} - (\phi_{CENTRE} + 0.5(\phi_{DEADZONE}))}{10} \quad (7.4)$$

$$P_{RIGHT} = \frac{(\phi_{CENTRE} - 0.5(\phi_{DEADZONE})) - \phi_{STEERING_DMA_AVE}}{10} \quad (7.5)$$

where, $\phi_{STEERING_DMA_AVE}$ is the average steering angle measurement from the DMA buffer, ϕ_{CENTRE} is the measurement for a central steering position, and $\phi_{DEADZONE}$ is the dead zone about the central steering position.

Figure 7.5 is a plot of the X_{GLOBAL} profiles that were tested on UCM16. It was initially planned to use linear profiles of varying gradients to find an approximation of the ideal response, and then consider a non-linear or step-wise profile; for example, one that would increase the effect of the vectoring once the steering angle exceeded a threshold. However, time constraints meant only the linear profiles were tested. The test procedure implemented was an iterative process in which the torque profile and front-rear bias were changed without informing the driver. The parameters were then refined based upon driver feedback. Whilst it would have been more appropriate to have included a quantifiable metric to the testing procedure (such as lap time), the torque parameters were not the only change being made to the car each time it stopped. This therefore meant any measurement was not an accurate representation of the changes made to the algorithm. Ultimately, a longitudinal bias of 0.85 was selected with X_{GLOBAL} profile 2 (Figure 7.5). No static bias was applied to the front-inside motor ($X_{FRONT-INSIDE}$).

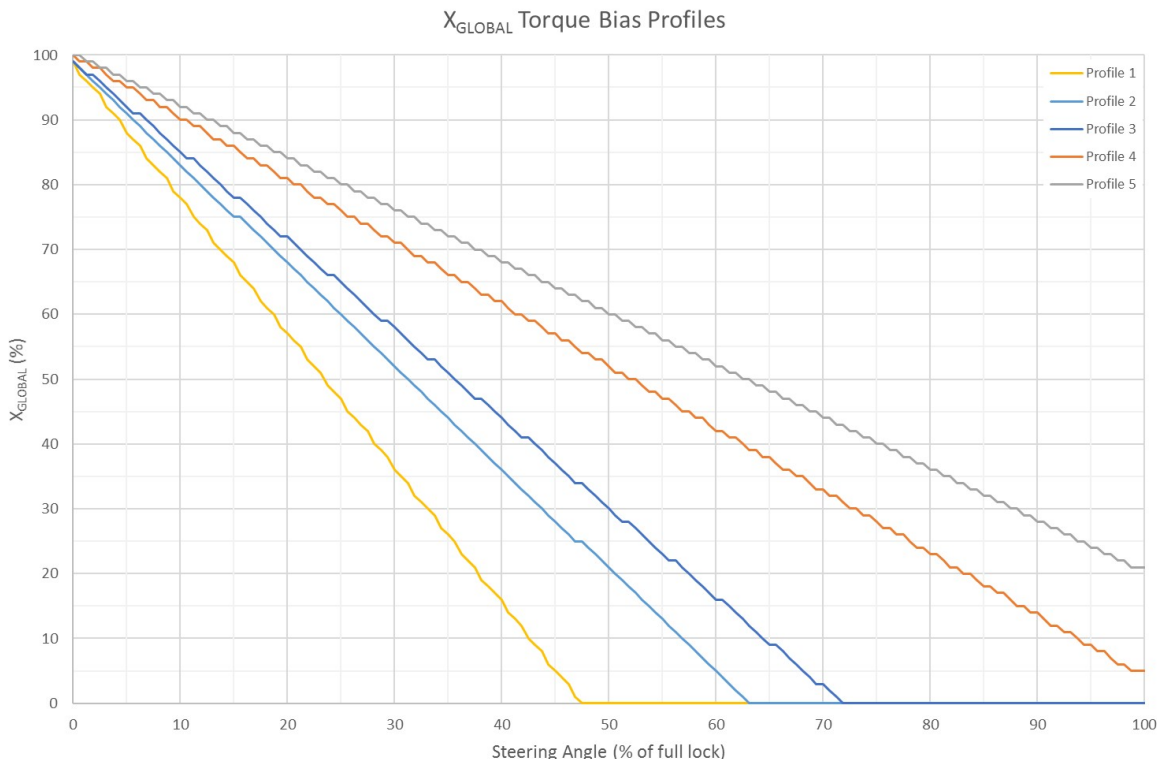


Figure 7.5. Plot of tested X_{GLOBAL} torque bias profiles against steering angle

Figure 7.6 is a plot of motor torque requested by the torque vectoring algorithm with respect to steering angle. The data was logged on a MoTeC C185 datalogger-display (using CAN) whilst UCM16 was competing in the skid-pad event at the Formula SAE-A competition. The skid-pad event best shows the effect of torque vectoring because the continuous radii of the corners means the data is much more intuitive to interpret, and makes relationships between measured variables easier to spot. For clarity, the rear-right motor data was not plotted, as it is unnecessary for proving the individual parameters of the torque vectoring algorithm were working as expected.

The effect of the static longitudinal bias (parameter Y) can be seen by comparing the requested torque of the front-left motor (INV3) with that of the rear-left (INV4). Since the motors are on the same side of the vehicle, the lateral bias (parameter X_{GLOBAL}) is irrelevant to the calculated torque. The data traces in Figure 7.6 (where the yellow trace is INV3 and the orange trace INV4) show the requested torque of the front-left motor is an exact scaled copy of the rear-left motor, and is unaffected by steering angle. As an aside, if the rear-right motor torque was to be plotted, it would show INV2 to be a scaled copy of the rear-right motor torque.

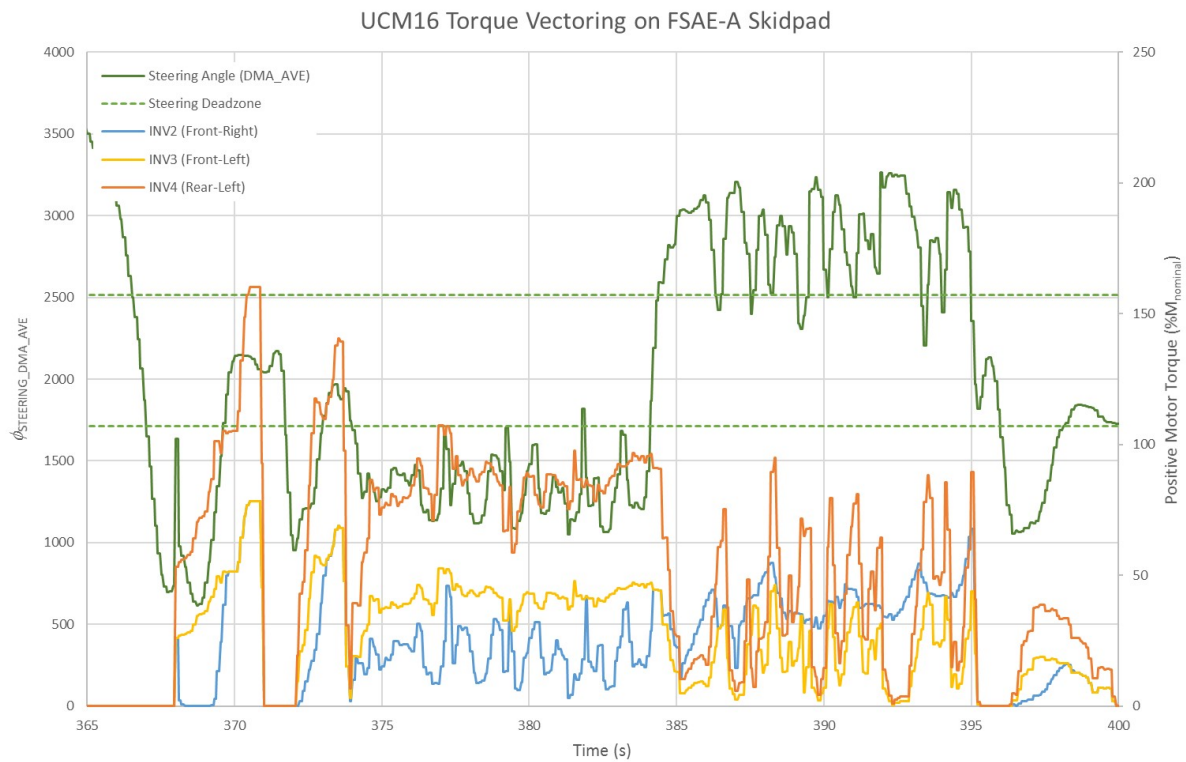


Figure 7.6. Plot of positive motor torque and steering angle measurement data during FSAE-A skid-pad event

Comparing the front-left motor with the front-right motor (blue trace) conversely shows only the effect of X_{GLOBAL} , and ignores the longitudinal bias. It can be observed that the traces vary from one another based upon steering angle. However, at the points where the steering angle (green trace) enters the steering dead zone (indicated by the zone between the dashed green traces) the requested torques

become identical (yellow trace overwriting blue trace), up until the steering angle exits the dead zone, hence proving the implementation of the dead zone removes any lateral biasing. A clear example of this is after 370 seconds of vehicle operation.

To further show the effect of the lateral parameter, and how it tracks the steering angle, a comparison between steering angle and the corresponding inside motor(s) must be made. Between 375 and 380 seconds, the measured steering angle is below the dead zone, therefore implying the vehicle is turning right. Within this period, the requested torque for the front-right motor is a translation of the steering angle, whilst the left-hand side motors show no correlation. Conversely, between 385 and 395 seconds, the vehicle is turning left; and the left-hand side motors become an inverse translation. Note, it is an inverse because the torque is reduced to the corresponding side of the vehicle.

Figure 7.7 is a plot (over the same period as Figure 7.6) showing data logged for both rear motor torques, steering angle and throttle position. For clarity, the opacity of the steering angle trace has been reduced. The purpose of Figure 7.7 is to show how the torque vectoring algorithm tracks the position of the throttle pedal, and how the torques requested by the driver is transferred between the rear motors. When the vehicle is turning right (steering angle below the dead zone), the rear-left motor torque (orange trace) is a direct translation of the throttle position (blue trace), as it is the rear-outside motor. The opposite occurs when the vehicle is turning left, in which the rear-right motor torque (yellow trace) becomes a translation of throttle position. As with the front motors, when the steering angle is within the dead zone, the rear motor torques are equal (and a translation of the throttle).

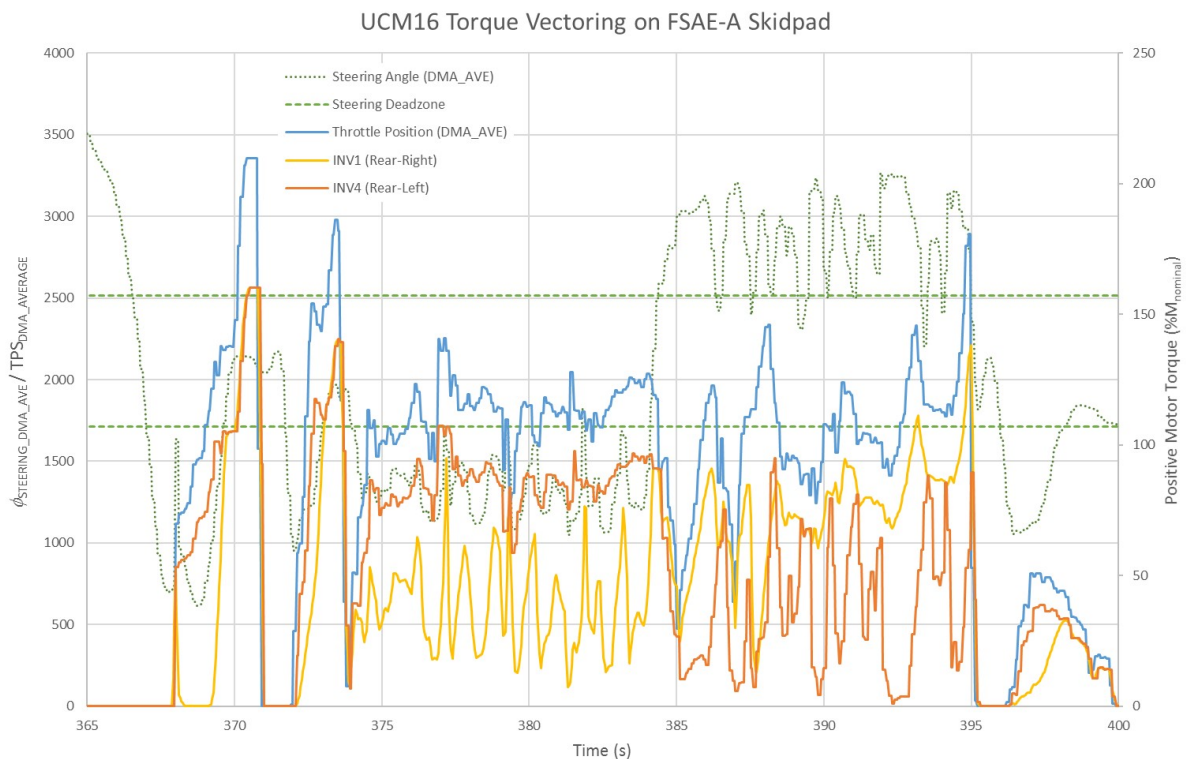


Figure 7.7. Plot of motor torque, steering angle and throttle measurement data during FSAE-A skid-pad event

7.1.3. TRACTION CONTROL

Converting the motor control model from speed to torque control had a significant setback. If a tyre lost traction, the respective motor would attempt to accelerate to its speed setpoint. If the requested torque was high enough, the almost instantaneous increase in current would cause the current control loop of the respective sub-inverter to overshoot and consequently disable the drive to protect the power electronics. Due to the safety protocol implemented by AMK, once a sub-inverter declares an error it cannot be restarted whilst moving, resulting in the car driving with a significantly impeded powertrain.

The main cause for a wheel to lose traction was weight transfer; in particular, the front-inside wheel lifting during a corner. Figure 7.8 is a plot of data collected from the third testing session in Australia showing the velocities of the left-hand side motors and the front-left motor current. The most noticeable feature in this data plot is the large spike in velocity of the front-left motor (orange trace) with respect to the rear-left motor (blue trace), which is directly associated with a loss of traction. The velocity spike corresponds exactly with the point at which the front-left motor current (yellow trace) drops to zero, where it remains for the remainder of the plot, therefore implying the sub-inverter disabled the motor drive. Further analysis shows there to be more velocity spikes of a smaller magnitude prior to the main spike, which are no longer present after the drive has been disabled.

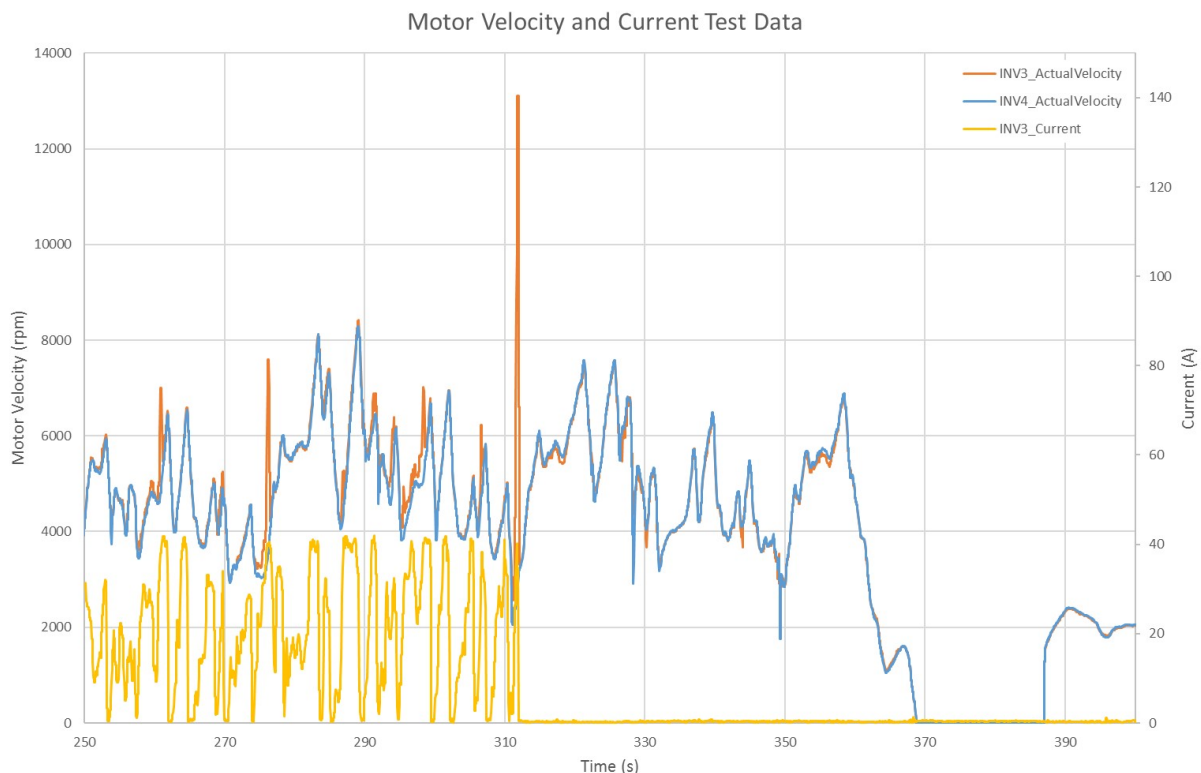


Figure 7.8. Plot of motor velocity and current data showing motor becoming disabled

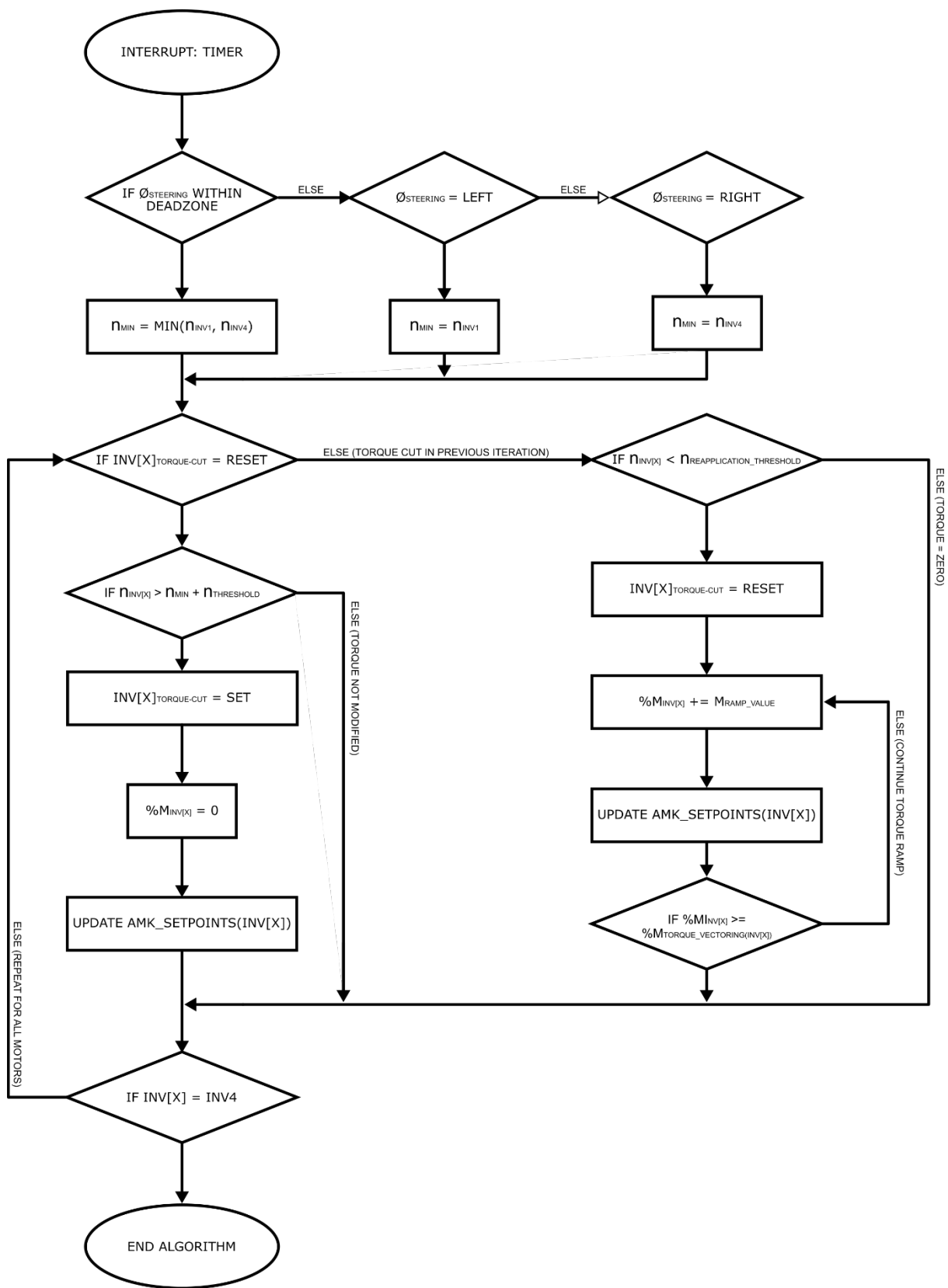


Figure 7.9. Traction control ("Anti-slip") algorithm process diagram

To prevent wheel spin, a traction control algorithm (called “Anti-spin” by the software team) was appended to the torque vectoring algorithm. A process diagram for the algorithm is shown in Figure 7.9. Anti-spin works by first finding the minimum velocity of a reference motor. As with the torque vectoring algorithm, the reference motor is the rear-outside motor, of which the corresponding tyre is assumed to have the greatest traction. If the vehicle is travelling within the steering angle dead zone, the minimum velocity of the two rear motors is chosen as the reference. The algorithm then iterates through each motor and, if its velocity has exceeded the reference motor velocity plus a threshold, the torque will be set to zero. Once the velocity of the undriven motor has reduced to below the “reapplication threshold”, the torque is incrementally reapplied until it reaches the torque requested by the torque vectoring algorithm. Increasing the torque incrementally was found to be extremely important, as simply re-enabling the drive would result in the motor overshooting the anti-spin threshold if traction had not been regained; consequently causing the motor to be disabled again.

Figure 7.10 is a plot of motor and current data collected with the Anti-spin algorithm enabled (on the same track as Figure 7.8). The anti-spin threshold was set at 500 rpm above the minimum reference motor velocity, and the reapplication threshold was set to 250 rpm (with a reapplication increment of 50 rpm). The lack of velocity spikes from a single motor proves the algorithm was successful in preventing wheel spin. In addition, the current traces (dashed traces) show that none of the motors were disabled by their respective sub-inverter. After implementing the anti-slip algorithm, there were no further cases of a motor becoming disabled due to overcurrent.

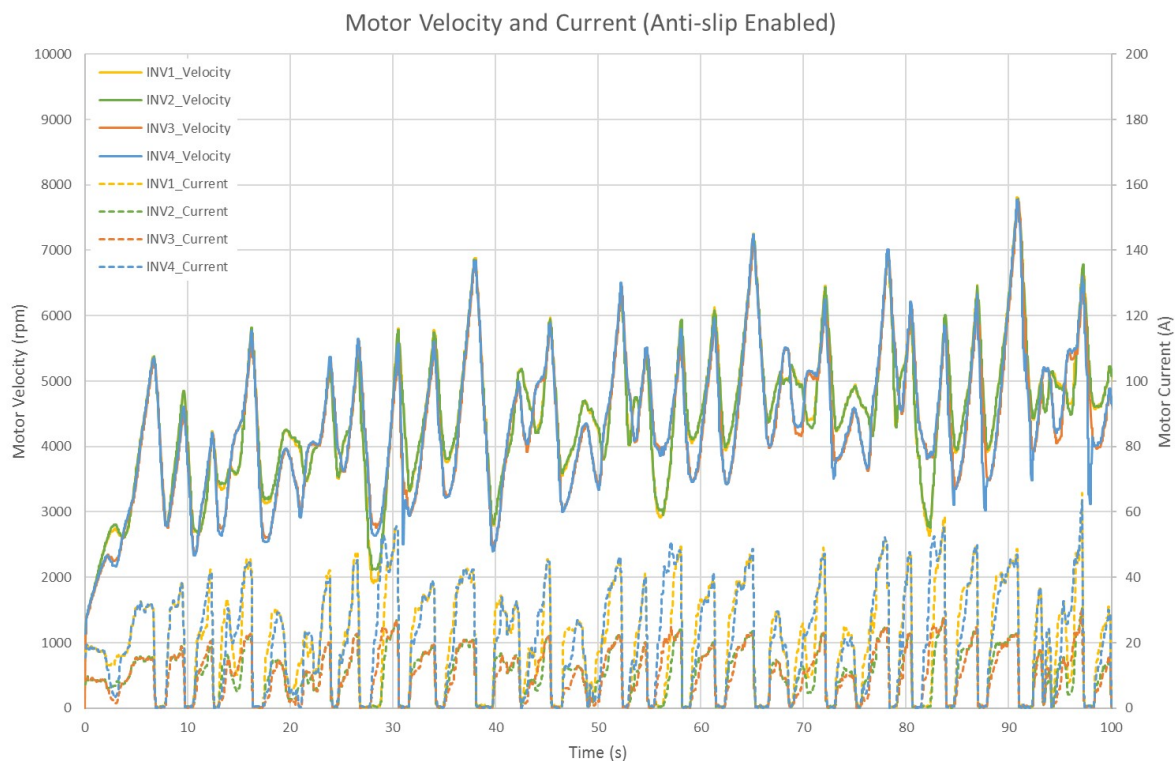


Figure 7.10. Plot of motor velocity and current data with anti-slip algorithm enabled

7.1.4. POWER LIMITATION

The final vehicle dynamic software development to be discussed is the power limiting algorithm. Since the AMK Racing Kit had the capability to exceed the 80 kW power limit enforced by the Formula SAE rules, the output power of UCM16 needed to be limited through software. Of the numerous algorithms trialled, only the final (and most promising) concept will be discussed in this section.

A process diagram for the power limiting algorithm is documented in Figure 7.12. As with the Anti-spin algorithm, the power limiting algorithm was appended to the main torque vectoring algorithm. The concept is based on the manipulation of $TPS_{DMA_AVERAGE}$ (refer to Section 7.1.2 for definition), to create a dynamic maximum throttle limit based upon tractive power. Since $TPS_{DMA_AVERAGE}$ is one of two inputs to the torque vectoring algorithm, decreasing its value will reduce the torque globally across the powertrain. If the tractive power (calculated as a multiplication of the tractive current, measured by the Shutdown PCB, and the tractive voltage, measured by the AMS) exceeds the 80 kW power limit, $TPS_{DMA_AVERAGE}$ is decreased incrementally until the tractive power drops below the limit.

It should be mentioned that the power limiting algorithm was never fully validated during testing as, once again, time constraints meant the algorithm could not be tested in isolation. Of the testing that was conducted, driver feedback reported the sensation of being slowed at the end of the test track's straights; therefore, suggesting the algorithm was somewhat working as expected. However, the layout of the test track meant it was impossible to prove if the driver or the algorithm was limiting $TPS_{DMA_AVERAGE}$ (a

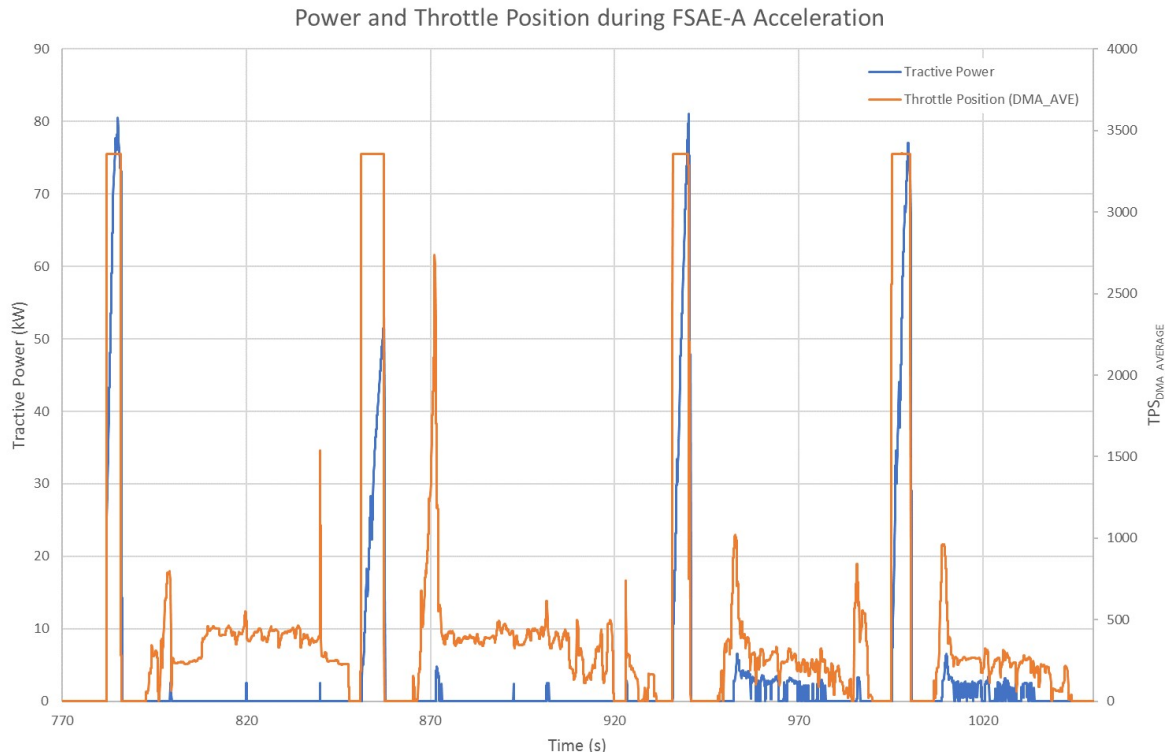


Figure 7.11. Plot of tractive power and throttle position data during FSAE-A acceleration event

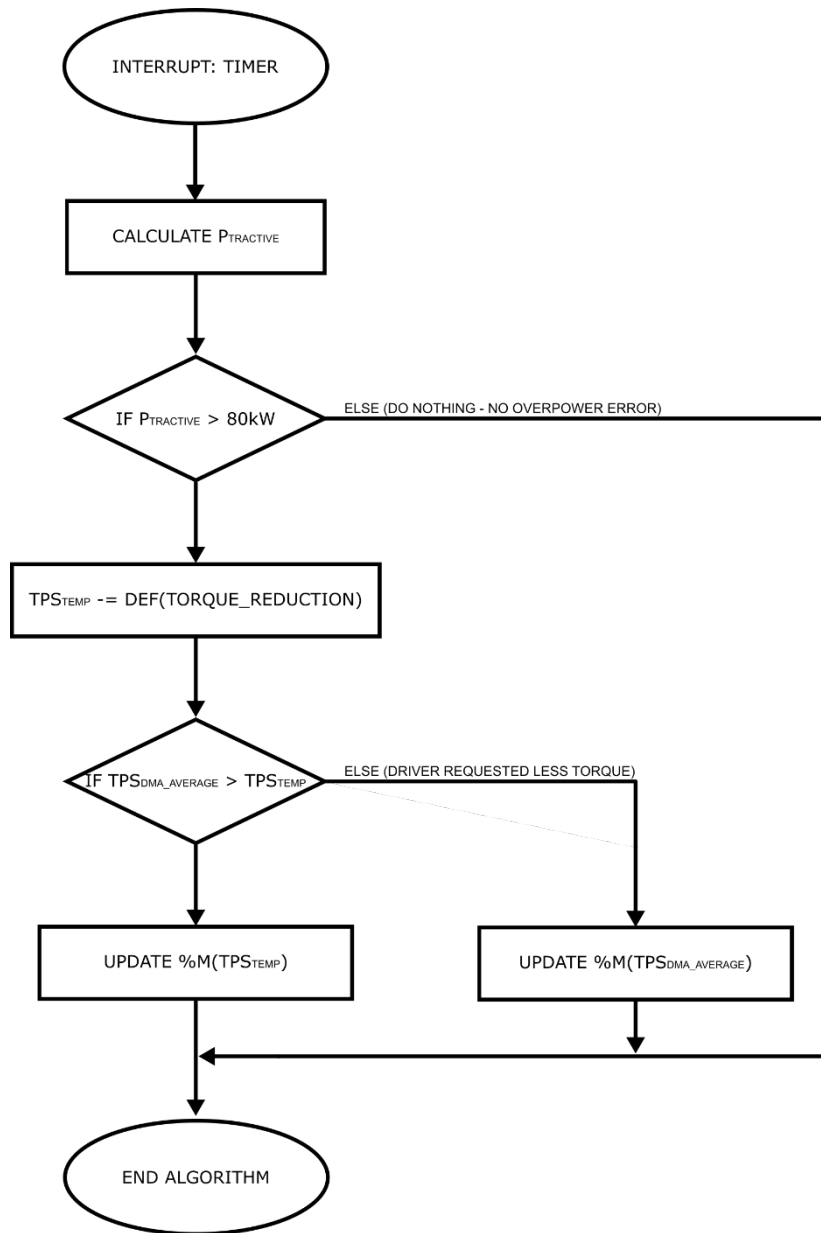


Figure 7.12. Tractive power limiting algorithm process diagram

combination of not logging a separate throttle variable and the fact that the drivers would ease off the throttle pedal whilst driving).

In hindsight, the most appropriate way to measure the effectiveness of the power limitation algorithm is during an acceleration event; in which it is assumed that the driver would either be at full throttle position or zero. This would produce a “square” throttle response when plotted, clearly indicating the start and finish points. Figure 7.11 is a plot of the tractive power and throttle position during the FSAE-A acceleration event. It should be noted that the lack of validation meant the algorithm was not implemented during the competition, and hence the power exceeded 80 kW momentarily on the first and third acceleration runs (indicated by the large impulses). If it had been implemented, it would be expected that the throttle trace would decrease (not square) at the point where the power exceeded 80 kW.

7.2. FORMULA SAE-A COMPETITION RESULTS

The University of Canterbury Motorsport placed 12th in the overall standings for the 2016 Formula SAE Australasia competition. This correlated to 5th in the electric-only category. Whilst this was not the success the team believed the car was capable of, it was still a great result for such a new concept.

Table 7.1 lists the points scored in the individual events, along with the three podium results achieved by the team. Most notably, the first-place finish in the Skid-pad event meant UCM became the first electric FSAE team to win a dynamic event at the FSAE-A competition. It was also the second back-to-back win for the team, following UCM15’s first place at the 2015 Skid-pad event.

Table 7.1. Table of 2016 FSAE-A event results for UCM

Event	Points
Design (3 rd)	142.0
Business Presentation (2 nd)	72.5
Cost	53.8
Skid-pad (1 st)	75.0
Acceleration	58.6
Autocross	86.2
Endurance	8.0
Efficiency	0.0
Overall	496.1

The parameterisation of UCM16's torque vectoring algorithm was extremely beneficial during the Skid-pad event (Figure 7.13). Feedback from the driver, in terms of understeer and oversteer, allowed the lateral and longitudinal biasing to be tweaked after the car had completed each run⁴⁹. The best time set by the team was 5.073 seconds; 0.001 seconds faster than second place.

UCM placed 8th in the Acceleration event (Figure 7.14), with a time of 4.395 seconds (0.336 seconds slower than the first placed team). This was disappointing, as theory suggests a 4WD electric car would have far greater acceleration than a RWD combustion car. The main cause for not placing higher was lack of time (a common theme), in which the team choose to focus more on handling (for the Skid-pad, Autocross and Endurance events) than acceleration.

As the competition progressed, the performance of UCM16 diminished, ultimately resulting in a DNF (Did Not Finish) for both endurance events. The following sections will hence discuss the data collected during the Autocross and Endurance events, and attempt to theorise the cause.



Figure 7.13. UCM16 competing in the FSAE-A skid-pad event

⁴⁹ To clarify, teams are permitted as many runs of the Acceleration and Skid-pad events within a specified limit (which is unlike other Formula SAE competitions, where teams are given a set number of runs).



Figure 7.14. UCM16 returning from an acceleration run at FSAE-A

7.2.1. AUTOCROSS

UCM placed 5th in the Autocross event with a fastest lap time of 82.901 seconds (3.750 seconds slower than the first placed car), out of the five full runs completed. Although this appears a good result (which it was considering the new concept and limited testing) the final lap time was not a good representation as to how UCM16 performed throughout the event. Figure 7.15 is a plot of the tractive power recorded over the whole event, in which each autocross run can be distinguished as a grouping of data points. Note, UCM16 did not complete its sixth run (data points after 600 seconds) due to the rear-left wheel spokes shearing mid-run.

The magnitude of the data in Figure 7.15 shows that the third and fourth runs used significantly more power than the first, second and fifth. It was on the fourth run that the fastest time was set. All five runs were conducted under almost identical conditions; there was no change to the torque vectoring parameterisation or track layout, and any interference from slower cars would have not been reflected across the entire lap.

From further analysis of the data, the cause for lack of power was found to be the rear-left motor (INV4) not being powered during some of the runs. Figure 7.16 is a plot of the rear-left motor velocity, current and error data recorded over the period of the Autocross event. First observations show the rear-left motor was only being driven during the third, fourth and sixth runs (as indicated by the presence of motor current (yellow trace)). However, the most interesting observation is the lack of correlation between the error information (blue data points), sent by the associated sub-inverter, and the motor current. Each sub-inverter sends an error code as part of the *AMK_ActualValues2* CAN message

(Appendix D), which can be used to diagnose faults in the powertrain. What is interesting about the error information shown in Figure 7.16 is that the first two runs have an error code equal to zero (no error), despite the motor clearly not operating as intended.

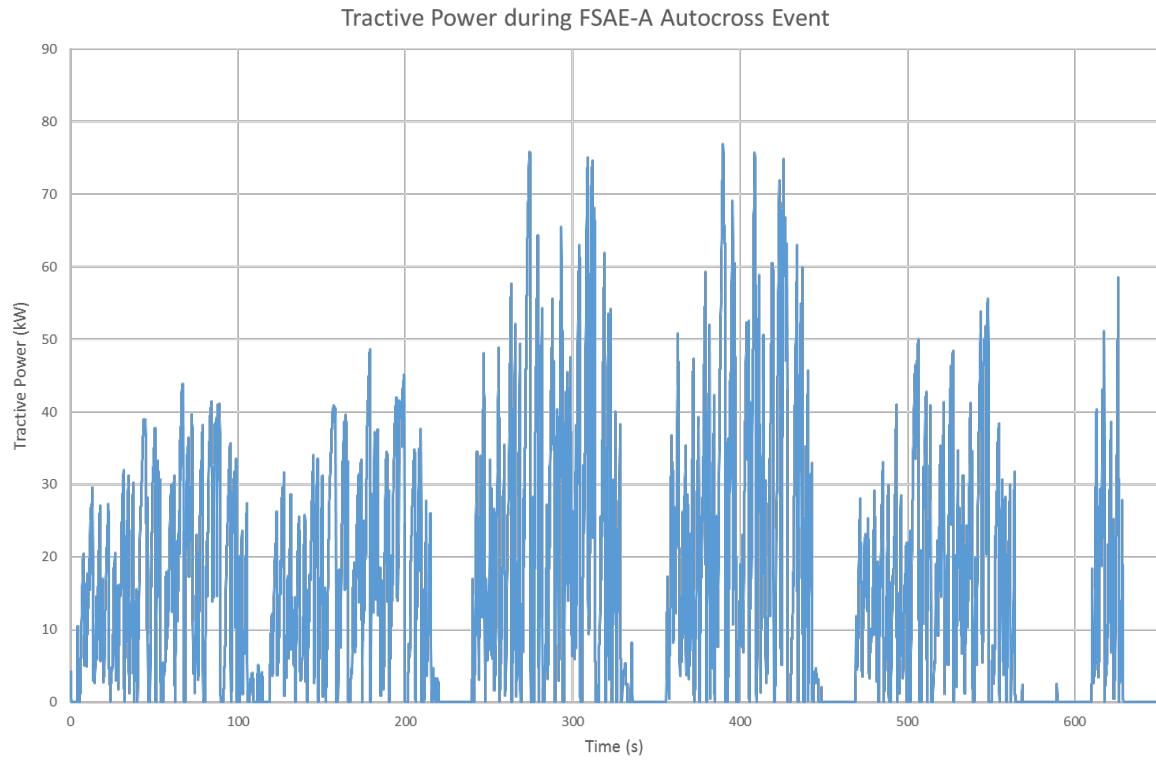


Figure 7.15. Plot of tractive power data during FSAE-A autocross event

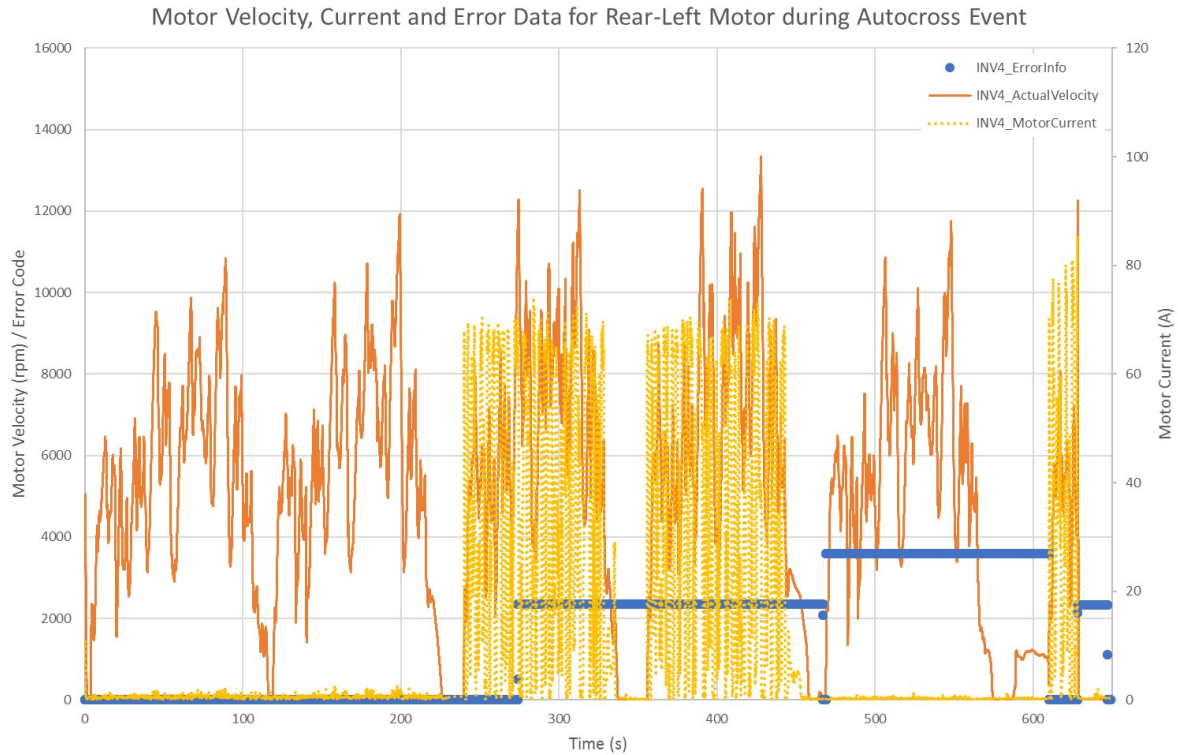


Figure 7.16. Plot of motor velocity, current and error data for rear-left motor during autocross event

The most obvious assumption for the rear-left motor not being powered by a supposed error-free sub-inverter is the lack of a torque command from the VCU. However, as shown by the data of Figure 7.17, the VCU was correctly sending torque commands. Note, for clarity the torque commands for the rear-left motor (blue trace) has been compared only with that of the front-left motor (orange trace), and measured throttle position (green trace). Since the MoTeC datalogger records data directly from the vehicle's CAN bus, it can be confirmed that the torque commands were being sent to the inverter. Since the inverter declares an error if a CAN message is not received from the VCU, it can be confirmed that the inverter received the torque commands. There is, however, no data (nor means of obtaining data) that proves the inverter unpackaged the torque commands and actuated them correctly.

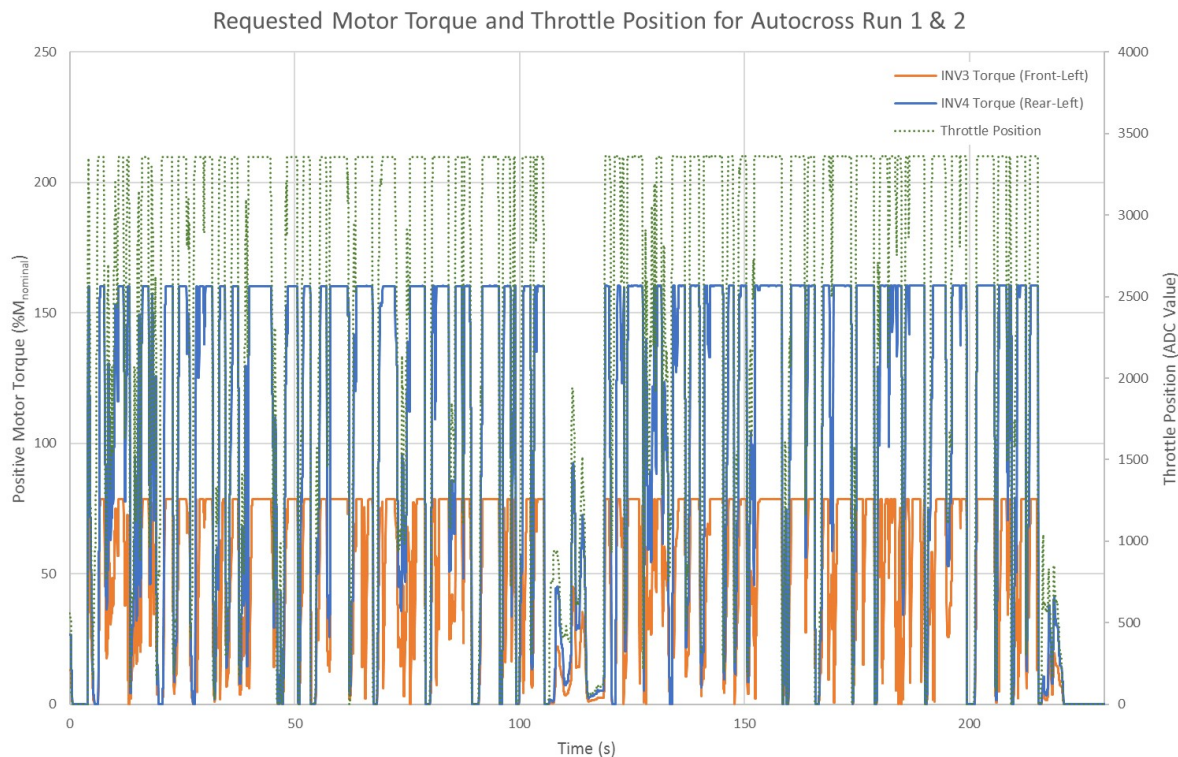


Figure 7.17. Plot of requested motor torque and throttle position for first two runs of autocross event

Referring to Figure 7.16, the two non-zero error codes⁵⁰ recorded were 2359 (Motor Overload Warning) and 3585 (“Systems Diagnostic: Special Software Message”). It is important to distinguish at this point that 2359 is a *warning*, whilst 3585 is an *error*; the difference being that a warning does not disable the output drive, whilst an error does. This is why the rear-left motor was not disabled during the third and fourth autocross runs (despite having a non-zero error code), and disabled during at the start of the fifth run.

Although the motor overload warning did not disable the motor, it is important to analyse its cause for both completeness, and for future electric vehicle development at UCM. To clarify, the following

⁵⁰ The single isolated data points in the error code series do not correlate to an AMK error code and were therefore ignored.

information regarding the warning was only understood after the competition, as there is no mention of such a warning in the supplied AMK Racing Kit documentation⁵¹. The motor overload warning is generated when half the overload time of the motor (*ID32920*), defined as the maximum time limit at which the motor can be operated at twice its rated current, is reached. For the DD5 motor, the overload time is set at 5 seconds for a rated current of 41 A. Furthermore, the maximum time limit (t_{MAX}) for any motor current (I) greater than the rated current (I_N) can be calculated using Equation (7.6).

$$t_{MAX} = \frac{3 \times ID32920}{\left(\frac{I}{I_N}\right)^2 - 1} \quad (7.6)$$

Figure 7.18 is a plot of the rear-left (INV4) error information and motor current for the third autocross run. The data shows the motor overload warning is generated during a period of high current draw (highlighted orange) with a longer duration than its predecessors. The maximum recorded current draw within this period was 70.56 A; which equates to a warning being generated after 3.823 seconds (assuming a constant current for Equation (7.6)). The actual time was 3.28 seconds; which suggests there is an element of history involved with the software, such that a return to zero current does not necessarily reset the time limit. Since an error code must be manually reset, or overridden by a different code, it is impossible to confirm if the motor overload warning was generated multiple times over the duration of the run, or if it was a single instance.

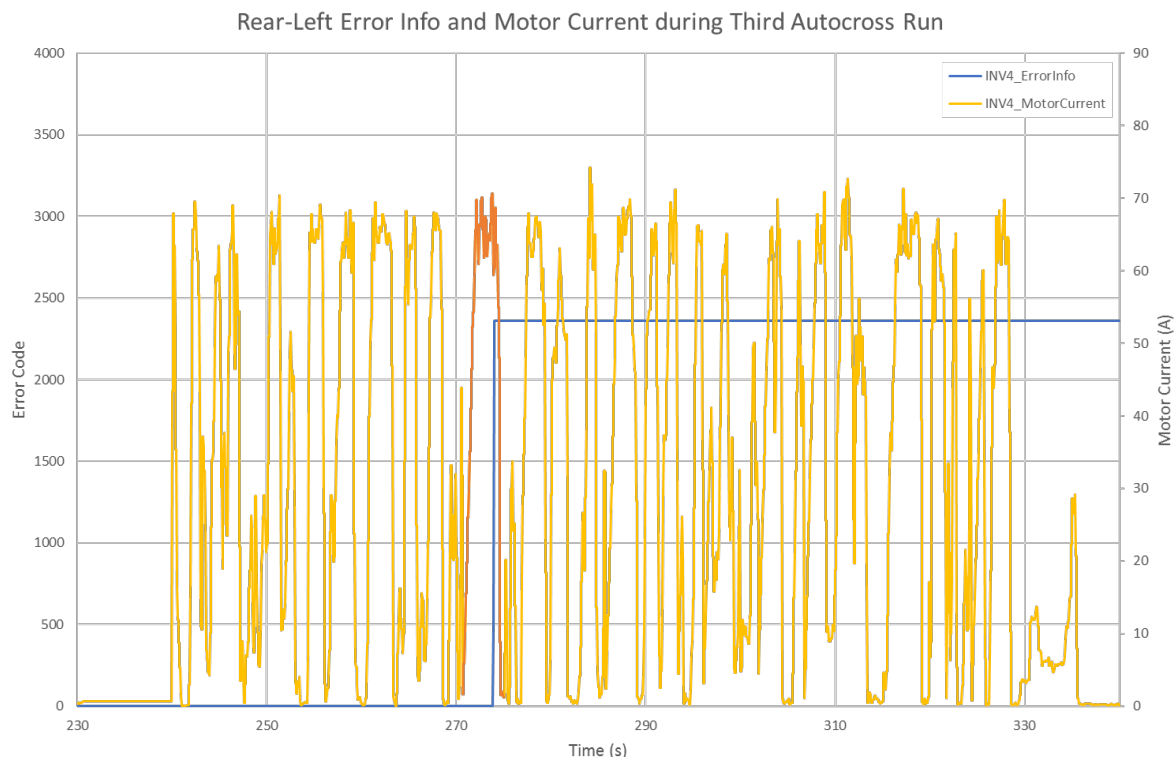


Figure 7.18. Plot of rear-left error information and motor current during the third autocross run

⁵¹ The warning/error information was found in the Aipex Pro Software database, which covers all AMK's product range.

The cause for the “Systems Diagnostics” error, which was generated at the beginning of the fourth autocross run, could not be determined. Due to the nature of AMK’s error information protocol, in which an error code has numerous sub-codes (that can only be viewed using the Aipex Pro software), a generated error can be one of many causes. In the case of 3585, there are four sub-code categories resulting in 25 possible causes. The theorised cause was a software initialisation error in the sub-inverter, for which a simple power reset would have resolved the problem. However, as the error was undetected when the car was released by the author, there was nothing that could have been done during the lap.

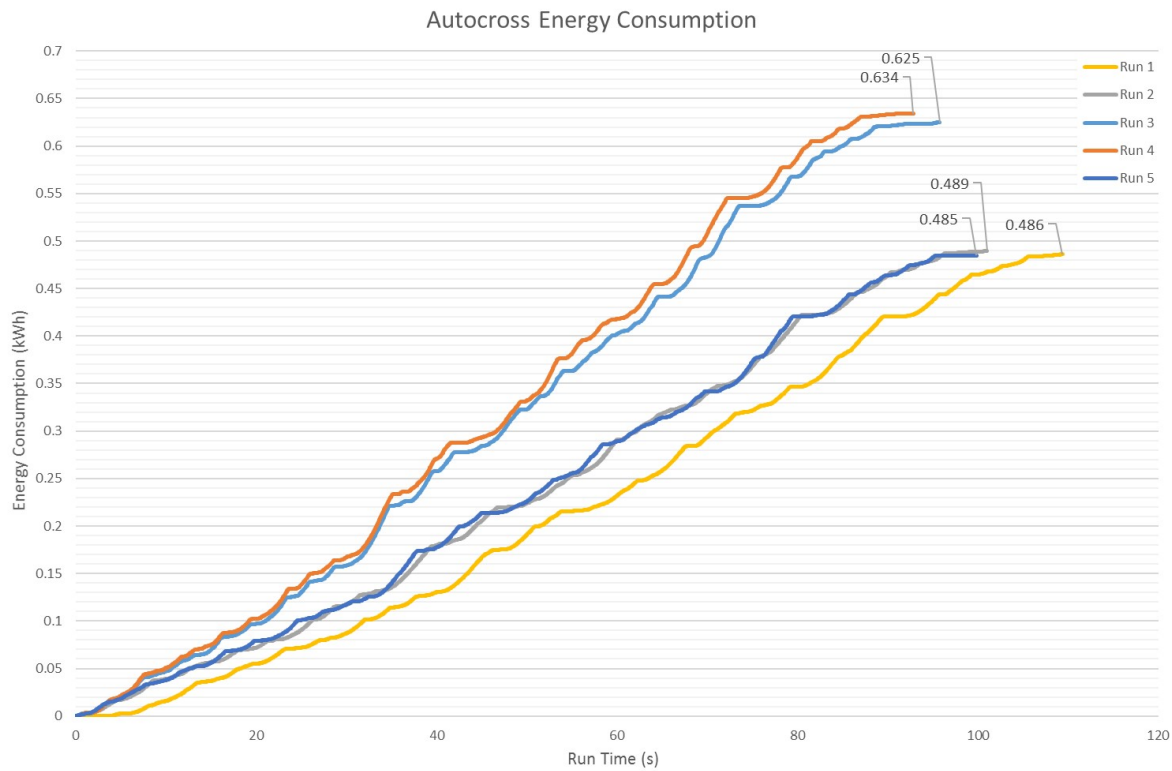


Figure 7.19. Plot of energy consumption for each run of FSAE-A autocross event

Since the autocross event is one lap of the endurance event, the data collected was useful for predicting certain performance metrics. Figure 7.19 is a plot of accumulated energy consumption for the completed autocross runs. The sixth autocross run was neglected as the vehicle did not complete a full lap. Based on the final data points of the third and fourth runs (which were at full power), the energy consumed per run was 0.625 and 0.634 kWh respectively. It should be noted that the track layout meant there was a small amount of track at the entry and exit of the pit box that would have contributed to the overall consumption but not the lap itself. Lack of position data meant this could not be factored into the consumption data, and is therefore a slight over-approximation on the energy required to complete a lap.

Averaging and then extrapolating the energy consumption (third and fourth runs) over the full 18 lap endurance event resulted in an approximated energy consumption of 11.331 kWh. This is within 5% of

the accumulator capacity predicted in Section 4.1.1, therefore suggesting the assumptions made had validity. The result, however, meant UCM16 would not be able to complete the endurance event at full power. Due to lack of time, regenerative braking had not been implemented in the control system, thereby limiting the available energy to 7.94 kWh, which was the capacity of the 7p126s accumulator. Extrapolating the average energy consumption of the three lower power runs (0.487 kWh) resulted in a predicted consumption of 8.76 kWh, which was still greater than the capacity of the accumulator. As such, the drivers were instructed to drive at a slower pace to sacrifice lap time for efficiency. The results of the endurance event will be discussed in the following section.

As a final remark, the point at which the rear-left wheel sheared can be seen towards the end of Figure 7.16 as the impulse in motor velocity that suddenly drops to zero. Whilst it may seem suspicious that the sheared wheel was on the same corner of the car as the problematic sub-inverter and motor, it has been confirmed through post-competition testing (in which the front-right wheel began to shear) that this was a coincidence. It can be concluded from the data that the Anti-slip algorithm (Section 7.1.3) limited the motor velocity when the wheel sheared, further proving its effectiveness. The sudden loss of load would have caused the motor to accelerate to its maximum speed (16,500 rpm) almost instantaneously, with the potential to cause further damage to the wheel assembly or motor. Instead, the velocity was limited to 12,200 rpm.

7.2.2. ENDURANCE EVENT

UCM received a DNF for the endurance event, ultimately placing in 18th position. On both runs, the powertrain stopped working and, after a few restarts, would not drive the car for the remainder of the run. This was a devastating result for the team, and was the main reason behind UCM not placing higher in the overall competition.

As shown by the following data, the car setup and driver behaviour differed significantly between runs. The first was a conservative run aimed at conserving energy, based on the predictions of the autocross event. It was on this run that the car first stopped. During the interval between runs, the author attempted to find the cause by analysing data collected from the first run. However, as discussed below, it could not be determined. Following this, the second run was at maximum performance; an executive decision made against the recommendation of both the author and the team's technical director. It was argued that a second conservative approach would result in a higher chance of finishing, thus collecting valuable points from the event. As it turns out, the second run was intended as a statement of UCM16's potential in the competition; a decision made more out of pride than engineering and logic.

Figure 7.20 is a plot of the motor current data recorded during the first endurance run. From the data, it can first be seen that the rear-left motor (INV4, yellow trace) stopped drawing current 382 seconds into

the run. This is a similar scenario to that of the autocross event, in which the error information indicated no error. The dashed red lines in Figure 7.20 indicate the four points at which the powertrain stopped, and the motor currents dropped to zero. The first event occurred after 909 seconds (15 minutes and 9 seconds), which was the longest time UCM16 had been driven continuously. The following three pulses in motor current show the powertrain being restarted by the driver and subsequently shutting down.

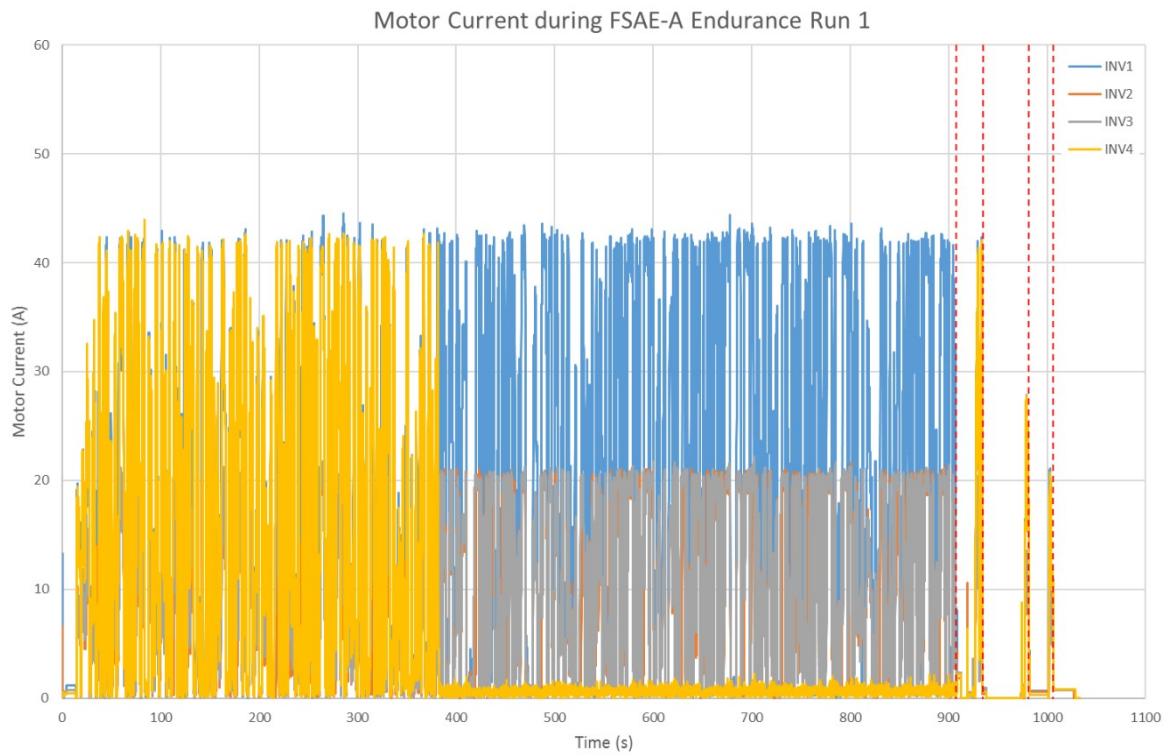


Figure 7.20. Plot of motor current data and powertrain shutdown points (red lines) during first endurance run

Figure 7.21 shows that a similar scenario occurred during the second endurance run. The rear-left motor current (yellow trace) shows the motor stopped driving after 137.8 seconds. As this was a higher power run (indicated by the greater current magnitude) it suggests the issue could be dependent on motor loading. However, as the error information once again suggested no error with the sub-inverter, this is a theory and has yet to be proven. The entire powertrain shutdown after 733 seconds (12 minutes and 13 seconds), as shown by the first dashed red line, which was just under three minutes sooner than that of the first run. The two pulses in motor current indicate the driver was only successful in restarting the car twice before it would no longer respond.

Comparing the motor current data of each run at the point in time that the powertrain first shutdown resulted in an interesting similarity. Figure 7.22 and Figure 7.23 are plots of motor current for both endurance runs starting three seconds prior to their respective first shutdown times. The comparison shows that, in both cases, the motor currents all reduced to an average of 2.1 A for a duration of 3.84

seconds. Analysing the currents at the other points of shutdown reveal a similar scenario, only with differing durations.

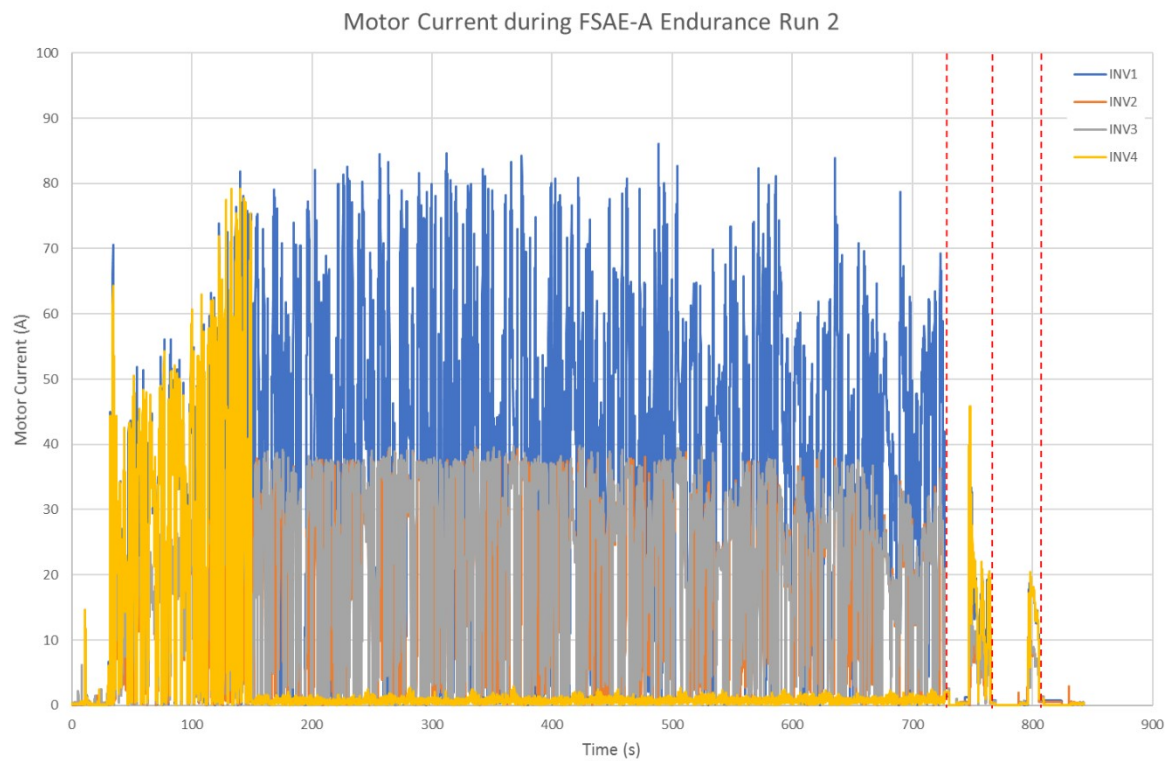


Figure 7.21. Plot of motor current data and powertrain shutdown points (red lines) during second endurance run

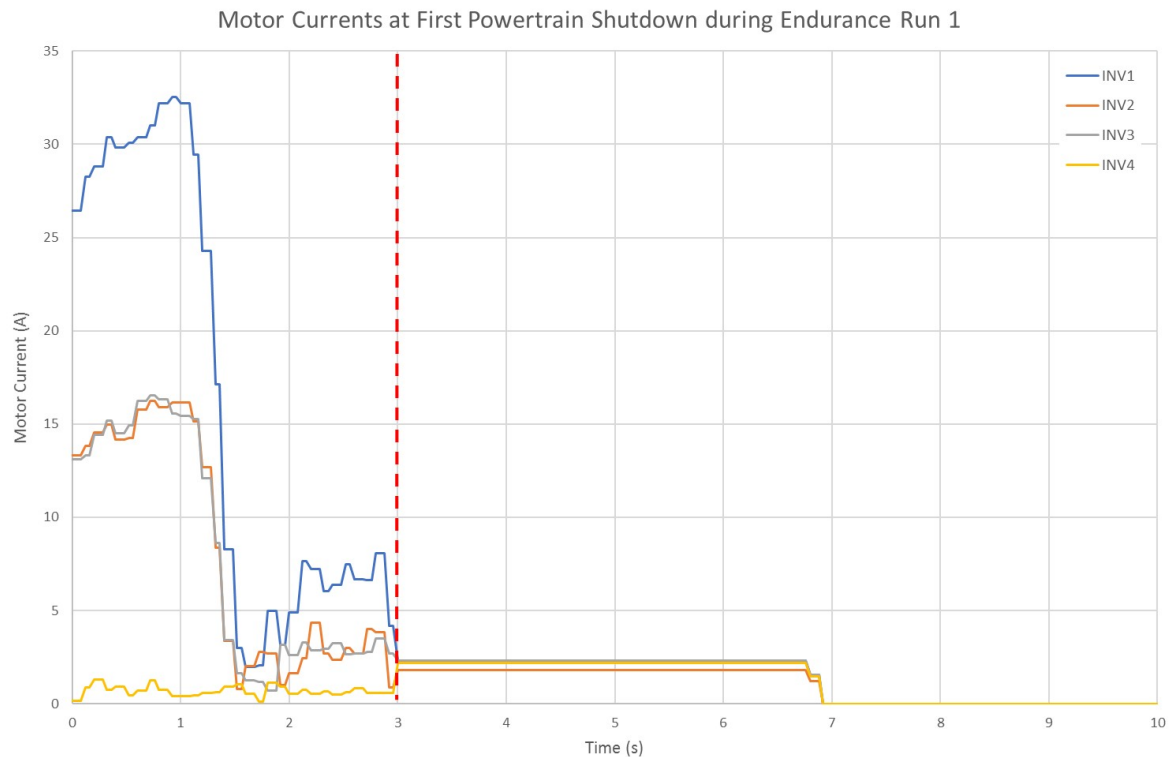


Figure 7.22. Plot of motor current data at first shutdown point (dashed red line) for endurance run 1

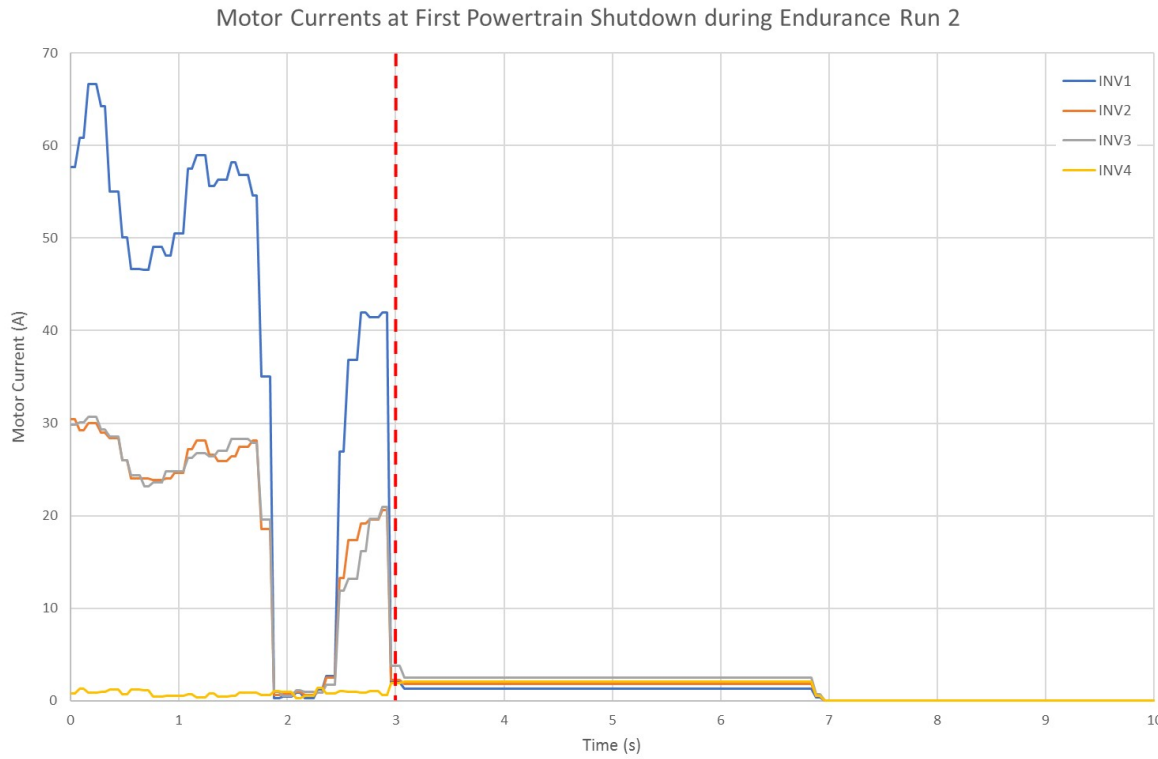


Figure 7.23. Plot of motor current data at first shutdown point (dashed red line) for endurance run 2

The fact that the durations shown in Figure 7.22 and Figure 7.23 are identical suggests the shutdown incidents were not coincidental, rather caused by the same fault. The error codes outputted by the sub-inverters during the first endurance run were zero (no error) over the entire run. However, during the second run all four sub-inverters generated error code 2318 just after the powertrain shutdown, as shown by Figure 7.24. This code refers to a “*Control deviation*” error, which is generated when the difference between the motor’s control position and actual position exceed a deviation parameter. The error code generated by the rear-right sub-inverter (INV1, orange trace) for much of the run (prior to the control deviation error) is the aforementioned motor overload warning (Section 7.2.1), and is not related to the powertrain stopping. The warning is only present on the rear-right since the rear-left sub-inverter had already disabled its output drive.

Figure 7.24 shows the control deviation error is generated only momentarily before the driver resets the car, and is delayed by ten seconds from when the tractive power drops to zero (indicating the powertrain has shut down). What is interesting is that, if this error was the cause for the powertrain to shut down, it was not generated during any other shutdown incident. In addition, the error occurs simultaneously across all four sub-inverters, which are controlled independently of each other by their respective controller cards. As the cause has yet to be determined (at the time of writing this thesis), it can only be theorised that error 2318 was either the cause of the powertrain shutdown, or a symptom exhibited as a result of a greater problem.

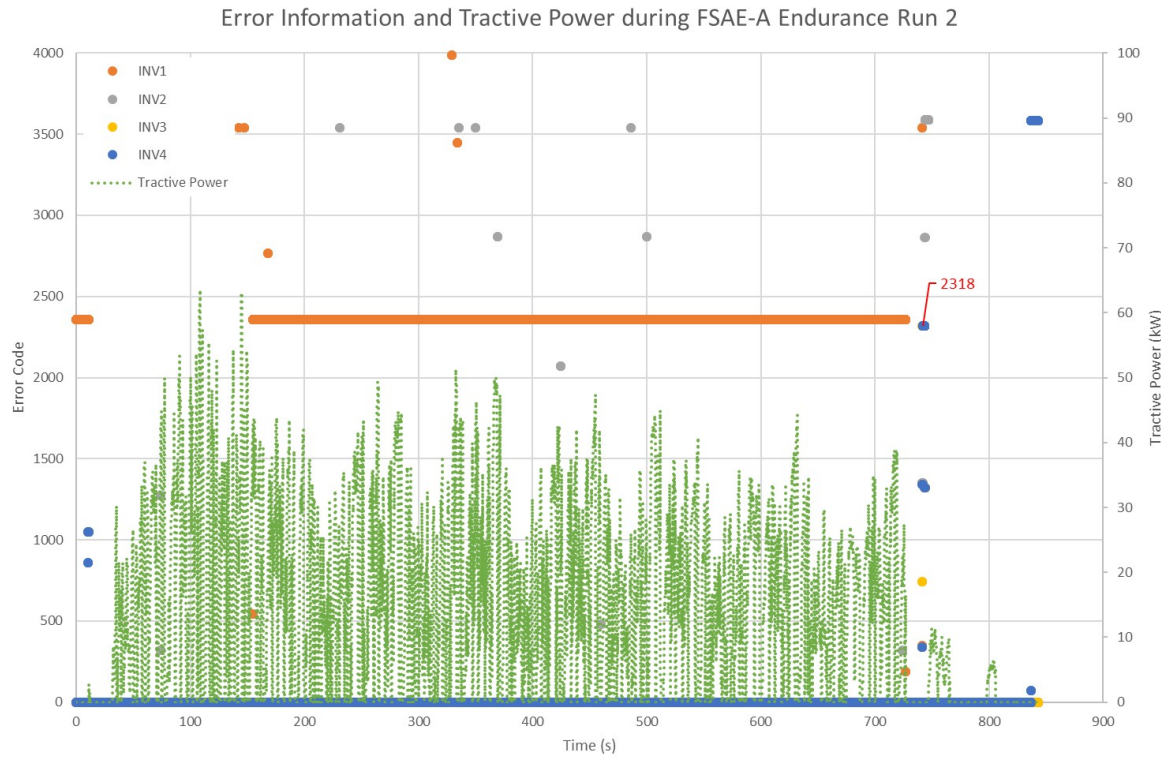


Figure 7.24. Plot of error information and tractive power during second endurance run, showing error code 2318 (data label) at first powertrain shutdown

Another theory for the powertrain to shut down is a software fault within the VCU. Since UCM16 had never been driven continuously for as long as both endurance events during testing, there was a possibility that a fault (for example a memory buffer overflowing) could have entered the control software. Considering this has happened previously in the development of the car (refer to Section 7.1.1), it was not an unlikely assumption.

In an attempt to prove this theory, the author drove UCM16 around a test track once the car had returned to New Zealand (post-competition) until the powertrain shut down. This occurred after approximately 10 minutes of drive time. As soon as the car stopped, the power to the VCU was cycled, thereby resetting the on-board microcontroller. Although the car would drive after the reset, it stopped after approximately 30 seconds and would no longer start (a similar occurrence to the endurance event). If the cause had been software related, it was expected that resetting the microcontroller would prevent the fault from occurring for another ten minutes (if the fault was time based). A second test, in which the entire powertrain was reset (in an attempt to remove any software faults within the inverter) resulted in a similar outcome. This hence suggests the cause is not related to vehicle software, rather a factor that is independent of the electrical system.

The most likely of these factors is inverter and motor temperature. The cooling system, designed by an undergraduate mechanical engineer, connected the inverter and four motors in series with a heat exchanger (radiator) and water pump. It is therefore assumed that each element in the system was not

cooled to its maximum potential due to heat transfer from the previous elements. This could have been resolved by splitting the system into five parallel streams with pressure regulating valves. Figure 7.25 and Figure 7.26 are plots of the inverter and motor temperatures during the second endurance run. The inverter temperature measures the temperature of the cooling plate at the location of the relevant sub-inverter. It shows the temperatures increasing from ambient (approximately 30 °C) over the duration of the run, and appears to plateau at maximum of 52.4 °C just prior to the powertrain stopping. Although this was within the default derating region (50 °C – 60 °C) set by AMK (refer to Table 3.3 in Section 3.1.2), the temperature limits were increased on the second endurance run (60 °C – 70 °C) in an attempt to remove temperature as the cause for stopping. Even if the limits had been set as default, the inverter temperature did not reach the maximum temperature and the inverter should have only reduced output power, not stop it. The same can be stated for the motor temperatures (Figure 7.26), whereby the derating region was adjusted from 125 °C – 140 °C to 135 °C – 150 °C. As shown by the motor temperatures plotted, the motors remained below this region over the duration of the run, and therefore should not have been an issue either.

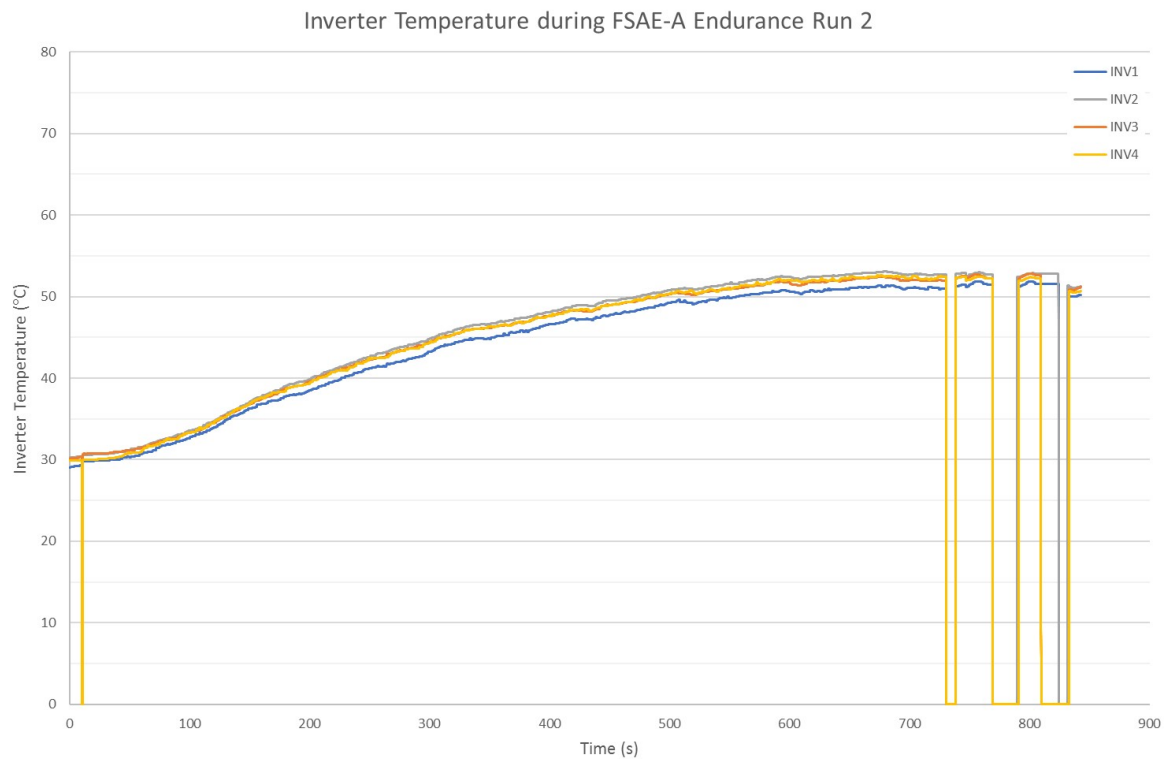


Figure 7.25. Plot of inverter temperature data during second endurance run

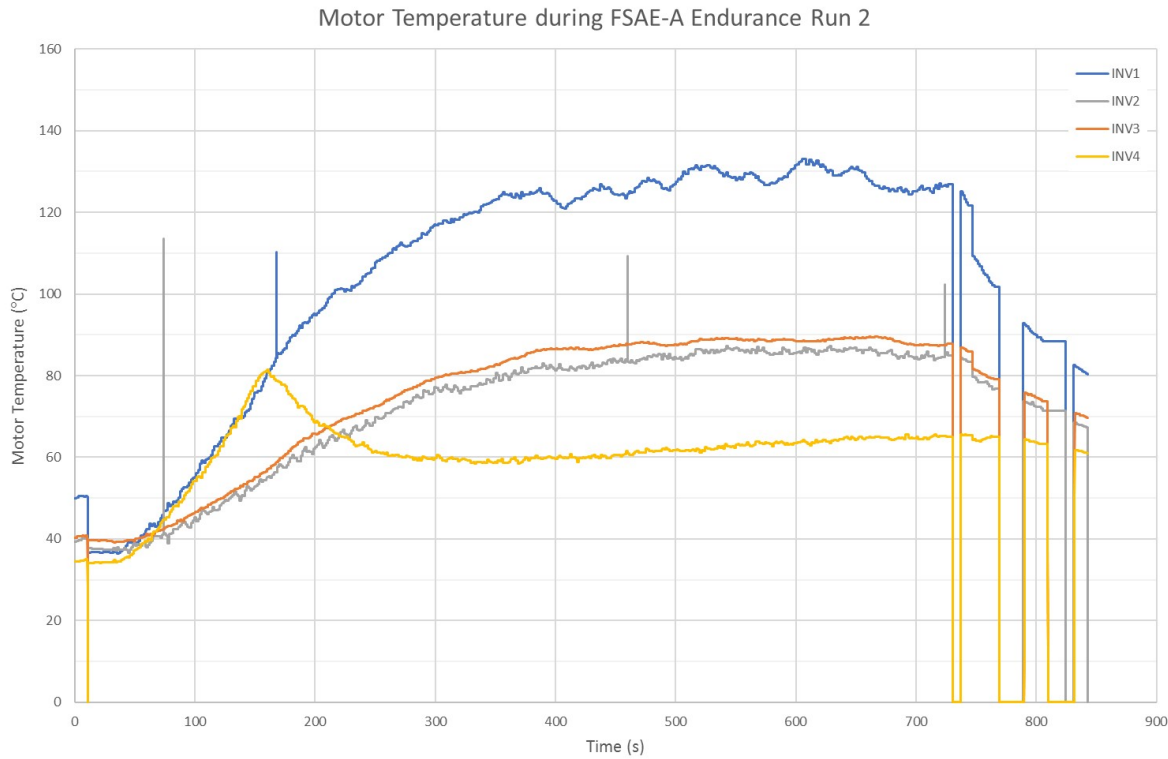


Figure 7.26. Plot of motor temperature data during second endurance run

Out of interest, and for the benefit of UCM's future designs, the energy consumption of both endurance runs have been plotted in Figure 7.27. The data cannot be compared directly, as the nature of each run differed significantly. Instead, a comparison based upon energy consumed per lap can be made, and thus suggest if UCM16's accumulator had enough capacity to finish the event. A total of 2.37 kWh was consumed on the first (conservative) run, resulting in a consumption of 0.263 kWh per lap for the nine laps completed. The second (performance) run consumed a total of 3.52 kWh, resulting in 0.44 kWh per lap for the eight laps completed⁵².

Based upon these consumption rates, the accumulator would have had enough energy to complete both runs. Over 18 laps, the total predicted consumptions were 4.73 kWh and 7.92 kWh for the first and second runs respectively. It should be noted that, had the rear-left inverter been operating correctly, the energy consumed per lap would have increased. In turn, the consumption of the second run would have been expected to align itself more with the consumption predicted from the simulation results (Section 4.1.1) and the autocross data (Section 7.2.1).

⁵² Interestingly, the second run had a per lap consumption less than that consumed in the Autocross event.

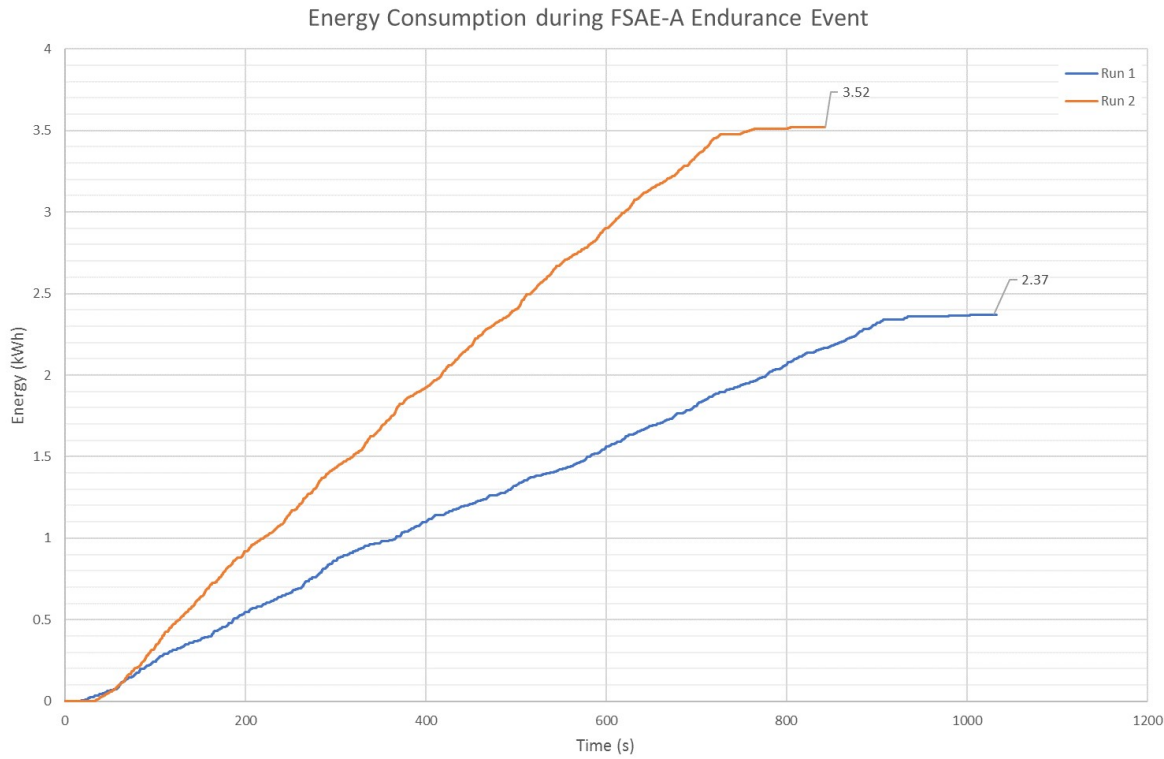


Figure 7.27. Plot of UCM16’s energy consumption during FSAE-A endurance event

7.3. CHAPTER SUMMARY

Chapter 7 was dedicated to the development of UCM16’s vehicle dynamic software, and then the results of the 2016 Formula SAE Australasian competition. After a potentially catastrophic software fault (in which the car started at maximum throttle) the code used to measure the throttle, brake and steering angle position sensors was rewritten to use direct memory access. In doing so, the microcontroller’s central processing unit was relieved of unnecessary analog conversions, which was causing interrupt subroutines to become nested.

Once UCM16 was driving in its final four-wheel drive configuration, the major improvement to its performance was through the torque vectoring and traction control algorithms. Torque vectoring was implemented by simplifying the car’s torque model into three parameters; a longitudinal bias, a lateral bias, and a front-inside-wheel bias. Each of these parameters were defined as a percentage, that was then used to manipulate the torque requested by the driver (through the throttle pedal). The longitudinal and front-inside parameters were defined as static biases, whilst the lateral bias was configured as a range of linear functions with respect to steering angle. Driver feedback was used to determine suitable values for each parameter. Ultimately, a longitudinal bias of 0.85 with lateral bias profile 2 was selected. No front-inside bias was applied.

Traction control was implemented to prevent a motor from experiencing an overcurrent fault in the event of a loss in traction. Loss of traction was assumed if a motor's speed exceeded that of the rear-outside motor by a predefined threshold. If detected, the algorithm immediately reduced motor torque to zero, and then gradually reapplied it once the motor's speed entered a “reapplication” threshold. Once applied, the traction control algorithm prevented any further motor overcurrent faults.

The University of Canterbury Motorsport team finished 12th overall in the 2016 FSAE-A competition, with podium places in the skid-pad, design and business events. As such, UCM was the first electric team to ever win a dynamic event at FSAE-A. Unfortunately, a series of unreliability issues prevented UCM16 from performing at its previously observed potential during the autocross and endurance events. The final section of this chapter discussed the data collected during these events, and attempted to speculate the cause of the electric powertrain stopping.

CHAPTER 8

CONCLUSION

This thesis presented the design, manufacture, development and testing of the electrical systems implemented in New Zealand's first four-wheel drive electric Formula SAE race car. The powertrain of UCM16 was selected to be the FSE Racing Kit, provided by AMK. This package included a liquid-cooled quad-inverter unit and four DD5-14-10-POW permanent magnet servo motors, which could be mounted within each wheel hub via a custom-designed, single-stage reduction planetary gearbox. A vehicle control unit was designed in-house to collate throttle, brake and steering angle sensors, and then control each motor independently via two dedicated CAN networks.

Three concepts were proposed for UCM16's tractive battery pack (accumulator), whereby a 588 Vdc (peak), 8.8 kWh pack consisting of 980 Samsung 18650-25R5 lithium-ion cells was selected. This concept featured eight modules of 126 cells that were to be connected in series to complete the final system. However, due to dimensional discrepancies between the 3D-model and manufactured product, the eighth module had to be removed, thereby reducing the peak voltage and capacity to 529.2 Vdc and 7.9 kWh respectively. At the front of the final accumulator assembly, a series of energy management and signal isolation circuits were designed, which monitored the status of each cell and initiated a predefined shutdown procedure in the event of a failure. Coupled with this, numerous circuits were designed external to the accumulator to monitor and then safely discharge the tractive system in the event of an emergency.

UCM16 was first driven as a rear-wheel drive race car, therefore allowing the preliminary designs to be tested in their intended application. The results highlighted the detrimental effect of electromagnetic interference (emitted from the quad-inverter) on the proprietary communication protocol used by the purchased battery management system. To resolve this, monitoring functionality was transferred from the supplied master controller to the self-developed isolation PCB (which served as the galvanically isolated interface between the car and accumulator). Electromagnetic interference was also found to affect the supplied current sensor, and was therefore replaced with a circuit that converted the measured current to the considerably more robust CAN protocol.

A large amount of focus was placed upon the development of the various vehicle dynamic software algorithms that were implemented on the vehicle control unit. Torque vectoring, which dynamically adjusted the application of motor torque across all four wheels, and traction control, which prevented excessive wheel spin due to loss of traction or vehicle weight transfer, were found to be extremely beneficial to the handling and performance of UCM16.

The University of Canterbury Motorsport team placed 12th overall in the 2016 Formula SAE Australasian competition (5th in the electric-vehicle category). Unfortunately, a series of reliability issues during the autocross and endurance events resulted in the race car not performing to the high standard that had been previously witnessed during test sessions. However, the team's endeavours and hard work resulted in three podium positions (design, business and skid pad), therefore making UCM the first electric team to win a dynamic event at the Australasian competition. Furthermore, the competition points gained meant UCM was ranked 25th worldwide for electric FSAE teams, and were the highest ranked first-year electric team of 2016.

8.1. RECOMMENDATIONS

In hindsight, there are numerous elements of the electrical system that the author would change, should the opportunity to be a part of Formula SAE arise again. For the benefit of UCM's future electrical teams (or other engineers considering an electric car), the most significant changes are summarised below (ordered according to their relevance to the designs described in this thesis).

- Vehicle Control Unit: The idea of developing an in-house VCU was incredibly ambitious and, whilst the car could drive using either revision, it was not without the expense of considerable time and effort that could have been focussed on refining other systems. It would have been more beneficial to select an off-the-shelf solution (for example a dSPACE AutoBox) which would guarantee a robust hardware platform on which the software could be developed. Innovation is important in Formula SAE, of which self-developing a VCU is a prime example. However, such a unit should have been developed as a non-crucial element of the race car, and integrated at a later stage.
- Accumulator construction: Using a home-made resistance welder to construct the first accumulator was a flawed idea, and resulted in the pack becoming all but useless after a month of testing. As recommended by the author, the team should have either invested in a professional product, or considered using a preassembled battery unit. Although either option requires greater financial investment, it is less expensive (both time and money) long-term.
- Accumulator Management System (AMS): There was no way of knowing that the Elithion Lithiumate BMS system was going to be so vulnerable to electromagnetic interference. To prevent a similar situation from occurring again, the author recommends that the only board-

to-board communication protocols used (for any system) are CAN or LIN (Local Interconnect Network), which are both designed for automotive applications.

- Tractive voltage indication: The tractive voltage indicator for the accumulator was redesigned multiple times and was never fully refined. In hindsight, the author admits they had tunnel-vision and thought the indicator could only be powered directly from the tractive bus. It is admitted that there were other forms of indication (for example an analogue voltage meter) that could have been used instead of an LED. However, an LED option was chosen from a style perspective. Regardless, a more elegant design would have been to utilise the pre-existing voltage measurement circuit on the Precharge PCB, and then power the indication LED from a rechargeable low voltage battery. Consideration would have to be taken when sizing the battery, such that the LED would remain active long enough to be detected by a user. To simplify this, a safety circuit could be introduced that illuminates a secondary LED dependent on the auxiliary battery's state of charge.

8.2. FINAL MENTIONS

As a final mention, the author would like to once again thank all those involved with UCM16. Although there are individuals who see the lack of an overall podium position a failure, the fact that the team managed to design and build a four-wheel drive electric car within a year (an undertaking many people considered unachievable) should be considered a win in itself. It was the dedication, teamwork and “never give up” attitude portrayed by all team members that made the author proud to be a member of the University of Canterbury Motorsport team. It is hence appropriate to finish this thesis by quoting Willem Toet, a motorsport, Formula One and aerodynamics specialist, who was present as an honorary guest at the Australasian competition.

“The University of Canterbury (NZ) have written themselves into the history books by, in just their 4th year in total in the competition, being the first electric team to win a dynamic event at Formula SAE-A. Last year they had a petrol car. This year 4-wheel drive electric. The team arrived in Melbourne without having practised energy recovery or torque vectoring. In testing at Oakleigh they got the computer programming done for torque vectoring and that helped them win the Skid pan. The fact that they did so much that was new to them meant they were let down by reliability concerns with their control electronics overheating in Endurance. One of many teams to watch out for in the future.”

Willem Toet – Motorsport, F1 and Aerodynamics Specialist [74]

APPENDIX A

RESEARCHED ELECTRIC FSAE TEAMS

Team	Country	Vehicle Name	Year	Mass (kg)	Motor(s)	Inverter(s)	Peak Power (kW)	RWD/4WD	Peak Voltage (V)	Capacity (kWh)	Cell Type
AMZ Racing	Switzerland	Furka	2010	227	2x AMZ BLDC	n.s.	60	RWD	n.s.	n.s.	LiPo
		Novena	2011	181	2x AMZ M1 PMSM ²	n.s.	70	RWD	n.s.	n.s.	LiPo
		Umbrail	2012	170	2x AMZ M2 PMSM ²	n.s.	80	RWD	n.s.	n.s.	LiPo
		Jullier	2013	180	4x AMZ M3 PMSM ²	n.s.	148	4WD	n.s.	n.s.	LiPo
		Grimsel	2014	168	4x AMZ M4 PMSM ²	n.s.	148	4WD	n.s.	n.s.	LiPo
		Flüela	2015	173	4x AMZ M5 PMSM ²	n.s.	148	4WD	n.s.	n.s.	LiPo
FS Team Delft	Netherlands	Gothard	2016	181	4x AMZ M6 PMSM ²	n.s.	156	4WD	n.s.	n.s.	LiPo
		DUT11	2011	177	2x AMK DT5-30-10	AMK	n.s.	RWD	355	5.7	LiPo
		DUT12	2012	148	4x AMK DT5-12-10	AMK	92	4WD	600	4.2	n.s.
		DUT13	2013	173	4x AMK DT5-14-10	AMK	104	4WD	n.s.	n.s.	n.s.
		DUT14	2014	152	4x AMK DT5-14-10	AMK	107	4WD	n.s.	n.s.	n.s.
		DUT15	2015	163	4x AMK DT5-14-10	AMK	131	4WD	n.s.	n.s.	n.s.
GreenTeam Stuttgart	Germany	DUT16	2016	160	4x AMK DT5-14-10	AMK	131	4WD	600	7.6	LiPo
		E0711-1	2010	280	2x AMK PMSM	AMK	94	RWD	n.s.	8.5	n.s.
		E0711-2	2011	260	2x AMK PMSM	AMK	104	RWD	n.s.	8.4	LiPo
		E0711-3	2012	230	2x AMK PMSM	AMK	112	RWD	600	6.9	LiPo
		E0711-4	2013	200	4x AMK PMSM	AMK	120	4WD	n.s.	6.2	n.s.
		E0711-5	2014	165	4x AMK PMSM	AMK	100	4WD	n.s.	6.62	n.s.
KA-Racing	Germany	E0711-6	2015	173	4x AMK PMSM	AMK	128	4WD	n.s.	6.8	n.s.
		KT10E	2010	298	1x PMSM ¹	n.s.	55	RWD	400	7.4	LiMn ₂ O ₄
		KT11E	2011	250	2x PMSM ¹	n.s.	84	RWD	410	5.6	LiFePO ₄
		KT12E	2012	220	2x PMSM ¹	n.s.	64	RWD	370	7.4	LiFePO ₄ (112s4p)
		KT13E	2013	<200	4x PMSM ¹	n.s.	85	4WD	355	6.4	LiPo
		KT14F	2014	<200	4x PMSM ¹	n.s.	85	4WD	355	6.4	LiPo
RMIT Electric Racing	Australia	KT15E	2015	195	4x PMSM ²	n.s.	n.s.	4WD	518	6.5	LiPo
		KT16E	2016	187	4x PMSM ²	n.s.	n.s.	4WD	518	6.5	LiPo
		R13e	2013	262	2x Motoenergy ME-0913 BDDC	2x Kelly KHB 14401	12	RWD	122	4.44	n.s.
		R14e	2014	262	Enstroj Emrax 228	Unitek Bamocar D3	45	RWD	470.4	6.6	n.s.
		R15e	2015	250	Enstroj Emrax 228	Unitek Bamocar D3	45	RWD	470.4	6.6	n.s.
		R16e	2016	197	Enstroj Emrax 228HV	Unitek Bamocar D3	75	RWD	487	6.4	n.s.
TU Fast Racing	Germany	t5_13	2013	289	2x Enstroj Emrax LC 228	2x Tritium WaveSculptor 200	80	RWD	453.6	6.39	UNiCoMnO ₂
		t5_14	2014	250	2x Enstroj Emrax LC 228	2x Tritium WaveSculptor 200	70	RWD	396.4	7	UNiCoMnO ₂
		EB011	2011	220	2x PMSM ¹	n.s.	200	RWD	n.s.	n.s.	n.s.
		EB012	2012	172	2x PMSM ¹	n.s.	120	RWD	n.s.	5.28	LiPo
		EB013	2013	186	2x Enstroj Emrax 228	Self-developed	120	RWD	400	5.28	LiPo
		EB014	2014	220	4x PMSM ¹	Self-developed	85	4WD	n.s.	6.7	LiPo
team Swinburne	Australia	EB015	2015	185	4x AMK DT5	AMK	124	4WD	600	7.6	LiPo
		EB016	2016	n.i.s.	4x AMK DT5	AMK	124	4WD	n.s.	7.6	n.s.

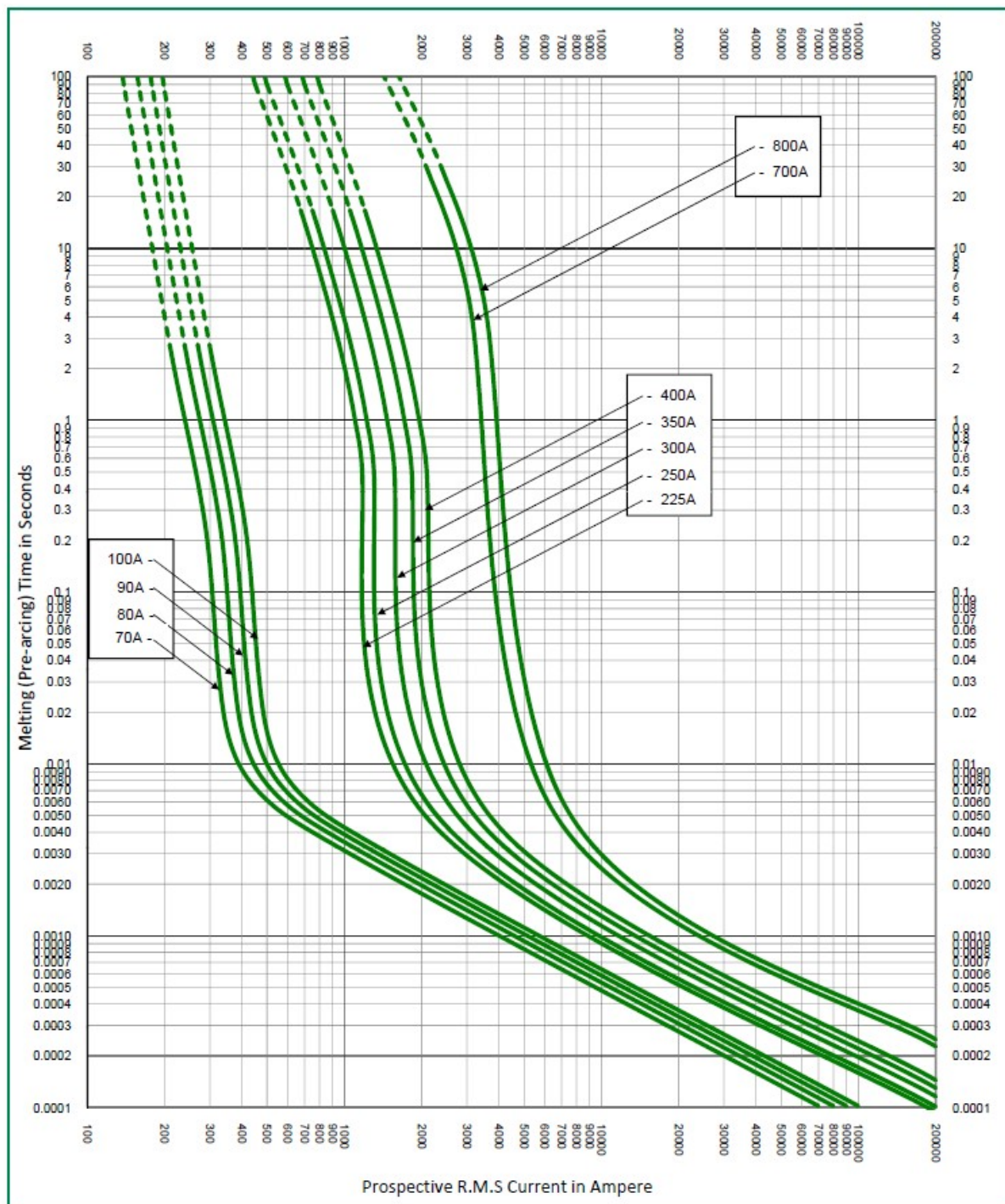
Data collected from respective team's website (updated April 2017)

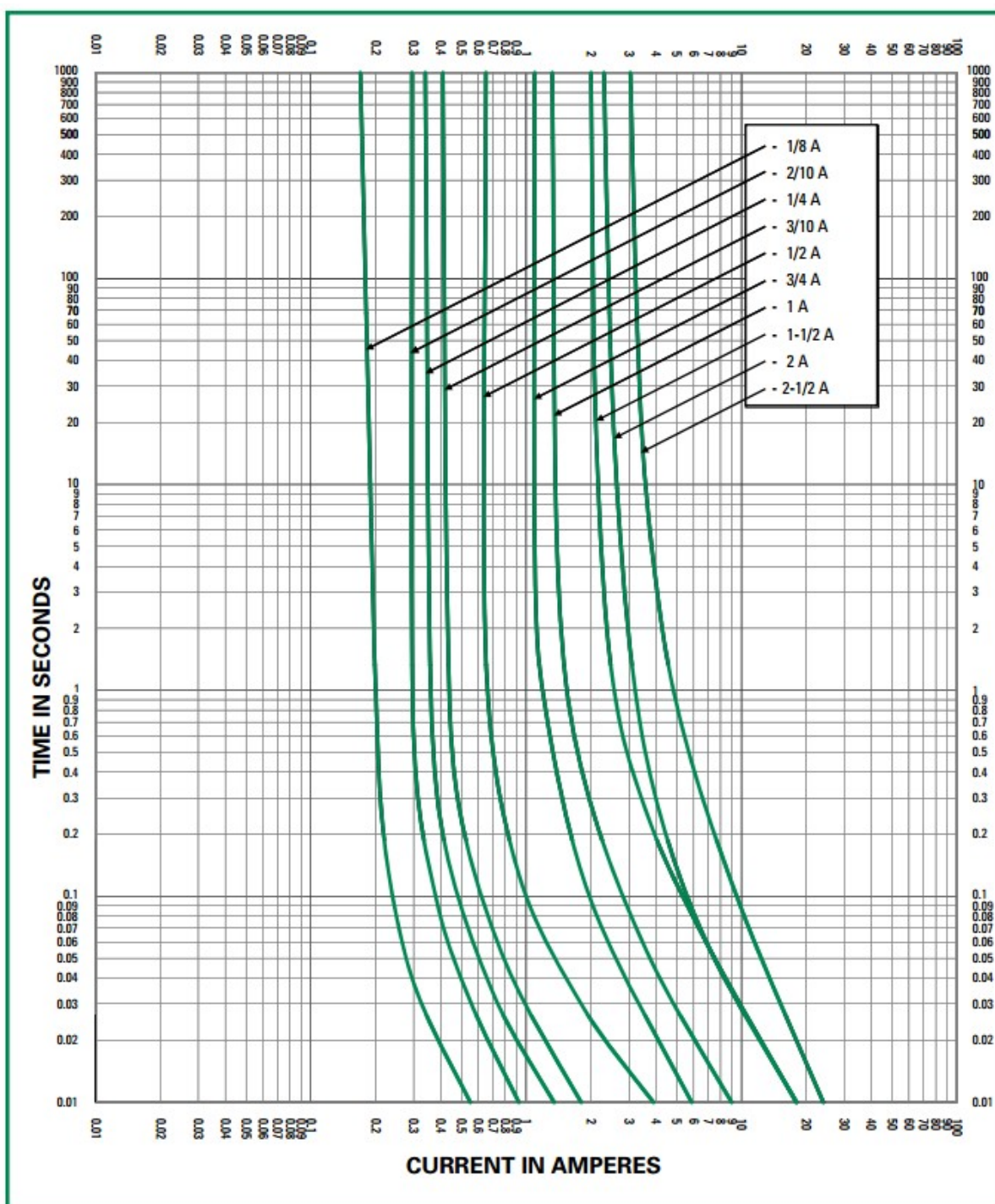
¹ Manufacturer not specified² Self-developed

APPENDIX B

LITTELFUSE L70S & KLKD FUSE TIME-CURRENT CURVES

L70S SERIES TIME-CURRENT CURVES [75]



KLKD SERIES TIME-CURRENT CURVES ($\frac{1}{8}$ – $2\frac{1}{2}$ A) [76]

APPENDIX C

DD5-14-10-POW MOTOR DATASHEET

AMK

Motor-Datenblatt motor data sheet

Bezeichnung/name **DD5-14-10-POW - 18600-B5**

Teile-Nr./part number **A2370DD**

Motorbeschreibung motor description:

Motorprinzip/motor principle:

Kühlart/cooling type:

Bauform/mounting type:

Schutzart/degree of protection:

Isolierklassef/insulation class:

Leistungsdaten performance data:

Betriebsart/duty type:

Dauerstillstandsmoment/continuous Stall Torque "Mo":

Maximales Moment/maximum torque "Mmax":

Bemessungsmoment/rated torque "Mr" (ID32771):

Bemessungsleistung/rated power "Pn":

Bemessungsdrehzahl/rated speed "Nr" (ID32772):

Theo. Leerlaufdrehzahl/theor. no-load-speed "No":

Betriebszeitkonstante/rotor time constant "Tr" (ID32774):

Stromregler current controller:

Nennstrom/rated current "In" (ID11-1):

Dauerstillsstrom/cont. stall current "Io" (ID34096):

Maximalstrom/maximum current "Imax" (ID109):

Maximale Dauer für/duration for "Imax" (ID34168):

Drehmomentkonstante/torque constant "Kt":

Spannungskonstante/voltage constant "Ke" (ID 34234):

Schaltung/connection type:

Polizahl/number of poles "2p" (ID32775):

Klemmenwiderstand/terminal resistance "Rtt" (ID34164):

Klemmeninduktivität/terminal inductance "Ltt" (ID34167):

Querachseninduktivität/quadrature axis inductance "Lq" (ID34046):

Hauptachseninduktivität/direct axis inductance "Ld" (ID34045):

Magn.-Strom/magn. current "Im" (ID32769):

Magn.-Spannung/magn. current "In" (ID32770):

Rotorzeitkonstante/rotor time constant "Tr" (ID32774):

Regelereinstellung controller settings:

Drehzahlregler speed controller (default for plain motor):

Verstärkung/gain "Kp" (ID34151):

Verstärkung d-Achse/gain d-axis "Kpd" (ID34152):

Nachsteilzeitkonstante/time constant "Tnq" (ID34050):

Nachsteilzeitkonstante/time constant "Trd" (ID34052):

Adaption Verstärkung/adaption gain "Kpq2" (ID 34179)

Adaption Nachstellzeit/adaption time constant "Trq2" (ID 34180)

Untere Anpaßschwelle/lower adaption limit "Iua" (ID34177):

Obere Anpaßschwelle/upper adaption limit "Ioa" (ID34178):

Verstärkung/gain "Kp_n" (ID100):

Nachsteilzeitkonstante/time constant "Tn_n" (ID101):

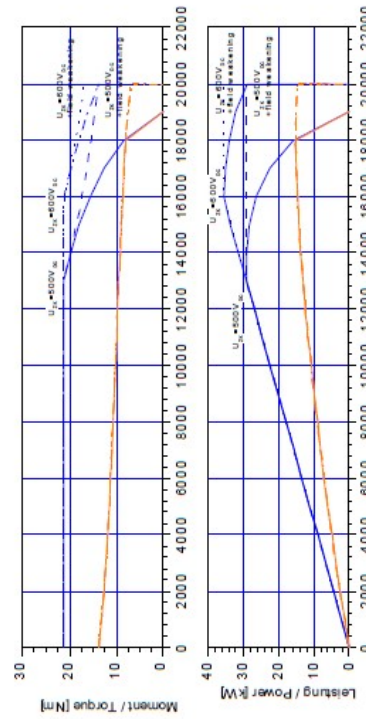
Spannungsregler voltage controller:

Spannungsregler/voltage controller "Kp" (ID34148):

Spannungsregler/voltage controller "Tr" (ID34149):

Spannungsüberhöhung "dU" (ID34235):

Systemwiderstand "Rs" (ID34233):



Kennlinie kann die maximal zulässige Drehzahl überschreiten! / Characteristic may exceed mechanical speed limit of motor

Für dieses Dokument und die darin enthaltenen Angaben behalten wir uns alle Rechte und technische Änderungen vor
All rights reserved for this document and all information included. Technical modifications reserved
[c] AMK Antriebs- und Steuerungstechnik GmbH Co. KG

AMK**Motor-Datenblatt motor data sheet****DD5-14-10-POW - 18600-B5****A2370DD**

- Formula Student Datum/date: 24.06.2015

Zeichn.-Nr./drawing no.: 12703-01260

Mechanische Daten mechanical data:

Gesamtmasse/motor mass "m":

Motorträgheitsmoment/inertia "J":

Mech. zul. Drehzahl/mech. speed limit "Nmax":
Rundlauf/run out (DIN 42955):Wuchtgüte/balancing quality:
Schwingstärke/vibration level (DIN ISO 2373):Passfeder/shaft key:

Bremssendaten brake data:

Typ/type:

Bremsmoment/brake torque:

Bremsstrom/brake current:

Bremsspannung/brake voltage:

Spannungsart/voltage type

Einfallzeit/engagement time "T_e":
max. Bremsenergie/max. braking energy:einmalig/single engagement:
Lebensdauer/lifetime:**Lüfterdaten fan data:**

AMK-TNr./AMK part number:

Luftspannung/fan voltage:

Strom/current:

Frequenz/frequency:

Lagerbelastung bearing load:**A/B - Lager/AB - side bearing:**Lagertyp/bearing type:
Fettsorte/type of grease:theo. Fettgebrauchsdaue/grease life time:
bei Nenndrehzahl und 70°C Lageraußenringtemp/at rated speed and 156°F at outer bearing ring
erforderliche Fettmenge/necessary grease quantity :Maximale Axialkraft bei Montage/max. axial force for assembly:
A - Lager/A - side bearing:

(Lastangriff Mitte Antriebswelle):

(Force to the middle of the shaft):

6005 / 6003

GE2 / GE2

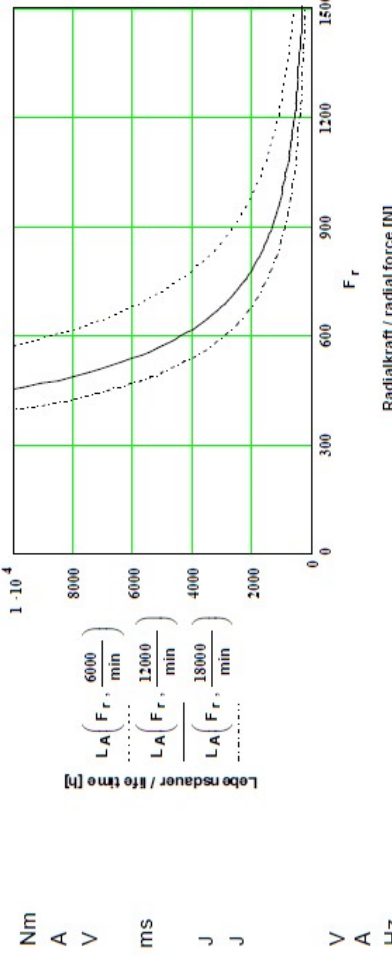
h

13000 / 18000

g

0 /

3275 N

**Geberdaten position encoder data:**AMK-TNr./AMK part number: 108072
Typ/type: PImpulszahl/number of pulses: 262144
Daten nur gültig mit entsprechender Wasserkühlung**Wicklungsschutz thermistor:**Typ/type (ID34166): KTY84
Ansprechtemp./operation temp: - °C
Widerstand/resistance (25°C) <=: 629 ΩÄnderungsstand Mechanik/revision motor-mechanics: 0.00
Änderungsdatum/motor revision motor date 30.03.2015**Bemerkungen remarks:**

automatisch erstellt, Geber 18 Bit

* Typenschildbezeichnung unterstrichen; bitte bei Rückfragen immer angeben/Namplate data underlined; please state with every inquiry

Zeichn.-Nr./drawing no.: 12703-01260

Datum/date: 24.06.2015

Änderungsdatum/motor revision motor date 30.03.2015

Zeichn.-Nr./drawing no.: 12703-01260

Datum/date: 24.06.2015

Änderungsdatum/motor revision motor date 30.03.2015

Zeichn.-Nr./drawing no.: 12703-01260

Datum/date: 24.06.2015

Änderungsdatum/motor revision motor date 30.03.2015

Zeichn.-Nr./drawing no.: 12703-01260

Datum/date: 24.06.2015

Änderungsdatum/motor revision motor date 30.03.2015

Zeichn.-Nr./drawing no.: 12703-01260

Datum/date: 24.06.2015

Änderungsdatum/motor revision motor date 30.03.2015

Zeichn.-Nr./drawing no.: 12703-01260

Datum/date: 24.06.2015

Änderungsdatum/motor revision motor date 30.03.2015

Zeichn.-Nr./drawing no.: 12703-01260

Datum/date: 24.06.2015

Änderungsdatum/motor revision motor date 30.03.2015

Zeichn.-Nr./drawing no.: 12703-01260

Datum/date: 24.06.2015

Änderungsdatum/motor revision motor date 30.03.2015

Zeichn.-Nr./drawing no.: 12703-01260

Datum/date: 24.06.2015

Änderungsdatum/motor revision motor date 30.03.2015

Zeichn.-Nr./drawing no.: 12703-01260

Datum/date: 24.06.2015

Änderungsdatum/motor revision motor date 30.03.2015

Zeichn.-Nr./drawing no.: 12703-01260

Datum/date: 24.06.2015

Änderungsdatum/motor revision motor date 30.03.2015

Zeichn.-Nr./drawing no.: 12703-01260

Datum/date: 24.06.2015

Änderungsdatum/motor revision motor date 30.03.2015

Zeichn.-Nr./drawing no.: 12703-01260

Datum/date: 24.06.2015

Änderungsdatum/motor revision motor date 30.03.2015

Zeichn.-Nr./drawing no.: 12703-01260

Datum/date: 24.06.2015

Änderungsdatum/motor revision motor date 30.03.2015

Zeichn.-Nr./drawing no.: 12703-01260

Datum/date: 24.06.2015

Änderungsdatum/motor revision motor date 30.03.2015

Zeichn.-Nr./drawing no.: 12703-01260

Datum/date: 24.06.2015

Änderungsdatum/motor revision motor date 30.03.2015

Zeichn.-Nr./drawing no.: 12703-01260

Datum/date: 24.06.2015

Änderungsdatum/motor revision motor date 30.03.2015

Zeichn.-Nr./drawing no.: 12703-01260

Datum/date: 24.06.2015

Änderungsdatum/motor revision motor date 30.03.2015

Zeichn.-Nr./drawing no.: 12703-01260

Datum/date: 24.06.2015

Änderungsdatum/motor revision motor date 30.03.2015

Zeichn.-Nr./drawing no.: 12703-01260

Datum/date: 24.06.2015

Änderungsdatum/motor revision motor date 30.03.2015

Zeichn.-Nr./drawing no.: 12703-01260

Datum/date: 24.06.2015

Änderungsdatum/motor revision motor date 30.03.2015

Zeichn.-Nr./drawing no.: 12703-01260

Datum/date: 24.06.2015

Änderungsdatum/motor revision motor date 30.03.2015

Zeichn.-Nr./drawing no.: 12703-01260

Datum/date: 24.06.2015

Änderungsdatum/motor revision motor date 30.03.2015

Zeichn.-Nr./drawing no.: 12703-01260

Datum/date: 24.06.2015

Änderungsdatum/motor revision motor date 30.03.2015

Zeichn.-Nr./drawing no.: 12703-01260

Datum/date: 24.06.2015

Änderungsdatum/motor revision motor date 30.03.2015

Zeichn.-Nr./drawing no.: 12703-01260

Datum/date: 24.06.2015

Änderungsdatum/motor revision motor date 30.03.2015

Zeichn.-Nr./drawing no.: 12703-01260

Datum/date: 24.06.2015

Änderungsdatum/motor revision motor date 30.03.2015

Zeichn.-Nr./drawing no.: 12703-01260

Datum/date: 24.06.2015

Änderungsdatum/motor revision motor date 30.03.2015

Zeichn.-Nr./drawing no.: 12703-01260

Datum/date: 24.06.2015

Änderungsdatum/motor revision motor date 30.03.2015

Zeichn.-Nr./drawing no.: 12703-01260

Datum/date: 24.06.2015

Änderungsdatum/motor revision motor date 30.03.2015

Zeichn.-Nr./drawing no.: 12703-01260

Datum/date: 24.06.2015

Änderungsdatum/motor revision motor date 30.03.2015

Zeichn.-Nr./drawing no.: 12703-01260

Datum/date: 24.06.2015

Änderungsdatum/motor revision motor date 30.03.2015

Zeichn.-Nr./drawing no.: 12703-01260

Datum/date: 24.06.2015

Änderungsdatum/motor revision motor date 30.03.2015

Zeichn.-Nr./drawing no.: 12703-01260

Datum/date: 24.06.2015

Änderungsdatum/motor revision motor date 30.03.2015

Zeichn.-Nr./drawing no.: 12703-01260

Datum/date: 24.06.2015

Änderungsdatum/motor revision motor date 30.03.2015

Zeichn.-Nr./drawing no.: 12703-01260

Datum/date: 24.06.2015

Änderungsdatum/motor revision motor date 30.03.2015

Zeichn.-Nr./drawing no.: 12703-01260

Datum/date: 24.06.2015

Änderungsdatum/motor revision motor date 30.03.2015

Zeichn.-Nr./drawing no.: 12703-01260

Datum/date: 24.06.2015

Änderungsdatum/motor revision motor date 30.03.2015

Zeichn.-Nr./drawing no.: 12703-01260

Datum/date: 24.06.2015

Änderungsdatum/motor revision motor date 30.03.2015

Zeichn.-Nr./drawing no.: 12703-01260

Datum/date: 24.06.2015

Änderungsdatum/motor revision motor date 30.03.2015

Zeichn.-Nr./drawing no.: 12703-01260

Datum/date: 24.06.2015

Änderungsdatum/motor revision motor date 30.03.2015

Zeichn.-Nr./drawing no.: 12703-01260

Datum/date: 24.06.2015

Änderungsdatum/motor revision motor date 30.03.2015

Zeichn.-Nr./drawing no.: 12703-01260

Datum/date: 24.06.2015

Änderungsdatum/motor revision motor date 30.03.2015

Zeichn.-Nr./drawing no.: 12703-01260

Datum/date: 24.06.2015

Änderungsdatum/motor revision motor date 30.03.2015

Zeichn.-Nr./drawing no.: 12703-01260

Datum/date: 24.06.2015

Änderungsdatum/motor revision motor date 30.03.2015

Zeichn.-Nr./drawing no.: 12703-01260

Datum/date: 24.06.2015

Änderungsdatum/motor revision motor date 30.03.2015

Zeichn.-Nr./drawing no.: 12703-01260

Datum/date: 24.06.2015

Änderungsdatum/motor revision motor date 30.03.2015

Zeichn.-Nr./drawing no.: 12703-01260

Datum/date: 24.06.2015

Änderungsdatum/motor revision motor date 30.03.2015

Zeichn.-Nr./drawing no.: 12703-01260

Datum/date: 24.06.2015

Änderungsdatum/motor revision motor date 30.03.2015

Zeichn.-Nr./drawing no.: 12703-01260

Datum/date: 24.06.2015

Änderungsdatum/motor revision motor date 30.03.2015

Zeichn.-Nr./drawing no.: 12703-01260

Datum/date: 24.06.2015

Änderungsdatum/motor revision motor date 30.03.2015

Zeichn.-Nr./drawing no.: 12703-01260

Datum/date: 24.06.2015

Änderungsdatum/motor revision motor date 30.03.2015

Zeichn.-Nr./drawing no.: 12703-01260

Datum/date: 24.06.2015

Änderungsdatum/motor revision motor date 30.03.2015

Zeichn.-Nr./drawing no.: 12703-01260

Datum/date: 24.06.2015

Änderungsdatum/motor revision motor date 30.03.2015

Zeichn.-Nr./drawing no.: 12703-01260

Datum/date: 24.06.2015

Änderungsdatum/motor revision motor date 30.03.2015

Zeichn.-Nr./drawing no.: 12703-01260

Datum/date: 24.06.2015

Änderungsdatum/motor revision motor date 30.03.2015

Zeichn.-Nr./drawing no.: 12703-01260

Datum/date: 24.06.2015

Änderungsdatum/motor revision motor date 30.03.2015

Zeichn.-Nr./drawing no.: 12703-01260

Datum/date: 24.06.2015

Änderungsdatum/motor revision motor date 30.03.2015

Zeichn.-Nr./drawing no.: 12703-01260

Datum/date: 24.06.2015

Änderungsdatum/motor revision motor date 30.03.2015

Zeichn.-Nr./drawing no.:

APPENDIX D

AMK CAN MESSAGES

Tables are extracted from AMK FSE Racing Kit User Manual [50].

AMK ACTUAL VALUES 1

Name	Offset	Length in bits	Value type	Unit	Meaning
AMK_Status	0	16	Unsigned	-	Status word See the table below: Content of the 'AMK_Status' status word
AMK_ActualVelocity	16	16	Signed	rpm	Actual speed value
AMK_TorqueCurrent	32	16	Signed	-	Raw data for calculating 'actual torque current' I_q See 'Units' on page 61.
AMK_MagnetizingCurrent	48	16	Signed	-	Raw data for calculating 'actual magnetizing current' I_d See 'Units' on page 1.

“AMK_STATUS” WORD CONTENTS

Name	Offset	Length in bits	Meaning
AMK_bReserve	0	8	Reserved
AMK_bSystemReady	8	1	System ready (SBM)
AMK_bError	9	1	Error
AMK_bWarn	10	1	Warning
AMK_bQuitDcOn	11	1	HV activation acknowledgment
AMK_bDcOn	12	1	HV activation level
AMK_bQuitInverterOn	13	1	Controller enable acknowledgment
AMK_bInverterOn	14	1	Controller enable level
AMK_bDerating	15	1	Derating (torque limitation active)

AMK ACTUAL VALUES 2

Name	Offset	Length in bits	Value type	Unit	Meaning
AMK_TempMotor	0	16	Signed	0.1 °C	Motor temperature
AMK_TempInverter	16	16	Signed	0.1 °C	Cold plate temperature
AMK_ErrorInfo	32	16	Unsigned	-	Diagnostic number
AMK_TempIGBT	48	16	Signed	0.1 °C	IGBT temperature

AMK_SETPOINTS

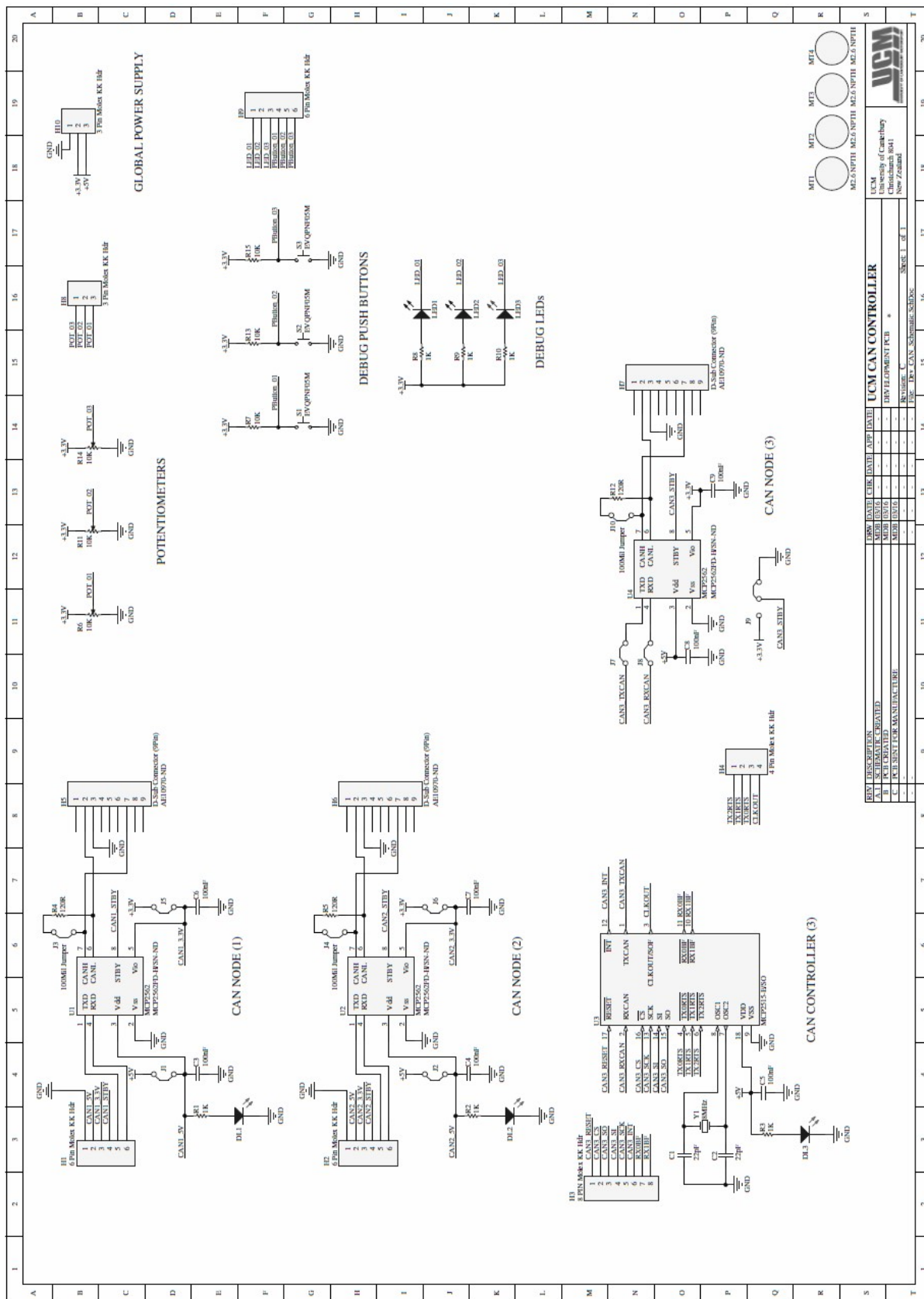
Name	Offset	Length in bits	Value type	Unit	Meaning
AMK_Control	0	16	Unsigned	-	Control word See the table below: Content of the 'AMK_Control' control word
AMK_TargetVelocity	16	16	Signed	rpm	Speed setpoint
AMK_TorqueLimitPositiv	32	16	Signed	0.1% M_N	Positive torque limit (subject to nominal torque)
AMK_TorqueLimitNegativ	48	16	Signed	0.1% M_N	Negative torque limit (subject to nominal torque)

“AMK_CONTROL” WORD CONTENTS

Name	Offset	Length in bits	Meaning
AMK_bReserve	0	8	Reserved
AMK_bInverterOn	8	1	Controller enable
AMK_bDcOn	9	1	HV activation
AMK_bEnable	10	1	Driver enable
AMK_bErrorReset	11	1	Remove error*
AMK_bReserve	12	4	Reserved

APPENDIX E

CAN CONTROLLER PCB SCHEMATIC



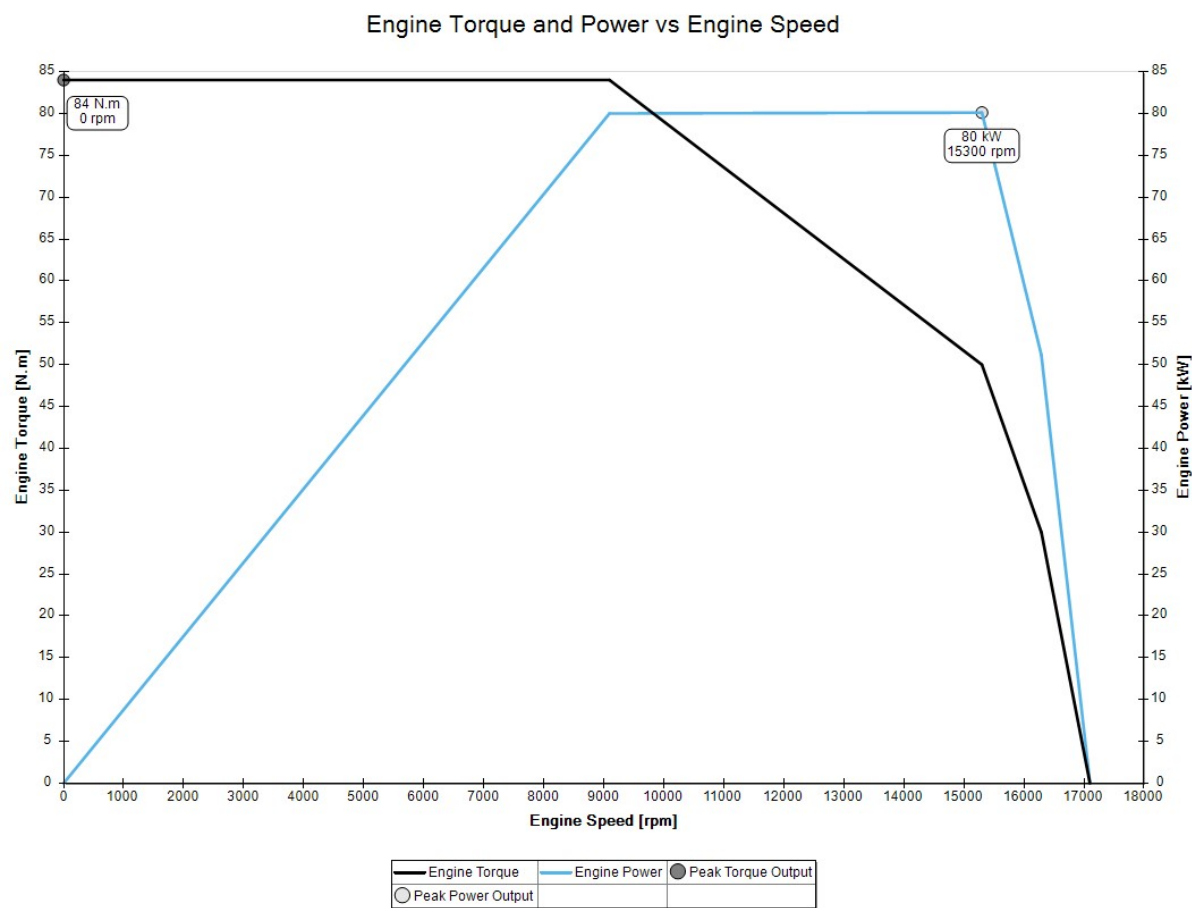
APPENDIX F

OPTIMUM LAP VEHICLE SIMULATION MODEL

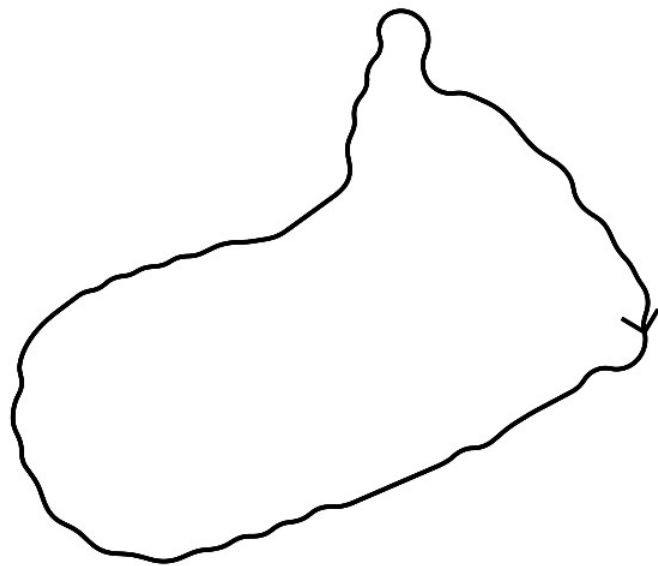
VEHICLE SETUP PARAMETERS

VEHICLE SETUP	
General Data	
Vehicle Type <input type="button" value="FSAE"/>	
Mass <input type="text" value="260.000"/> kg	Driven Type <input checked="" type="radio"/> 2WD <input type="radio"/> AWD
Aero Data	
<input checked="" type="radio"/> Drag-Lift	<input type="radio"/> Efficiency-Lift
Drag Coefficient <input type="text" value="1.600"/> -	Downforce Coefficient <input type="text" value="4.000"/> -
Front Area <input type="text" value="1.090"/> m ²	Air Density <input type="text" value="1.260"/> kg/m ³
Tire Data	
Tire Radius <input type="text" value="0.226"/> m	Rolling Resistance <input type="text" value="0.030"/> -
Longitudinal Friction <input type="text" value="2.200"/> -	Lateral Friction <input type="text" value="2.200"/> -
ENGINE DATA	
Add / Remove Torque Data	
<input type="button" value="L1"/> <input type="button" value="L2"/> <input type="button" value="L3"/>	
Engine Speed (rpm) <input type="text" value="0"/>	Engine Torque (N.m) <input type="text" value="84.00"/>
9095	84.00
15300	50.00
16290	30.00
17100	0.00
Thermal Efficiency (optional) <input type="text" value="85.000"/> %	
Fuel Energy Density (optional) <input type="button" value="Lithiumion"/> <input type="text" value="720000"/> J/kg	
TRANSMISSION DATA	
Transmission Type <input type="button" value="Sequential Gearbox"/>	
Add / Remove Gears	
<input type="button" value="Add"/>	<input type="button" value="Remove"/>
Gear Ratios	
<input type="button" value="Gear 1"/>	<input type="text" value="1.0000"/>
Final Drive Ratio <input type="text" value="12.500"/> -	
Drive Efficiency <input type="text" value="90.000"/> %	
SCALING FACTORS	
Power Factor <input type="text" value="100.000"/> %	Aero Factor <input type="text" value="100.000"/> %
Grip Factor <input type="text" value="100.000"/> %	

MOTOR OUTPUT PERFORMANCE CURVES



2011 FORMULA SAE AUSTRALASIA ENDURANCE TRACK MODEL



APPENDIX G

A123 AMP20M1HD-A CELL SELECTION TOOLS

TOOL 1: DETERMINE NUMBER OF SERIES CELLS

Accumulator Limitations		A123 AMP20M1HD-A						
Vacc, max	600 Vdc	V _{cell} , max	3.6 Vdc	I _{cell, cont, max}	200 A			
Pacc, max	80 kW	V _{cell} , nom	3.3 Vdc	I _{cell, pulse, max}	600 A			
		V _{cell} , min	2.0 Vdc					
		Cap. _{cell, nom}	20 Ah					
		Cap. _{cell, min}	19.5 Ah					
		M _{cell}	0.495 kg					
N _{cells} (NSTP)	V _{acc, max} (V)	V _{acc, nominal} (V)	V _{acc, min} (V)	Capacity _{acc, nom} (kWh)	Capacity _{acc, min} (kWh)	M _{acc} (kg)	I _{acc, max} (A)	P _{acc, cont, out} (kW)
100	360	330	200	6.60	6.44	49.50	400.0	66.0
101	363.6	333.3	202	6.67	6.50	50.00	396.0	66.7
102	367.2	336.6	204	6.73	6.56	50.49	392.2	67.3
103	370.8	339.9	206	6.80	6.63	50.99	388.3	68.0
104	374.4	343.2	208	6.86	6.69	51.48	384.6	68.6
105	378	346.5	210	6.93	6.76	51.98	381.0	69.3
106	381.6	349.8	212	7.00	6.82	52.47	377.4	70.0
107	385.2	353.1	214	7.06	6.89	52.97	373.8	70.6
108	388.8	356.4	216	7.13	6.95	53.46	370.4	71.3
109	392.4	359.7	218	7.19	7.01	53.96	367.0	71.9
110	396	363	220	7.26	7.08	54.45	363.6	72.6
111	399.6	366.3	222	7.33	7.14	54.95	360.4	73.3
112	403.2	369.6	224	7.39	7.21	55.44	357.1	73.9
113	406.8	372.9	226	7.46	7.27	55.94	354.0	74.6
114	410.4	376.2	228	7.52	7.34	56.43	350.9	75.2
115	414	379.5	230	7.59	7.40	56.93	347.8	75.9
116	417.6	382.8	232	7.66	7.46	57.42	344.8	76.6
117	421.2	386.1	234	7.72	7.53	57.92	341.9	77.2
118	424.8	389.4	236	7.79	7.59	58.41	339.0	77.9
119	428.4	392.7	238	7.85	7.66	58.91	336.1	78.5
120	432	396	240	7.92	7.72	59.40	333.3	79.2
121	435.6	399.3	242	7.99	7.79	59.90	330.6	79.9
122	439.2	402.6	244	8.05	7.85	60.39	327.9	80.5
123	442.8	405.9	246	8.12	7.92	60.89	325.2	81.2
124	446.4	409.2	248	8.18	7.98	61.38	322.6	81.8
125	450	412.5	250	8.25	8.04	61.88	320.0	82.5
126	453.6	415.8	252	8.32	8.11	62.37	317.5	83.2
127	457.2	419.1	254	8.38	8.17	62.87	315.0	83.8
128	460.8	422.4	256	8.45	8.24	63.36	312.5	84.5
129	464.4	425.7	258	8.51	8.30	63.86	310.1	85.1
130	468	429	260	8.58	8.37	64.35	307.7	85.8
131	471.6	432.3	262	8.65	8.43	64.85	305.3	86.5
132	475.2	435.6	264	8.71	8.49	65.34	303.0	87.1
133	478.8	438.9	266	8.78	8.56	65.84	300.8	87.8
134	482.4	442.2	268	8.84	8.62	66.33	298.5	88.4
135	486	445.5	270	8.91	8.69	66.83	296.3	89.1

136	489.6	448.8	272	8.98	8.75	67.32	294.1	89.8
137	493.2	452.1	274	9.04	8.82	67.82	292.0	90.4
138	496.8	455.4	276	9.11	8.88	68.31	289.9	91.1
139	500.4	458.7	278	9.17	8.94	68.81	287.8	91.7
140	504	462	280	9.24	9.01	69.30	285.7	92.4
141	507.6	465.3	282	9.31	9.07	69.80	283.7	93.1
142	511.2	468.6	284	9.37	9.14	70.29	281.7	93.7
143	514.8	471.9	286	9.44	9.20	70.79	279.7	94.4
144	518.4	475.2	288	9.50	9.27	71.28	277.8	95.0
145	522	478.5	290	9.57	9.33	71.78	275.9	95.7
146	525.6	481.8	292	9.64	9.40	72.27	274.0	96.4
147	529.2	485.1	294	9.70	9.46	72.77	272.1	97.0
148	532.8	488.4	296	9.77	9.52	73.26	270.3	97.7
149	536.4	491.7	298	9.83	9.59	73.76	268.5	98.3
150	540	495	300	9.90	9.65	74.25	266.7	99.0
151	543.6	498.3	302	9.97	9.72	74.75	264.9	99.7
152	547.2	501.6	304	10.03	9.78	75.24	263.2	100.3
153	550.8	504.9	306	10.10	9.85	75.74	261.4	101.0
154	554.4	508.2	308	10.16	9.91	76.23	259.7	101.6
155	558	511.5	310	10.23	9.97	76.73	258.1	102.3
156	561.6	514.8	312	10.30	10.04	77.22	256.4	103.0
157	565.2	518.1	314	10.36	10.10	77.72	254.8	103.6
158	568.8	521.4	316	10.43	10.17	78.21	253.2	104.3
159	572.4	524.7	318	10.49	10.23	78.71	251.6	104.9
160	576	528	320	10.56	10.30	79.20	250.0	105.6
161	579.6	531.3	322	10.63	10.36	79.70	248.4	106.3
162	583.2	534.6	324	10.69	10.42	80.19	246.9	106.9
163	586.8	537.9	326	10.76	10.49	80.69	245.4	107.6
164	590.4	541.2	328	10.82	10.55	81.18	243.9	108.2
165	594	544.5	330	10.89	10.62	81.68	242.4	108.9
166	597.6	547.8	332	10.96	10.68	82.17	241.0	109.6

TOOL 2: DETERMINE VALID MODULE CONFIGURATION

A123 AMP20M1HD-A
V _{nom} = 3.3 V
V _{max} = 3.6 V
C _{nom} = 20 Ah

FSAE Accumulator Max Limits
V _{max} = 120 V
E _{max} = 6 MJ

MODULE CONFIGURATION

Total Cells	N	Cells	V _{max} (V)	Capacity _{max} (kWh)	Capacity _{max} (MJ)	Valid
120	1	120.0	432.00	8.64	31.10	0
	2	60.0	216.00	4.32	15.55	0
	3	40.0	144.00	2.88	10.37	0
	4	30.0	108.00	2.16	7.78	0
	5	24.0	86.40	1.73	6.22	0
	6	20.0	72.00	1.44	5.18	1
	7	17.1	61.71	1.23	4.44	0
	8	15.0	54.00	1.08	3.89	1
121	1	121.0	435.60	8.71	31.36	0
	2	60.5	217.80	4.36	15.68	0
	3	40.3	145.20	2.90	10.45	0
	4	30.3	108.90	2.18	7.84	0
	5	24.2	87.12	1.74	6.27	0
	6	20.2	72.60	1.45	5.23	0
	7	17.3	62.23	1.24	4.48	0
	8	15.1	54.45	1.09	3.92	0

122	1	122.0	439.20	8.78	31.62	0
	2	61.0	219.60	4.39	15.81	0
	3	40.7	146.40	2.93	10.54	0
	4	30.5	109.80	2.20	7.91	0
	5	24.4	87.84	1.76	6.32	0
	6	20.3	73.20	1.46	5.27	0
	7	17.4	62.74	1.25	4.52	0
	8	15.3	54.90	1.10	3.95	0
123	1	123.0	442.80	8.86	31.88	0
	2	61.5	221.40	4.43	15.94	0
	3	41.0	147.60	2.95	10.63	0
	4	30.8	110.70	2.21	7.97	0
	5	24.6	88.56	1.77	6.38	0
	6	20.5	73.80	1.48	5.31	0
	7	17.6	63.26	1.27	4.55	0
	8	15.4	55.35	1.11	3.99	0
124	1	124.0	446.40	8.93	32.14	0
	2	62.0	223.20	4.46	16.07	0
	3	41.3	148.80	2.98	10.71	0
	4	31.0	111.60	2.23	8.04	0
	5	24.8	89.28	1.79	6.43	0
	6	20.7	74.40	1.49	5.36	0
	7	17.7	63.77	1.28	4.59	0
	8	15.5	55.80	1.12	4.02	0
125	1	125.0	450.00	9.00	32.40	0
	2	62.5	225.00	4.50	16.20	0
	3	41.7	150.00	3.00	10.80	0
	4	31.3	112.50	2.25	8.10	0
	5	25.0	90.00	1.80	6.48	0
	6	20.8	75.00	1.50	5.40	0
	7	17.9	64.29	1.29	4.63	0
	8	15.6	56.25	1.13	4.05	0
126	1	126.0	453.60	9.07	32.66	0
	2	63.0	226.80	4.54	16.33	0
	3	42.0	151.20	3.02	10.89	0
	4	31.5	113.40	2.27	8.16	0
	5	25.2	90.72	1.81	6.53	0
	6	21.0	75.60	1.51	5.44	1
	7	18.0	64.80	1.30	4.67	1
	8	15.8	56.70	1.13	4.08	0
127	1	127.0	457.20	9.14	32.92	0
	2	63.5	228.60	4.57	16.46	0
	3	42.3	152.40	3.05	10.97	0
	4	31.8	114.30	2.29	8.23	0
	5	25.4	91.44	1.83	6.58	0
	6	21.2	76.20	1.52	5.49	0
	7	18.1	65.31	1.31	4.70	0
	8	15.9	57.15	1.14	4.11	0
128	1	128.0	460.80	9.22	33.18	0
	2	64.0	230.40	4.61	16.59	0
	3	42.7	153.60	3.07	11.06	0
	4	32.0	115.20	2.30	8.29	0
	5	25.6	92.16	1.84	6.64	0
	6	21.3	76.80	1.54	5.53	0
	7	18.3	65.83	1.32	4.74	0
	8	16.0	57.60	1.15	4.15	1
129	1	129.0	464.40	9.29	33.44	0
	2	64.5	232.20	4.64	16.72	0
	3	43.0	154.80	3.10	11.15	0
	4	32.3	116.10	2.32	8.36	0
	5	25.8	92.88	1.86	6.69	0
	6	21.5	77.40	1.55	5.57	0
	7	18.4	66.34	1.33	4.78	0
	8	16.1	58.05	1.16	4.18	0

	1	130.0	468.00	9.36	33.70	0
	2	65.0	234.00	4.68	16.85	0
	3	43.3	156.00	3.12	11.23	0
	4	32.5	117.00	2.34	8.42	0
	5	26.0	93.60	1.87	6.74	0
	6	21.7	78.00	1.56	5.62	0
	7	18.6	66.86	1.34	4.81	0
	8	16.3	58.50	1.17	4.21	0
	1	131.0	471.60	9.43	33.96	0
	2	65.5	235.80	4.72	16.98	0
	3	43.7	157.20	3.14	11.32	0
	4	32.8	117.90	2.36	8.49	0
	5	26.2	94.32	1.89	6.79	0
	6	21.8	78.60	1.57	5.66	0
	7	18.7	67.37	1.35	4.85	0
	8	16.4	58.95	1.18	4.24	0
	1	132.0	475.20	9.50	34.21	0
	2	66.0	237.60	4.75	17.11	0
	3	44.0	158.40	3.17	11.40	0
	4	33.0	118.80	2.38	8.55	0
	5	26.4	95.04	1.90	6.84	0
	6	22.0	79.20	1.58	5.70	1
	7	18.9	67.89	1.36	4.89	0
	8	16.5	59.40	1.19	4.28	0
	1	133.0	478.80	9.58	34.47	0
	2	66.5	239.40	4.79	17.24	0
	3	44.3	159.60	3.19	11.49	0
	4	33.3	119.70	2.39	8.62	0
	5	26.6	95.76	1.92	6.89	0
	6	22.2	79.80	1.60	5.75	0
	7	19.0	68.40	1.37	4.92	1
	8	16.6	59.85	1.20	4.31	0
	1	134.0	482.40	9.65	34.73	0
	2	67.0	241.20	4.82	17.37	0
	3	44.7	160.80	3.22	11.58	0
	4	33.5	120.60	2.41	8.68	0
	5	26.8	96.48	1.93	6.95	0
	6	22.3	80.40	1.61	5.79	0
	7	19.1	68.91	1.38	4.96	0
	8	16.8	60.30	1.21	4.34	0
	1	135.0	486.00	9.72	34.99	0
	2	67.5	243.00	4.86	17.50	0
	3	45.0	162.00	3.24	11.66	0
	4	33.8	121.50	2.43	8.75	0
	5	27.0	97.20	1.94	7.00	0
	6	22.5	81.00	1.62	5.83	0
	7	19.3	69.43	1.39	5.00	0
	8	16.9	60.75	1.22	4.37	0

APPENDIX H

MELASTA CELL SELECTION MACRO & RESULTS

“PROCESS MELASTA CELLS” MACRO CODE

```

Type BatteryPack
    ModelNumber As String
    Capacity As Double
    TotalCells As Integer
    NumParallel As Integer
    PowerOut As Double
    Mass As Double
    Volume As Double
End Type

Public typeBatteryPack As BatteryPack

Sub Process_Cells()
    Sheets("Cell Calculations").Activate

    Dim row As Integer
    Dim parallel As Integer
    Dim minCapacity As Double
    Dim maxCapacity As Double
    Dim minPowerOut As Double
    Dim maxContPowerModule As Double
    Dim capacityTemp As Double

    Dim resultsRow As Integer
    resultsRow = 2

    minPowerOut = Cells(2, "O").Value
    minCapacity = Cells(1, "N").Value
    maxCapacity = Cells(1, "P").Value

    For row = 7 To 722
        For parallel = 5 To 14
            maxContPowerModule = Cells(row, "D").Value * (parallel - 4)
            capacityTemp = Cells(row, parallel).Value
            If (minCapacity <= capacityTemp) And (maxCapacity >= capacityTemp) And (maxContPowerModule >= minPowerOut) Then
                typeBatteryPack.ModelNumber = Cells(row, "A").Value
                typeBatteryPack.Capacity = Cells(row, parallel).Value
                typeBatteryPack.TotalCells = Cells(2, "E").Value * (parallel - 4)
                typeBatteryPack.NumParallel = parallel - 4
                typeBatteryPack.PowerOut = maxContPowerModule
                typeBatteryPack.Mass = Cells(row, "P").Value * typeBatteryPack.TotalCells / 1000
                typeBatteryPack.Volume = Cells(row, "T").Value * typeBatteryPack.TotalCells * 0.000000001

                Sheets("MacroResults").Activate

                Cells(resultsRow, "A").Value = typeBatteryPack.ModelNumber
                Cells(resultsRow, "B").Value = typeBatteryPack.Capacity
                Cells(resultsRow, "C").Value = typeBatteryPack.TotalCells
                Cells(resultsRow, "D").Value = typeBatteryPack.NumParallel
                Cells(resultsRow, "E").Value = typeBatteryPack.PowerOut
                Cells(resultsRow, "F").Value = typeBatteryPack.Mass
                Cells(resultsRow, "G").Value = typeBatteryPack.Volume

                Sheets("Cell Calculations").Activate
                resultsRow = resultsRow + 1
            End If
        Next
    Next

    Sheets("MacroResults").Activate
End Sub

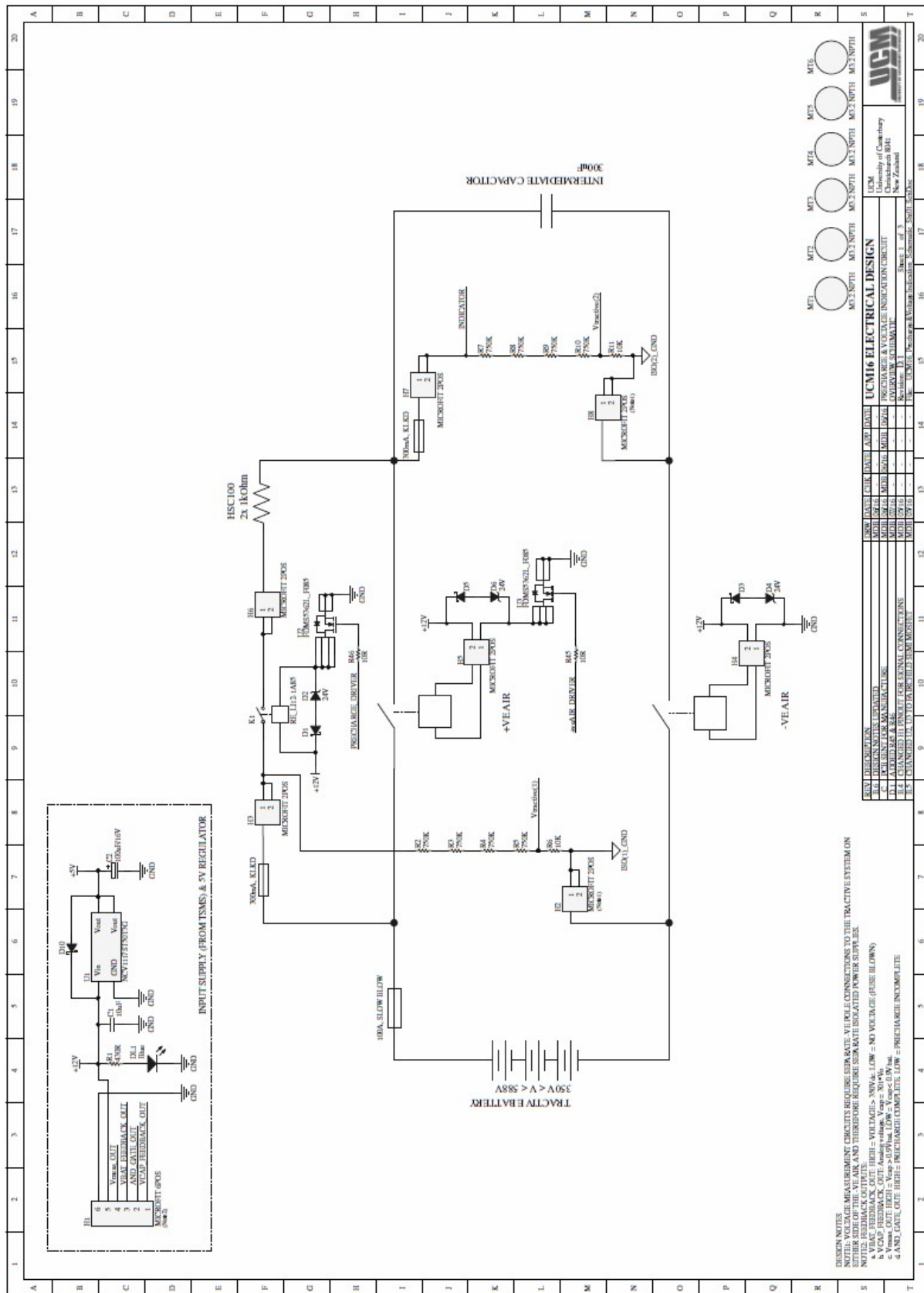
```

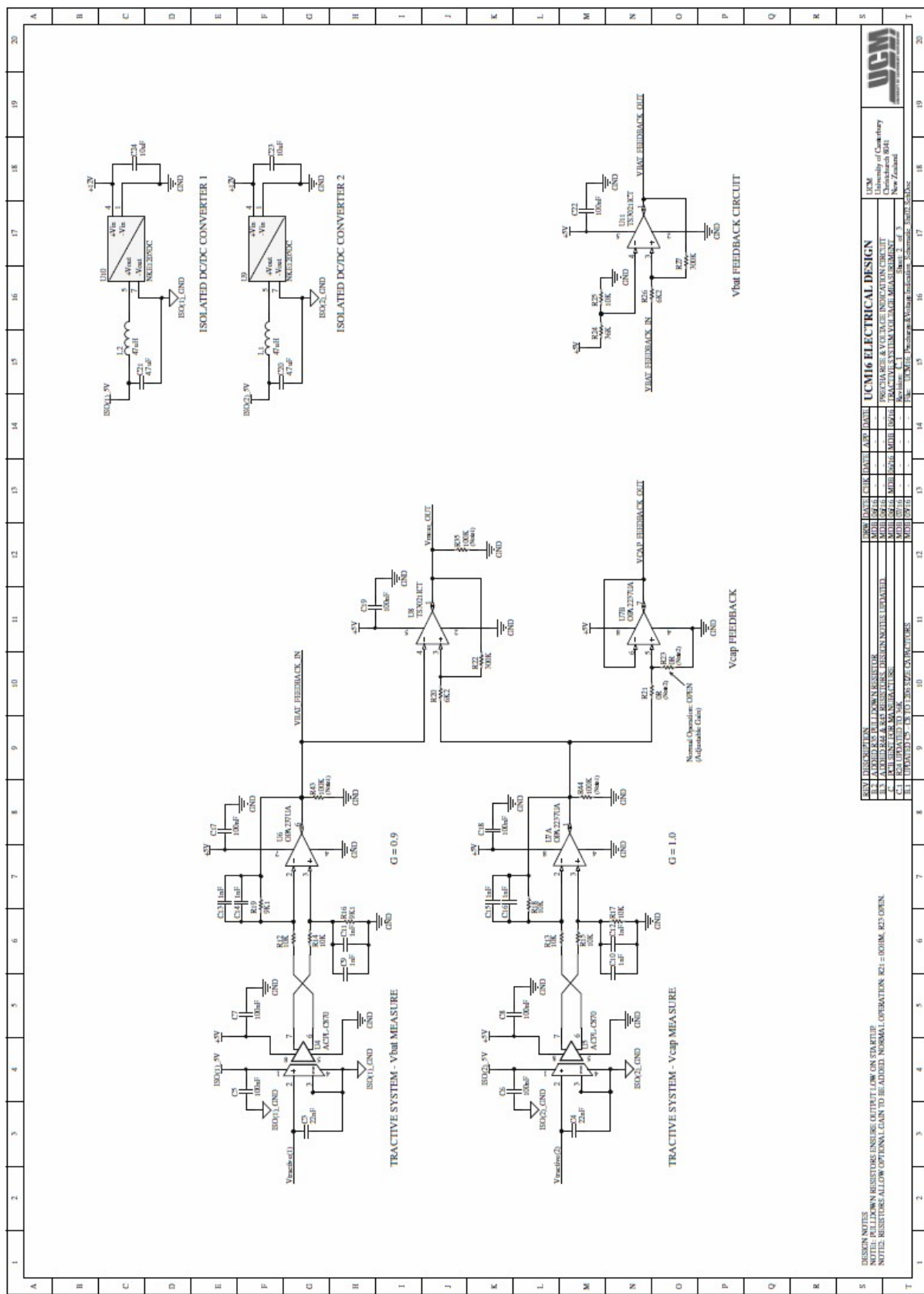
EXTRACT OF MELASTA CELLS SELECTED BY MACRO

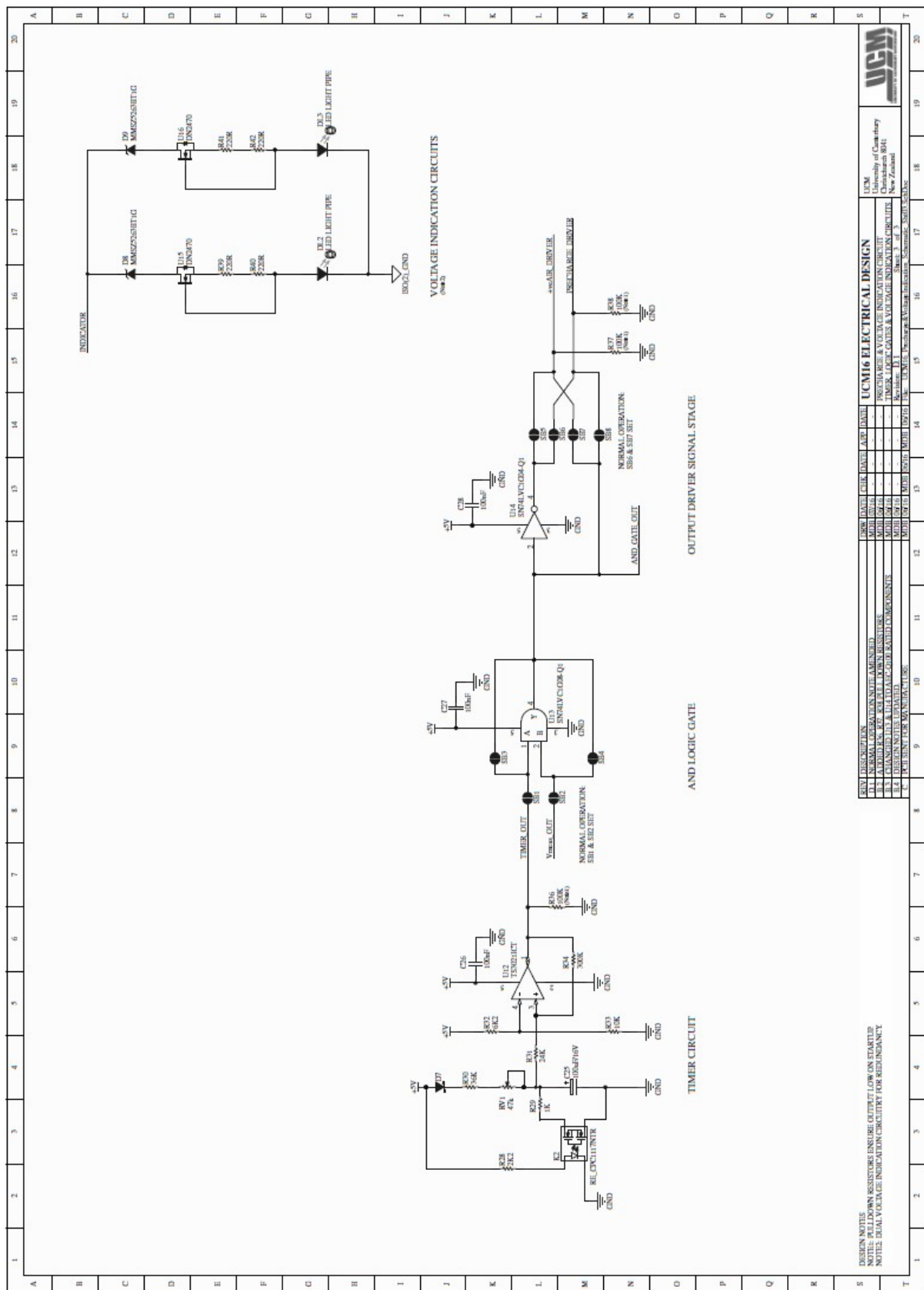
Model Number	Capacity Total (kWh)	Total Cells	No. Parallel	Cont. Power Out (kW)	Total Mass (kg)	Total Volume (m^3)
SLPB6743060	8.04	1278	9	64.31	43.45	0.022
SLPB8834122	8.41	568	4	84.06	45.16	0.020
SLPB041080	8.20	568	4	122.94	45.72	0.020
SLPB7934076	8.20	1136	8	122.94	46.58	0.023
SLPB6934096	8.09	994	7	80.91	46.72	0.022
SLPB5743080	8.11	1136	8	121.68	47.14	0.022
SLPB5634096	8.04	1278	9	120.58	47.29	0.023
SLPB6034082	8.14	1420	10	81.44	47.57	0.023
SLPB7864155	8.41	284	2	126.10	47.71	0.021
SLPB7664155	8.41	284	2	126.10	47.71	0.021
SLPB7834076	8.41	1136	8	126.10	47.71	0.022
LP8859098	8.35	426	3	83.54	47.71	0.021
SLPB7649135	8.04	426	3	160.77	47.71	0.021
SLPB7843080	8.04	852	6	160.77	48.14	0.022
SLPB7334096	8.09	994	7	161.82	48.21	0.022
SLPB9643128	8.20	426	3	163.92	48.78	0.022
SLPB5849073	8.41	1136	8	126.10	48.85	0.023
SLPB4849135	8.41	710	5	126.10	48.99	0.022
SLPB7230082	8.41	1420	10	126.10	48.99	0.025
SLPB5742085	8.41	1136	8	168.13	49.42	0.022
SLPBA342126	8.20	426	3	163.92	49.63	0.023
SLPB7530085	8.28	1278	9	124.13	49.84	0.024
LP6733088	8.28	1278	9	165.50	50.48	0.025
LP7530085	8.28	1278	9	124.13	50.48	0.024
SLPB8264155	8.41	284	2	168.13	50.55	0.023
SLPB8164159	8.41	284	2	168.13	50.55	0.023
SLPB8245150	8.35	426	3	167.08	50.69	0.023
SLPB5242126	8.20	852	6	163.92	50.69	0.023
SLPB7834096	8.09	994	7	161.82	50.69	0.025
SLPB7034106	8.09	994	7	161.82	50.69	0.024

APPENDIX I

PRECHARGE PCB SCHEMATIC

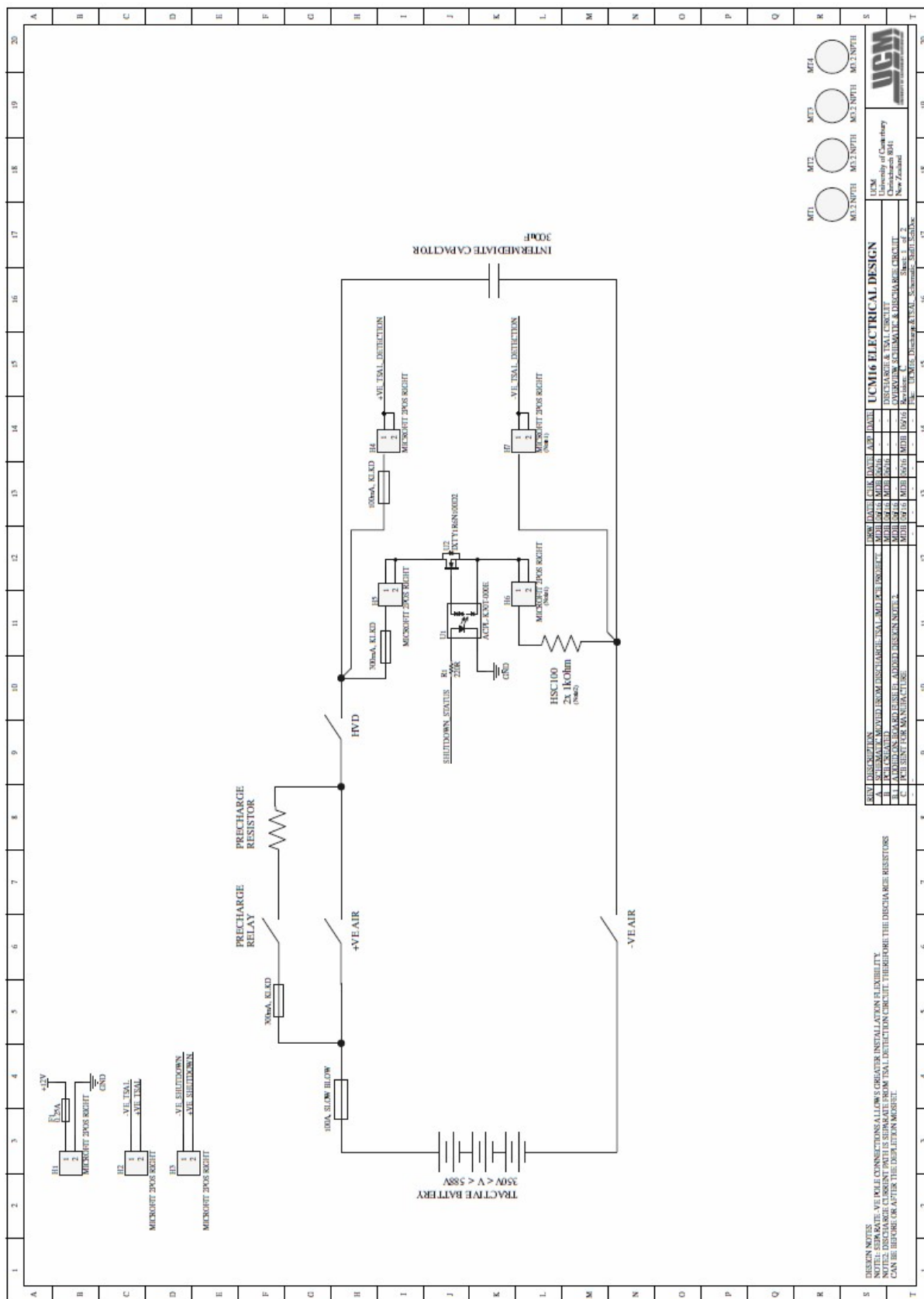


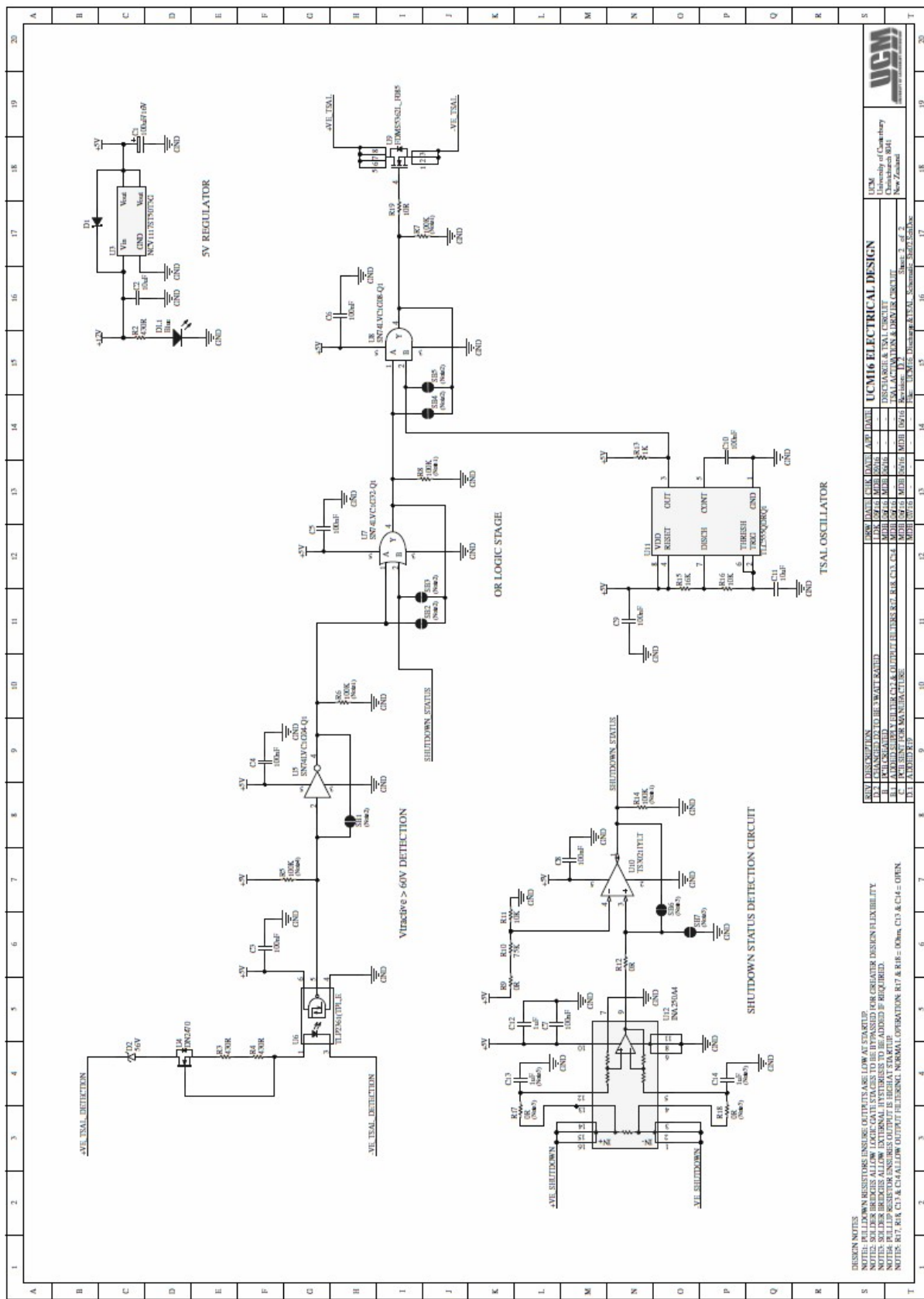




APPENDIX J

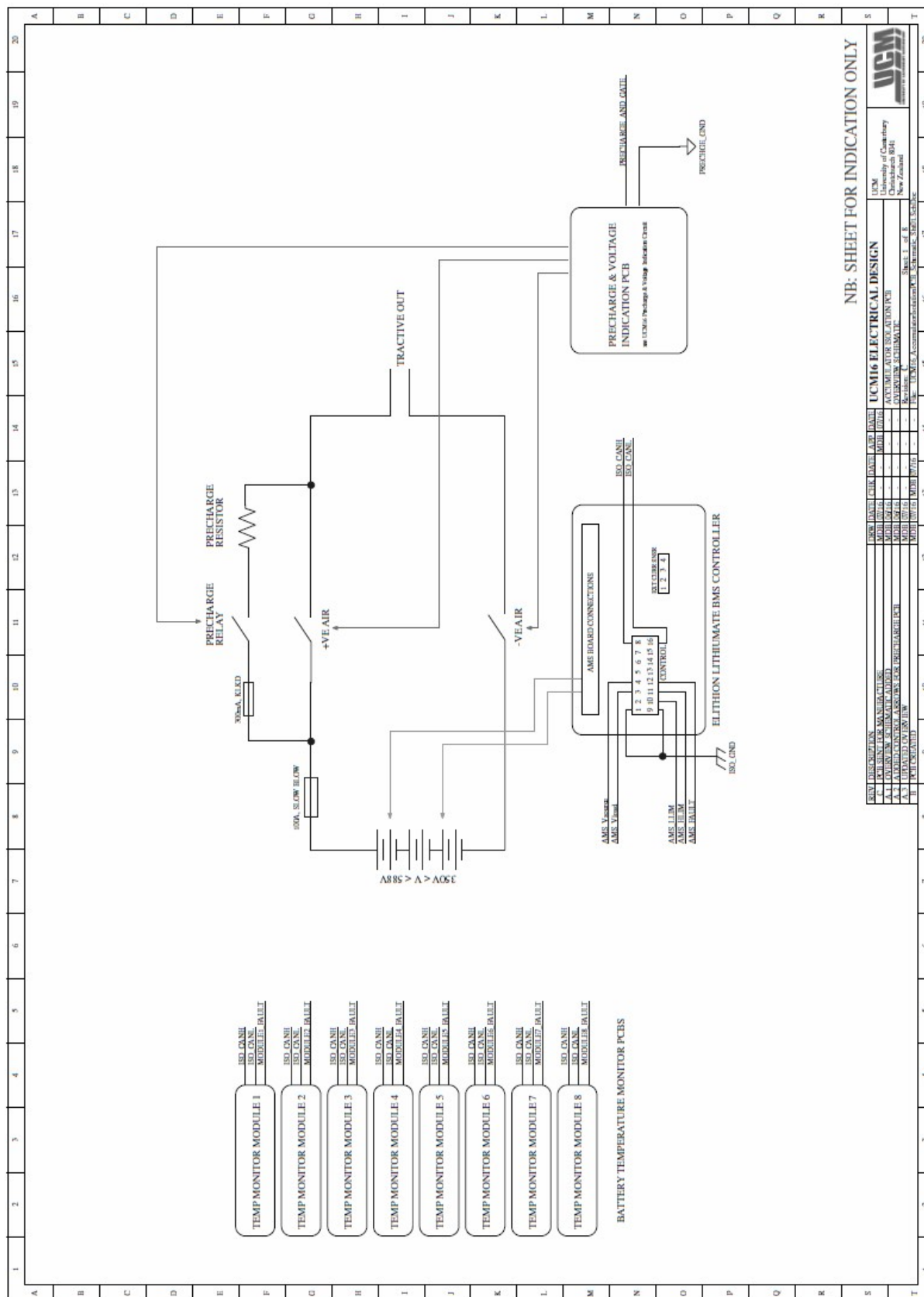
DISCHARGE PCB SCHEMATICS

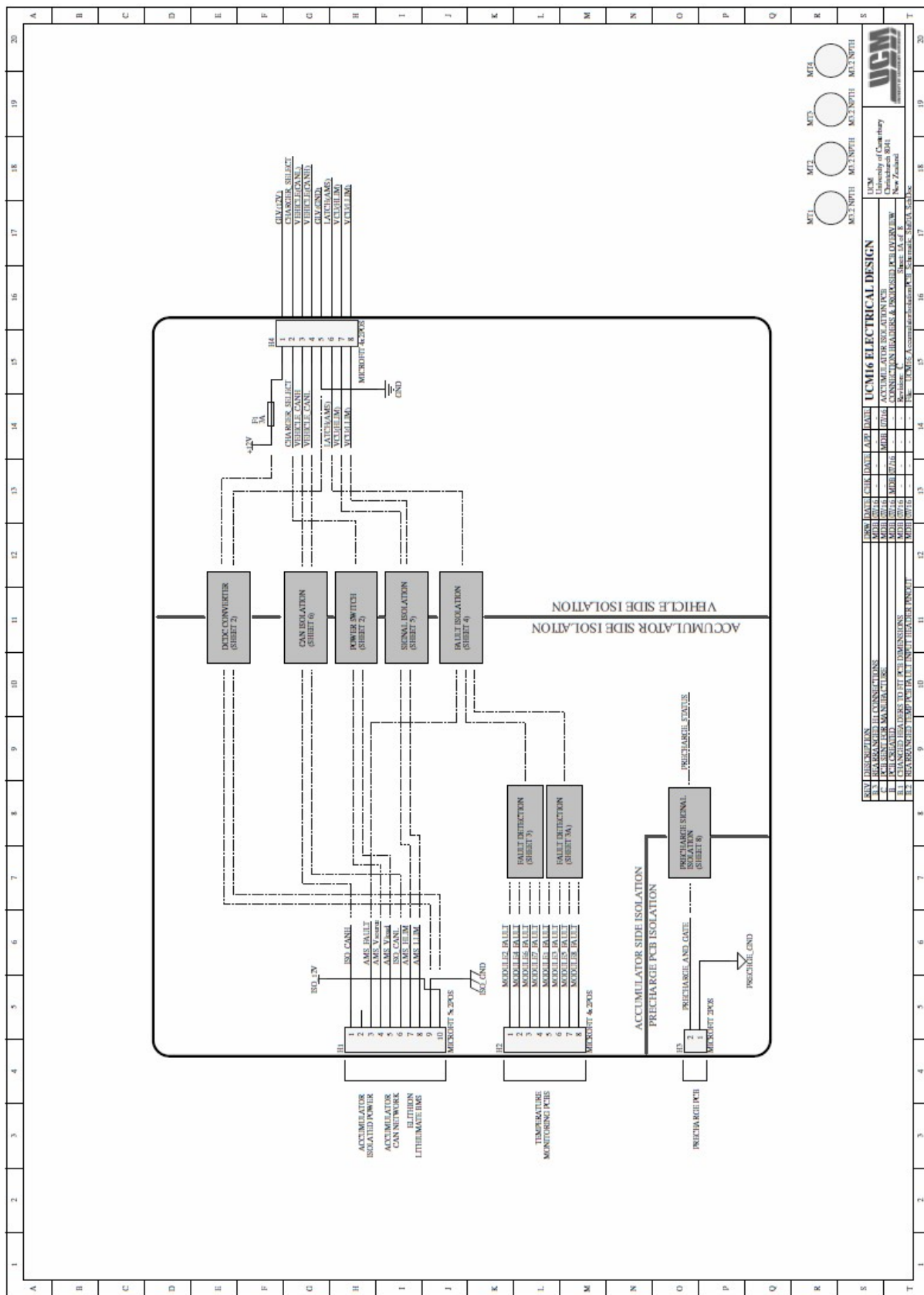


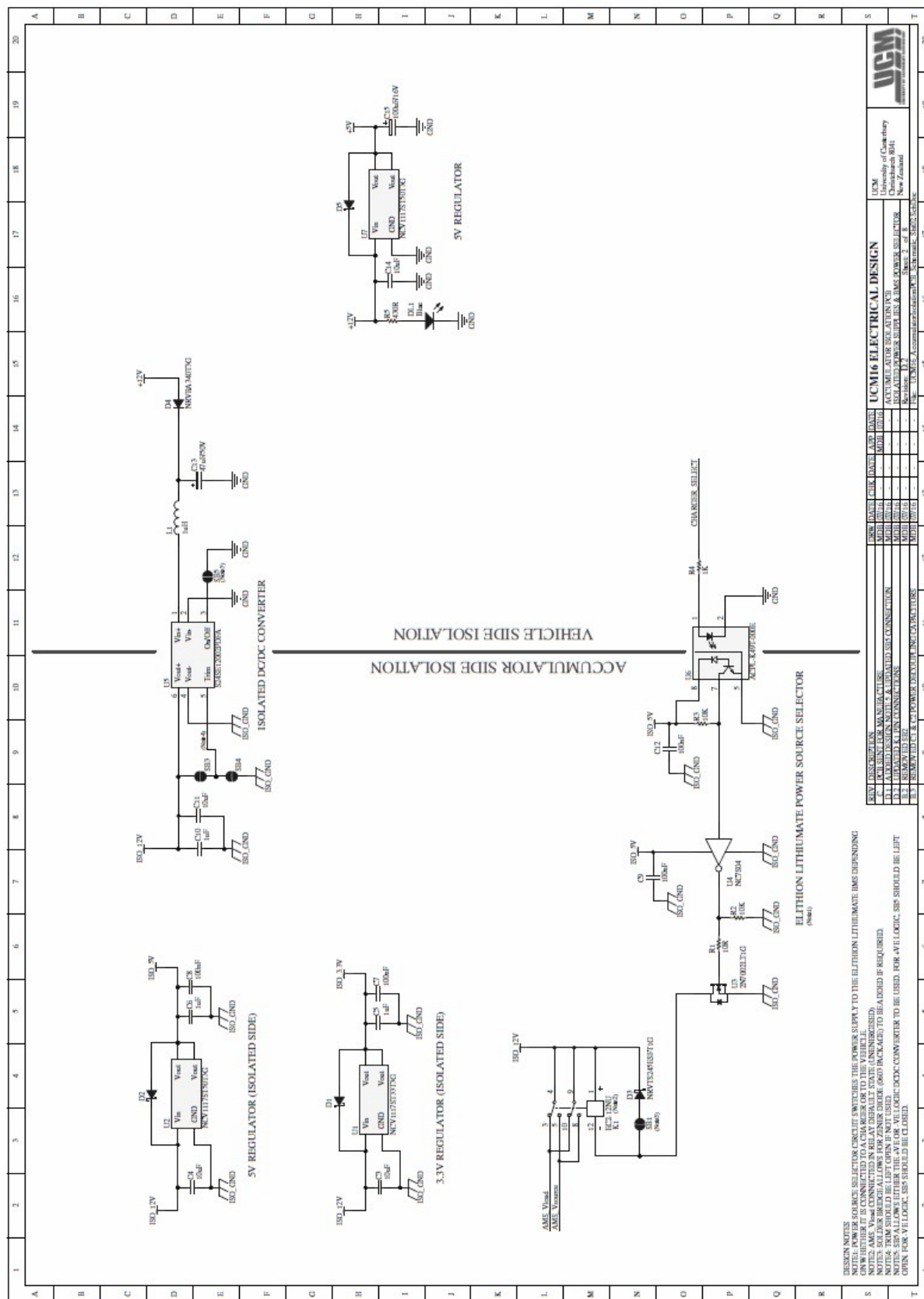


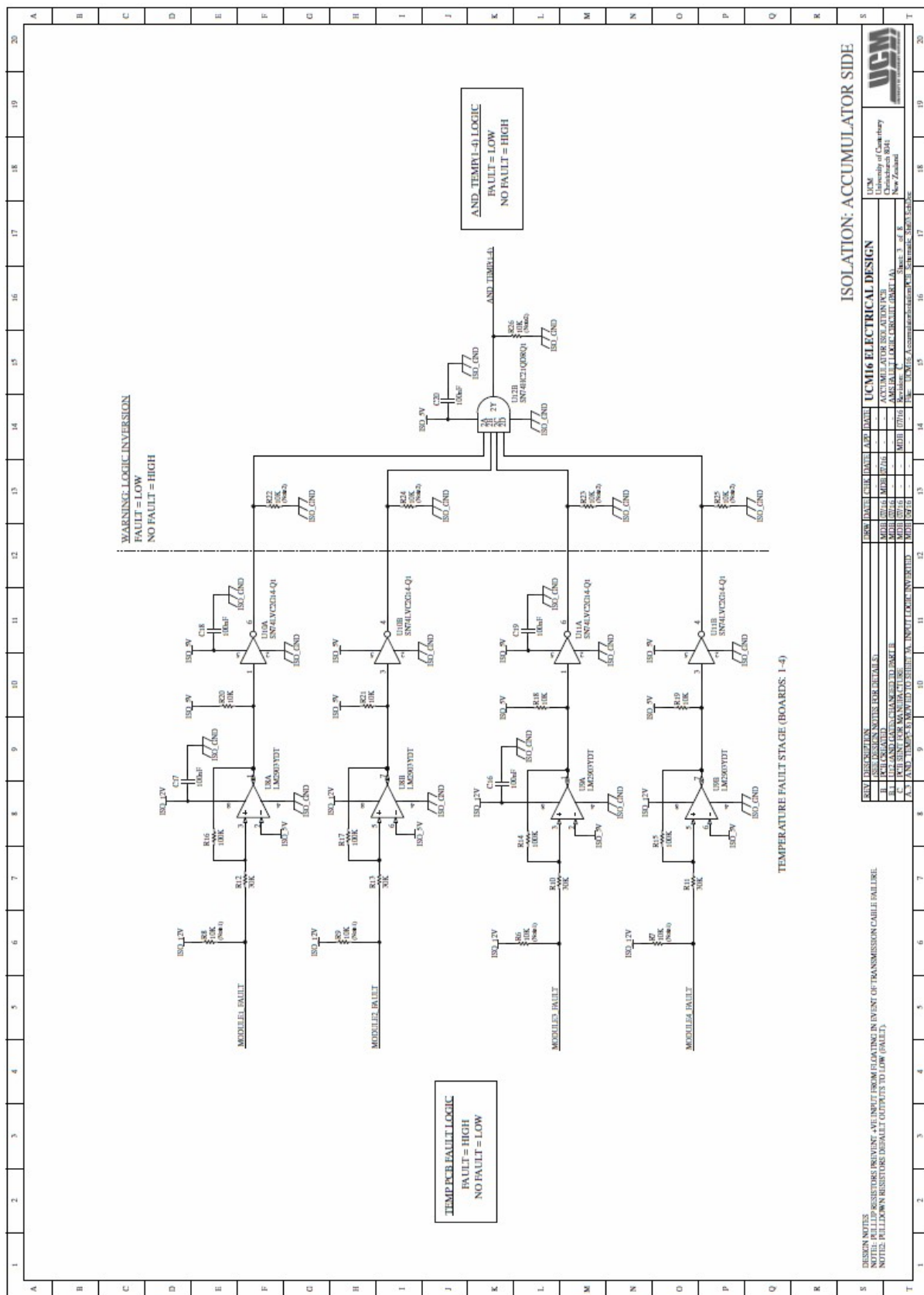
APPENDIX K

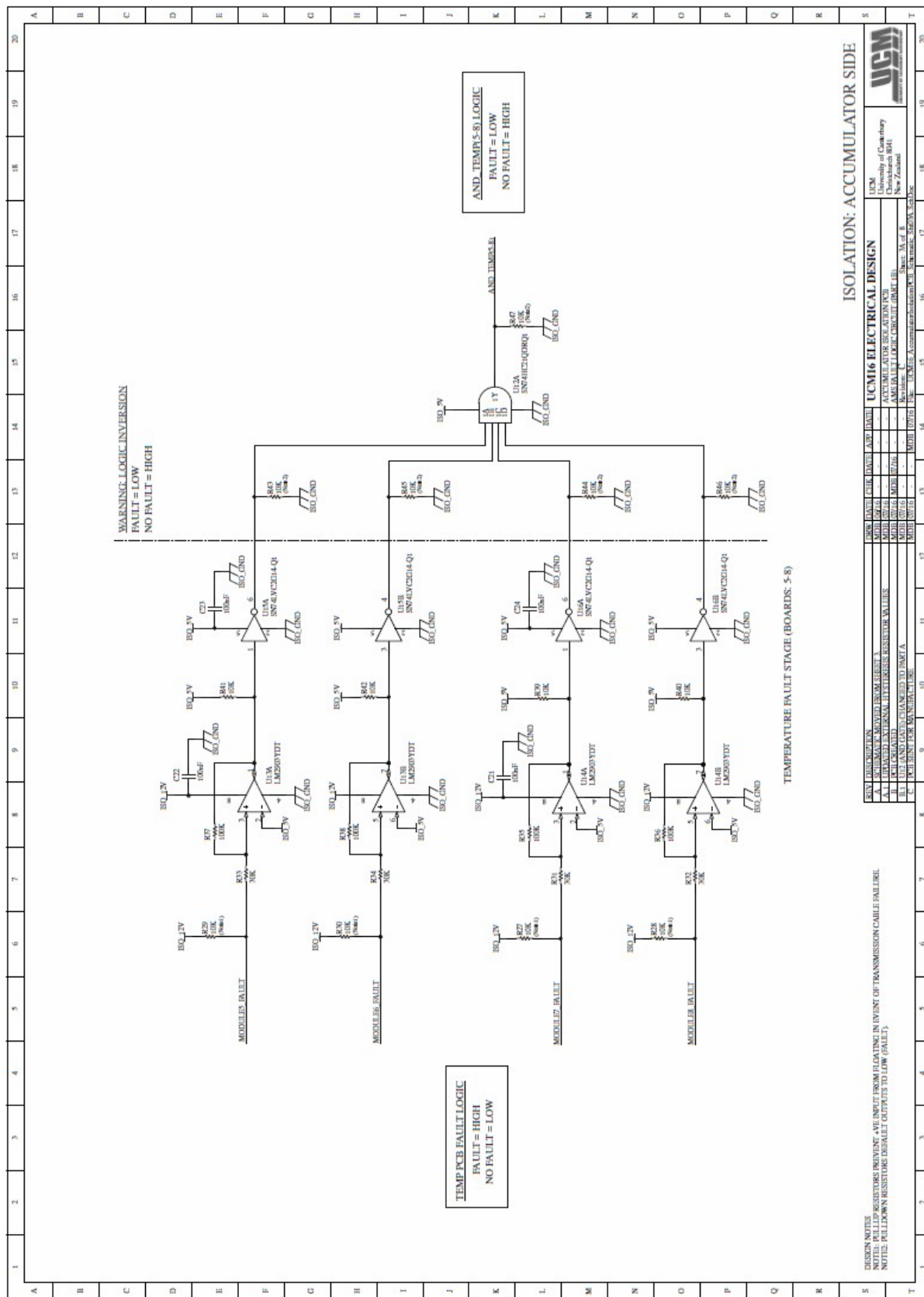
ACCUMULATOR ISOLATION PCB SCHEMATICS

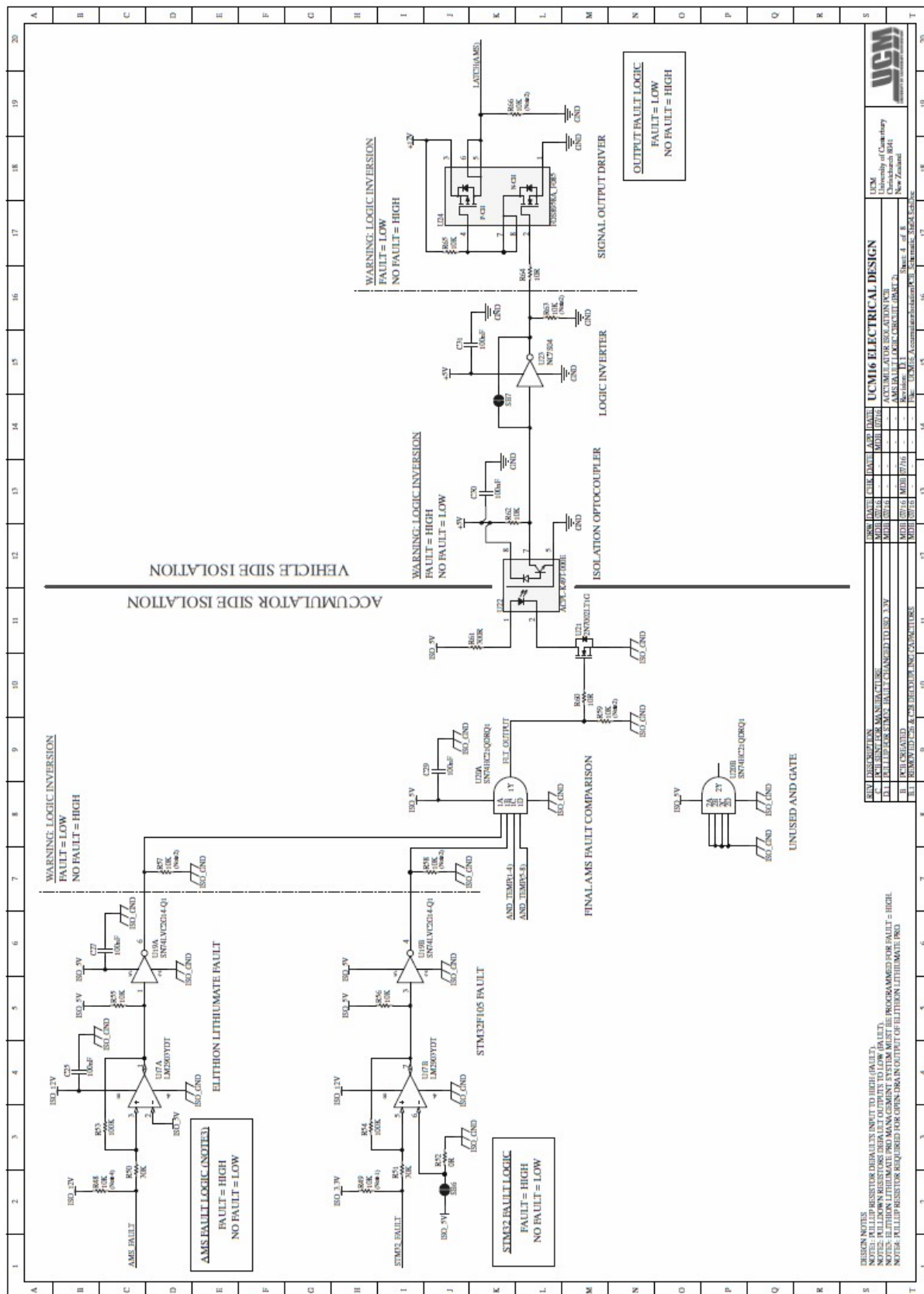


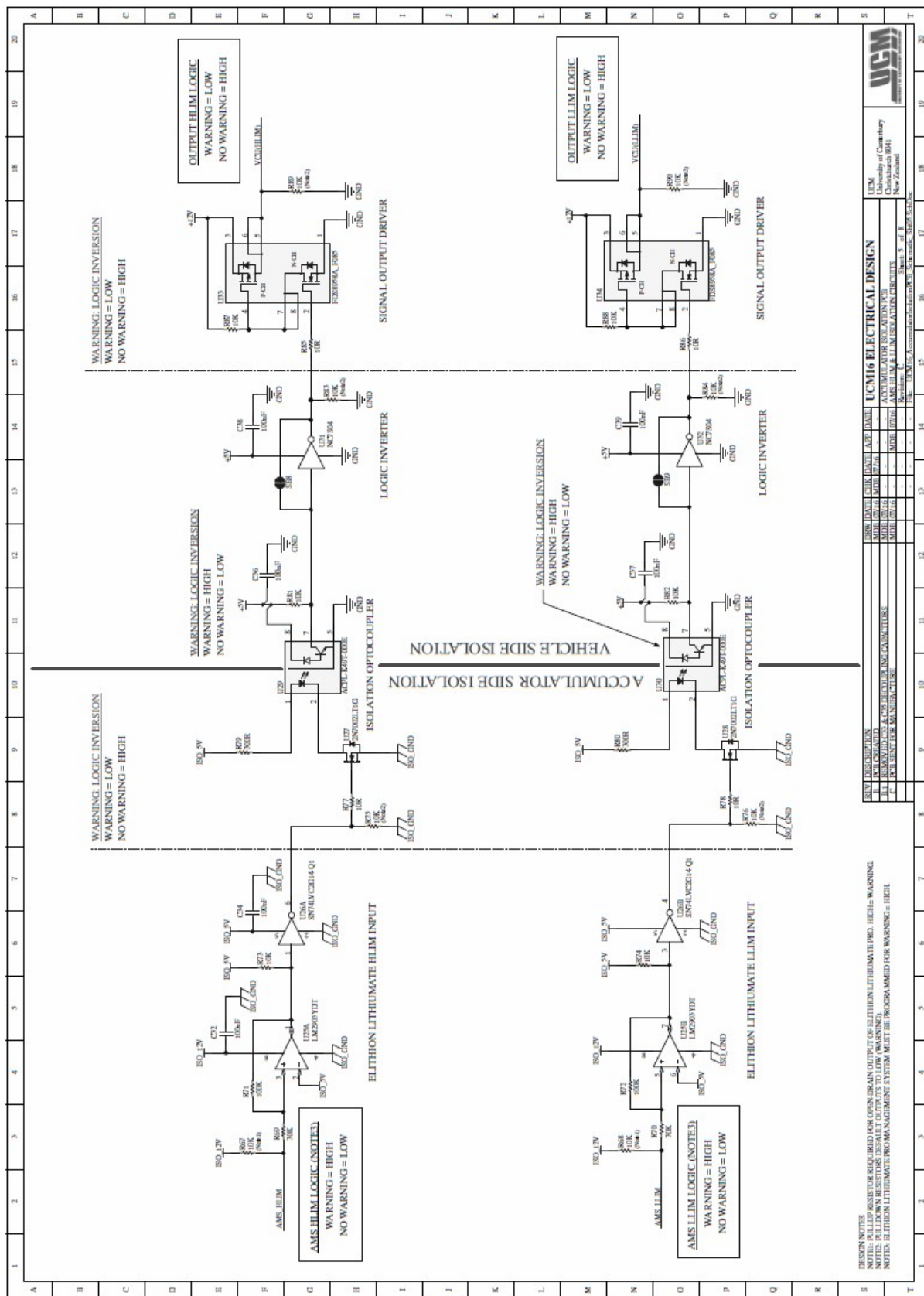


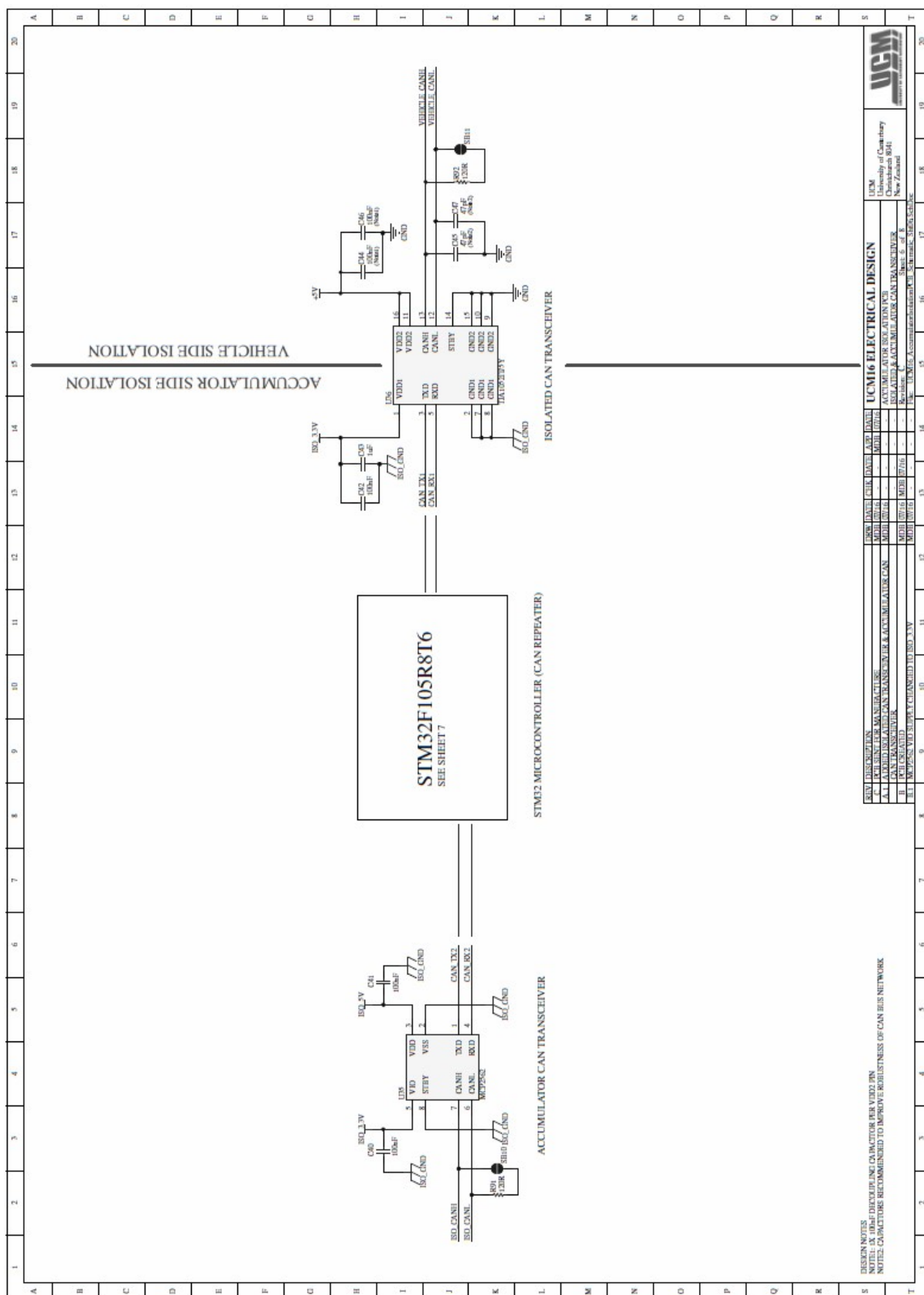


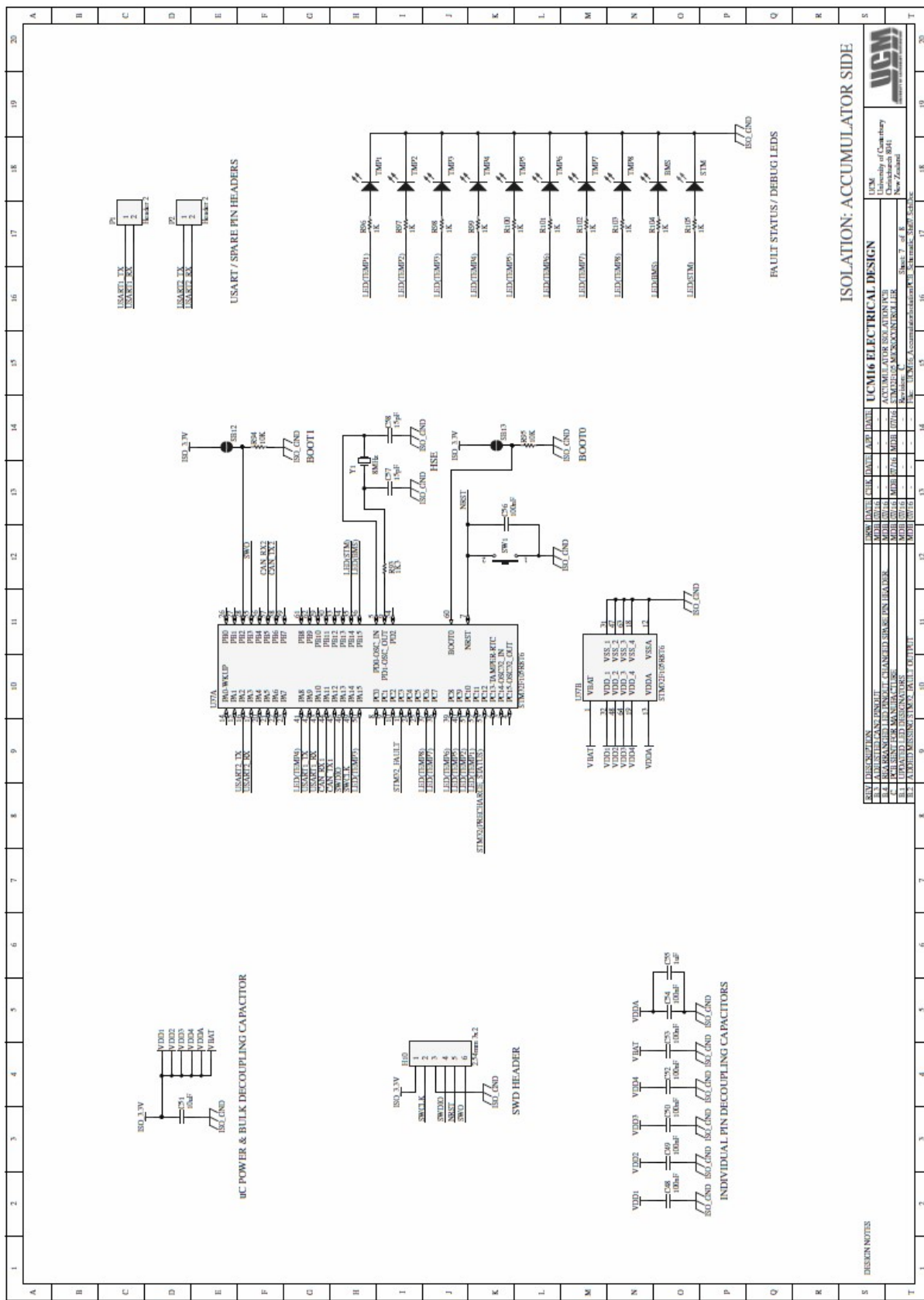


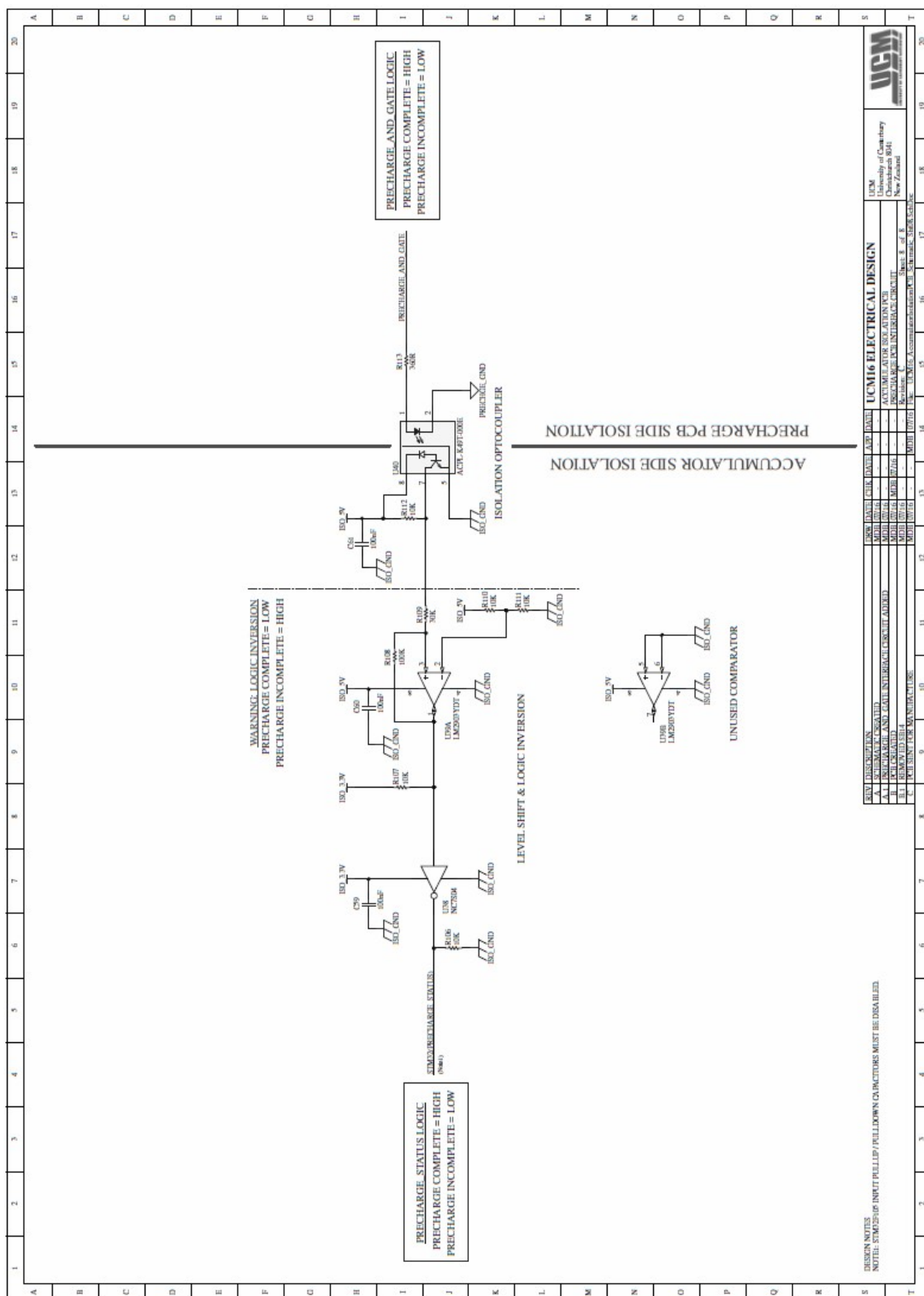






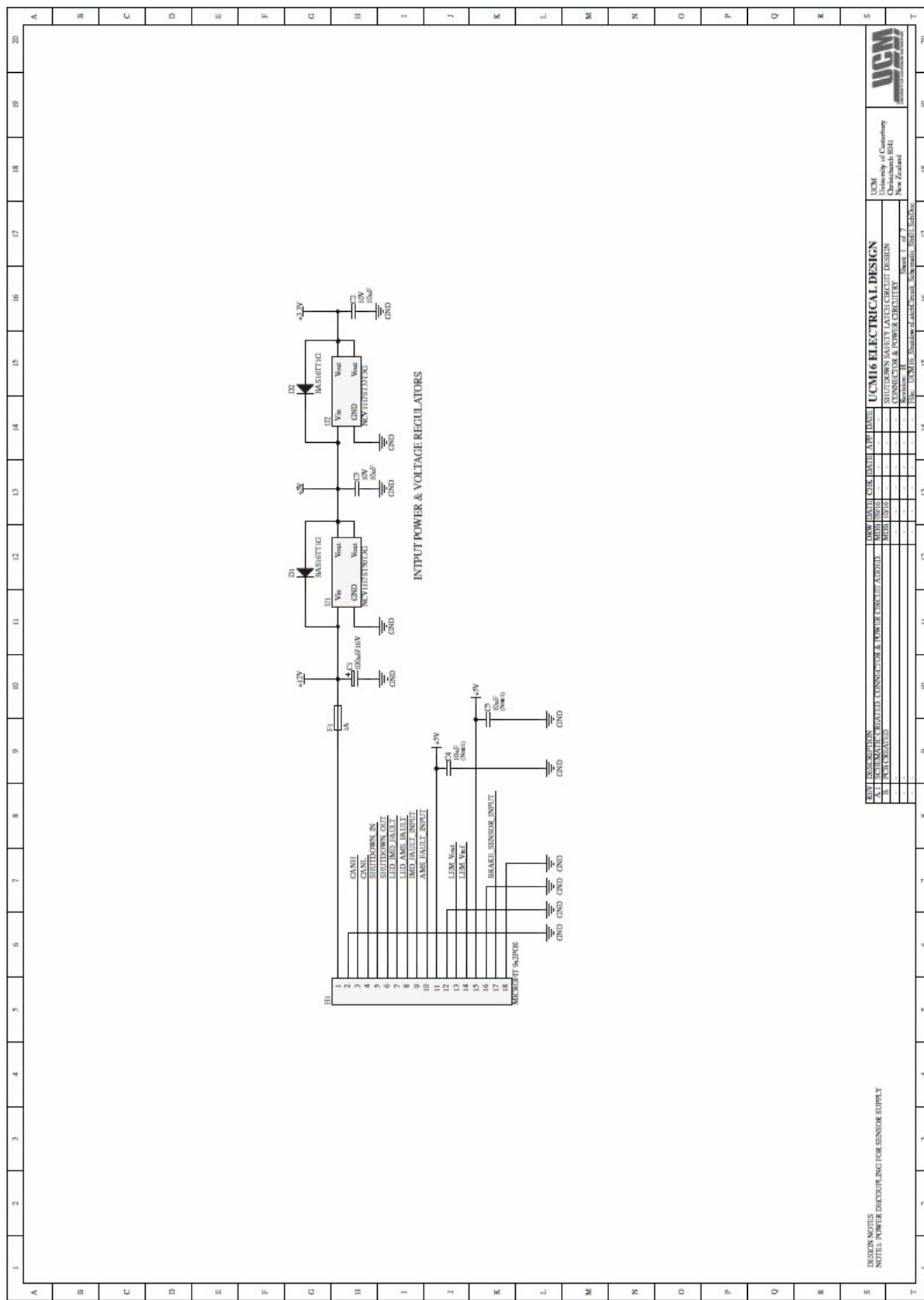


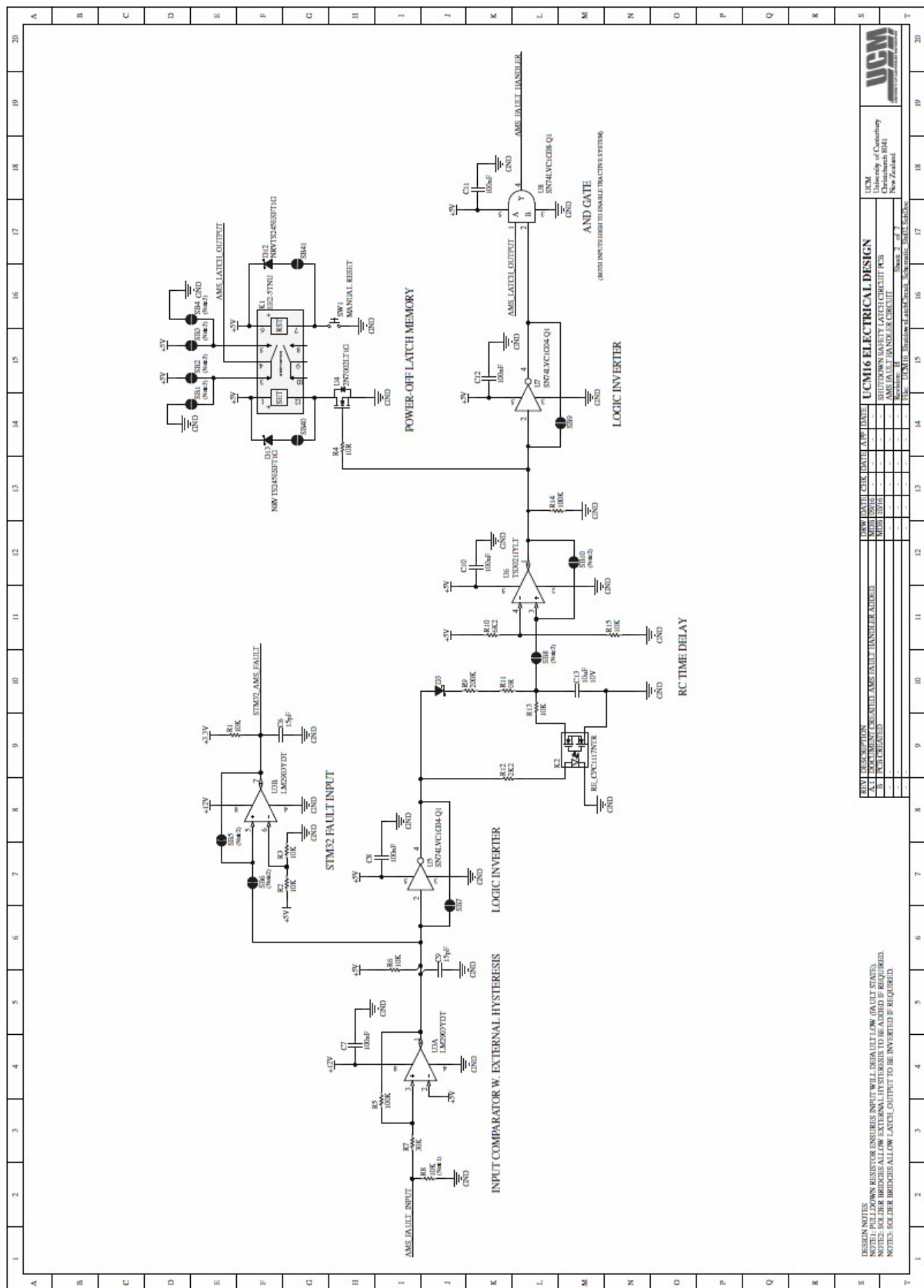


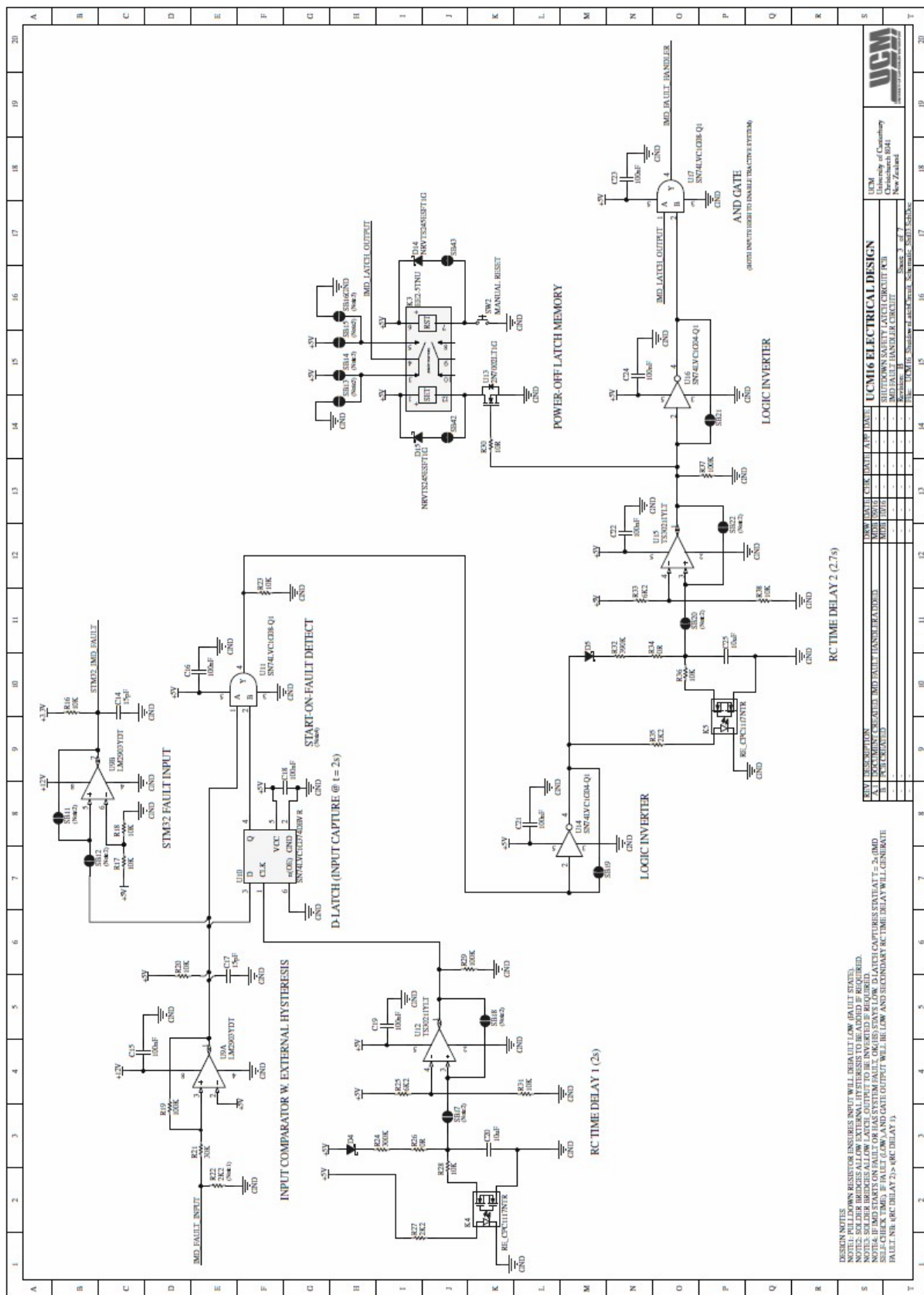


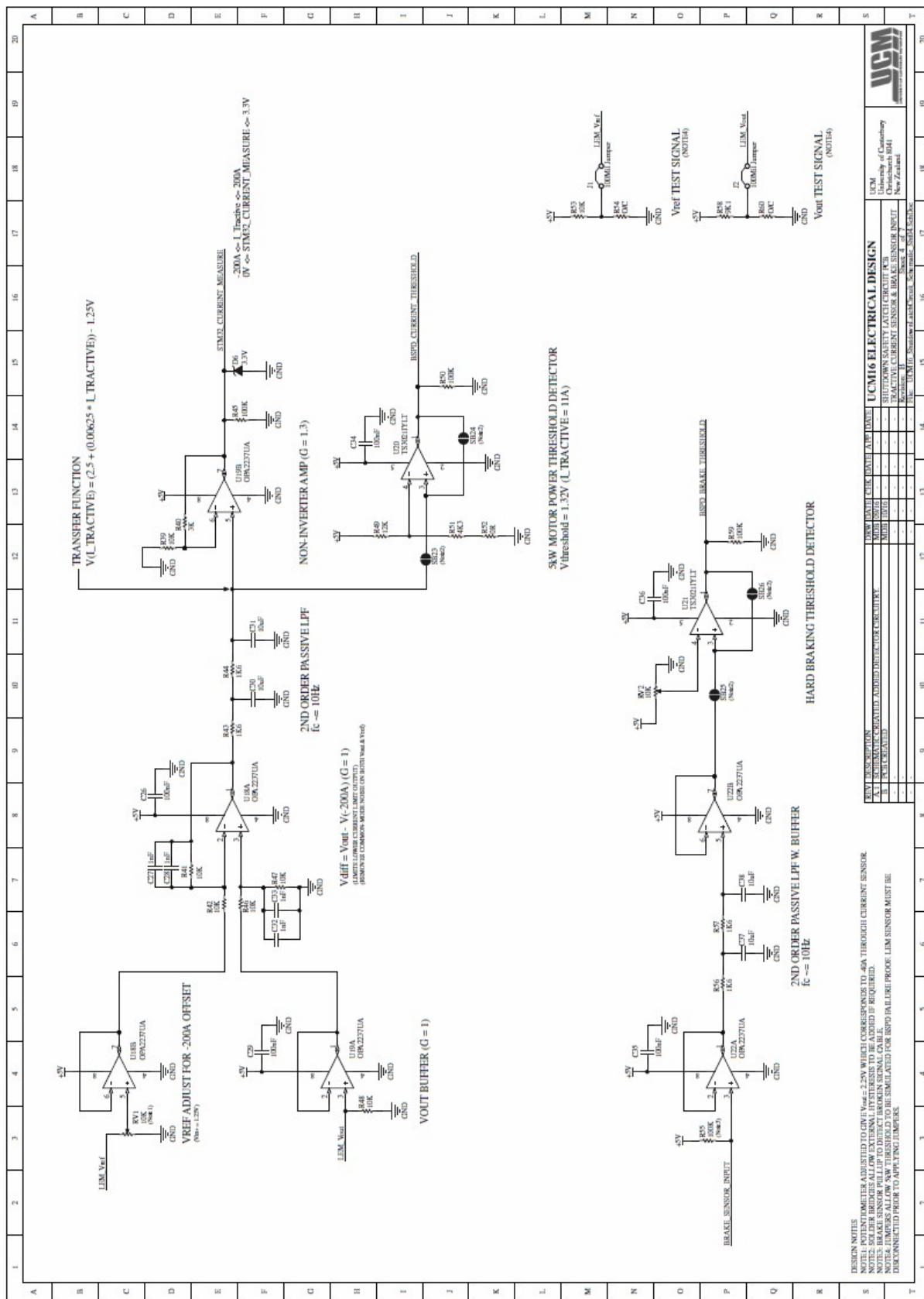
APPENDIX L

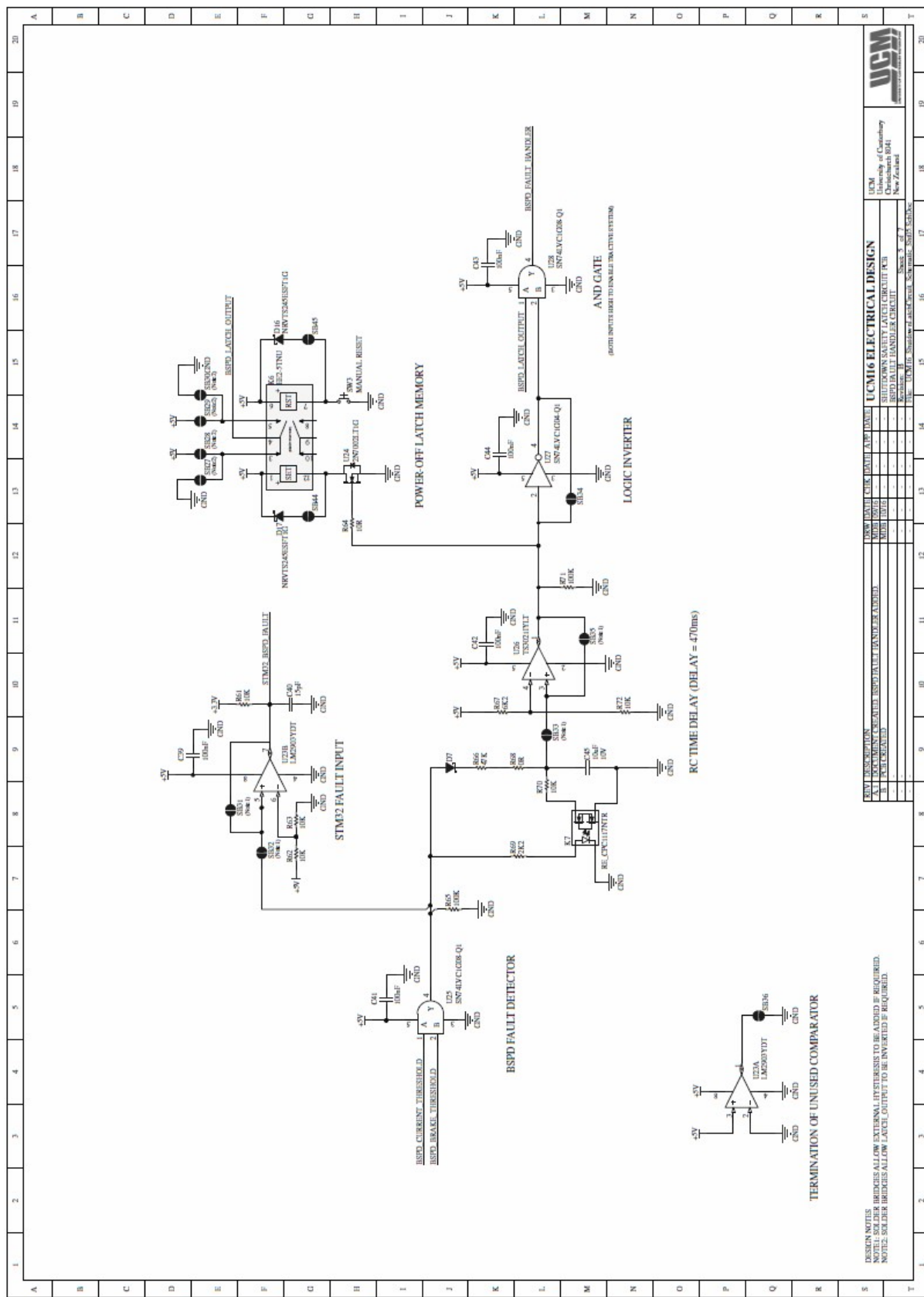
SHUTDOWN PCB SCHEMATICS

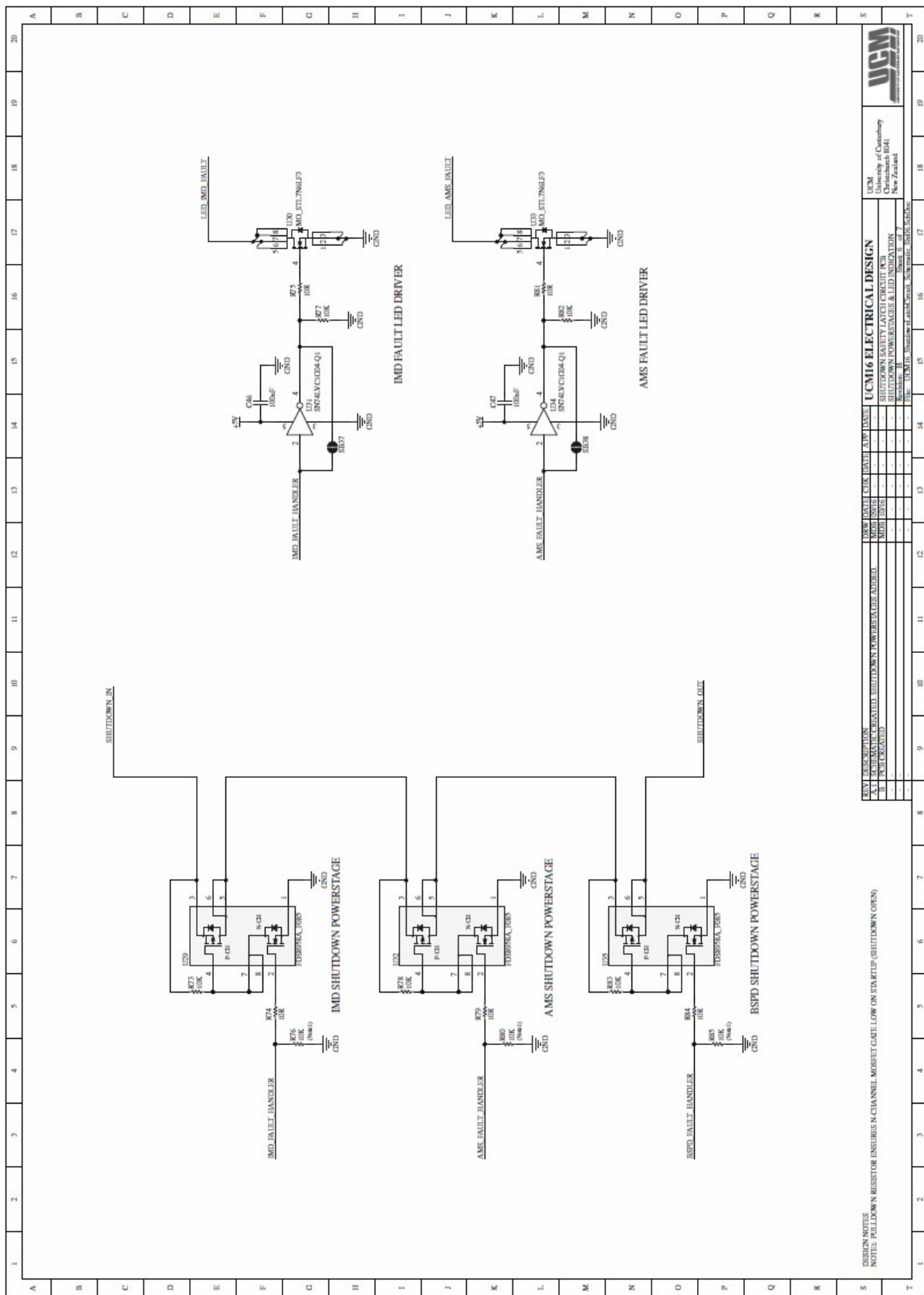


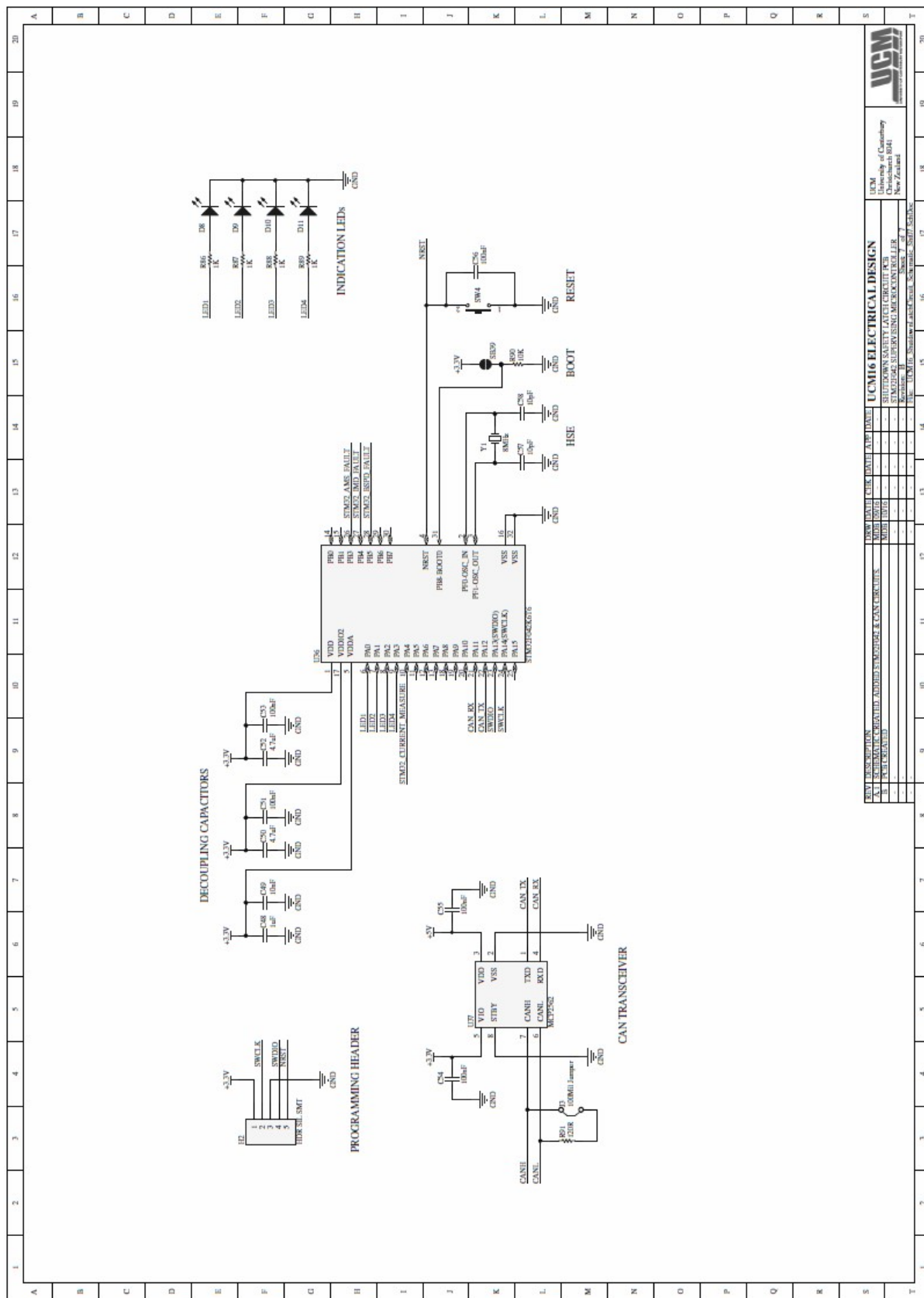






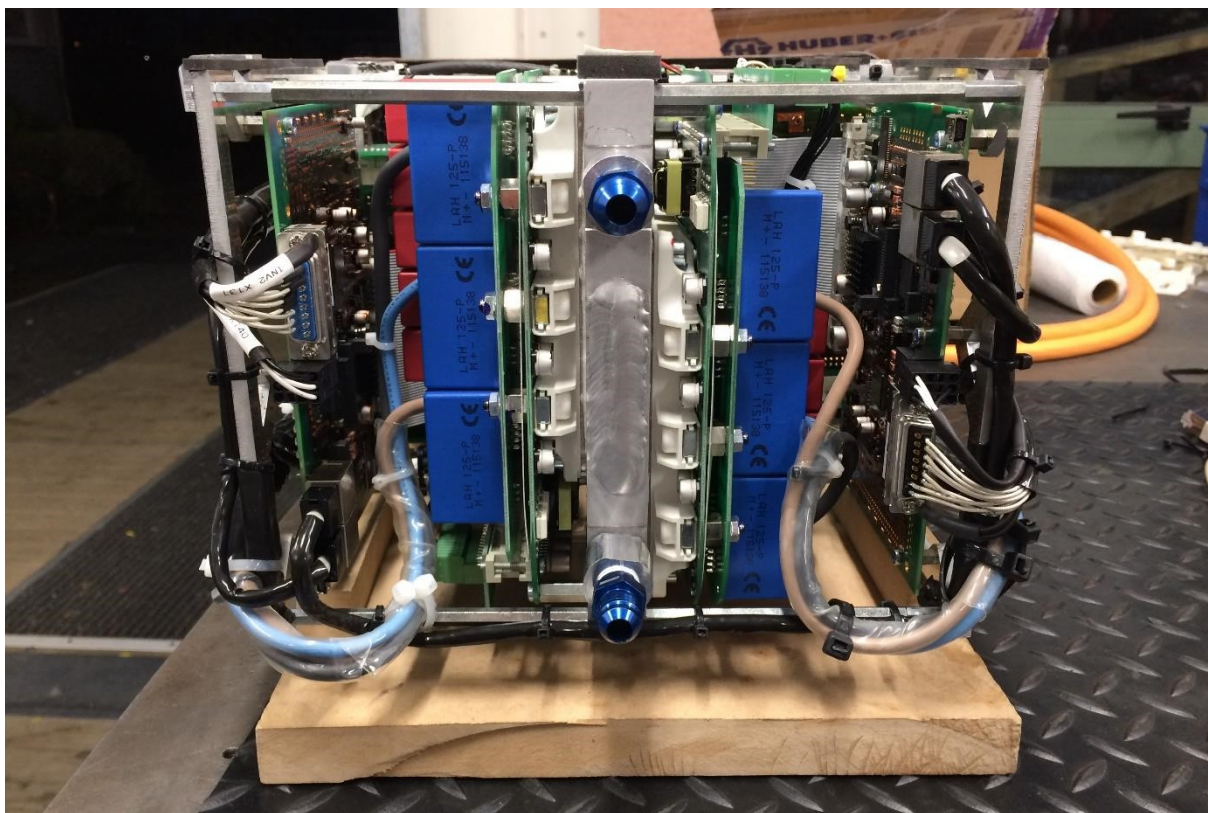
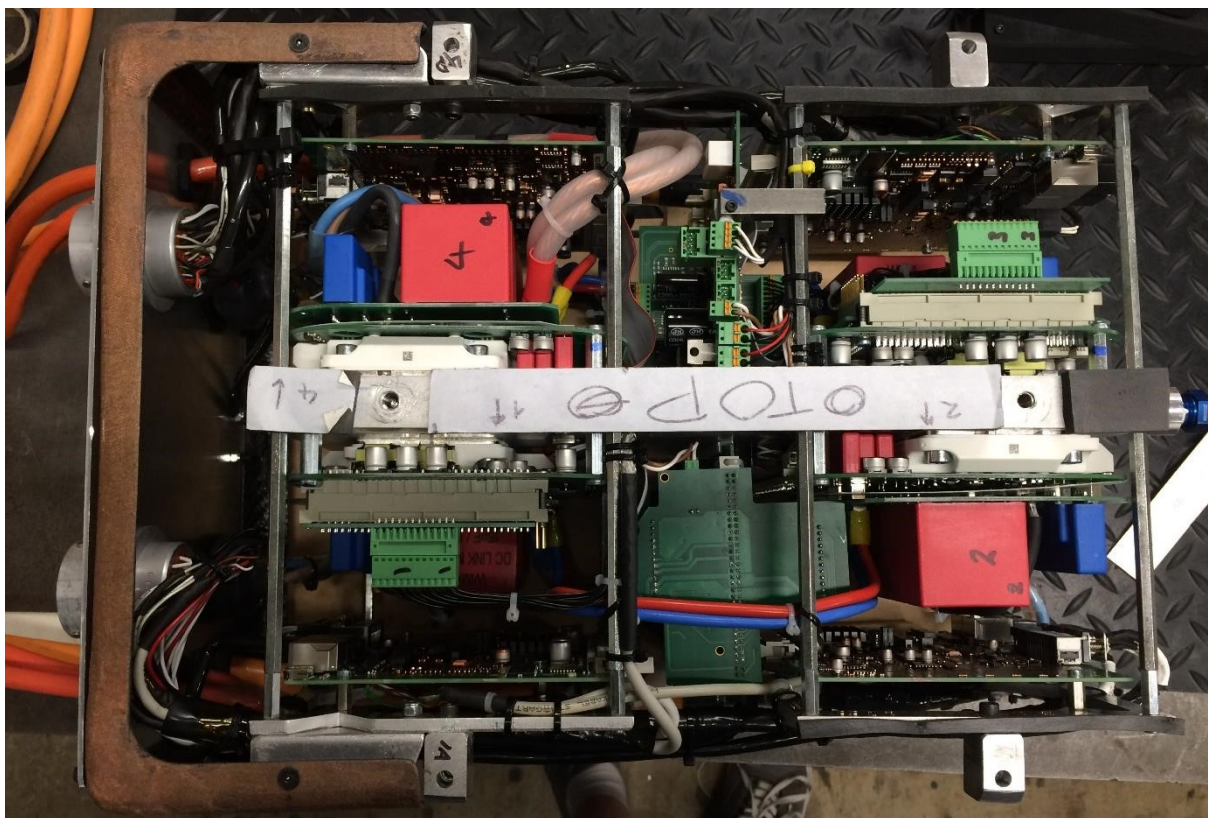


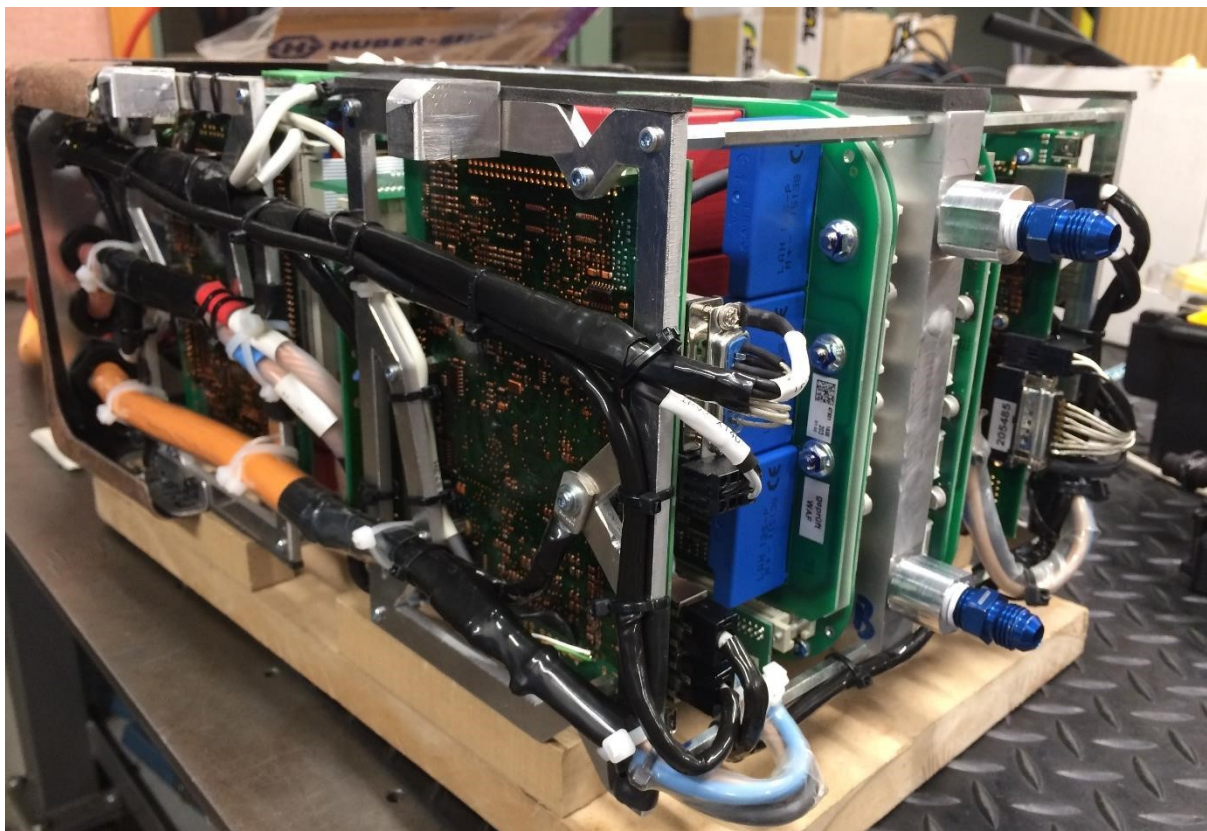




APPENDIX M

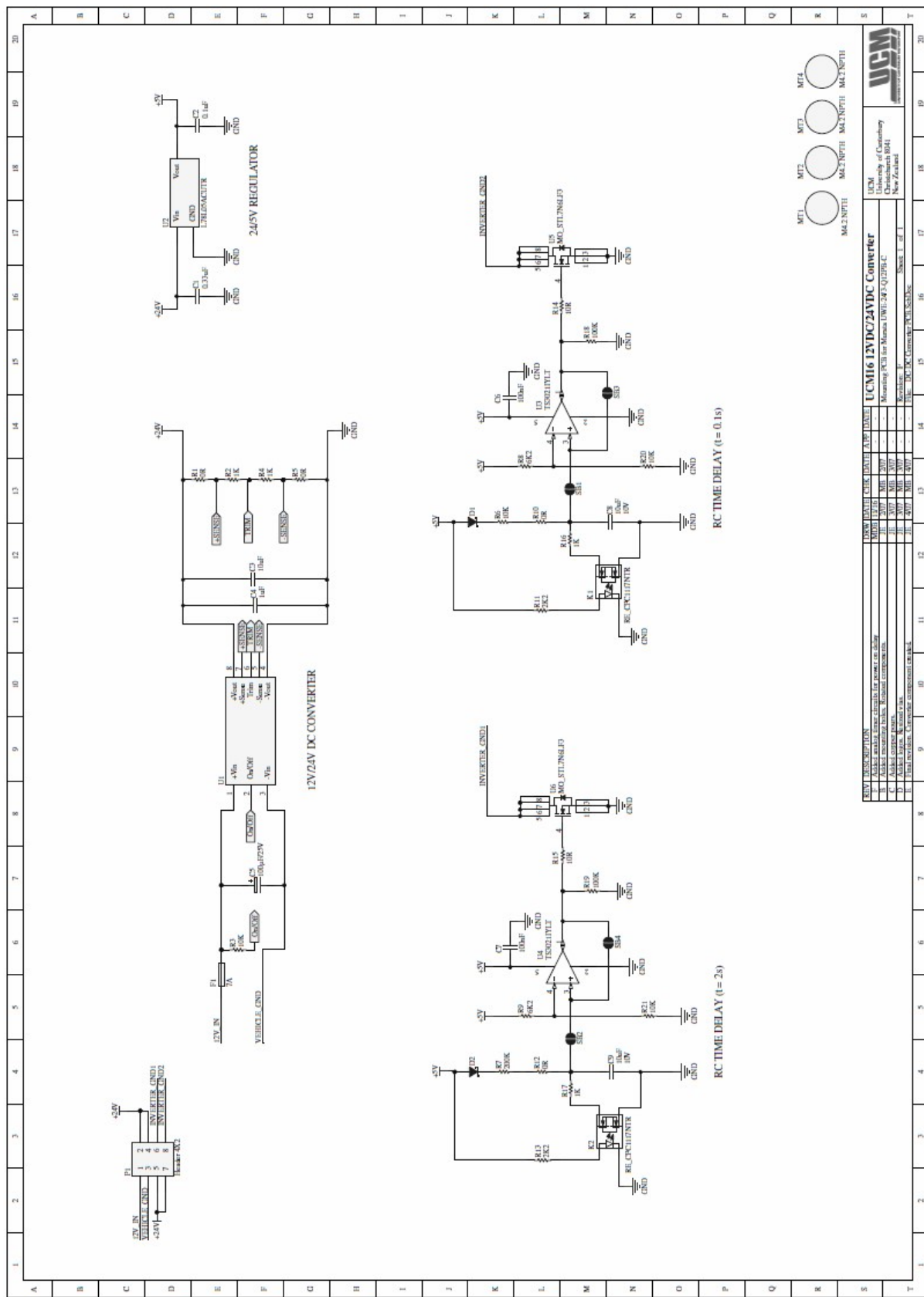
IMAGES OF INVERTER WIRING





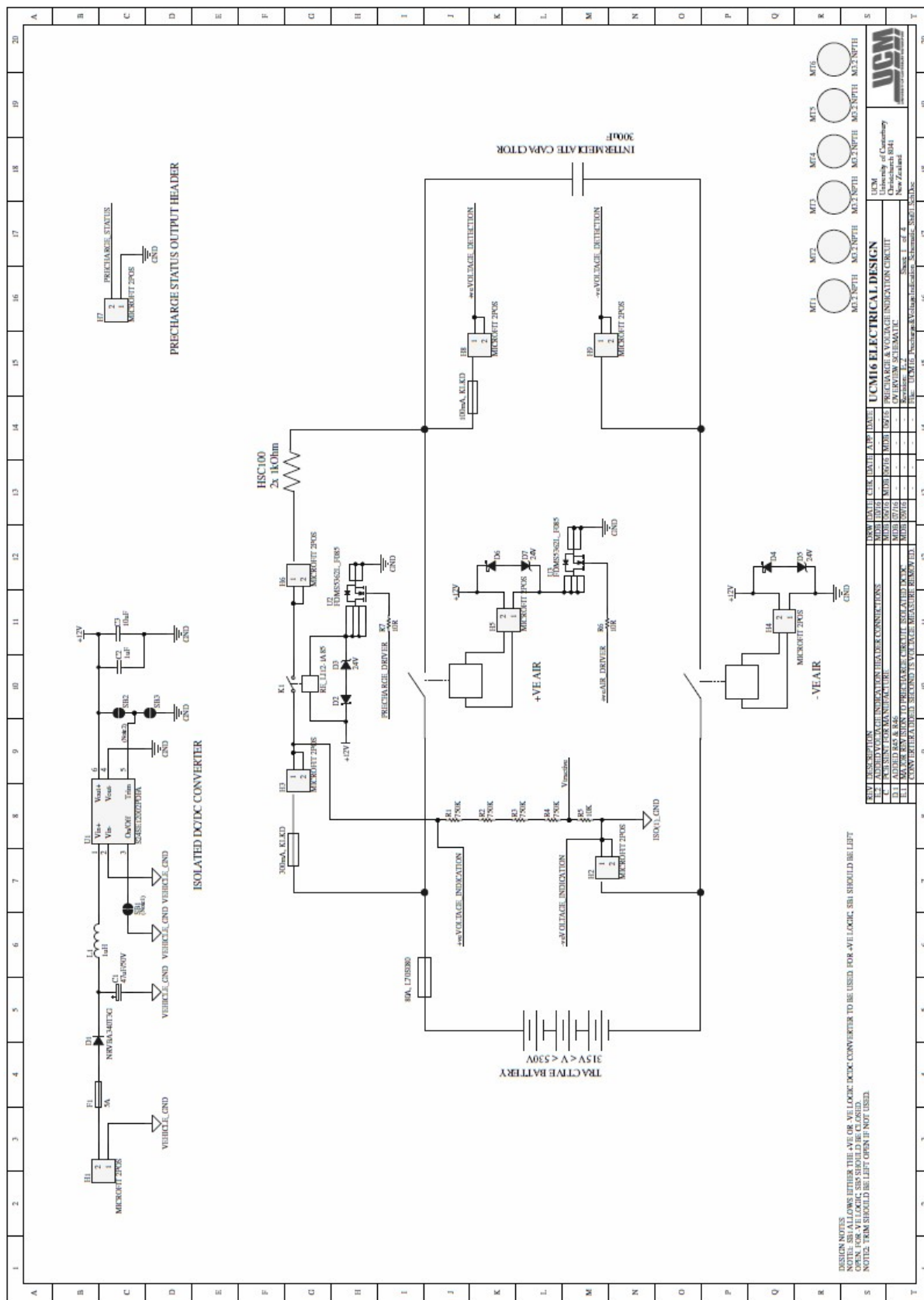
APPENDIX N

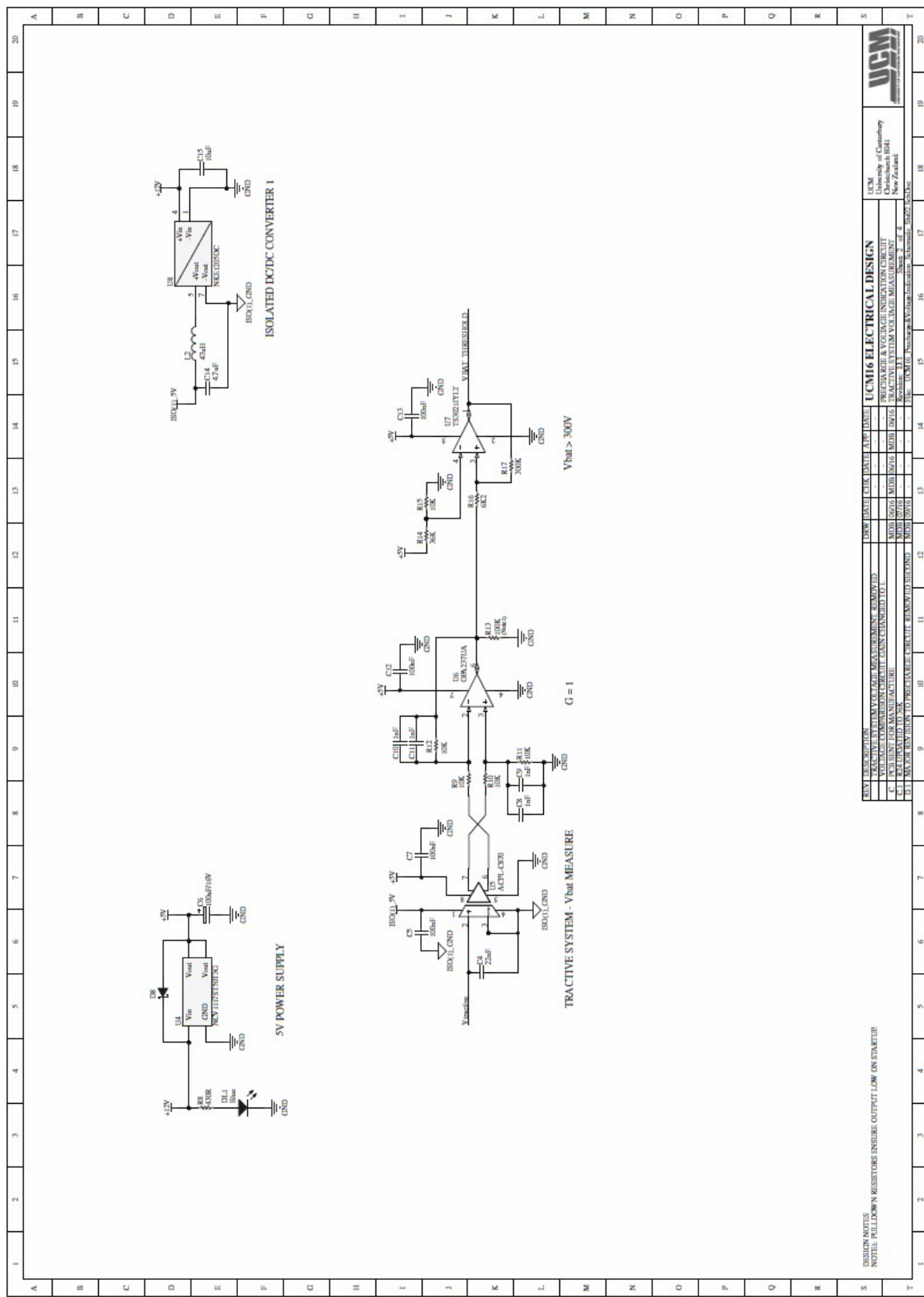
DC/DC CONVERTER SCHEMATIC

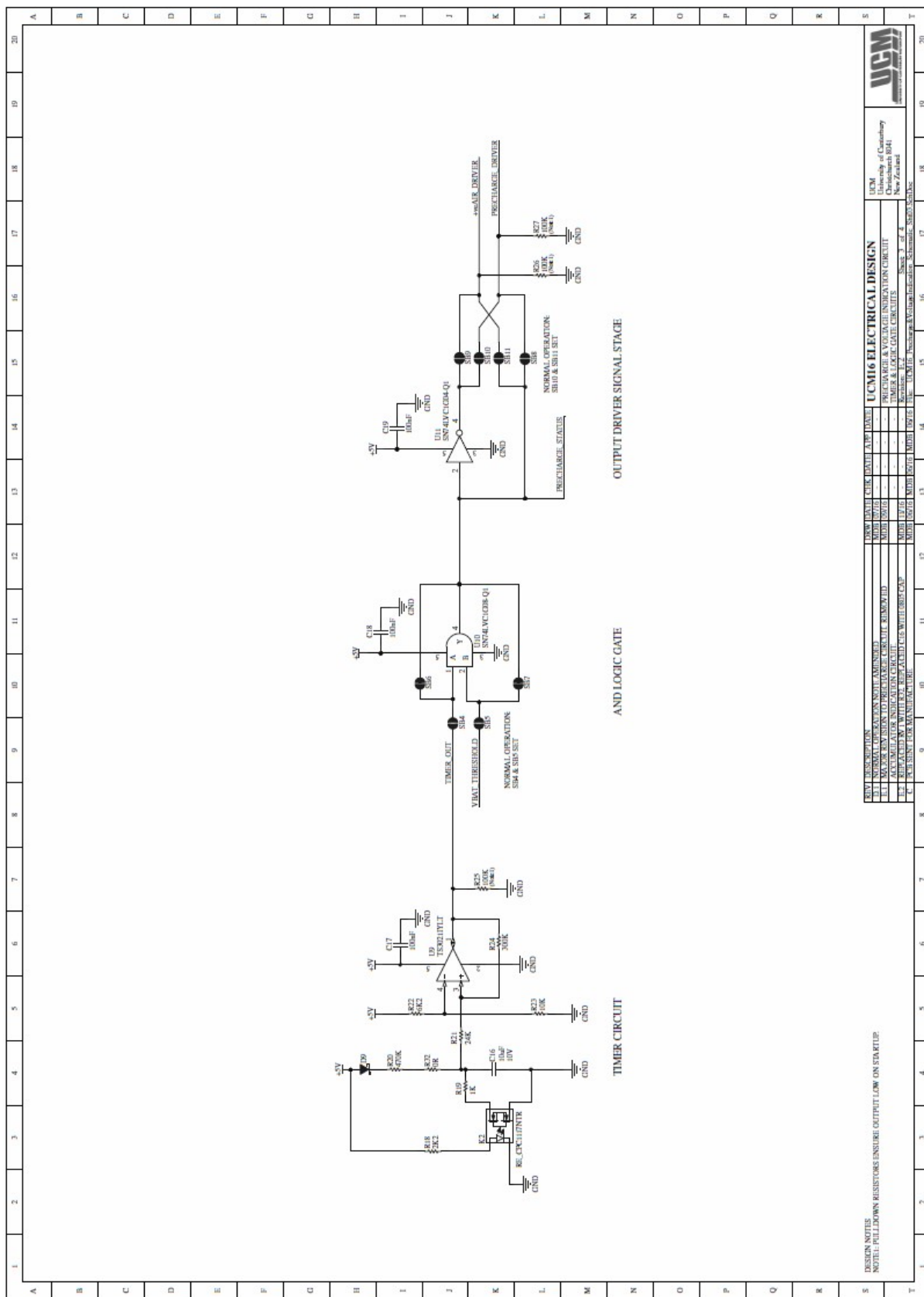


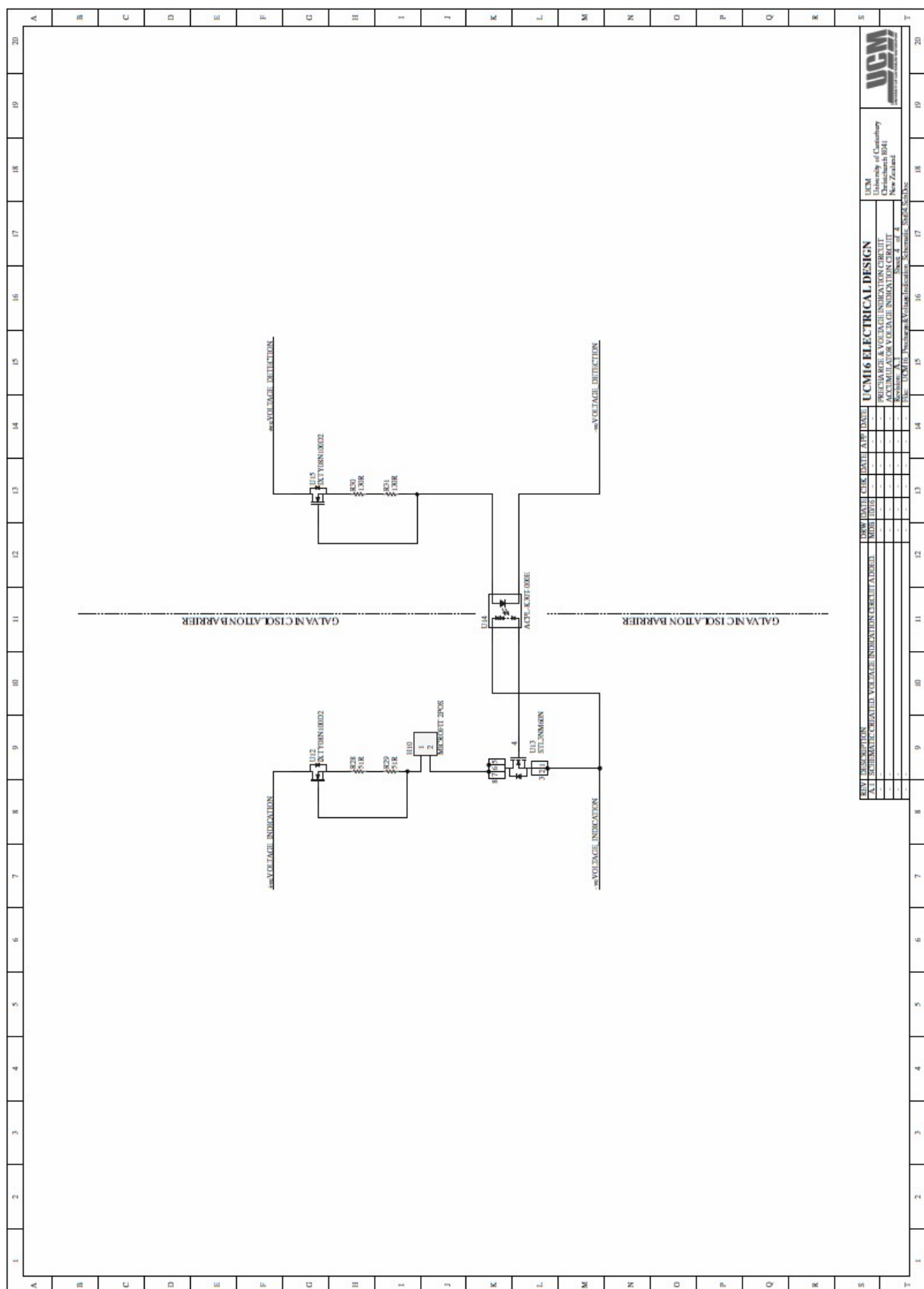
APPENDIX O

REDESIGNED PRECHARGE PCB SCHEMATICS



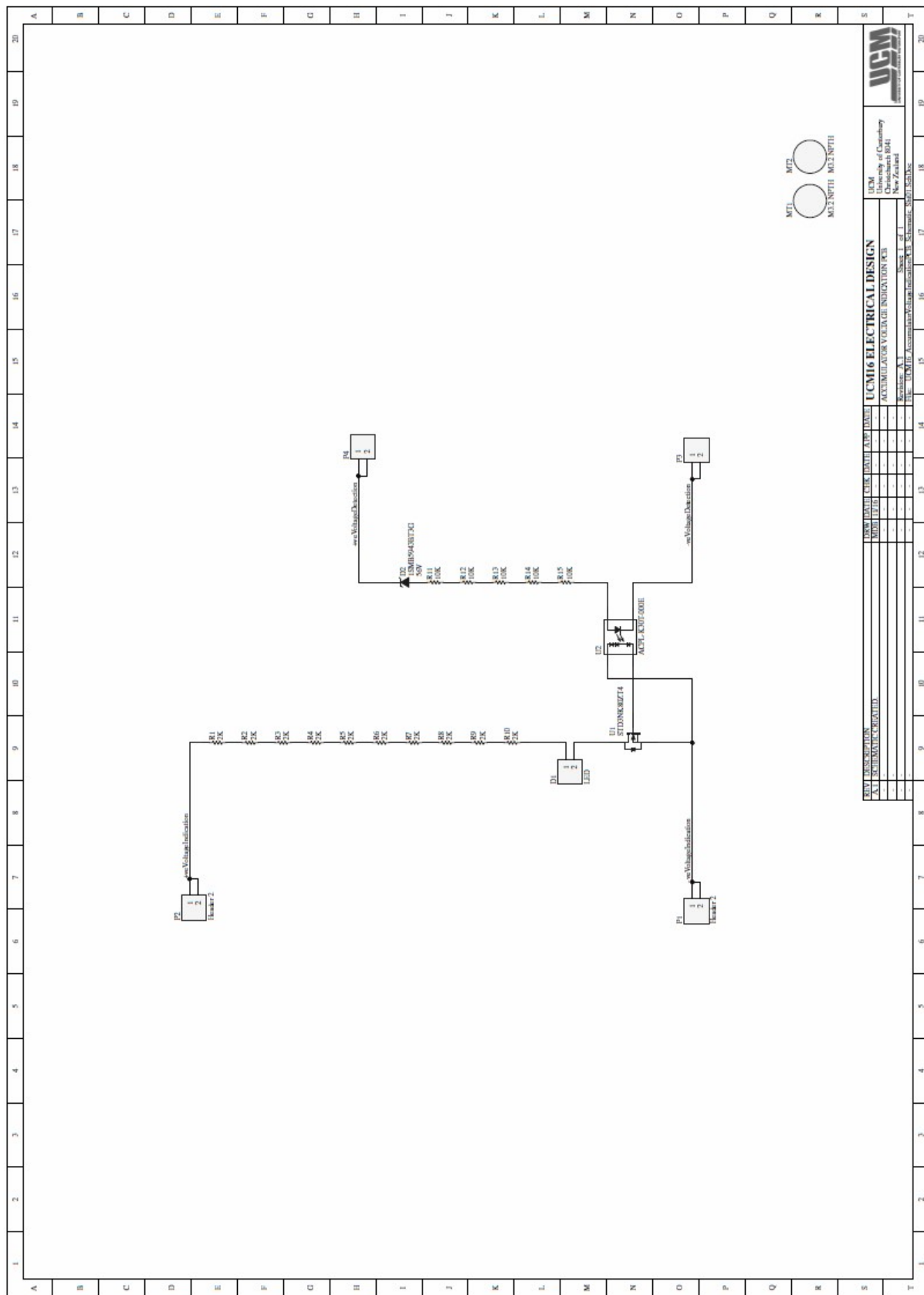


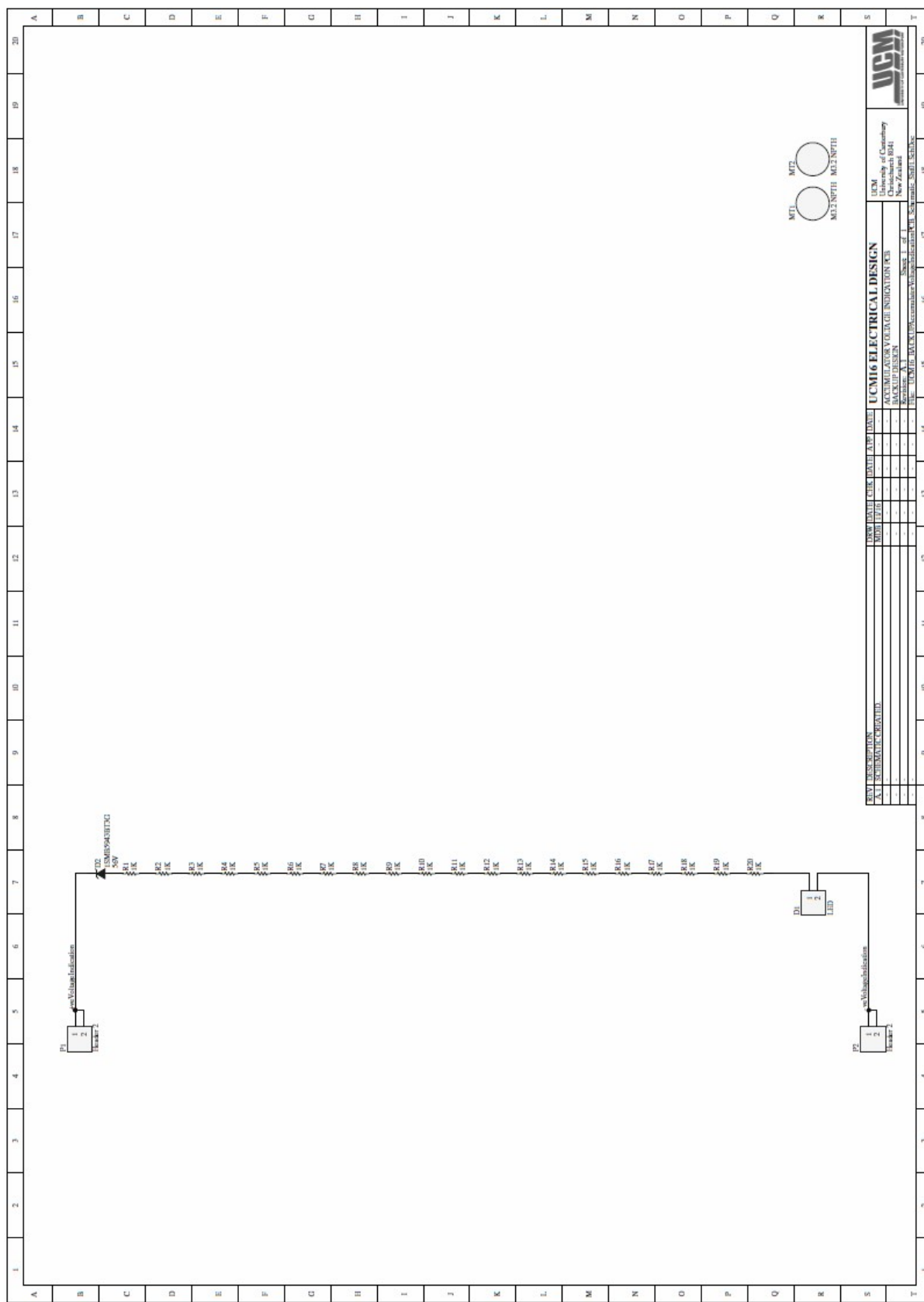




APPENDIX P

VOLTAGE INDICATION PCB SCHEMATICS





REFERENCES

- [1] SAE International, “History of Formula SAE,” n.d.. [Online]. [Accessed March 2017].
- [2] Mazur, “Formula Student Combustion - World Ranking List,” 2017. [Online]. Available: <https://mazur-events.de/fs-world/C/>. [Accessed March 2017].
- [3] Mazur, “Formula Student Electric - World Ranking List,” 2017. [Online]. Available: <https://mazur-events.de/fs-world/E/>. [Accessed Jan 2017].
- [4] Institution of Mechanical Engineers, “About Formula Student,” 2016. [Online]. Available: <http://www.imeche.org/events/formula-student/about-formula-student>. [Accessed March 2017].
- [5] SAE International, “2015 Formula SAE Rules,” Sep 2014. [Online]. Available: http://www.sae.org/images/cds/selfservice/410986855_2015-16%20FSAE%20Rules%20revision%2091714%20kz.pdf. [Accessed Jan 2017].
- [6] Formula SAE-Australasia, “Local Addendum to Formula SAE 2016 Rules,” 1 March 2016. [Online]. Available: <http://www.saea.com.au/resources/Documents/FORMULA%20SAE-A%20Addendum%202016.pdf>. [Accessed April 2017].
- [7] J. S. Reid, “Robert Davidson - pioneer electrician,” n.d.. [Online]. Available: <https://homepages.adbn.ac.uk/npmuseum/Scitour/Davidson.pdf>. [Accessed June 2017].
- [8] Z. Shahan, “Electric Car Evolution,” Clean Technica, 26 April 2015. [Online]. Available: <https://cleantechnica.com/2015/04/26/electric-car-history/>. [Accessed April 2017].
- [9] International Energy Agency, “Global EV Outlook 2016,” 2016. [Online]. Available: https://www.iea.org/publications/freepublications/publication/Global_EV_Outlook_2016.pdf. [Accessed March 2017].
- [10] Clean Energy Ministerial, “Fact Sheet: Electric Vehicles Initiative,” May 2015. [Online]. Available: <http://www.cleanenergyministerial.org/Portals/2/pdfs/factsheets/EVI-CEM6FactSheet.pdf>. [Accessed April 2017].

- [11] A. Miller, “How motorsport has changed every car on the road,” Thrillist, 2 December 2016. [Online]. Available: <https://www.thrillist.com/cars/nation/motorsports-racing-cars-automotive-engineering>. [Accessed April 2017].
- [12] Formula One World Championship Limited, “Understanding F1 Racing: Aerodynamics,” n.d.. [Online]. Available: <https://www.formula1.com/en/championship/inside-f1/understanding-f1-racing/Aerodynamics.html>. [Accessed April 2017].
- [13] McLaren Honda Formula One Team, “History of the F1 Engine,” 19 February 2016. [Online]. Available: <http://www.mclaren.com/formula1/car/history-of-the-f1-engine/>. [Accessed April 2017].
- [14] A123 Systems, “Case Study: Mercedes-Benz High Performance Engines,” n.d.. [Online]. Available: <http://www.a123systems.com/baef9f26-39e3-4173-8d99-fe08ad5130af/resources-detail.htm>. [Accessed April 2017].
- [15] FIA Formula E Championship, “Specification,” 2015. [Online]. Available: <http://www.fiaformulae.com/en/guide/car.aspx?page=1334>. [Accessed 27 May 2015].
- [16] FIA Formula E Championship, “FIA Formula E Championship Overview,” n.d.. [Online]. Available: <http://www.fiaformulae.com/en/championship/overview/>. [Accessed April 2017].
- [17] S. O’Kane, “Here’s why Jaguar, BMW, and Faraday Future all joined Formula E, the all-electric racing series,” The Verge, 7 October 2016. [Online]. Available: <http://www.theverge.com/2016/10/7/12076876/formula-e-season-3-electric-racing-jaguar-bmw-faraday-future-preview>. [Accessed April 2017].
- [18] FIA Formula E Championship, “Formula E: Teams and Drivers,” n.d.. [Online]. Available: <http://www.fiaformulae.com/en/championship/teams-and-drivers/>. [Accessed April 2017].
- [19] RMIT Electric Racing, “The Cars: 2008,” n.d.. [Online]. Available: <http://rmitelectricracing.com/2008/>. [Accessed April 2017].
- [20] Formula Student Germany, “2010 Formula Student Electric Rules,” August 2008. [Online]. Available: http://www.formulastudent.de/uploads/media/FSE_Rules_2010_v1.1.pdf. [Accessed April 2017].
- [21] Formula Student Germany (Peter Jakowski), “FSE Overall Results (2010),” 9 August 2010. [Online]. Available:

https://www.formulastudent.de/uploads/media/2010_FSE_Competition_Results_overall_01.pdf. [Accessed April 2017].

- [22] J. de Santiago, H. Bernhoff, B. Ekergard, S. Eriksson, S. Ferhatovic, R. Waters and M. Leijon, "Electrical Motor Drivelines in Commercial All-Electric Vehicles: A Review," *IEEE Transactions on Vehicular Technology*, vol. 61, no. 2, pp. 475 - 484, 2012.
- [23] J. Murphy, "What's the Difference Between AC Induction, Permanent Magnet, and Servomotor Technologies?," *Machine Design*, 1 Apr 2012. [Online]. Available: <http://machinedesign.com/motorsdrives/whats-difference-between-ac-induction-permanent-magnet-and-servomotor-technologies>. [Accessed Jan 2017].
- [24] N. Mohan, T. M. Undeland and W. P. Robbins, *Power Electronics. Converters, Applications and Design*, John Wiley & Sons, Inc., 2003.
- [25] Freescale Semiconductor, "3-phase BLDC Motor Control with Sensorless Back-EMF ADC Zero Crossing Detection using 56F80x," Nov 2005. [Online]. Available: <http://www.nxp.com/assets/documents/data/en/application-notes/AN1913.pdf>. [Accessed Jan 2017].
- [26] Z. Q. Zhu and D. Howe, "Electrical Machines and Drives for Electric, Hybrid, and Fuel Cell Vehicles," *Proceedings of the IEEE*, vol. 95, no. 4, pp. 746 - 765, 2007.
- [27] B. Akin and M. Bhardwaj, "Sensorless Field Oriented Control of 3-Phase Permanent Magnet Synchronous Motors," July 2013. [Online]. Available: <http://www.ti.com/lit/an/sprabq3/sprabq3.pdf>. [Accessed Jan 2017].
- [28] P. Yedamale, "AN885: Brushless DC (BLDC) Motor Fundamentals," 2003. [Online]. Available: http://download.ourdev.cn/bbs_upload782111/files_11/ourdev_469172.pdf. [Accessed Jan 2017].
- [29] S. S. Kuruppu and J. K. Rote, "Replacing single-phase ACIMs with three-phase BLDC motors saves energy," Apr 2016. [Online]. Available: <http://www.ti.com/lit/wp/slyy083/slyy083.pdf>. [Accessed Jan 2017].
- [30] W. Rippel, "Induction Versus DC Brushless Motors," Tesla Motors, 7 Jan 2007. [Online]. Available: <https://www.tesla.com/blog/induction-versus-dc-brushless-motors>. [Accessed Jan 2017].

- [31] J. G. West, "DC, induction, reluctance and PM motors for electric vehicles," *Power Engineering Journal*, vol. 8, no. 2, pp. 77 - 88, 1994.
- [32] M. Yildirim, M. Polat and H. Kurum, "A Survey on Comparison of Electric Motor Types and Drives used for Electric Vehicles," in *16th International Power Electronics and Motion Control Conference and Exposition*, Antalya, 2014.
- [33] M. Zeraoulia, M. El Hachemi Benbouzid and D. Diallo, "Electric Motor Drive Selection Issues for HEV Propulsion Systems: A Comparative Study," *IEEE Transactions on Vehicular Technology*, vol. 55, no. 6, pp. 1756 - 1764, 2006.
- [34] STMicroelectronics, "Low cost self-synchronizing PMAC motor drive using ST7FLITE35," Mar 2006. [Online]. Available: http://www.st.com/content/ccc/resource/technical/document/application_note/69/1b/4b/3b/26/d8/47/0a/CD00081382.pdf/files/CD00081382.pdf/jcr:content/translations/en.CD00081382.pdf. [Accessed Jan 2017].
- [35] Freescale Semiconductor, Inc., "Sensorless PMSM Field-Oriented Control," Feb 2016. [Online]. Available: <http://cache.nxp.com/assets/documents/data/en/reference-manuals/DRM148.pdf>. [Accessed Jan 2017].
- [36] Y. Hori, "Future Vehicle Driven by Electricity and Control—Research on Four-Wheel-Motored "UOT Electric March II"," *IEEE TRANSACTIONS ON INDUSTRIAL ELECTRONICS*, vol. 51, no. 5, pp. 954 - 962, 2004.
- [37] M. Ahman, "Primary energy efficiency of alternative powertrains in vehicles," *Energy*, vol. 26, no. 11, pp. 973 - 989, 2001.
- [38] W. F. Milliken and D. L. Milliken, "Tire Behavior," in *Race Car Vehicle Dynamics*, Warrendale, Society of Automotive Engineers, 1995, p. 26.
- [39] L. De Novellis, A. Sorniotti, P. Gruber and A. Pennycott, "Comparison of Feedback Control Techniques for Torque-Vectoring Control of Fully Electric Vehicles," *IEEE Transactions on Vehicular Technology*, vol. 63, no. 8, pp. 3612 - 3623, 2014.
- [40] L. De Novellis, A. Sorniotti and P. Gruber, "Wheel Torque Distribution Criteria for Electric Vehicles with Torque-Vectoring Differentials," *IEEE Transactions on Vehicular Technology*, vol. 63, no. 4, pp. 1593 - 1602, 2014.

- [41] National Instruments, "Controller Area Network (CAN) Overview," Aug 2014. [Online]. Available: <http://www.ni.com/white-paper/2732/en/>. [Accessed Jan 2017].
- [42] Texas Instruments, "Introduction to the Controller Area Network (CAN)," July 2008. [Online]. Available: <http://www.ti.com/lit/an/sloa101a/sloa101a.pdf>. [Accessed Jan 2017].
- [43] M. M. Thackeray, C. Wolverton and E. D. Issacs, "Electrical energy storage for transportation - Approaching the limits of, and going beyond, lithium-ion batteries," *Energy and Environmental Science*, vol. 5, no. 7, pp. 7854-7863, 2012.
- [44] K. Young, C. Wang, L. Y. Wang and K. Strunz, "Electric Vehicle Battery Technologies," in *Electric Vehicle Integration into Modern Power Networks*, New York, Springer, 2013, pp. 15 - 56 .
- [45] Battery University, "BU-1003: Electric Vehicle (EV)," 2017. [Online]. Available: http://batteryuniversity.com/learn/article/electric_vehicle_ev. [Accessed Jan 2017].
- [46] M. M. Doeff, "Battery Cathodes," in *Batteries for Sustainability*, New York, Springer, 2012, pp. 5 - 49.
- [47] G. Mulder, N. Omar, S. Pauwels, M. Meeus, F. Leemans, B. Verbrugge, W. De Nijs, P. Van den Bossche, D. Six and J. Van Mierlo, "Comparison of commercial battery cells in relation to material properties," *Electrochimica Acta*, vol. 87, pp. 473 - 488, 2013.
- [48] Element Energy Limited, "Cost and performance of EV batteries," Element Energy Limited, Cambridge, 2012.
- [49] W. J. H. Hayt, J. E. Kemmerly and S. M. Durbin, "The Source-Free RC Circuit," in *Engineering Circuit Analysis*, New York, McGraw-Hill, 2012, pp. 272 - 275.
- [50] GreenTeam Uni Stuttgart, "World record attempt," 2017. [Online]. Available: <http://www.greenteam-stuttgart.de/en/world-record-attempt/>. [Accessed Jan 2017].
- [51] AMK Arnold Müller GmbH & Co. KG, "AMK RACING KIT 4 wheel drive "Formula Student Electric"," AMK Arnold Müller GmbH & Co. KG, Kirchheim/Teck, 2015.
- [52] Enstroj, "Technical Data Table for EMRAX 228 - December 2014," Dec 2014. [Online]. Available: <http://www.enstroj.si/Electric-products/emrax-228-motorsgen.html>. [Accessed Jan 2017].

- [53] Optimum G, “OptimumLap Documentation,” 2012. [Online]. Available: <http://www.optimumg.com/software/optimumlap/optimumlap-documentation/>. [Accessed Jan 2017].
- [54] Formula Student Team Delft, “DUT16 Design Presentation Live Stream,” 15 Jan 2016. [Online]. Available: <https://www.youtube.com/watch?v=cZMoflK1F-Y>. [Accessed Jan 2017].
- [55] A123 Systems, “Battery Pack Design, Validation, and Assembly Guide using A123 Systems AMP20M1HD-A Nanophosphate Cells,” 7 Feb 2014. [Online]. Available: http://www.formula-hybrid.org/wp-content/uploads/A123_AMP20_battery_Design_guide.pdf. [Accessed Jan 2017].
- [56] Shenzhen Melasta Battery Co., Ltd, *Product Specification Polymer Li-ion Battery V1 3.7V 8000mAh 15C (Model No.: SLPB7864155)*, Shenzhen, 2014.
- [57] Underwriters Laboratories, “Plastics Testing,” UL LLC, 2017. [Online]. Available: <http://industries.ul.com/plastics-and-components/plastics/plastics-testing>. [Accessed Jan 2017].
- [58] A123 Systems, “Cylindrical Battery Pack Design, Validation, and Assembly Guide,” Feb 2013. [Online]. Available: <http://www.formula-hybrid.org/wp-content/uploads/A123-Pack-Design-Guide-for-Cylindrical-Cells.pdf>. [Accessed Feb 2017].
- [59] Samsung SDI, “Specification of Product, INR18650-25R,” 2013.
- [60] TE Connectivity, “Aluminium Housed Power Resistors - Type HS Series,” Oct 2011. [Online]. Available: <http://www.te.com/commerce/DocumentDelivery/DDEController?Action=srchrtrv&DocNm=1625966&DocType=Customer+Drawing&DocLang=English>. [Accessed Jan 2017].
- [61] Gigavac, “Coil Suppression,” 2016. [Online]. Available: <http://www.gigavac.com/application-notes/high-voltage-relays/coil-supression>. [Accessed Jan 2017].
- [62] P. K. Tamma, “Applications for Depletion MOSFET,” 03 Feb 2015. [Online]. Available: http://www.infineon.com/dgdl/Infineon-Application_Note_Applications_for_Depletion_MOSFETs-AN-v01_00-EN.pdf?fileId=5546d4624cb7f111014cd63d1a197d94. [Accessed Jan 2017].
- [63] Kingbright, “APTD1608LSECK/J4-PF Datasheet,” Apr 2016. [Online]. Available: <http://www.kingbrightusa.com/images/catalog/SPEC/APTD1608LSECK-J4-PF.pdf>. [Accessed Jan 2017].

- [64] Molex, “Product Specification Micro-fit,” 27 Oct 2016. [Online]. Available: http://www.molex.com/pdm_docs/ps/PS-43045.pdf. [Accessed Feb 2017].
- [65] Coto Technology, “5500 Series / High Voltage Reed Relays,” 2017. [Online]. Available: <http://cotorelay.com/product/5500-series-high-voltage-reed-relays/>. [Accessed Jan 2017].
- [66] Gigavac, “G81B Datasheet,” n.d.. [Online]. Available: http://www.gigavac.com/sites/default/files/catalog/spec_sheet/g81b.pdf. [Accessed Jan 2017].
- [67] IXYS, “IXTY1R6N100D2 Depletion Mode MOSFET,” 2011. [Online]. Available: [http://ixapps.ixys.com/DataSheet/DS100185B\(IXTY-TA-TP1R6N100D2\).pdf](http://ixapps.ixys.com/DataSheet/DS100185B(IXTY-TA-TP1R6N100D2).pdf). [Accessed Jan 2017].
- [68] TE Connectivity, “Kilovac LEV100 Series 900 Vdc Contactor,” 2017. [Online]. Available: [http://www.te.com/commerce/DocumentDelivery/DDEController?Action=srchtrv&DocNm=6-1773450-9_LEV100_0908.pdf](http://www.te.com/commerce/DocumentDelivery/DDEController?Action=srchtrv&DocNm=6-1773450-9_LEV100&DocType=DS&DocLang=English&DocFilename=ENG_DS_6-1773450-9_LEV100_0908.pdf). [Accessed Jan 2017].
- [69] IPC-2221 Task Group, “IPC-2221B: Generic Standard on Printed Board Design,” IPC, Bannockburn, 2012.
- [70] Elithion, “Installing and programming a Brusa charger with a Lithiumate BMS,” morninglori, 2017. [Online]. Available: <http://lithiumate.elithion.com/php/brusa.php>. [Accessed Feb 2017].
- [71] Bender, “Operating principle of an insulation monitoring device,” Bender GmbH & Co. KG, n.d.. [Online]. Available: <https://www.bender-de.com/en/know-how/it-system/operating-principle-of-an-insulation-monitoring-device.html#>. [Accessed Jan 2017].
- [72] LEM, “Current Transducer HASS 50 .. 600-S,” Nov 2014. [Online]. Available: http://www.lem.com/docs/products/hass_50_600-s.pdf. [Accessed Jan 2017].
- [73] Murata Power Solutions, “UWE Series,” n.d.. [Online]. Available: <http://power.murata.com/data/power/uwe.pdf>. [Accessed Feb 2017].
- [74] Souriau, “8STA/8TA Series Compact Circular Connectors,” n.d.. [Online]. Available: www.souriau.com/fileadmin/Souriau/product_pdf/8STA-8TA-Series.pdf. [Accessed Feb 2017].
- [75] Murata Power Solutions, “NKE Series Datasheet,” n.d.. [Online]. Available: http://power.murata.com/data/power/ncl/kdc_nke.pdf. [Accessed Feb 2017].

- [76] W. Toet, “Innovative problem solving & surprising results at F-SAE-A,” LinkedIn, 7 February 2017. [Online]. Available: <https://www.linkedin.com/pulse/innovative-problem-solving-surprising-results-f-sae-a-willem-toet?trk=hp-feed-article-title-share>. [Accessed April 2017].
- [77] Littelfuse, “L70S Series High-Speed Fuse,” 2015. [Online]. Available: <http://www.littelfuse.com/~/media/electrical/datasheets/fuses/semiconductor-fuses/littelfuse-fuse-l70s-datasheet.pdf>. [Accessed Jan 2017].
- [78] Littelfuse, “KLKD Series 10x38 Fuses,” 2015. [Online]. Available: http://www.littelfuse.com/~/media/electrical/datasheets/fuses/industrial-and-ul-fuses/littelfuse_fuse_klkd_datasheet.pdf. [Accessed Jan 2017].

